



UNIVERSITY OF OTTAWA

Numerical Modelling of Gas Migration from a DGR in Ontario's Sedimentary Rocks

**Final report
Prepared by**

**Dr. Mamadou Fall
Associate Professor
Department of Civil Engineering
University of Ottawa**

and

**Othman Nasir, PEng
Department of Civil Engineering
University of Ottawa**

3/28/2012

**Safety-Related Aspects of a Radioactive Waste Repository in Sedimentary
Rock Formations - Generation and Migration of Gas from the Waste
Repository**

**Numerical Modelling of Gas Migration from a DGR in
Ontario's Sedimentary Rocks**

Final report

Prepared by

Dr. Mamadou Fall
Associate Professor
Department of Civil Engineering
University of Ottawa

and

Othman Nasir, PEng
Department of Civil Engineering
University of Ottawa

A report submitted to the CNSC

Ottawa, Canada, March 28th, 2012

Contract No. and Title: 87055-08-1075: R413.3 - "Coordinated Assessment and Research Program on Safety-Related Aspects of a Radioactive Waste Repository in Sedimentary Rock Formations: Generation and Migration of Gas from the Waste Repository"

Preface

Gas generation and migration from a nuclear waste repository have potential implications on its long term safety. In order to assess the above implications, an understanding of the mechanisms responsible for gas generation and migration is needed. Therefore, the Canadian Nuclear Safety Commission (CNSC) is contributing to the present study. The study consists of the development of mathematical models of gas migration in sedimentary rock formations and their use in performing scoping calculations for gas migration from a proposed deep geological repository for low and intermediate wastes in Ontario. The principal investigator of the project is Prof. Mamadou Fall.

Contents

Preface.....	3
1 Introduction.....	6
2 Background and literature review	9
2.1 Gas generation and transport mechanisms.....	9
2.1.1 Gas generation mechanisms.....	9
2.1.2 Gas transport paths and mechanisms	14
2.2 Main conceptual and modelling approaches for simulation of gas generation and transport	20
2.2.1 Models for predicting and simulating gas generation.....	20
2.2.2 Conceptual and modeling approaches for simulating gas transport	25
2.3 Case studies on gas generation and migration	40
2.3.1 Laboratories studies	40
2.3.2 Field studies	48
2.4 Summary and Conclusions	58
3 Geological and geotechnical characteristics of sedimentary rock formations in Ontario and comparison with European formations	61
3.1 Introduction.....	61
3.2 Review of geomechanical, geochemical, hydraulic and thermal properties of sedimentary rock formations in Southwest Ontario	62
3.2.1 Geological and geomechanical properties	63
3.2.2 Hydraulic and hydrochemical properties	73
3.2.3 Thermal properties	77
3.3 Review of experimental data related to gas migration in European low permeable formations	80
3.3.1 Introduction.....	80
3.3.2 Gas transport properties of Opalinus clay.....	81
3.3.3 Boom Clay	88
3.3.4 Gas migration test (GMT) at the Grimsel Test Site (Switzerland)	91
3.3.5 Gas threshold pressure test at Andra underground research laboratory, Bure (France)	95
3.3.6 Relevant gas migration behaviour in low permeability samples (small-scale tests) ...	98
3.4 Comparison, Discussion and Analysis of the Collected Data and Results	102
3.4.1 Introduction.....	102
3.4.1 Comparison and discussion of geomechanical, geochemical, hydraulic and thermal data on sedimentary host rock formations from Ontario and Europe.....	103
3.5 Gas migration.....	110
3.6 Conclusion	111
4 Development and validation of a mathematical model to predict gas migration from in DGR in sedimentary rocks	113
4.1 Introduction.....	113
4.2 Development of the THM model.....	114
4.2.1 Basis of the mathematical formulations and general assumptions	114
4.2.2 Mechanical response.....	115
4.2.3 Solid mass conservation equations	121
4.2.4 Liquid flow model.....	123

4.2.5 Gas flow model	131
4.2.6 Heat transport.....	139
4.3 Model validation against experimental data and simulation.....	141
4.3.1 Introduction.....	141
4.3.2 Model validation against laboratory tests and numerical simulations	141
4.3.3 Model validation against field tests	150
4.4 Conclusion	157
5 Numerical simulations of gas injection tests and gas migration from in DGR in Ontario's sedimentary rocks	158
5.1 Model conceptualization, initial and boundary conditions	158
5.2 Simulation results.....	160
6 Conclusion	169
7 References.....	171

1 Introduction

Significant quantities of gas could be generated in underground repositories for radioactive waste from several processes, such as the degradation of waste forms or corrosion of waste containers. These gases could migrate through engineered and natural geological barrier systems. The gas pressure buildup if sufficiently large could induce the formation of either microcracks or macrocracks, which would affect the integrity of the barriers and geosphere as a long-term contaminant barrier (Figure 1.1). Furthermore, these gases could significantly impact the biosphere and groundwater as shown in Figure 1.1. Thus, the assessment of the long term safety of a repository for nuclear waste in deep geological rock formation requires a good understanding of the mechanisms of gas generation and migration as well as their effects on the mechanical (M) and hydraulic (H) stability of the geosphere.

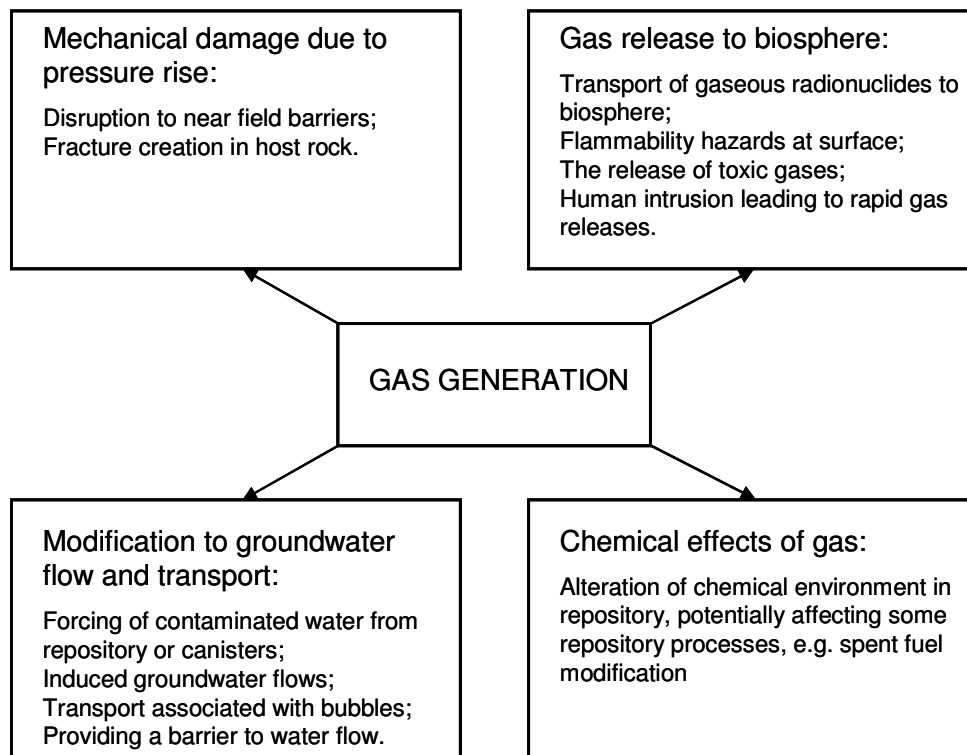


Figure 1.1. Schematic of the range of effects that may follow from gas generation in a repository (Rodwell et al. 2003)

At the time of writing, the implications of gas generation and migration on the long term safety of underground repositories for radioactive waste are the subject of very active research activities. The objective of these research activities is to improve the understanding of the mechanisms of

gas generation and migration and their effects on mechanical (M), and hydraulic (H) stability of the geosphere. The CNSC is contributing to the present study in order to obtain independent tools and data for the assessment of gas generation and migration from proposed geological repositories.

The study consists of the following steps:

- To review current experimental and theoretical research on Thermal-Hydraulic-Mechanical-Chemical disturbances in sedimentary rock due to gas generation from a repository in sedimentary rock formations. Particular attention is given to state-of-art conceptual and mathematical models for simulation of gas generation and transport.
- To compile published geochemical, mechanical, hydraulic and thermal data on sedimentary rock formations in Ontario, which are relevant to the study of gas generation and transport. Compare the data to those from European sedimentary rocks. Discuss and analyze the usefulness and transferability of the research results in Europe to the Ontario situation.
- To develop constitutive relationships and mathematical models to determine the THMC disturbances of sedimentary rock due to gas generation from a repository. The development of the models should be calibrated with results from in-situ tests performed in underground research laboratories (e.g., Tournemire in France, Mont-Terri in Switzerland).
- By using the developed model, to perform mathematical modeling of the impact of gas generation on a hypothetical repository in Ontario sedimentary rocks.

The report describes the results of the study, and will be organized as follows. **Chapter 1** provides an introduction to the issues that will be addressed and the objectives of the project. **Chapter 2** deals with the following points: (i) the mechanisms of gas generation and transport in underground repositories for radioactive waste are presented , (ii) this is followed by a review of the main concepts and modelling approaches with regards to the simulation of gas generation and transport through engineered and natural barriers, (iii)and finally relevant case studies carried out in laboratories and/or in European Underground Research Laboratories (URLs) will be presented and discussed. **Chapter 3** presents a review and analysis of the existing geological and geotechnical data from Ontario's sedimentary rocks, which are relevant to the study of gas

generation and transport. Furthermore, the aforementioned data are compared with those from European sedimentary rocks. This is followed by the discussion about usefulness and transferability of the research results in Europe to the Ontario situation. **Chapter 4** deals with the development and verification of a mathematical model for the prediction of gas migration from a Deep Geological Repository (DGR) for nuclear wastes as well as for the assessment of the impacts of gas migration on sedimentary rocks. **Chapter 5** presents the application of the developed mathematical model to numerically analyze the gas migration from a proposed DGR for low and intermediate level wastes in Ontario's sedimentary rocks and the disturbance of the sedimentary rocks by the gas generation and transport. **Chapter 6** presents our conclusion.

2 Background and literature review

2.1 Gas generation and transport mechanisms

This chapter presents the current understanding of the main mechanisms of gas generation and migration in underground radioactive waste repositories.

2.1.1 Gas generation mechanisms

In deep repositories, several mechanisms have been identified which could contribute to gas generation in different degrees. The main gas generation mechanisms are:

- The anaerobic corrosion of metals in waste and packaging (production of hydrogen).
- The radiolysis of water and certain organic materials in packaging (mainly production of hydrogen; also oxygen, carbon dioxide, methane, etc., which can be produced in lower quantities).
- The microbial degradation of organic waste components (production of methane and carbon dioxide).

The gas generating materials will be mainly the wastes and their containers. However, in some repository concepts, there may also be significant quantities of “construction” steel, including for example, rock bolts, abandoned machinery, and concrete reinforcement (Rodwell et al. 2003). The gas generation rates are likely to be significantly higher for repositories with Intermediate Level Waste (ILW) and Low Level Waste (LLW) than for those for High Level Waste (HLW) or spent fuel. The reason is that there are larger volumes of metals and organic materials in the former compared to the two latter (Rodwell 1999) types of repositories. The aforementioned gas generation mechanisms are described below.

2.1.1.1 Corrosion of metals

The following metals are considered corrodible: iron (including carbon steel and various stainless steels): "Inconel" (refers to a family of austenitic nickel-chromium-based superalloys), aluminium, zinc, magnesium, Zircaloy, lead, and the alloy "Ag80/In15/Cd5" (Nagra 2008). Several studies have been conducted on gas generation through the corrosion of metals. Most of these studies focussed on gas generation through iron corrosion. The reason is that iron is the dominating metallic component in radioactive waste, waste packaging and eventually, the

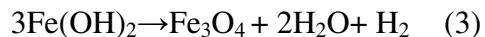
engineered structure of a repository. Corrosion is an electrochemical process by which a metal is transformed into a higher oxidation rate, i.e. the metal releases electrons. Under repository conditions, oxygen and water are mainly considered for this process (Mueller 2000).

It is widely accepted that the largest source of gas generation will be the anaerobic corrosion of iron. Indeed, after closure of an underground nuclear waste repository, anaerobic conditions will be reached rapidly in the repository (within a few hundred years). Two chemical reactions are involved in anaerobic corrosion (Ortiz et al. 2001):



Corrosion may further depend on a number of physical and chemical parameters, some of which have been studied for their effects on gas generation extensively. Examples of such physical parameters are temperature, pressure and radiation. The primary chemical factor is the waste itself. In addition, the geochemical conditions determined by the groundwater composition and the host rock material have to be considered. Investigations normally use groundwater samples or comparable synthetic solutions to cope with the latter parameter. Other chemical factors that have been checked in experiments include pH value, Eh value, mineralisation of groundwater (salt content) and impurities contained in the groundwater (Mueller 2000).

For example, the ferrous hydroxide shown in Equation 2 is metastable in low temperature anaerobic groundwater environments (Reardon, 1995) and converts thermodynamically to magnetite according to the Schikorr reaction (Schikorr, 1929):



The presence of some catalysts (such as surfaces containing nickel) as well as dissolved oxygen can lower the activation energy of this reaction (Joshi et al. 1993) and accelerate the transformation process.

In practice, most safety assessments prescribe a constant metal corrosion rate, in conjunction with estimates of the metal surface areas in order to determine the rates of gas generation. Table 2.1 summarises some typical corrosion rates in different host rock environments. The values are meant as indicators for the range of corrosion rates that might be expected. For a detailed

assessment, the individual site and concept specific conditions have to be taken into regard, which can lead to substantial changes in corrosion rates (Mueller 2000).

Table 2.1. Typical corrosion rates in different geological environments (in $\mu\text{m/a}$; Mueller 2000).

Material	Hard rock	Clay	Salt
Iron			
low allow steel			
• ca. 25	1	2	0
• ca. 50	0-6.5	-	0.1
• ca. 90	1-2.5	5-8	0.2-2
• ca. 150	-	9	0.1-0.5
cast iron/steel			
• ca. 25	-	0	0
• ca. 50	-		0
• ca. 90	0-5		0-5
• ca. 150	1.7-13		25
copper/Cu alloys	0	0	-
titanium	0-0.15	0	0-0.5

2.1.1.2 Radiolysis

Over the past decade, consideration has been given to radiolysis as a source of gas generation by several research groups. Internal and external radiolyses have been recognized as the two mechanisms that can lead to the decomposition of chemical compounds by radiation (Mueller 2000). Internal radiolysis means processes that take place in the waste product and its packaging. External radiolysis occurs in the backfill material that surrounds the waste and possibly in the host rock. Inside the waste packages, all kinds of radiation (α , β , γ , n) may contribute to gas generation by radiolysis. In the backfill, γ -radiation dominates due to the shielding properties of the packaging.

Gas generation by radiolysis means that gases are produced as primary or secondary decomposition products of radiolytic processes (Mueller 2000). The leading example for this kind of reaction is the decomposition of water (H_2O) resulting under idealised conditions in the formation of stoichiometric amounts of hydrogen and oxygen gas. Since oxygen is generated in an atomic form, it normally reacts immediately with its environment. Therefore, gas generation by radiolysis of H_2O is commonly characterised by the amount of hydrogen produced per unit mass of substrate and applied radiation dose (Mueller 2000). This model implies a linear

relationship between gas generation and the applied dose, which is expressed by a constant; the so-called G value (Mueller 2000):

$$B = G \cdot D \cdot m$$

where

B = generated gas volume

D = radiation dose

m = mass of irradiated material.

G is specific for the generated gas – for example G(H₂) - and the irradiated material.

Mueller (2000) reported that internal radiolysis mainly appears with LLW and ILW and may have an effect on waste, the matrix and eventually, the container (e.g., if made from concrete). Typical G(H₂) values for different waste products are published in Rodwell et al. (1999), and Mueller (1992). Due to the low activity concentration, radiolysis in general, plays a secondary role for gas generation in these wastes. It is only for some cemented waste producing heat (fuel element hardware, dissolver sludge from reprocessing) that the contribution of internal radiolysis to total gas generation may be relevant.

In contrast, HLW gas generation by radiolysis happens mainly in the surrounding backfill or host rock material, since the waste contains nearly no material that may be decomposed by radiation. If thin-walled containers are used, this may even contribute to gas generation. Otherwise, the container walls have a shielding effect which substantially prevents gas generation (Mueller 2000).

However, this shielding ability may change in the long term if container degradation by corrosion allows for direct contact between the groundwater and waste. Table 2.2 provides some common G(H₂) values for different host rocks and backfill materials (Mueller 2000).

Table 2. 1. G(H₂) values (µl/kg.Gy) in host rock and backfill materials (Mueller 2000)

Material	G(H₂)
salt	0.002
granite	0.005 ¹⁾
clay	0.05-0.26
bentonite (α radiation)	2.3
concrete	0.14-0.7
¹⁾ assuming 0.2 % water content	

2.1.1.3 Microbial degradation

Gas generation from microbial degradation of organic wastes is only an issue for certain types of ILW and LLW (Rodwell 2003). As reported by Small et al. (2008), microbial generation of gas is particularly important for LLW/ILW that contains organic matter (Humphreys et al. 1997, Small et al. 2000, BNFL 2002a, Rodwell et al. 2003). Organic matter includes a variety of materials, such as cellulose waste materials, ion-exchange resins, bitumen, plastics, rubbers, and oils. Some organic wastes are easily degradable, such as cellulose, while others, such as plastics, resins and bitumen, may resist complete degradation. Carbon dioxide and CH₄ are the main gases produced by microbial degradation of organic matter. It is often assumed that carbon dioxide will react with cementitious backfill and be precipitated as calcium carbonate (Rodwell 2003). Furthermore, some bacteria are able to consume hydrogen, producing methane or hydrogen sulphide as observed in Belgian Boom clay (Rodwell 2003). If a reaction that produces methane occurs, it will reduce the rate and volume of total gas production.

However, it should be emphasized that there are some prerequisites for microbial gas generation to be considered when deriving the rates and limiting factors for gas generation potential. The proportion of microbial gas generation is influenced by several factors, such as: (i) the availability of H₂O; (ii) the existence of nutrients; and (iii) further environmental factors (pH value, temperature, oxygen supply, salinity or impurities in H₂O, radiation, and pressure).

Finally, it should be mentioned that an accurate assessment of microbial gas generation rates from organic waste is scientifically challenging. Many safety assessments rely on simple

bounding estimates of gas generation rates based on available experimental data in an attempt to ensure that these rates are the upper limits (Rodwell 2003). Only a few assessments have used complex computer models or codes to predict the rates of microbial gas generation from organic waste as will be discussed later in the report.

2.1.1.4 Other

There are other possible mechanisms that could contribute to gas generation, however the amount of gases produced would be generally less significant as compared to the previous mechanisms. These mechanisms are:

- (i) gas release from the host rock. However, the production of radioactive gas is insignificant relative to non-radioactive gases in term of volume; and
- (ii) radioactive decay or chemical reactions other than corrosion. The volume of gases that is produced may be significant compared to that for non-radioactive gases.

2.1.2 Gas transport paths and mechanisms

A crucial aspect in assessing the effects of gas generated in a repository is analyzing how the gas will migrate away from the repository (gas migration mechanisms), thus dissipating pressure rise and avoiding the ensuing consequences (Rodwell, 2003). However, in order to understand and predict gas migration, it is necessary to identify potential gas transport paths in a repository system.

2.1.2.1 Potential gas transport paths

Figure 2.1 shows a schematic sketch of the potential transport paths of gases generated in a repository. The transport routes of the gases include:

- The engineered barrier systems, backfill in the repository chambers, galleries and drifts and shafts(❶).
- The excavation-damaged zone (EDZ) around the backfilled and sealed underground structures (❷). The EDZ is generally considered as a hydraulic transition zone between the repository and host rock, and offers a more favourable transport medium (Alkan and Mueller 2008).

- The host and overlying rocks (⑤), and the transport through the host and overlying rocks, might also be disturbed by structural discontinuities, such as faults (④).

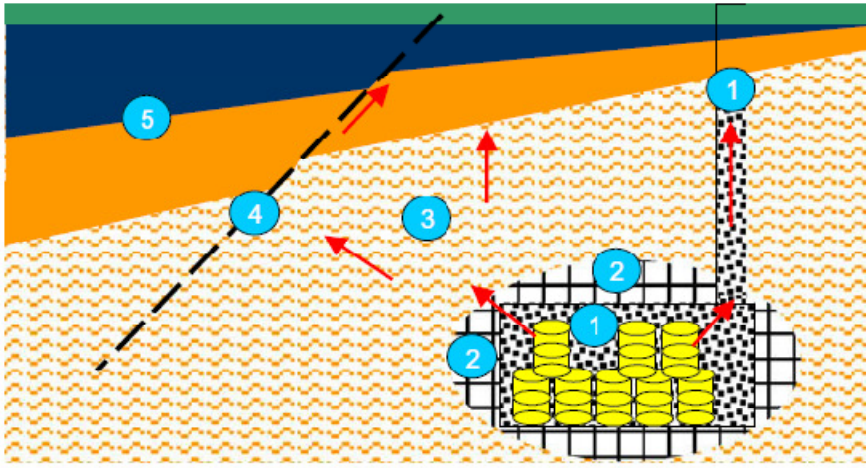


Figure 2.1. The pathways of gas transport in underground repository systems (Alkan and Mueller 2008).

2.1.2.2 Gas transport mechanisms

The transport of gases through low-permeability rock of geological repository systems is controlled not only by hydraulic (H) and mechanical (M) properties of the rock mass or engineered barriers (intrinsic permeability, porosity, rock strength), but also by the gas pressure at the place of gas entry and the hydromechanical state of the rock or engineered barrier (i.e. water saturation, pore water pressure, stress state) (Nagra 2008). Consequently, the mechanisms of gas transport are strongly related to the individual gas paths (intact rock, EDZ, sand/bentonite) and specific features of gas transport need to be addressed for the different paths (e.g. scale effects) (Nagra 2008). A phenomenological description of the transport mechanisms of gases in clay (engineered or natural) was made by Nagra (2008).

Phenomenological considerations suggest the following subdivision of basic transport mechanisms (Figures 2.2 and 2.3):

- advective-diffusive transport of gas dissolved in pore water,
- visco-capillary two-phase flow,
- dilatancy-controlled gas flow, and
- gas transport along macroscopic tensile fractures (hydro- and gas-fracturing).

For any of the aforementioned mechanisms, gas transport is controlled by the microscopic structure of the porous medium. Small-scale heterogeneities may have a distinct impact on large-scale transport processes (Nagra 2008). On the other hand, it is practically impossible to resolve heterogeneities in sufficient detail for inclusion in the numerical simulation of the transport process on a large-scale. Hence, simplified models which still capture the impact of the heterogeneities as much as possible are needed (Dagan 1989, Gelhar 1993, Nagra 2008).

- **Advective-diffusive transport of gas dissolved in pore water**

The advection and diffusion of gas dissolved in pore water is governed by Darcy's law which describes advective groundwater flow under the impact of pressure and gravitational forces, Fick's law which represents the diffusion of dissolved gas due to concentration gradients in the pore water, and Henry's law which describes the solubility of gas in pore water. Table 2.3 gives solubilities and diffusion coefficients of selected gases. It should be mentioned that for a repository in clay, mud rock, or salt, advection is not likely to contribute significantly to dissolved gas transport in the host rock.

- **Visco-capillary two-phase flow**

If a gas exceeds its solubility limit or the gas generation rate is higher than its transport by advection-diffusion, a free gas phase will form, and a (visco-capillary) two-phase flow will start. Basically, a visco-capillary two-phase flow is defined as a transport process whereby pore water in the pore volume of a rock formation is displaced by gas under the influence of viscous and capillary forces (e.g. Bear 1972). The controlling factor for the two-phase flow is the gas entry value (also known as the capillary threshold pressure). Once the gas entry pressure has been exceeded, gas mobility is controlled mostly by the intrinsic permeability (k) of the rock medium, relative permeability (permeability-saturation relationship) and capillary pressure curves (Alkan and Mueller 2008).

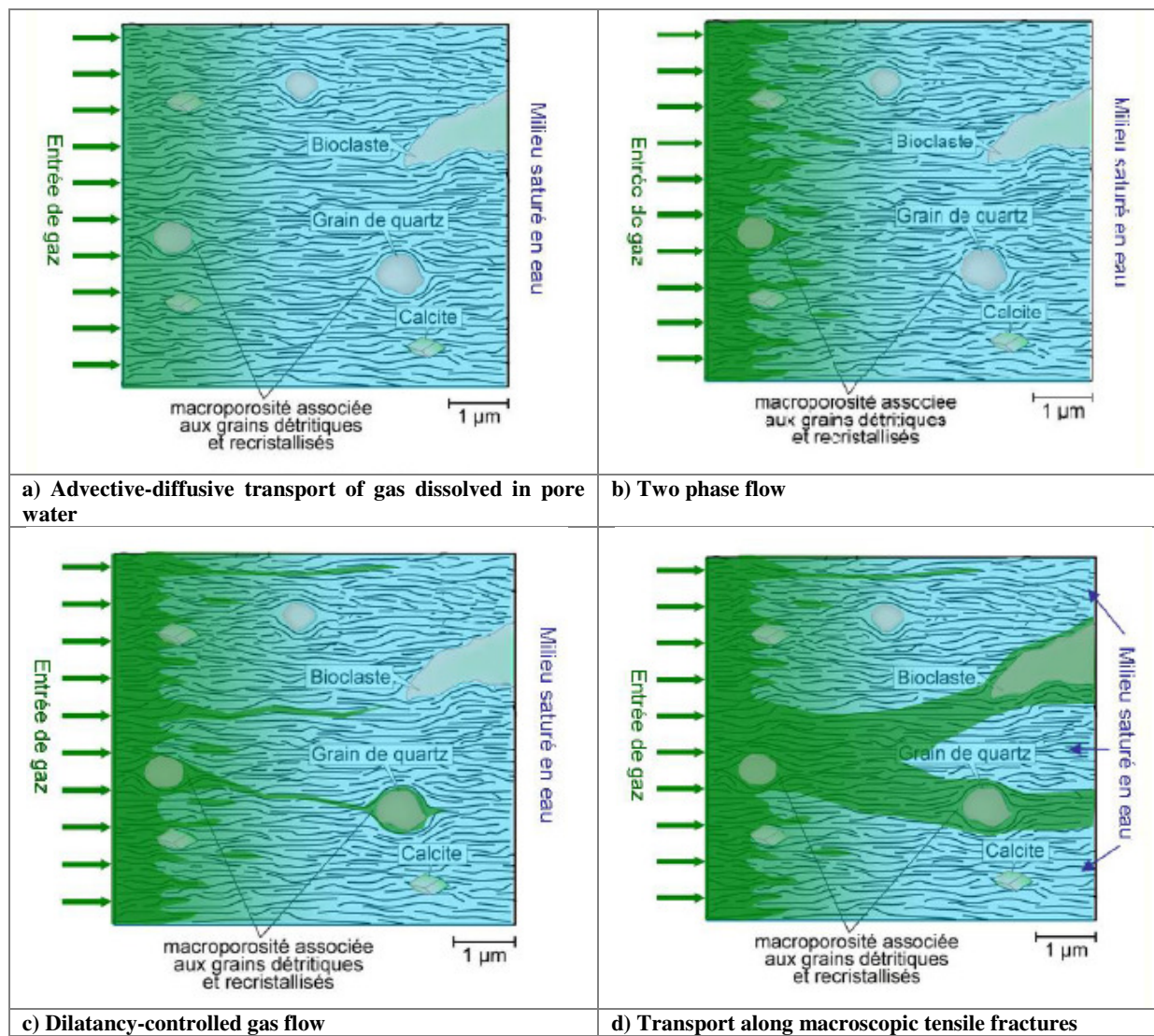


Figure 2.2. Phenomenological description of gas transport mechanisms through low-permeability rock in a geological repository (Andra 2005)

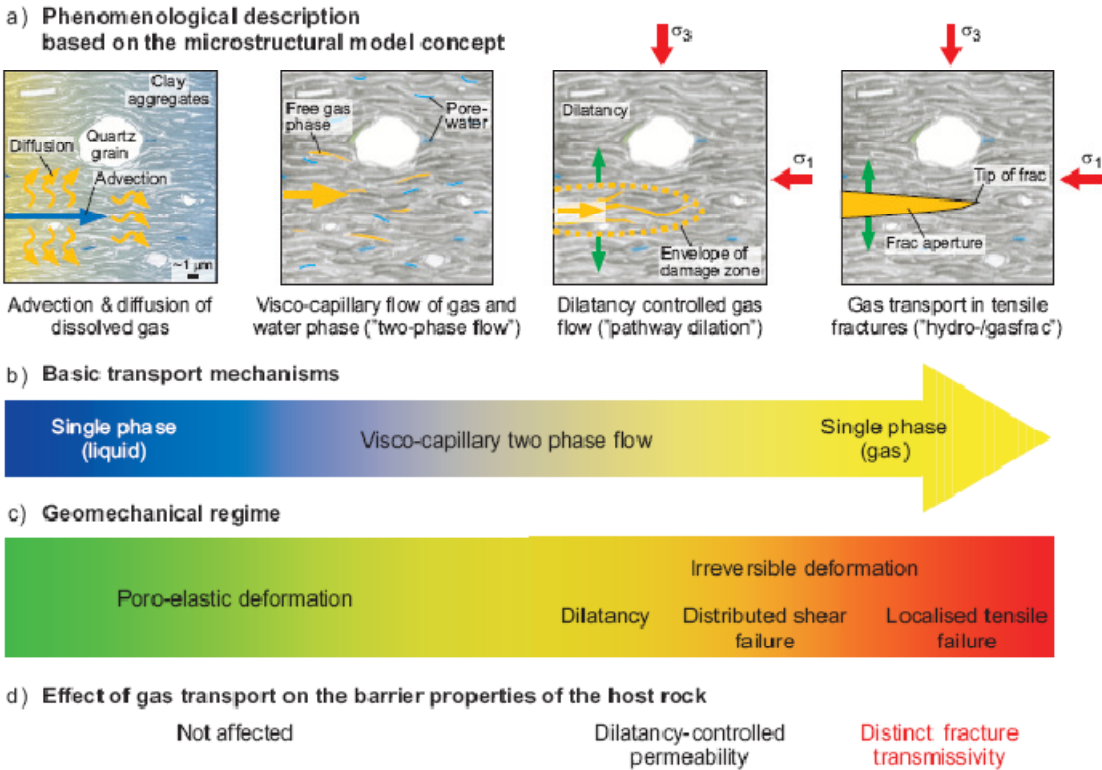


Figure 2.3. Classification and analysis of gas transport processes in Opalinus clay (Nagra 2008)

Table 2.2. Solubility and diffusion coefficients of a selection of gases in H₂O for standard conditions (25°C, 1 atm) (Lide 2000)

Gas	Formula	Solubility (25°C, 1 atm) (mg l ⁻¹)	Diffusion (25°C) (x10 ⁻⁹ m ² s ⁻¹)
Hydrogen	H ₂	1.58	5.11
Helium	He	1.56	7.28
Oxygen	O ₂	40.76	2.42
Nitrogen	N ₂	18.41	2.00
Carbon dioxide	CO ₂	1503.52	1.91
Methane	CH ₄	22.74	1.84

- **Dilatancy-controlled gas flow ("pathway dilatation")**

If gas pressures continue to increase, microscopic gas pathways may form as the result of the poroelastic effects (Alkan and Mueller 2008) because a two-phase flow cannot transport gas quickly enough. This dilatancy controlled gas transport is known as a coupled hydromechanical

transport mechanism with a high gas transport capacity. It is associated with rock deformation. The critical level of pressure that characterizes the onset of pathway dilation is determined by both the strength of the host rock and local stress conditions around the emplacement caverns (Nagra 2008). This transport mechanism is especially important for argillaceous media with low tensile strength. Clay-rich rock cannot withstand long-term gas pressure with a magnitude greater than the minimum principal stress acting on the rock mass (Nagra 2008). The process of gas-driven microfracturing leads to an increase in pore space, which is accompanied by a detectable increase in intrinsic permeability and a change in the capillary pressure-saturation relationship. In the terminology of multiphase flow concepts, gas flow is still controlled by visco-capillary forces (phase interaction between wetting and non-wetting fluid). The main difference with respect to the conventional two phase flow is that the transport properties of the solid phase (rock permeability, relative permeability, capillary pressure relationship) can no longer be viewed as invariants since they depend on the state of deformation of the rock (Marschall et al. 2005).

– **Gas transport along macroscopic tensile fractures (hydro- and gas- fracturing)**

As a rule of thumb, a macroscopic tensile fracture (hydrofrac/gasfrac) is expected when the gas pressure is higher than the sum of the minimum principal stress and the tensile strength of the medium (e.g. Valko and Economides 1997, Marschall et al. 2005, Nagra 2008). The macroscopic fracture is generated quasi-instantaneously and propagates at about the velocity of a shear wave. Gas flow in such a macroscopic tensile fracture can be viewed as a single-phase flow mechanism. The propagation stops when the gas pressure in the fracture becomes less than the value of the minimum principal stress (shut-in pressure, Nagra 2008). Large-size hydrofracs are characterized by fracture transmissivity which increases the bulk permeability of a rock by many orders of magnitude. In a rock with low tensile strength, a macroscopic fracture develops only when the gas pressure build-up is rapid, i.e. when the combined effect of pore water displacement and formation of small-scale fractures (i.e. dilatancy) no longer counterbalances the gas production rate (Nagra 2008).

It should be mentioned that extensile fractures in the EDZ around underground repository excavations are usually dilated, leading to enhanced gas permeability along the general line of excavations. The capillary threshold for gas entry into these dilated fractures will also be lower

than entry into an undisturbed host rock (Horseman 2000). However, the long-term self-healing of the EDZ will tend to increase the threshold for gas entry and reduce the gas transport and storage ability of the EDZ.

Aside from the aforementioned hydro-mechanical coupled processes, hydro-chemical interactions may significantly affect (reduce) the gas permeability of the seals and the host rock in the long-term. Such self-sealing processes might lead to an increase of the gas pressure in the emplacement caverns. These coupled hydro-chemical interactions are summarized in Figure 2.4.

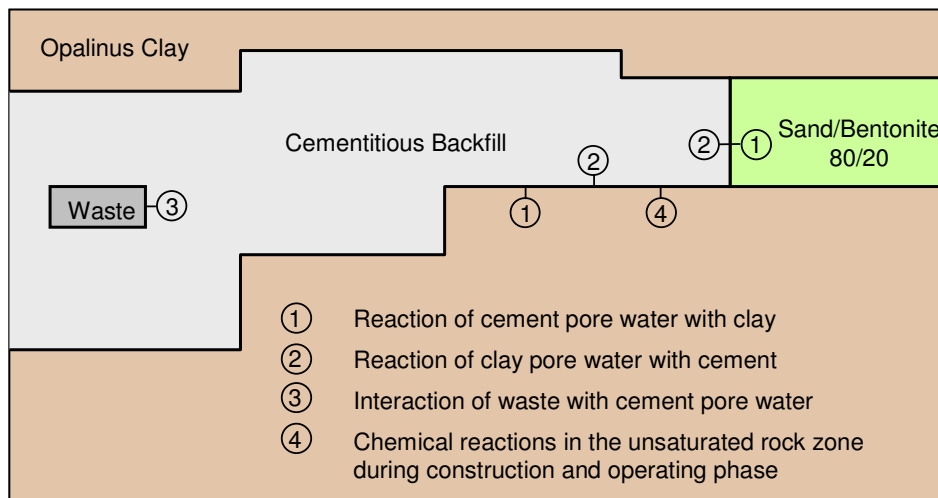


Figure 2.4. Self-sealing processes resulting from hydro-chemical interactions (Nagra 2008)

2.2 Main conceptual and modelling approaches for simulation of gas generation and transport

In this chapter, a compilation of the modeling efforts of gas generation and transport is presented.

2.2.1 Models for predicting and simulating gas generation

In practice, most safety assessments have used constant gas generation rates obtained from laboratory experimental tests or simple approximation models (Table 2.1 summarizes some typical corrosion rates in different host rock environments). However, this leads to high conservatism with regards to the quantity and rate of gas produced in a repository during its lifetime. Consequently, the above approach for predicting gas generation has resulted in an overly conservative assessment of the effects of gas on the safety of repositories for nuclear waste.

However, recent advances in geochemical modelling, including the consideration of kinetic microbial processes, provide a further means to investigate processes of gas generation.

Modelling of gas generation, including the effects of spatial heterogeneity, requires integration and coupling of reactive processes of corrosion, microbial activity and aqueous, mineral and gaseous speciation with transport models. Several codes or software have been developed in the last decades to predict gas generation and its main features. A description of these codes is given below with details available in the references given in the report.

2.2.1.1 GAMMON

GAMMON deals with gas generation in ILW and LLW. The mathematical model in GAMMON simulates the effects of various metal corrosion reactions (production of hydrogen) and different microbial reactions (production of methane and carbon dioxide) leading to gas generation. For both gas generation processes, the mathematical model is based on a set of chemical reactions that represent the reactions that are likely to occur under appropriate repository conditions, and encompass dominant gas generation mechanisms. GAMMON can be used to estimate the quantity, composition and generation rate of gas over the timescales of interest in operational and post-closure safety assessments (UKNL, 2003). GAMMON was used in a number of major assessments for about ten years in the early 1990s. Figure 2.5 shows an example of the prediction results for gas generation that are obtained by using GAMMON. This UK study applied GAMMON software to model gas generation from the disposal vaults as a whole, modelling all the ILW inventory as homogeneously distributed within the ILW vaults, and the ILW/LLW inventory as homogeneously distributed within the ILW/LLW vaults (UKLN, 2003).

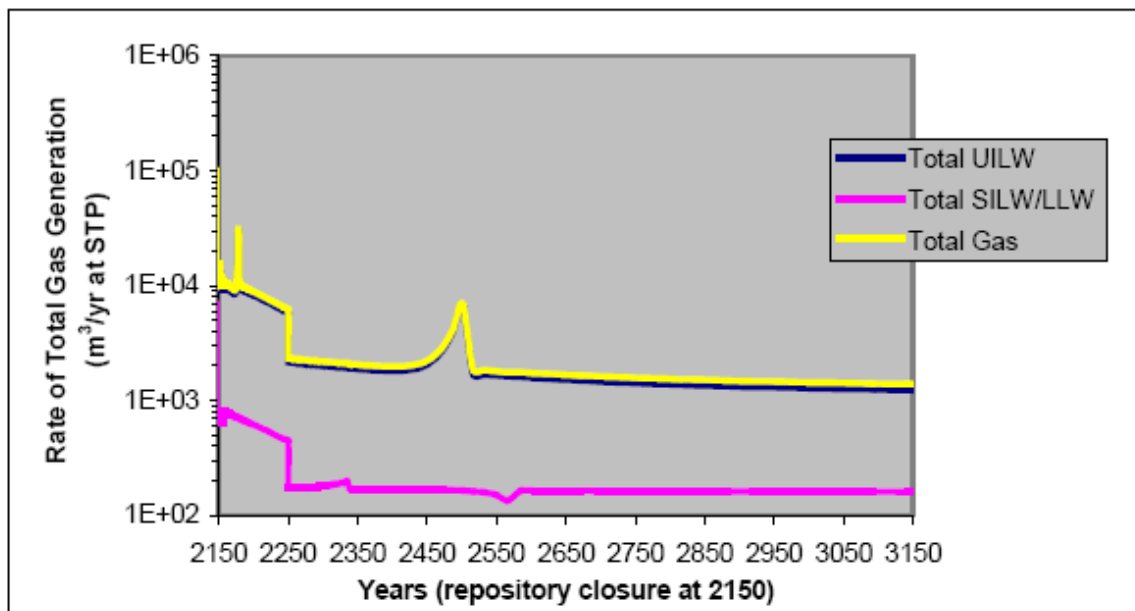


Figure 2.5. Rates of total bulk gas generation in the sample case that are calculated at a standard temperature and pressure (0°C, 0.1 MPa), for the entire repository, UILW vaults and SILW/LLW vaults (UKLN 2003)

Furthermore, several experimental studies on gas generation by nuclear waste were conducted to validate GAMMON. The validation tests showed that GAMMON predicts gas generation by corrosion relatively well. However, modelling the microbiological processes quantitatively appeared to be difficult and ascribed to heterogeneities in the gas-producing experiments, in contrast to the homogeneous system assumed in the model (UKLN, 2003). It was also argued by Rodwell et al. (2003) that a new gas generation model should be simpler than GAMMON. Thus, a simplified kinetic model needs to be produced (UKLN, 2003). This led to the development of a tool called the simplified model of gas generation (SMOGG).

2.2.1.2 SMOGG

SMOGG was developed to overcome the deficiencies of GAMMON as mentioned above. Overall, functionality is considerably increased to incorporate the following processes (Rodwell 2003, UKLN 2003): (i) corrosion of relatively unreactive (steels, Zircaloy and uranium) and more reactive (Magneox and aluminium) metals, leading to the formation of hydrogen; (ii) microbial degradation of cellulosic wastes, producing carbon dioxide and methane; (iii) radiolysis of water and organic wastes to yield hydrogen. Simplified kinetic equations are used (most notably in the model of microbial degradation) in comparison with GAMMON, enabling SMOGG to be implemented in a C++ computer program interfaced with an Excel work book. The model is in principle, easier to calibrate than its predecessor, runs faster and is designed to be numerically more stable (run times and obtaining a properly converged solution have, on occasion, been a problem when using GAMMON (UKLN 2003)).

2.2.1.3 GETAR

Gas Evolution, Transport and Reaction (GETAR) is a code that consists of several modules developed to describe C-14 release from a near-surface waste repository to the environment. One of these modules deals with gas generation. It models gas generation from LLW mainly by microbial activity and hydrolytic reactions. Corrosion is considered only for its effect on oxygen consumption (Yim et al. 1996). The mathematical model of GETAR includes a time-dependent

effect of gas generation, diffusion, advection, chemical reactions, and radioactive decay for each gas of concern. The resulting space- and time-dependent partial differential equations are solved through a model geometry with appropriate boundary conditions (Yim et al. 1996).

2.2.1.4 RadCalc

Radcalc was developed to assess gas generation by radiolysis in certain types of waste during transport. The main objective was to demonstrate compliance with the requirement to limit pressure build-up in waste containers and avoid explosive gas mixtures during transport (McFadden, 1999). The Windows version of RadCalc is user-friendly (McFadden, 1998). The RadCalc program has been extensively tested and validated (Green et al. 1995, McFadden et al. 1998, McFadden, 1999) by comparing each RadCalc algorithm to hand calculations. McFadden (1999) reported that RadCalc for Windows version 2.01 calculates the hydrogen gas volume as:

$$H(t) = K \sum_{ij} G_j D_i(t) E_{ij} \quad (4)$$

i = Index for radionuclide type

j = Index for radiation type. Radiation types are:

j = α (hereafter referred to as "heavy particle"), which are decays of heavy, charged particles, such as alpha and spontaneous fission as well as delayed neutrons,

j = β (hereafter referred to as "beta-type"), which are all electron-related radiation, such as electrons, positrons, conversion-electrons, and Auger electrons, and

j = γ (hereafter referred to as "gamma"), which includes all electromagnetic radiations, such as gamma rays, x-rays, annihilation radiation, and internal bremsstrahlung.

G = Hydrogen G value for the given radiation type (molecules/100 eV)

$D_i(t)$ = Total number of disintegrations for the radionuclide over time t

E_{ij} = Total energy absorbed per disintegration

K = Conversion factor from molecules to volume for an ideal gas at 20°C and standard pressure (101.325 kPa).

2.2.1.5 GRM

Small et al. (2008) developed the Generalised Repository Model (GRM) to represent the biogeochemical processes that occur in disposing LLW at the UK LLW repository (the LLWR) located nearby Drigg, Cumbria. The GRM code has detailed functionality that can describe the kinetic processes of cellulose hydrolysis, corrosion, and microbial activity, and is able to consider equilibrium reactions amongst mineral, aqueous and gaseous species (Small et al. 2008). In GRM, the corrosion process is modelled in an empirical manner and does not take into account the specific microbial processes and localized effects, such as pitting corrosion (extremely localized corrosion that results in the creation of small holes in the metal). The GRM corrosion model considers rates of steel corrosion under saturated and unsaturated groundwater conditions in both aerobic and anaerobic environments (Small et al. 2008). The microbial kinetic model used within the GRM is based on Monod kinetics (Koch 1988, Humphreys et al. 1995, Humphreys et al. 1997 and Graham et al. 2003). The ability to discretize the GRM model domain enables investigation of the effects of heterogeneity in the main features of gas generation. Version 5.1 of the GRM (Graham et al., 2003) can be also used to model the transport of chemical species under an imposed flow field in saturated groundwater. This calculation of solute transport is coupled to a calculation of equilibrium chemical speciation by using the PHREEQE source code (Parkhurst et al. 1980), which models the reaction of aqueous, mineral and gaseous species in each finite difference cell under a specified redox potential (Small et al. 2008).

2.2.1.6 The Reaction-Path Model (Brush et al. model)

Brush et al. (1994) developed a kinetic reaction path model based on thermodynamic equilibrium considerations. This reaction-path model includes: (i) oxic and anoxic corrosion of steels and other Fe-base alloys, including passivation by the adherent corrosion products; FeCO_3 and FeS , and depassivation caused by the destabilization of these phases due to changes in the composition of the gaseous phase; (ii) microbial degradation of cellulose; (iii) α radiolysis of brine; and (iv)

consumption of CO₂ by Ca(OH)₂ (in hydrated cementitious materials) or CaO (a proposed backfill additive) (Brush et al. 1994).

2.2.1.7 Other models

GaBi is a code developed for all types of waste and based on the German repository concept of salt with crushed salt backfill. Time dependent gas generation rates are calculated with an interactive selection of starting and boundary conditions. GASFORM deals with HLW in granitic host rock. Sand or bentonite is considered as backfill material. GASFORM was intended to be coupled with a gas transport code, such as TOUGH2 (Mueller 2000).

Finally, it can be concluded that modelling and prediction of gas generation in repositories for nuclear waste is most advanced with respect to corrosion. Radiolysis can be predicted with well established models. The accuracy is dependent on the available characterization of the activity contents in the waste package and the degree of details implemented in the model (Mueller 2000). The modelling of microbial gas generation is limited to well-defined scenarios, which are not necessarily similar to the long-term conditions in an underground repository. For an extrapolation outside their validation range, a better knowledge of the processes, their governing parameters and limiting conditions, are necessary. Interactions have to be considered in modelling between gas generation mechanisms (e.g. by water balance in the case of limited supply) as well as with other processes, such as fluid flow (water saturation), geochemical history and geomechanical forces (vs. pressure build-up) (Mueller 2000).

2.2.2 Conceptual and modeling approaches for simulating gas transport

During the past decades, significant research effort has been devoted to developing conceptual and modelling approaches for predicting and simulating gas transport in repository systems, especially in clay formations. This sub-chapter will present a summary of the main conceptual and modelling approaches that are developed to predict gas transport in a repository system (especially for clay or clayey formations). These approaches can be divided into three types:

- Approaches related to Darcy's law,
- Modified Darcy approaches, and
- Models for gas transport through EDZ.

2.2.2.1 Approaches related to Darcy's law

The models presented in this section are based on Darcy's law or its precursors, such as Navier-Stokes equations.

2.2.2.1.1 Capillary bundle model

Ortiz et al. (1996) developed the capillary bundle model, a two-phase flow through clay formations. The principle of this model is shown in Figure 2.6. It is assumed that the porous medium is made of a series of intersecting capillaries, characterized by a radius r and a tortuosity factor (τ). $N(r)dr$ represents the number of capillaries per unit cross sectional area of core, with r in the range of $[r, r + dr]$, while the length of each capillary is given by τL . A slow flow is assumed in the capillaries. A capillary pressure concept is brought into the picture. Hence, the position of the gas-water interface $R(r,t)$ is calculated based on a Navier-Stokes equation as follows (Alkan and Mueller 2008):

$$R^2(r,t) = \tau^2 L^2 - \frac{t}{4\mu_w} (r^2(p_g - p_w) - r\sqrt{2}\gamma) \quad (5)$$

This equation is valid in the region $0 \leq R(r,t) \leq \tau L$.

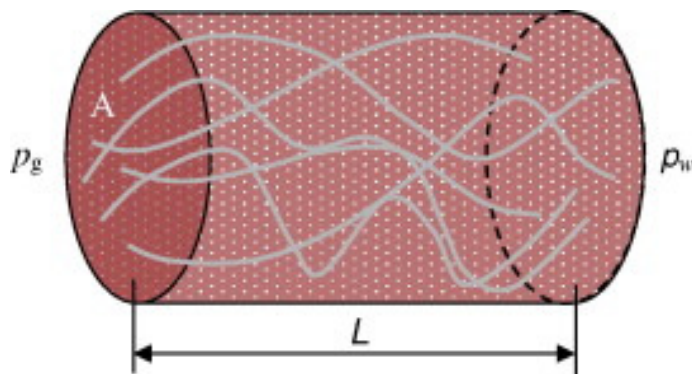


Figure 2.6. Schematic of the capillary bundle model (Ortiz et al. 1996).

It is known that a capillary begins to desaturate only if the gas pressure is higher than the combined water and capillary pressure. Furthermore, based on the capillary pressure concept, the smallest capillary pressure (r_s), can be calculated by using Eq. 6:

$$r_s = \frac{\gamma\sqrt{2}}{(p_g - p_w)} \quad (6)$$

The saturation degree of capillaries with an r smaller than r_s will remain equal to 100%. At a predetermined gas and water pressure, each capillary with r greater than r_s will be desaturated until gas breakthrough, which happens when the length of the part filled with water is zero (Alkan and Mueller 2008). After breakthrough in a capillary of r at time $t_b(r)$, the gas pressure distribution along the capillary reaches equilibrium at a rate controlled by the conservation of mass and Darcy's law (Alkan and Mueller 2008). The saturation profile of the core can be computed at any point by adding the contribution of each capillary. The capillary bundle model which is presented above was used to simulate flow experiments performed with Boom clay core samples from HADES (Belgian Underground Research Laboratory). Ortiz et al. (1996) showed that the simulation results obtained with the capillary bundle model are close to those obtained experimentally. Further details on the model development and validation are given in Ortiz et al. (1996).

2.2.2.1.2 Multiple interacting media

The basic idea of the model presented here is the fact that clay formations or the porous medium is considered as a microfractured media. Several studies were conducted to model fluid transport in clay as a problem of fractured porous media. For example, based on the theory of dual porosity (DP) or multiple interacting media, various researchers (Barrenblatt et al. 1960, Warren and Root 1963, Gerke and van Genuchten 1993, Du et al. 2006) developed models to describe and predict fluid movement in microfractured clay systems. The models combine two systems: a macropore or fracture pore system at the macroscopic level by fracture continuum (FC) and a less permeable matrix pore system by matrix continuum (MC) (Alkan and Mueller 2009). In the DP model, the transfer value between these two continua plays an important role for model accuracy (Alonso et al., 2006).

Figure 2.7 shows a finite element composed by a rock matrix and a series of n fractures. The number of fractures in an element depends on the width associated with each fracture (a), which is a common size of the material, and the element size (s) (Alkan and Mueller 2008). H and M effects have to be included because gas flow depends critically on the mechanical interactions as they control fracture aperture or porosity changes (Alonso et al. 2006). Liquid and gas flow will be calculated using Darcy's law, when the flow mechanisms through a single fracture are considered first. The most important parameter in this law is the intrinsic permeability. It can be calculated with cubic law for discrete fractures, assuming laminar flow as:

$$k_{\text{fracture}} = b^2/12 \quad (7)$$

When a set of n fractures is included in a finite element (Figure 2.7), the equivalent intrinsic permeability of the element can be calculated as (Alkan and Mueller 2008):

$$k = k_{\text{matrix}} \left[\frac{s - nb}{s} \right] + \sum_{i=1}^n \left[k_{\text{fracture}} \frac{b}{a} \frac{1}{n} \right] \quad (8)$$

$$\cong k_{\text{matrix}} + \frac{b^3}{12a}$$

where k_{matrix} is the reference intrinsic permeability of the matrix. In the case of gas propagation through rock, the matrix refers to the rock without fractures (Alonso et al. 2006). The definition of basic capillary pressure in a fracture of width b can be used directly to calculate the air entry pressure value for the corresponding element (Alonso et al. 2006):

$$p = p_0 \frac{\sqrt[3]{k_{\text{fracture}_0}}}{\sqrt[3]{k_{\text{fracture}}}} \quad (9)$$

where subscript 0 refers to a reference (initial) aperture.

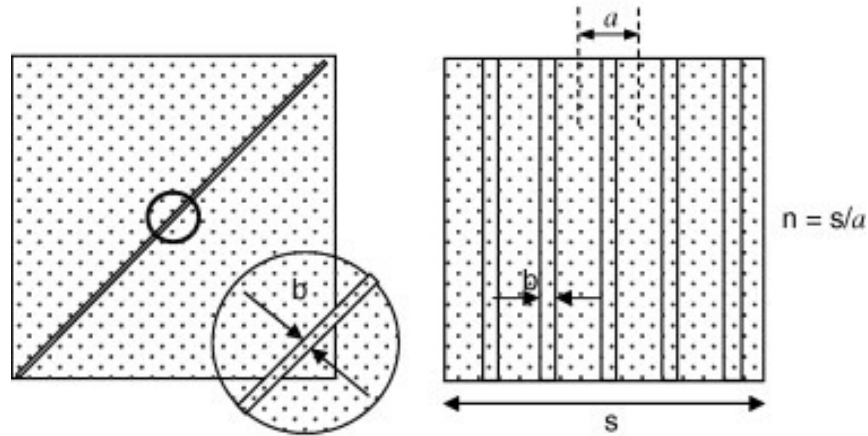


Figure 2.7. Rock with a single idealized fracture and a series of parallel fractures uniformly separated (Alkan and Mueller 2008).

It should be noted that the permeability of the matrix will be relevant only for very low apertures; otherwise, the total permeability will be entirely controlled by fracture permeability and matrix permeability will be negligible. Alonso et al. (2006) validated the model presented above against experimental results obtained from tests conducted on Boom clay samples in the framework of the MEGAS Project. They reported that the model calculations are in good agreement with the experimental results.

2.2.2.1.3. Matrix diffusion in fractured clay rock (Brush model)

Lege and Shao (1996) proposed the Brush model to better take into account matrix diffusion in clay formations. Figure 2.8 shows a schematic description of the modelling approach. The porous media is geometrically modelled as a fractured medium. Gravitational effects are ignored.

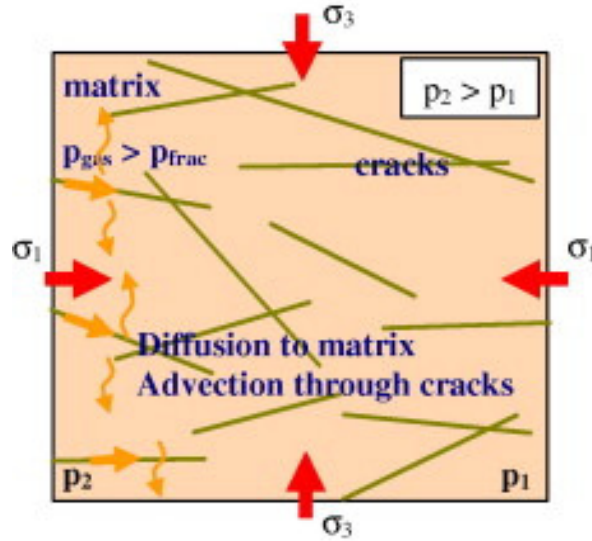


Figure 2.8. Transport mechanisms in fractured geological media (Alkan and Mueller 2008).

Advective–dispersive transport without retardation is assumed. The transport of a substance that is not sorbed through a fracture is modelled using the following 2-D advection–dispersion equation (Alkan and Mueller 2008):

$$\frac{\partial c}{\partial t} = D_L \frac{\partial^2 c}{\partial x^2} + D_T \frac{\partial^2 c}{\partial y^2} - \frac{v_D}{\phi_e} \frac{\partial c}{\partial x}, \quad (10)$$

where c is the solute concentration (mg/l). It is indicated that the tracer velocity (v_D/ϕ_e), is sufficiently high as the molecular diffusivity (D_m), does not significantly contribute to the total dispersion coefficients (D_L and D_T). Darcy’s law is applied for the flow velocity in the fracture (Alkan and Mueller 2008); and the concentration in the rock matrix satisfies the 1-D diffusion equation:

$$\frac{\partial c}{\partial t} = D_e \frac{\partial^2 c}{\partial z^2}, \quad (11)$$

where D_e is the effective diffusion coefficient.

The model is implemented in the computer code Rockflow. The flow velocities in fractures are described by Darcy's law. Alkan and Mueller (2008) reported application of the model for water-tracer transport. However, two-phase gas–water transport can also be modelled by using the basic principles of the model.

2.2.2.2 Modified Darcy approaches

Darcy's law is only applicable within certain limitations. It is not very suitable for non-linear flow. Therefore, attempts have been made to modify Darcy's law for coupling non-linearities resulting from mechanical and physico-chemical effects in clay formations or other low-permeability rock media. As reported in Alkan and Mueller (2008), it is known that the geomechanical effects play a leading role in controlling the shape of the pathways. For example, the gas may have to overcome the local effective stress to open or enlarge a microfracture as explained above. Swelling and other physico-chemical aspects of the fluid flow in clay media were also attempted for inclusion in the main flow equations. In the following, relevant models that use these approaches are presented: (i) empirical, (ii) planar pathway, (iii) modified capillary bundle, (iv) extended multiple interacting media, (v) multiple front propagation, and (vi) models that incorporate swelling.

2.2.2.2.1 Empirical models

Experimental studies on gas transport in clays have been performed by many authors. This has resulted in the development of empirical relationships for predicting relevant gas flow parameters, such gas discharge, and gas entry pressure for specific types of porous media. Rodwell et al. (1999) proposed the following relationship for the prediction of gas discharge for Pondita clay:

$$q = (3.984 + 9.01 \times 10^{-4} \sigma_v) p_g^{(1.2345 - 4.29 \times 10^{-5} \sigma_v)} 17.663 \left[\frac{(S_i - S)}{S} \right] \quad (12)$$

where q is the gas discharge, $\mu\text{l/s}$, p_g the excess gas pressure, σ_v the vertical stress, Pa, S the saturation in the sample and S_t the saturation limit below which the threshold pressure needed for the gas to penetrate the medium is equal to zero. Push et al. (1995) developed empirical equations to correlate the gas entry pressure to permeability and bentonite swelling pressure for compacted clays. It should be emphasized that these empirical models are specific to the cases studied rather than universally accepted models.

2.2.2.2.2 Planar pathway model

Figure 2.9 illustrates a schematic description of the planar model (Horseman and Harrington 1996). In this model, the flow rate through a planar fracture is determined by using the cubic law that originated from the Poiseuille equation. In Figure 2.9, the pressures p_1 and p_2 allow for the determination of the source and sink terms. It is assumed that the aperture of the pathway (fracture) is a function of the applied overburden (confining) stress (σ) and pore pressure (p_g) (Alkan and Mueller 2000):

$$b = f(\sigma - p_g) \quad (13)$$

Following this concept, a critical value of $(\sigma - p_g)$ is assumed which results in total closure of the flow pathway with $b = 0$. This is identified as the sealing criterion and written as:

$$q = 0 \quad \text{for} \quad (\sigma - p_g) > (\sigma - p_g)_{\text{crit}} \quad (14)$$

When fluid pressure is progressively developed in the source reservoir, a point will be arrived where the sealing criterion is no longer met and fluid begins to flow towards the sink. The incorporation of a pathway aperture relationship in the cubic law makes the effective permeability of the pathway a highly non-linear function of the local fluid pressure and stress distribution. The resulting flow law therefore exhibits a threshold and also non-linearity. The critical pressure is physically comparable with the threshold or entry pressure (Alkan and Mueller 2008).

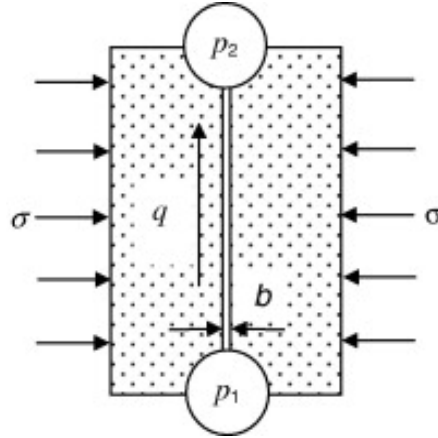


Figure 2.9. Simple conceptual model of pathway flow in clay formation (Horseman and Harrington, 1996).

2.2.2.2.3 Modified capillary bundle model

The capillary bundle model (Ortiz et al. 1996) presented above does not take the geomechanical effect into account. For this reason, the capillary bundle model was extended by Impey et al. (1996) to incorporate gas migration behaviour. In the model, pathways (bundles) are dynamically opened as the gas pressure surpasses a local threshold value, propagates through the material and closes if the gas pressure falls (Alkan and Mueller, 2008). Further details about the modified capillary bundle model are given in Impey et al. (1996).

2.2.2.2.4 Extended multiple interacting media

The fracture model described above is extended to incorporate rock deformation (ϵ). From a mechanical point of view, this means that we are interested in the process of fracture formation and aperture. The aperture of the fracture can be estimated as a function of deformation in the following way:

$$b = b_0 + \Delta b$$

$$\Delta b = a\Delta\epsilon = a(\epsilon - \epsilon_0) = (s/n)(\epsilon - \epsilon_0) \quad (15)$$

Here, it is assumed that deformation is localized and results in changes in aperture. A threshold value (ϵ_0) is considered. Therefore, the changes in aperture start when deformation reaches this value (Alonso et al. 2006, Alkan and Mueller 2008). Deformation normal to the fracture plane is

used when aperture changes have to be obtained. The ε_0 is associated with fracture initiation. This parameter will be set to zero if the fractures already exist and have an initial aperture (b_0). In practice, the b_0 can be essentially zero when fractures exist, but are closed (Alkan and Mueller 2008).

The stress-strain behaviour of the medium (clay barrier or rock), including fracture formation, is a crucial component of the aperture changes. If an elastoplastic model is considered for the mass behaviour, fracture initiation can be associated with tension stress or dilatancy. On the other hand, fracture orientation is sensitive to the stress tensor orientation so the plane where the minimum principal stress (compression positive) occurs will define the plane of fracture formation. Equation (15) is introduced into Equation (8) to calculate the element permeability in the following way (Alonso et al 2006):

$$k = k_{\text{matrix}} + \frac{b^3}{12a} = k_{\text{matrix}} + \frac{(b_0 + a(\varepsilon - \varepsilon_0))^3}{12a} \quad (16)$$

From this relationship, it is clear that the element permeability depends on a , which is a typical parameter of the material, but is independent from s . The so-formulated permeability is used as the Darcy permeability in flow equations as a function of elastoplastic deformation in clay formations. Figure 2.10 shows the general stress-strain behaviour coupled to aperture changes for tension that takes place in the medium. A threshold strain (ε_0) defines the initiation of fracture aperture, as mentioned before. A strain corresponding to failure is also considered (ε_1). In this case, failure is achieved when the normal stress reaches the tensile strength (σ_t). ε_0 , ε_1 and σ_t are the model parameters (Alonso et al. 2008).

The model presented above has been implemented in CODE_BRIGHT (Olivella et al. 1995) and in some cases, have been analyzed to investigate the response of the coupled behaviour. The analyses showed the sensitivity of the results to several parameters controlling the tests that are usually conducted. It is recommended that further improvements of the model may incorporate different aspects, such as the influence of the formation of infilling material due to shear displacements between crack interfaces (Alonso 2006).

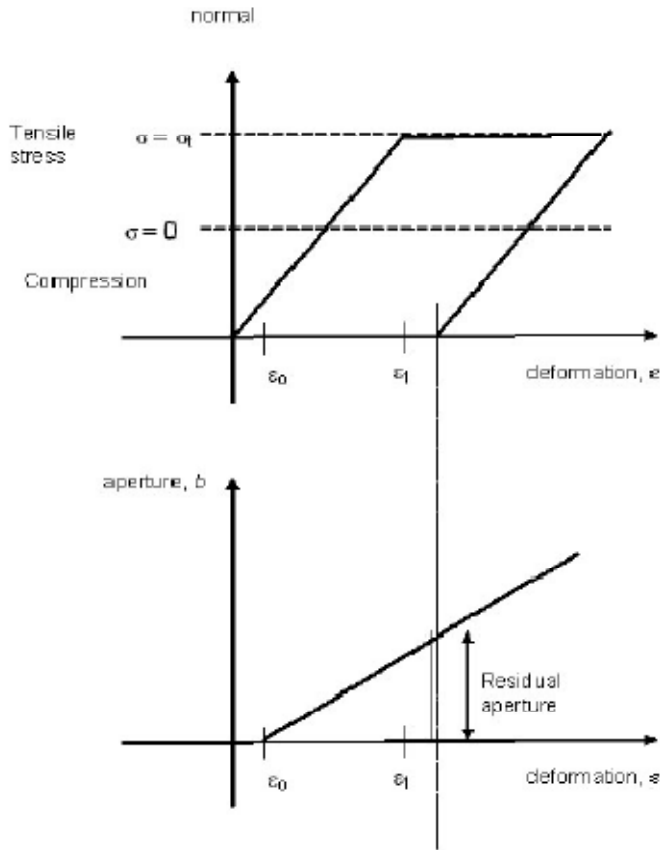


Figure 2.10. General stress-strain behaviour coupled to aperture changes for a tension opening (Alonso et al. 2006).

2.2.2.2.5 Multiple front propagation model

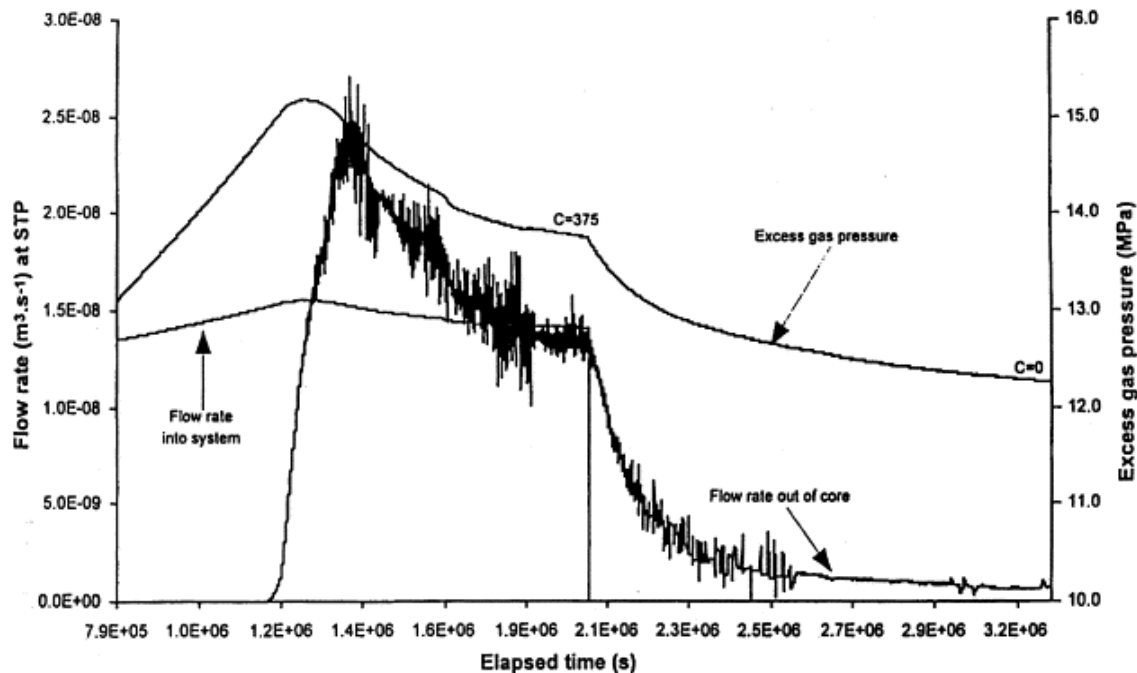
A “multiple front propagation model” (MFPM) with simpler dynamics has been proposed to simulate laboratory gas migration experiments on cylindrical clay cores (Brown, 1999). This model uses a stochastic representation of independent gas pathways to emulate the microstructural heterogeneity of the medium. It predicts gas pressure, gas and water fluxes with key expected features; namely (Brown, 1999): (i) a threshold effect which requires the gas pressure to rise above a critical value before migration can begin; (ii) a propagation phase during which the front moves along capillary-like paths; and (iii) pressure release and relaxation phases at and after breakthrough.

The MFPM consists of two parts; an outer part which handles experimental pressure stresses that may change with time, and an inner part which manages the migration of gas through the sample core (Brown, 1999). The model is based on the solution of mass conservation and Poiseuille flow

equations for the two types of fluids (wetting and non-wetting) and on the equation for advancing through the clay at the tip of the propagating gas flow channel. The gas-filled pathways are assumed to dilate elastically for small displacements (Alkan and Mueller, 2008).

The model operates within QuantiSci's uncertainty shell (QUEST) on a PC, and includes a time stepping routine to vary the experimental pressure stresses in a piecewise constant manner (Brown 1999). The QUEST shell allows parameter values to be assigned as definite or uncertain, or set as functions of other parameters, e.g. P_{start} may be made a function of $P_{confine}$. Due to the stochastic nature of the overall model, several instances or 'experiments' are normally run in QUEST to illustrate the variety of results that may be expected in real experiments (Brown 1999). Horseman and Harrington (1997) applied the MFPM to gas migration data for Mx80 bentonite. The MFPM was used to simulate experiment Mx80-1, with results shown in Figure 2.11. Details on the experiment Mx80-1 bentonite are given in Brown (1999).

Figure 2.12 shows the calculated history from 10 MFPM calculations for the excess pressure and gas flow. The variability in the results reflects the stochastic nature of the model. This figure compares well with Figure 2.11.



2.11. Experimental history for Mx80-1 (Brown, 1999).

Figure

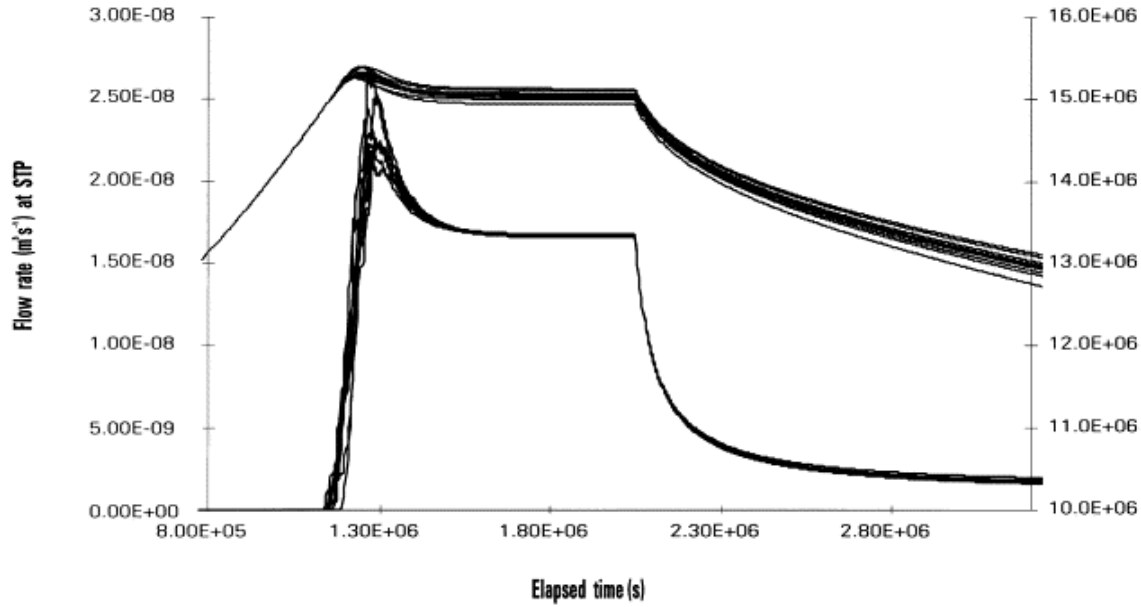


Figure 2.12. MFPM excess pressure and gas flow for Mx80-1 bentonite (Brown, 1999).

2.2.2.2.6 Modelling swelling

Swelling clays play a major role in current concepts for the underground disposal of nuclear waste in deep geological formations. Furthermore, some host rocks contain swelling clay minerals. The basic challenge in modelling the gas movement in bentonite buffers or rocks that contain expansive minerals is the incorporation of swelling into the fluid transport process. As presented above, often governing equations used in predicting gas transport through porous media do not take the swelling mechanism into account, i.e. they apply only to non-swelling porous media. Therefore, during recent years, some models have been developed to introduce the swelling mechanism into the predictive models for fluid transport through deformable porous media. Bennethum et al. (1997) summarized some generalizations of Darcy's law, Terzaghi's effective stress principle and Fick's law for swelling porous media obtained by using the hybrid mixture theory (HMT) which involves the averaging of field equations (mass, momentum balance and energy balances) and obtaining constitutive restrictions subject to the second law of thermodynamics. In the same way, Maßmann et al. (2006) used an extension of the Biot consolidation theory for integrating swelling or shrinkage (Alkan and Mueller, 2008).

2.2.2.3 Models for gas flow through EDZ

The EDZ around the backfilled underground structures may serve a dual function with respect to gas release. As a result of the increased porosity in comparison to the intact rock, the EDZ may provide additional gas storage capacity. In addition, the (self-sealed) fracture network within the EDZ may serve as a potential gas pathway through which gas generated in the emplacement caverns can be transported to the backfilled branch, operation and access tunnels (Nagra 2008). A recent overview of the time dependent behaviour of EDZs in clay formations is given in Blumling et al. (2007). Dilatancy boundary and unstable crack growth are also reported for EDZs in clay formations. The permeability induced by the dilatancy is the principal parameter representing the EDZs in transport equations (Alkan and Mueller 2008). As reported above, dilatancy controlled gas flow is known as a coupled hydromechanical transport mechanism with a high gas transport capacity. Alkan and Mueller (2008) reported that when crystalline and salt rocks are the repository host rocks, the dilatancy induced permeability, geometry and the extent of the EDZs are well studied (Tsang et al. 2005, Alkan et al. 2007). Principally, the concepts that originate from crystalline host rocks can be applied to plastics and indurated clays as well as other sedimentary rocks. However, EDZ studies for clay formations or other sedimentary rocks are not advanced enough to set a universal solution of coupling the changes on stress equilibrium onto H properties (Alkan and Mueller 2008). Attempts have been made to model gas propagation through swelling clay media. Some relevant models are described below.

The modelling approach for gas–oil migration in shales is used for modelling the dilation behaviour of the gas pathways in clay formations (Duppendercker et al., 1997). The model takes the linear elastic fracture mechanics as the theoretical basis (Alkon and Mueller 2008). The cracks are represented by ellipsoidal cavities with dimensions defined by semi-axes a , b and c in Figure 2.13.



Figure 2.13. Schematic description of the crack dilatation model (Duppenacker et al. 1997).

New models (discrete fracture propagation models) were developed within the Nagra project (Nagra 2008) to describe and predict the creation and propagation of "pathway dilation" in the EDZ. Compared to classical geomechanical continuum models, the discrete fracture propagation models have the advantage of more realistically reflecting observations (discrete fracture networks in the EDZ). In addition, discrete fracture network models are better suited for the simulation of self-sealing mechanisms in the EDZ after repository closure. The discrete fracture propagation models are expected to improve the understanding of the hydromechanical phenomena, associated with the gas flow along the EDZ. This includes not only the gas pressure-induced fracture propagation process, but also the self-sealing which takes place when the gas pressure decreases (Nagra 2008).

Johnson et al. (2005) developed a simplified model of gas pressure evolution and migration of corrosion gases in an underground nuclear waste disposal system in Finland. The conceptual model includes gas generation, pressure build-up, pore water displacement, dissolution and diffusion of gas in the aqueous phase, capillary leakage within fractures in the host rock, formation of gas pathways along the deposition holes and gas breakthrough to major geological features of enhanced transmissivity (Figure 2.14). In the model, gas leakage is assumed to occur within the fracture network in the host rock and the EDZ when the corrosion gas pressure exceeds the sum of formation pore pressure and gas entry pressure. The latter is calculated by using measured properties of microfracturing in the EDZ (Autio et al. 2006).

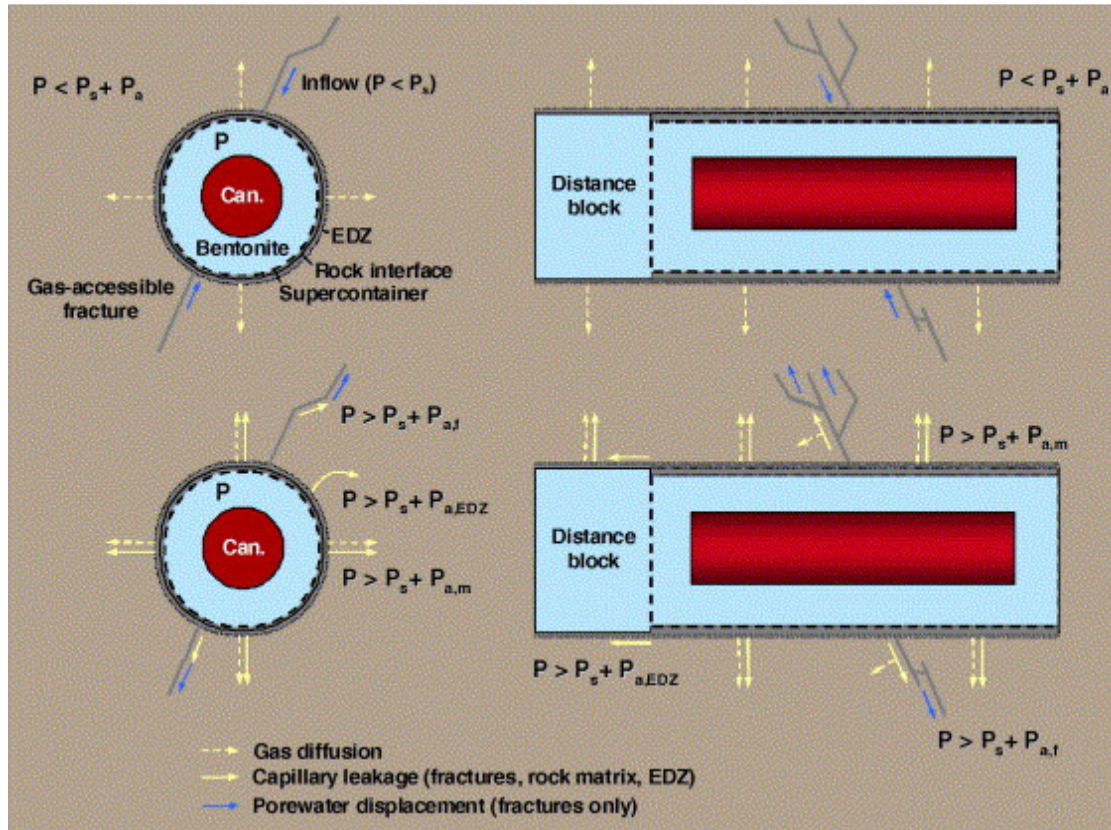


Figure 2.14. Different gas transport routes and repository domains (Autio et al. 2006)

2.3 Case studies on gas generation and migration

In this section, the main results from relevant studies on gas generation and migration performed in laboratory or URLs will be presented and discussed.

2.3.1 Laboratories studies

During the past decade, several laboratory studies have been performed to better understand gas generation by nuclear waste and its transport through and/or interaction with porous media (e.g. natural clays, bentonite) under various environmental or mechanical loading conditions. Some relevant laboratory studies are presented below. They provide a convenient background on gas transport and migration, and emphasize the role played by coupled hydro-mechanical effects in gas migration as well as coupled bio-chemo-hydraulic effects in gas generation.

2.3.1.1 Studies on gas migration

Many investigators have performed experimental and modeling studies on gas generation and migration.

Gallé (2000) reported controlled H₂ gas migration experiments (coupled with a simple modeling study) with Fo–Ca clay, a candidate engineered clay barrier considered in France. Experiments allowed measurements of gas permeability and estimated gas transport threshold pressures. The gas migration and permeability were determined by using an oedometer-type vessel (Figure 2.15) that was developed by Tanai and Gallé (1998). Gallé (2000) used compacted clay specimens with dry densities of 1.6, 1.7, 1.8 and 1.9 g/cm³ for water saturation degrees between 70% and 100%. During the gas injection tests, gas pressure was incrementally applied to one of the ends of the clay specimen without any water backpressure and mechanical stress. Each pressure step was maintained until steady flow was reached then, gas outflow rates were measured.

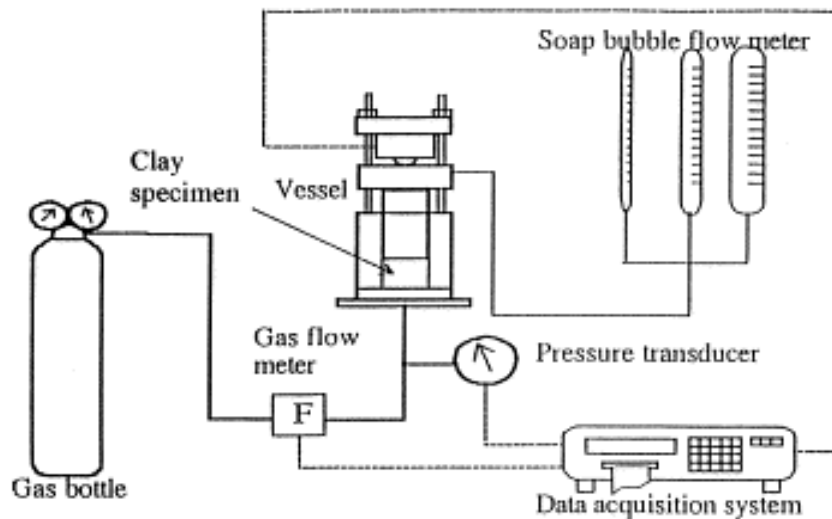


Figure 2.15. Schematic of the experimental gas migration testing system (Tanai et al. 1997)

He observed that gas transport starts at a gas threshold pressure called gas entry pressure. A second threshold pressure; the breakthrough pressure, was detected for sharp gas outflow increase. Their results showed that the breakthrough pressure is equal to the sum of the clay swelling pressure and water backpressure. The author suggested that the gas issue cannot be underestimated for long-term engineered clay barrier stability (Gallé 2000).

Arnedo et al. (2008) investigated gas flow through clay barriers on the basis of laboratory and modelling work. The mechanism of gas flow and the development of a preferential path in sand–

bentonite mixtures were experimentally investigated by conducting a series of “dipole” tests in a cylindrical sample that is confined volumetrically (Figure 2.16). The formation of preferential paths was achieved in dipole tests that used needles. Arnedo et al. (2008) reported that observations of the samples after testing revealed discontinuities that followed the compaction layers which could play a role during gas flow. A large scale breakthrough pressure was clearly observed when a marked pressure peak was recorded in the upstream vessel. Arnedo et al. (2008) also used a coupled hydro-mechanical model to simulate the gas flow. The coupled solution of the mechanical and two-phase flow equations is performed using finite elements with CODE_BRIGHT (Olivella et al.1996). The modelling results agree well with the experimental results (an example is shown in Figure 2.17).

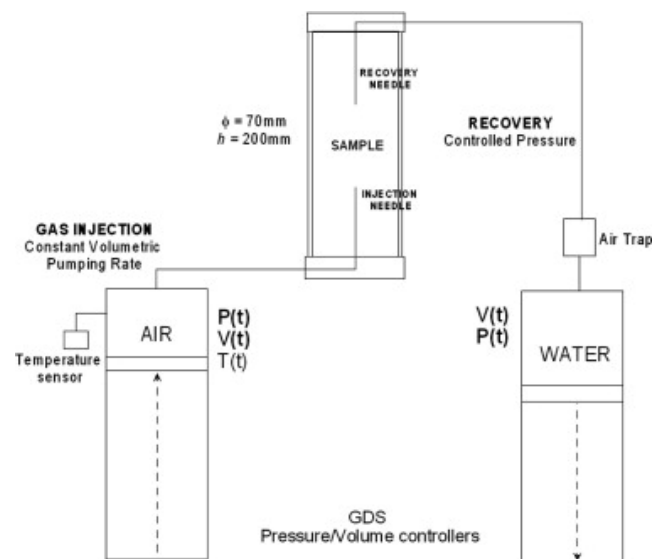


Figure 2.16. Schematic of experimental setup for gas injection in soil samples using needles (Arnedo et al. 2008).

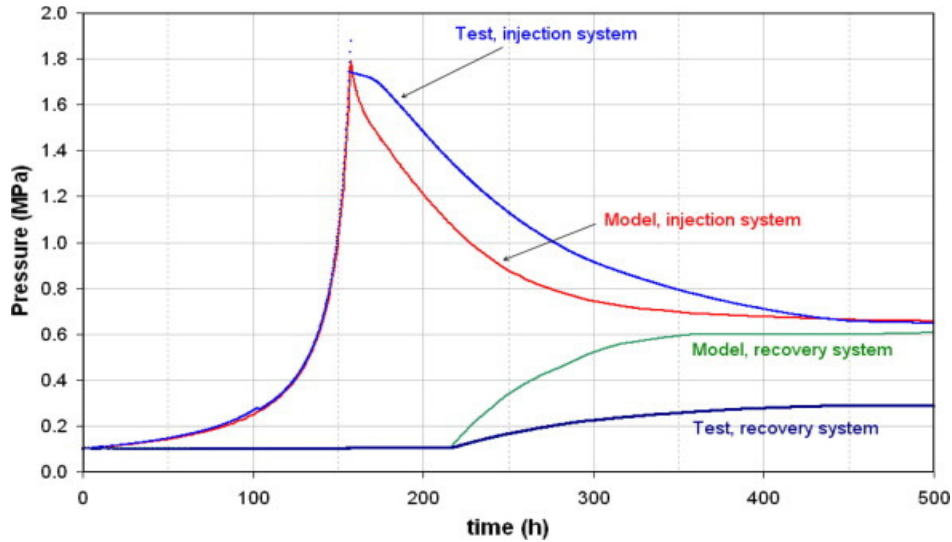


Figure 2.17. Computed versus measured injection and recovery pressures (“Model” stands for calculated results and “Test” stands for experiment measurements) (Arnedo et al. 2008).

Initiated by ANDRA, Davy et al. (2007) conducted an extensive experimental program that was 6 months in duration, to study the coupled effects of mechanical and chemo-hydraulic (chemically active fluid seepage (H_2O)) loadings on gas and water permeability of cracked argillite located in the EDZ. Argillite formations are currently studied in detail in many European countries (e.g. Belgium, France, Switzerland, and the UK) as a potential host for the implementation of a repository for radioactive waste. Davy et al. (2007) performed steady state gas flow and transient water flow tests on pre-cracked argillite samples. The argillite samples were macro-cracked along a diametral plane using a Brazilian splitting test. The samples were extracted from the French Meuse/Haute Marne URL, Bure site, at several depths in the argillite layers. The main petro-physical characteristics of the argillite samples and permeability tests that were performed on them are given in Table 2.4.

Table 2.3. Main petro-physical characteristics of the argillite plugs and permeability tests performed samples as received from ANDRA (Davy et al. 2007).

Plug no.	EST5600	MSE761	MSE748
Borehole no.	EST205	MSE101	MSE101
Extraction date	16/09/2000	–	14/01/1995
Upper extraction depth (m)	467.47	567.72	564.50
Lower extraction depth (m)	467.77	568.02	564.80
Cored sample quantity	2	4	2
Permeability test type	Steady state gas flow	Steady state gas flow (1 test) and transient water flow (3 tests)	Transient water flow
Density	2.43	2.31	2.35
Water content (%)	7.4	8.3	7.3
Sonic celerity V_p (m/s)	3170	3146	3170
CaCO ₃ (%)	24.0	19.4	25.2

Davy et al. (2007) drew the following conclusions from the experimental research: (i) according to the permanent gas flow test results, permeability K depends mainly on crack closure (cc), with values in the order of 10^{-13} – 10^{-16} m². Permeability from transient water flow tests varies with test duration from 10^{-18} to 10^{-21} m². In both types of tests, K also depends on confining pressure (P_c), mainly during the first three loading–unloading phases; (ii) swelling does not contribute to unloading in the crack zone, but rather creates additional closure and pressure in the crack area; (iii) there is a strong coupled effect between H₂O and the crack closure amplitude and permeability; and (iv) the physico-chemical phenomena that govern macro-crack self-sealing have extremely rapid kinetics.

Horseman and Harrington (1997, 1999) conducted seven gas migration tests on cylindrical samples of saturated compacted MX-80 bentonite subjected to different values of isotropic confining stress and a water backpressure of 1 MPa. Samples were divided in two groups; high swelling (HS, 4 samples) and medium swelling (MS, 3 samples). The samples were first saturated and consolidated under different values of isotropic confining stress and a water

backpressure of 1MPa. Figure 2.18 illustrates an example of the test results on specimen MX80-4A (HS). These results represent the experimental findings. The applied confining stress was 16.0 MPa. A gas breakthrough event was detected approximately on day 7 after the beginning of the injection. Gas injection was stopped on day 14 and the shut-in transient was monitored. Gas injection was restarted on day 30 at the same value of flow rate. After the second gas injection stage, the specimen was subjected to a decreasing history of pumping rates; 180, 90, 45 and 0 $\mu\text{l/h}$.

Horseman et al. (1999) reached several conclusions in their investigation. As commented by Alonso et al. (2006), the most relevant result is probably that no water displacement was observed to occur inside the specimen, despite the fact that the observed breakthrough pressure seems to be higher than the air entry pressure of the compacted bentonite. The peaks observed in gas pressure and measured flows in and out of the specimen are also quite typical. Such behaviour has been measured in other clay materials as well. There is a spontaneous decrease in pressure after the peak is reached which indicates the aperture of a preferential path of high conductivity. The absence of a marked peak during the second injection phase indicates that the initial path remained partially open (Alonso et al. 2006). This interpretation is also consistent with the lower gas pressure that is reached during the second injection phase. It was also checked that the gas pressure at peak is equal to the swelling pressure plus the existing pore pressure. In other words, the gas pressure has to reach the total stress in a critical plane in order to develop a preferential path (Alonso et al. 2006).

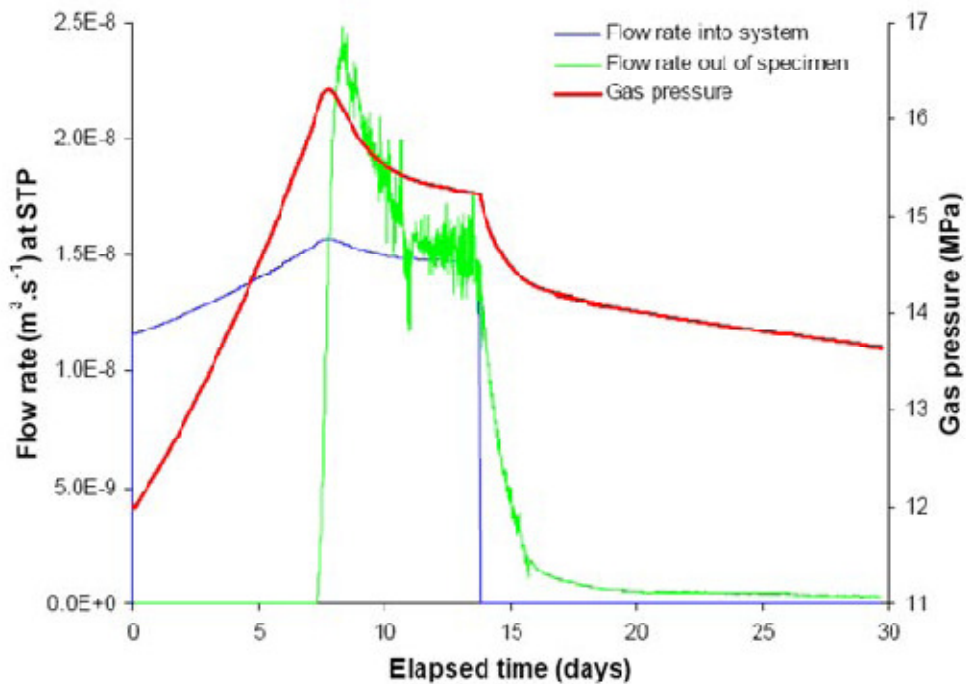


Figure 2. Evolution of flow rate into system, injection pressure and outgoing flux during the first injection and shut-in stage. Test MX80-4A (Horseman and Harrington 1999).

In conclusion, the analysis of the experimental studies presented above indicates that gas transport in underground repository media is mainly governed by coupled hydro-chemical-mechanical processes. However, It be should emphasized that most of the studies conducted have ignored the thermal effect. This effect may significantly affect the gas migration through the aforementioned porous media.

2.3.1.2 Studies on gas generation

Major experimental investigations on gas generation were performed by Small et al. (2008). They conducted extensive experimental studies by establishing a large-scale gas generation experiment at an LLW/ILW repository in Olkiluoto, Finland. They examined gas generation from LLW in waste drums that were disposed in the operational VLJ Repository (VLJ is a Finnish acronym which translates to “reactor operating waste”). In a period of 9 years, the experiment monitored the rate and composition of gas generated, and the aqueous geochemistry and microbe populations present in various locations within the experiment (Small et al. 2008). The large-scale gas generation experiment is presented in Figure 2.19. The experiment has been

also modelled (Figure 2.20) by using the biogeochemical reaction-transport code (GRM) for predicting gas generation that is presented in Section 3.1.5.

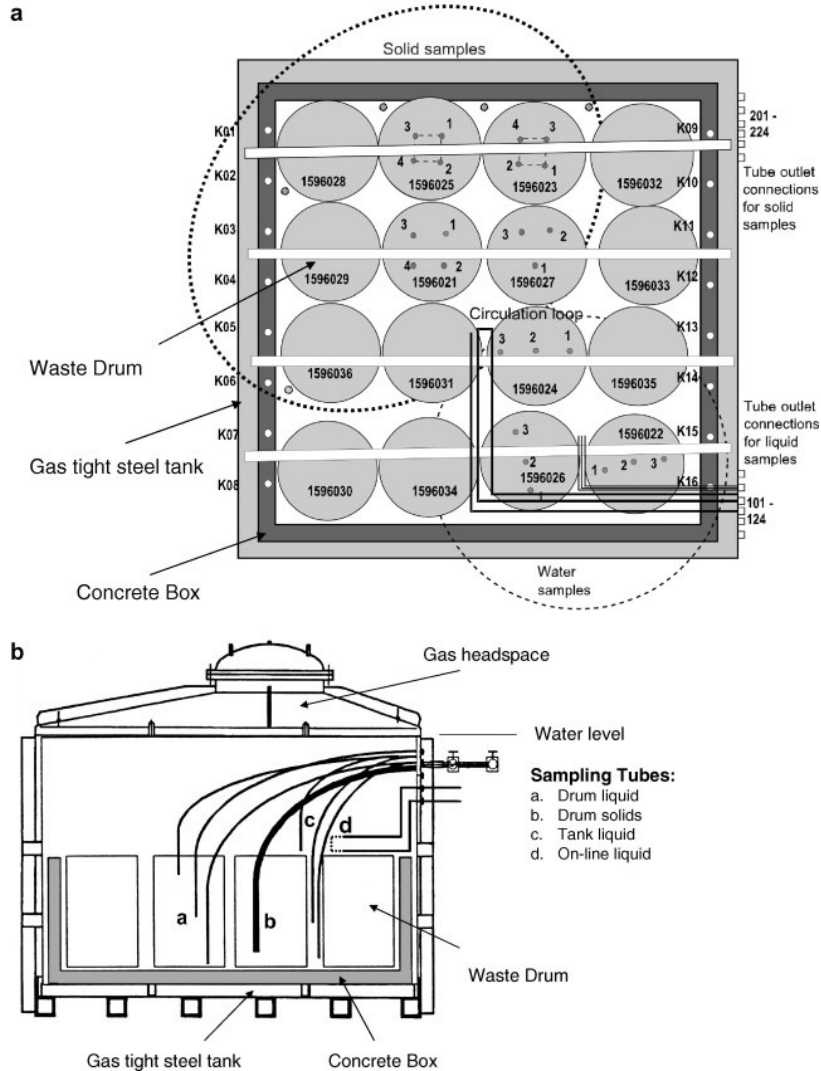


Figure 2.19. Plan (a) and side elevation (b) of the gas generation experiment showing the position of the waste drums and sampling lines.

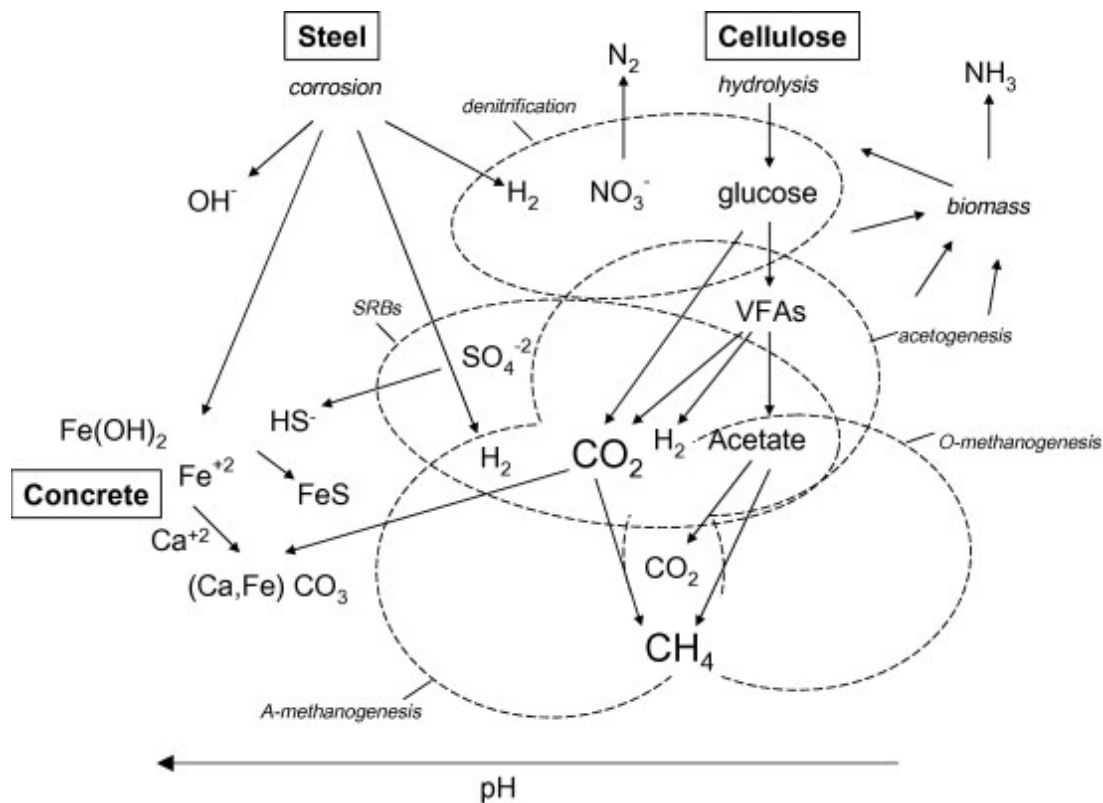


Figure 2.20 Conceptual model of biogeochemical processes occurring within the gas generation experiment and represented in the GRM model (Small et al. 2008).

The main conclusions of the experiment and modelling efforts are as follows: (i) gas generation is a complex mechanism that involves biological, geochemical and hydraulic factors; (ii) the GRM code is able to capture all of these factors and their interactions, and predict the gas production rate with relatively good accuracy; (iii) a key uncertainty in the current GRM model, particularly for simulation of pH variations, concerns the transport of species amongst the waste, water and concrete regions of the experiment. An understanding of these transport effects will be required in order to fully apply these models at the repository scale.

2.3.2 Field studies

2.3.2.1 Background

Key field studies on gas migration performed in European URLs will be presented in this section. In many European countries (e.g. Belgium, France, Italy, Switzerland, and the UK), deep

argillaceous rocks are considered as a potential host rock for the construction of repositories to dispose radioactive waste. Among these argillaceous rock formations, we have mentioned Opalinus clay in Switzerland, Boom clay in Belgium and Callovo-Oxfordian clay in France. The URLs of Mont Terri, HADES (Mol Site) and Meuse/Haute Marne are built in the formations of Opalinus, Boom and Callovo-Oxfordian clays, respectively. Those formations represent a spectrum ranging from clay with a 40% volumetric H₂O content with relatively high plasticity up to a highly consolidated stiff clay stone with a volumetric water content as low as 5%. The main characteristics of these formations are described by Su (2007) as follows:

Boom clay: Boom clay is marine fine-grained sediment from the Rupelian Age (about 30 million years before present). It shows distinctive layering, which is the result of variations in grain sizes, organic matters and carbonates (Su, 2007). The grain size distribution indicates a relatively wide variation; the clay fraction (< 2µm) ranges from 30 to 70% (average of 55%). The predominant clay minerals are: illite (50%), smectite and illite-smectite interstratifications (30%), kaolinite (10%), chlorite (5%), degraded chlorite and illite-chlorite interlayers, and glauconite (3%). Muscovite and biotite (mica minerals) are only present in small quantities. Boom clay also has 1-5% of carbonates, pyrite and organic matter. Its hydro-mechanical properties are usually considered homogeneous (Su 2007). The basic geomechanical characteristics and conditions of Boom clay that is located around the Mol Underground Laboratory (225 m in depth) are given in Table 2.5. The hydraulic conductivity of Boom clay in the flow direction parallel to the bedding plane is twice that of the orthogonal direction to the bedding plane.

Table 2.4. Geomechanical characteristics of Boom clay in the Mol Site, Belgium (Su 2007).

Initial total stress	4.5 MPa	Porosity n	0.39
Initial pore pressure	2.25 MPa	Water bulk modulus K_w	0.2-2 GPa
Young's modulus E'	300 MPa	Hydraulic conductivity k	$2 \cdot 10^{-12}$ m/s – $4 \cdot 10^{-12}$ m/s
Poisson's coefficient ν^h	0.125	Plastic limit	23-29 %
Cohesion c'	300 kPa	Liquid limit	55-80 %
Friction angle Φ	18°	Plasticity index	32-51 %
Rc	2 MPa	Water content	22-27 %

Callovo-Oxfordian argillites: Callovo-Oxfordian argillites are marine sediments from the Jurassic Age (about 150 million years ago). They are overlain and underlain by relatively impermeable carbonate formations. The argillites contain an average of 40-45% clay minerals (illite, regular mixed layer R1 illitesmectite, chlorite and kaolinite in the lower part, illite and irregular mixed layer R0 illite-smectite in the upper part), 20-30% carbonate and 20-30% quartz silts. The layer is almost horizontal. The mechanical behaviour of the rock is ruled by the geological characteristics of the argillites. Its mineralogical composition and sedimentation have led to a slightly anisotropic behaviour of the argillites. The combined effect of sedimentation, compaction and diagenesis has decreased the interstitial or connected pore space. Hence, Callovo-Oxfordian argillites are regarded in their natural state as a saturated porous medium with very low permeability. Their mechanical behaviour is closely coupled with the pore pressure and the degree of saturation. From a geomechanical viewpoint, the Callovo-Oxfordian formation may be subdivided into three rheological zones with different geomechanical properties: two stiff (higher carbonate) zones that surround a central and less stiff (more clayey) zone (Su 2007). Table 2.6 shows the basic mechanical characteristics of the three zones as observed at a depth varying between 420 and 550 m.

Table 2.5. Basic mechanical characteristics of the different geological zones in the Callovo-Oxfordian formation (Andra, 2005)

Characteristics	Rheological zone			Overall
	Upper	Median	Lower	
Depth (m)	420-455	455-515	515-550	420-550
Initial total stress	12-16 MPa at -500 m			
Initial pore pressure	~ 5 MPa at -500 m			
Density (g/cm ³)	2.42	2.42	2.46	2.40-2.45
Water content (% mass)	6.1	7.1	5.9	5.3-8.0
Porosity (%)	14	15.5	13	11.5-17
Young's modulus (GPa)	6.2	5.5	7.2	6.0
Uniaxial compressive strength (MPa)	30	21	21	24
Uniaxial tensile strength (MPa)				2.6
Hydraulic conductivity (m/s)	10 ⁻¹³ -10 ⁻¹⁴			10 ⁻¹³ -10 ⁻¹⁴

Opalinus clay: Opalinus clay generally consists of dark grey, silty, calcareous and micaceous clay stones from the Jurassic Age. In Zürcher Weinland, Northern Switzerland, the Murchisonae

Beds (approximately 20 m thick) that are located above the Opalinus clay, consist of black silty to fine sandy, calcareous claystones and are thus similar, in terms of lithology, to the uppermost Opalinus clay. Mineralogical investigations reveal that the phyllosilicate fraction contains mainly kaolinite, illite and illite/smectite interlayer minerals in about equal amounts (average amount is 54% at Benken) (Volckaert et al. 2004). The carbonate content is rather high, ranging from 10 to 50% (average 26% at Benken), and dominated by calcite. Quartz is also present in relatively large quantities (average 20% at Benken). The content of organic matter is about 0.5%. Figure 2.21 illustrates the mineralogical and structural features of the Opalinus clay in Zürcher Weinland at various scales. Petrophysical logs indicate moderate variability and a slight increase of clay content with depth, suggesting a division of the Opalinus clay into five lithostratigraphic sub-units (facies). The mechanical properties of Opalinus clay were found to be highly anisotropic (transversally isotropic). A dependency of the elastic properties and strength parameters on water content are observed. In addition, a transition was noticed from brittle behaviour at lower water content to more ductile behaviour at higher water content. The physical properties of the rock depend to a lesser extent, on its mineral composition. Although no direction dependency was observed for Poisson's ratio, the elasticity moduli showed a clear anisotropy in relation to stratification with $E_{\text{parallel}} > E_{45^\circ} > E_{\text{perpendicular}}$ (Su 2007). The following observations were made in Zürcher Weinland at a depth of about 600 m (Table 2.7).

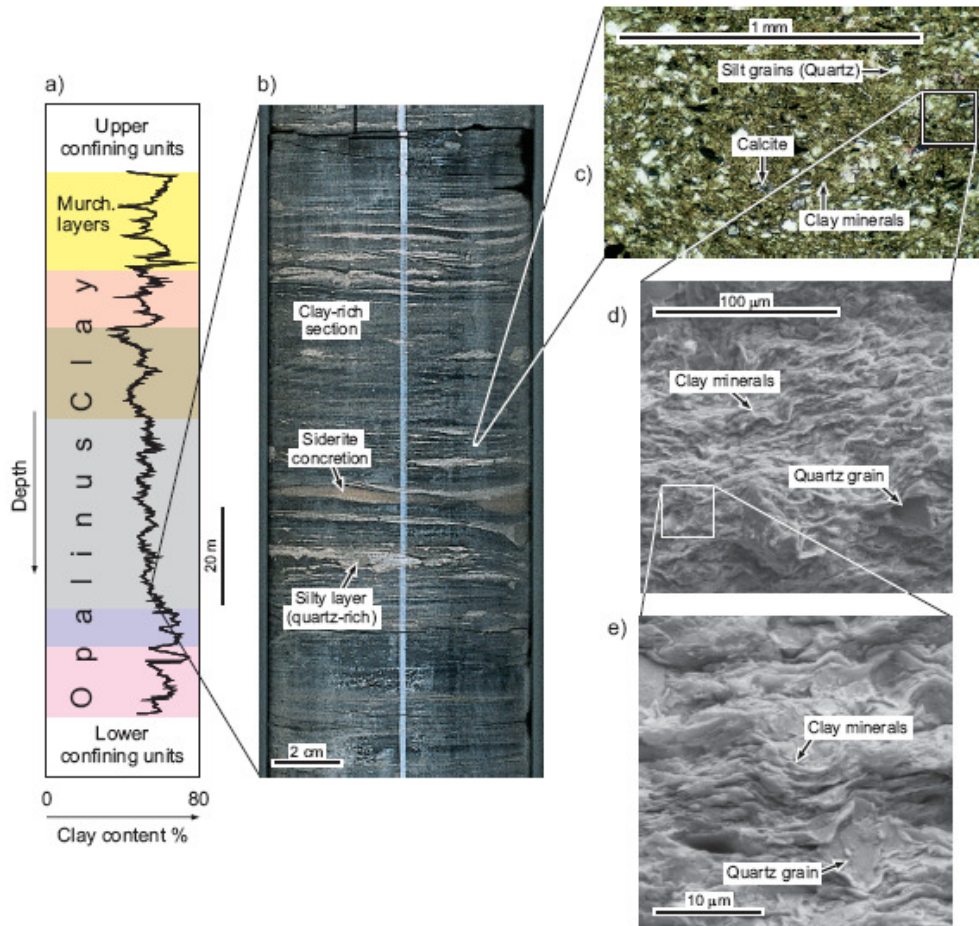


Figure 2.21. Illustration of the mineralogy and structure of Opalinus clay at different scales (Nagra, 2008)

- a) vertical profile of clay content determined by petrophysical logging
- b) Core samples
- c) Thin sections
- d) :e) SEM images (Nagra 2002a)

Table 2.6. Geomechanical characteristics of Opalinus clay (Volckaert et al. 2004)

Site	Mont Terri		Zuricher Weinland	
	Matrix	Bedding	Matrix	Bedding
Initial vertical stress	6-7 MPa		15.9 MPa	
Initial max./min. horizontal stress	2-3 MPa / 4-5 MPa		22.6-15.1MPa	
Initial total mean stress	4-5 MPa		18 MPa	
Initial pore pressure	1-2 MPa		6-7 MPa	
Porosity	0.16		0.12	
Young's modulus	6 GPa	3 GPa	10.5 GPa	5 GPa
Poisson's ratio	0.24	0.24	0.27	0.25
Cohesion	3 MPa	1 MPa	6.9-8.6 MPa	1.5-1.7 MPa
Friction angle	25°	23°	21-25°	20-24°
Uniaxial compressive strength	10-16 MPa	no data	30 MPa	6 MPa
Tensile strength	1 MPa	0.5 MPa	2.7 MPa	1.2 MPa
Hydraulic conductivity	$8 \cdot 10^{-14}$ m/s	$2 \cdot 10^{-13}$ m/s	$2 \cdot 10^{-14}$ m/s	$1 \cdot 10^{-13}$ m/s

It should be mentioned that most of the studies that were conducted in the aforementioned rock formations and URLs or other URLs, focussed on the hydrogeological, geochemical, and geomechanical aspects that are related to the safety of underground repositories of nuclear waste. Gas generation and migration problems were assigned a lower priority and their investigation has commanded fewer resources than issues which are regarded as most central to the safety case; all performance assessments include detailed analyses of the groundwater pathway, but only a few have addressed the gas problem, although this problem may potentially affect the safety of the nuclear repository. Consequently, there is relatively, fewer published field data and studies on the gas problem. Most investigations into gas migration through engineered and geological barriers of deep radioactive waste repositories have only taken place over the past 15 years, a shorter period of investigation than other issues that affect repository behaviour. The results of a major field study on gas migration conducted in an Opalinus clay formation will be presented and discussed below.

2.3.2.2 Gas migration field study in Opalinus clay formations

As part of the Swiss waste disposal programme, gas transport processes were investigated in Opalinus clay (Nagra, 2002a; Nagra, 2002b; Nagra, 2004). The studies focussed on Zürcher Weinland in Northern Switzerland, with a deep investigation borehole in the neighbourhood of the village of Benken, and the Mont Terri Rock Laboratory situated in the Folded Jura of north-west Switzerland close to the town of St-Ursanne. The field studies included mainly:

- (i) hydraulic packer tests (Figure 2.22): packer tests in boreholes have been the main source of field data that contribute to the characterization of gas transport properties (e.g. flow model identification, estimation of hydraulic conductivity, storage coefficient and hydraulic head) in Opalinus clay, and
- (ii) gas injection tests (Figures 2.22, 2.24). The primary purpose of the gas test sequence is to determine the gas entry pressure of the formation.

Table 2.8 gives the main results of the conducted gas parameter tests. The determined entry pressures range from 0.4 to 10 MPa and exhibit a marked dependence on intrinsic permeability as illustrated by Figure 2.24. Marschall et al. (2005) pointed out that both in situ gas tests and gas permeameter tests on drill cores demonstrate that gas transport through the rock is accompanied by pore water displacement, suggesting that classical flow concepts of immiscible displacement in porous media can be applied when the gas entry pressure (i.e. capillary threshold pressure) is less than the minimum principal stress that is acting within the rock. At elevated gas pressures (i.e. when gas pressure approaches the level of total stress that acts on the rock body) evidence was seen for dilatancy controlled gas transport mechanisms.

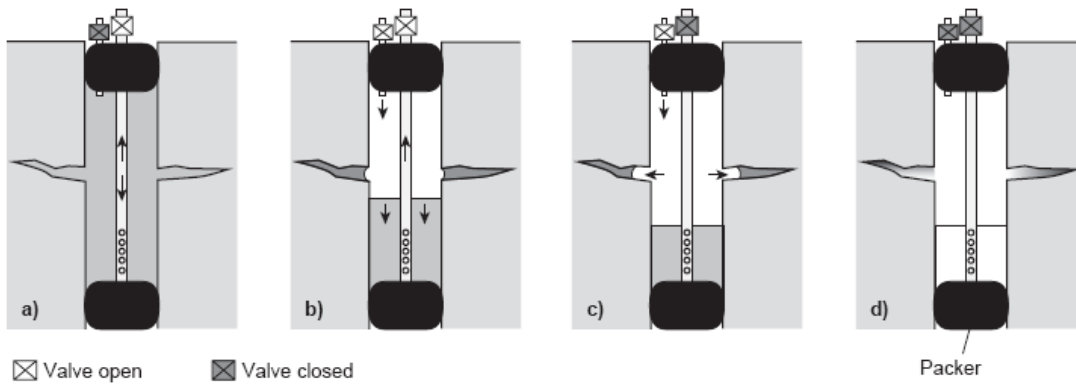


Figure 2.3. Gas threshold pressure testing in boreholes - test configuration and procedure: a) hydrotest sequence; b) water/gas displacement DISP; c) gas injection phase GRI; and d) gas pressure recovery phase GRIS.

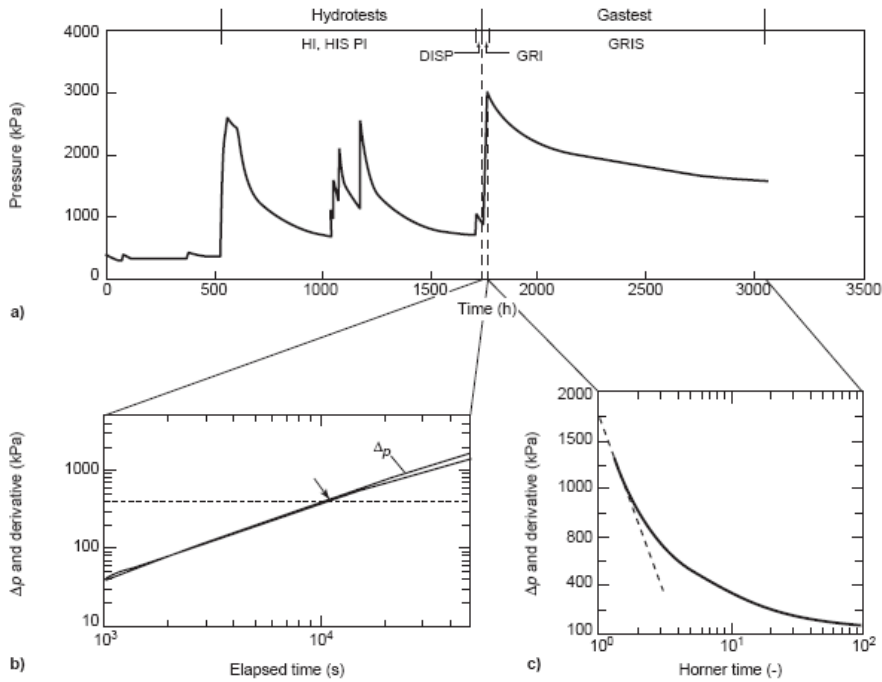


Figure 2.23. Gas threshold pressure test GP-4 at Mont Terri:

- a) entire test phase comprising of a hydrotest and gas test sequence; b) log-log derivative plot of the GRI phase; and c) Horner plot of the GRIS phase.

Table 2.7. Overview of gas parameter tests with core specimens from Benken and Mont Terri (Marschall 2005)

Core sample	Injection period (d)	Direction of flow relative to bedding	Intrinsic permeability ^(a) k (m ²)	Gas entry pressure p _{ae} MPa
OPA-1	140	90°	k _p = 3-6 * 10 ⁻²¹ k _n = 5-7 * 10 ⁻²²	~4
OPA-2	120	0°	3 * 10 ⁻²¹	7.5-10
BED-B3 06 ^(b)	60	0°	2 * 10 ⁻²⁰	<0.03
BFP 16	110	50°	1.5 * 10 ⁻²⁰	0.5
BWS-E4 06	180	90°	2 * 10 ⁻²⁰	0.2
BED-C5/7	174	35°	2 * 10 ⁻²⁰	0.2

a: intrinsic permeability: k_p parallel to bedding, k_n normal to bedding

b: core sample is not representative of undisturbed Opalinus clay (visible fracture in flow direction)

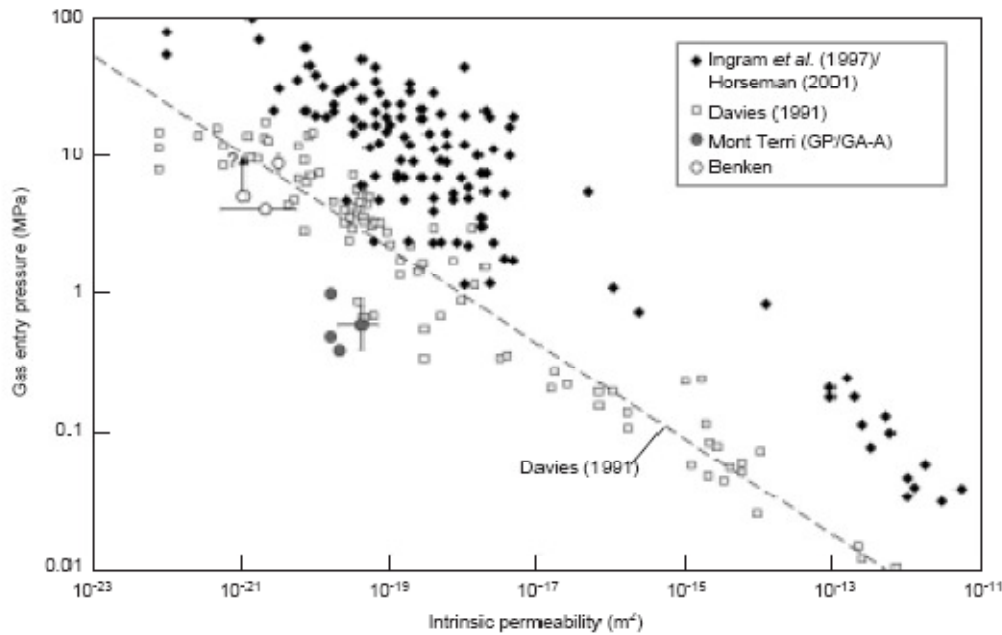


Figure 4. Relationship between gas entry pressure and intrinsic permeability for various low permeability rock formations (claystones, shales, sandstone) (Marschall 2005)

Beyond packer testing and gas injection in boreholes, laboratory tests were also conducted to determine the unsaturated properties of Opalinus clay. It is known that the key parameters required for the simulation of gas transport processes in the undisturbed rock zone around an L/ILW repository are porosity of the intact host rock, intrinsic permeability, capillary pressure-saturation relationship, and relative permeability-saturation relationship (Nagra 2008). Figure

2.24 summarizes the main results for determining the water retention curves of the Opalinus clay, while Figure 2.25 gives the capillary pressure - water saturation curves of the clay.

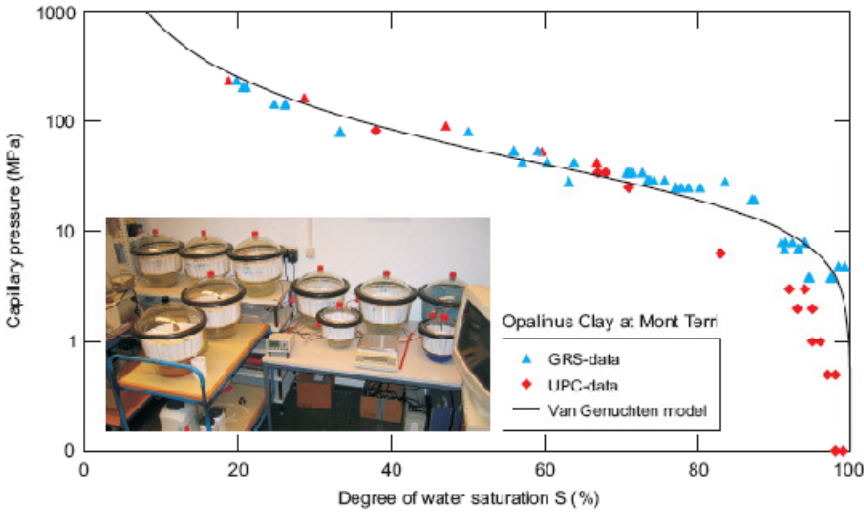


Figure 2.25. Capillary pressure measurements (water retention curves) by stepwise desaturation and resaturation in a desiccator (photo, Nagra 2008).

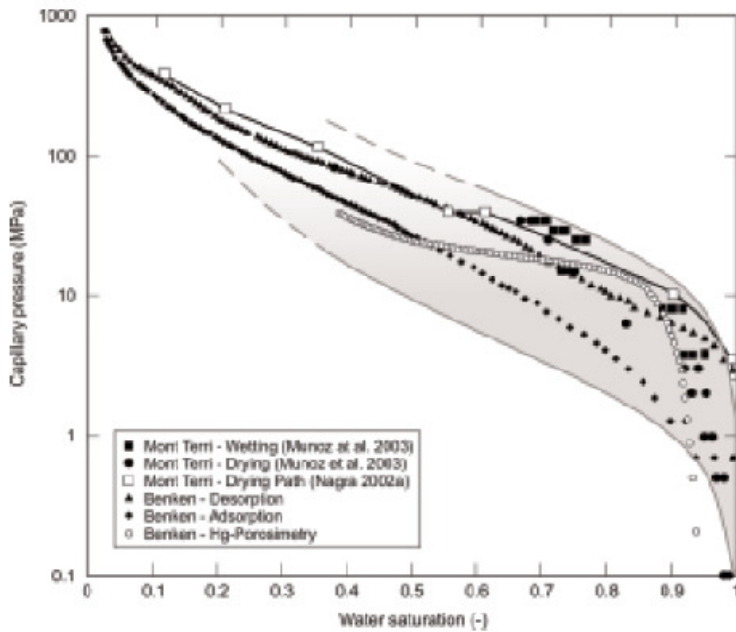


Figure 2.26. Capillary pressure - water saturation curves for Opalinus clay samples (Nagra 2008)

The results of field studies on gas migration presented above are in good agreement with the observations made at the laboratory scale. The field results presented above were used in the

development of numerical and simulation tools to assess issues on post-disposal gas generation for a generic geological repository in Northern Switzerland with regards to L/ILW in Opalinus clay. The main findings with respect to gas generation rates, gas pressure build-up, design measures to mitigate overpressures and pore water displacement, are presented in Nagra (2008).

2.4 Summary and Conclusions

In this chapter we reviewed current experimental and theoretical research on gas generation and migration from a repository in sedimentary rock formations. We gave particular attention to state-of-art conceptual and mathematical models for the simulation of gas generation and transport. Based on the information obtained and analyzed in this chapter, the following conclusions can be drawn:

- Significant quantities of gases can be generated in underground repositories for radioactive waste. These gases can potentially influence the safety of the repositories.
- The main gas generation mechanisms are: (i) the anaerobic corrosion of metals in waste and packaging (production of hydrogen); (ii) the radiolysis of H₂O and certain organic materials in the packages (mainly production of hydrogen, but also oxygen, carbon dioxide, methane, etc., can be produced in lower quantities); and (iii) the microbial degradation of organic waste components (production of methane and carbon dioxide). The most important mechanism is the corrosion of metals.
- In practice, the gas generation rates are often estimated by using constant gas generation rates obtained from laboratory experimental tests or simple approximation models. This results in a highly conservative estimation of the quantity and rate of gases produced in a repository during its lifetime. In order to avoid this overly high degree of conservatism, complex geochemical codes were developed to estimate and predict the type, amount and rate of generated gases.
- Several geochemical codes have been developed in the last decades to predict gas generation and its main features (e.g. GAMMON, SMOGG, GETAR, RadCalc, GRM, RPM). However, modelling and prediction of gas generation in repositories for nuclear waste is most advanced for corrosion. Radiolysis can be predicted with well established models. The modelling of microbial gas generation is only limited to well defined scenarios. Furthermore, interactions have to be considered in modelling between the gas

generation mechanisms (e.g. by water balance for limited supply) as well as with other processes, such as fluid flow (water saturation), geochemical history and geomechanical forces (vs. pressure build-up). This has been mostly ignored in previous studies.

- The gases that are generated can have various potential transport paths in a repository. These paths greatly influence the transport mechanisms of the gases. The transport paths include: (i) the engineered barrier systems, backfill in the repository chambers, galleries and drifts; (ii) the EDZ; (iii) the host and overlying rocks; and (iv) the structural discontinuities.
- The transport of gases through low-permeability rock of geological repository systems is controlled not only by the hydraulic and mechanical properties of the rock mass or engineered barrier (intrinsic permeability, porosity, rock strength), but also by the gas entry pressure and the hydromechanical state of the rock or engineered barrier.
- There are four main phenomenological gas transport mechanisms: (i) advective-diffusive transport of gas dissolved in the pore water; (ii) visco-capillary two-phase flow; (iii) dilatancy-controlled gas flow; and (iv) gas transport along macroscopic tensile fractures (hydro- and gas-fracturing).
- However, gas transport mechanisms are not only controlled by the above hydro-mechanical processes, but hydro-chemical interactions (self-healing processes) can also significantly affect the gas transport in an underground repository.
- The main conceptual and modelling approaches developed in the last decade that describe and predict the gas transport mechanisms can be divided into three types: (i) approaches related to Darcy's law; (ii) modified Darcy approaches; and (iii) models for gas transport through EDZ. These models have been validated against experimental results. There is a relatively good agreement between the modeling results and the experimental tests (mostly at laboratory scale). However, most of these models only consider the coupled hydro-mechanical effects without taking into account the mechanical damage or dilatancy effects; the thermal (e.g. heat generated by the waste) and chemical factors (e.g. chemical self-healing) are often ignored.
- Most of the previous experimental investigations which study gas generation and migration are performed at laboratory scale. These laboratory studies have allowed tremendous progress to be made in understanding the mechanisms of gas generation and

migration as well as acquiring a significant amount of laboratory data. These data will be very useful for the modeling part of the present study. The results of the laboratory studies generally confirm the good ability of the gas transport models (presented above) to capture the flow mechanisms of the gases that are generated with reasonable accuracy.

- However, there are relatively few published field data and studies on the gas problem. This is because most investigations into gas migration through engineered and geological barriers of deep radioactive waste repositories have only taken place over the past 15 years, which is a shorter period of investigation than any other issue that affects repository behaviour. The results of field studies performed in the URL Mont Terri are in good agreement with those obtained from laboratory tests as well as theories of gas transport mechanisms that are presented above. These field results can be used in the calibration for developing models in the present study.
- In conclusion, an analysis of the experimental and theoretical studies presented above indicates that gas generation and transport in underground repository systems are governed by complex coupled processes that can involve bio-hydro-chemical processes for gas generation, and hydro-chemical-mechanical processes for gas transport. The thermal factor which is mostly ignored should be taken into account in future work.

3 Geological and geotechnical characteristics of sedimentary rock formations in Ontario and comparison with European formations

3.1 Introduction

The objectives of the present chapter are: (i) to compile published geochemical, mechanical, hydraulic and thermal data on sedimentary rock formations in Ontario, which are relevant to the study of gas generation and transport. (ii) Compare the data to those from European sedimentary rocks. Discuss and analyze the usefulness and transferability of the research results in Europe to the Ontario situation.

To achieve the aforementioned objectives, three main stages are carried out:

- The first stage includes the collection of data on sedimentary rock formations in Ontario, which are necessary to build and validate a conceptual model for the area of study. Geological, geomechanical, geochemical, hydrological and thermal data are gathered and analyzed with regards to gas generation and migration.
- The second stage deals with a review and analysis of the experimental (laboratory and field) data from European sedimentary rocks and URLs for nuclear waste storage with respect of gas transport. Figure 3.1 summarizes the different components or units (container, buffer, backfill, excavation disturbed zone (EDZ), and host rock) of an underground repository system and the sources (e.g. URL tests, lab tests) of the data. Note that the current OPG's proposal for LILW relies on the multiple layers of low permeability shale for contaminant barriers, and not on other engineered systems such as container, buffer and backfill. From Figure 3.1, it can be seen that studies accomplished in the oil/gas-waste industry or CO₂ sequestration can also be valuable sources of data and information. Field tests performed in URLs, such as Opalinus Clay (OPA) at Mont Terri and Benken in Switzerland, Boom Clay under the MEGAS and PROGRESS projects in Belgium, Callovian-Oxfordian (COX) studied by Andra at the Bure URL in France and the Grimsel Test Site (GTS) in Switzerland as well as results from laboratory tests conducted on materials that (mainly) originate from the aforementioned URLs, are reported and analyzed.
- The third stage includes an analysis of the quality, suitability and transferability of the data gathered with respect to the investigation of gas generation and migration in a hypothetical repository in Ontario's sedimentary rocks (especially limestone).

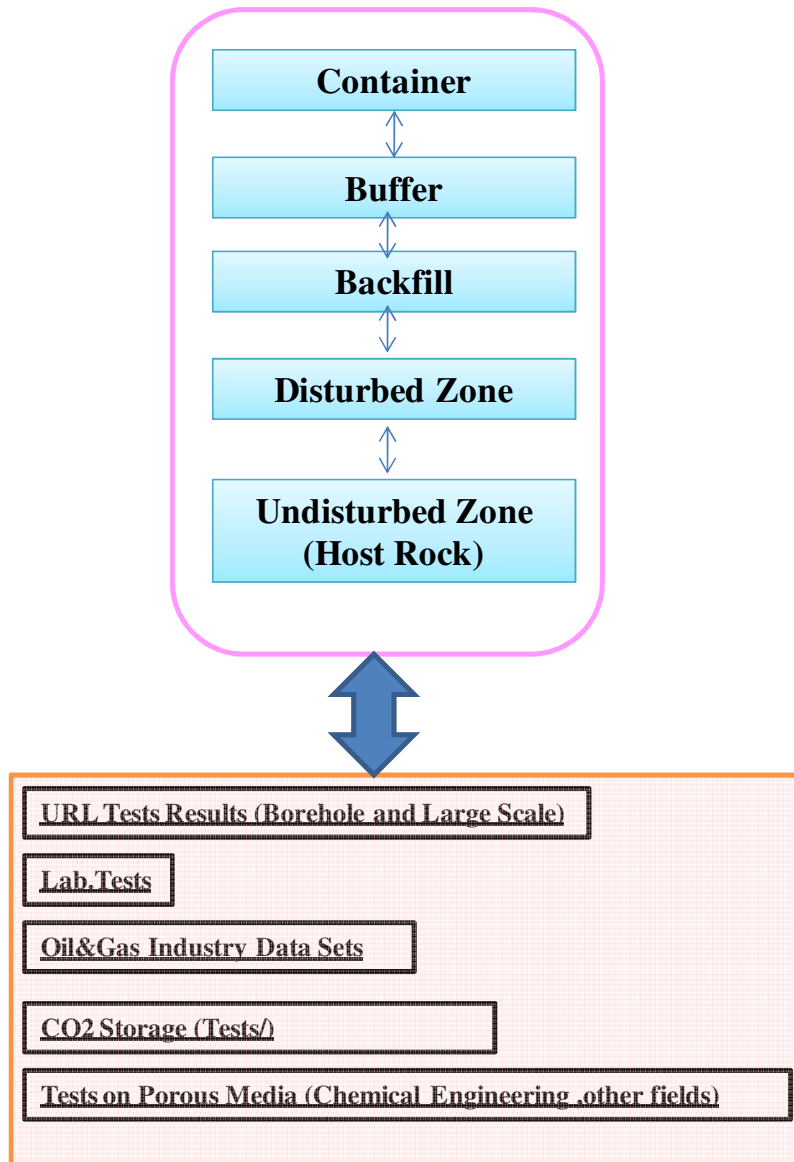


Figure 3.1. Types and sources of collected information

3.2 Review of geomechanical, geochemical, hydraulic and thermal properties of sedimentary rock formations in Southwest Ontario

The main source of the data gathered in this section comes from Ontario Power Generation (OPG). In order to obtain the information needed to present their safety case for a DGR for LILW, OPG has gathered published data on the regional scale, and has conducted a site investigation to obtain site-specific data. The OPG's proposed repository will be at a depth of approximately 680 m in a limestone formation overlain by multiple low permeability formations. The goal of this section is to collect and present the data and parameters which will possibly play relevant roles in the analysis of gas generation/migration in such a repository.

3.2.1 Geological and geomechanical properties

The OPG's proposed DGR will be located at a depth of 680 m below the surface. The repository would be situated within the Cobourg Formation, a low permeability limestone that is overlain by more than 200 m of low permeability shale. The results of a site characterization program have provided a conceptual model of the site (Figure 3.1) and allowed refinement to the geology and hydrogeology aspects of the model. The conceptual model shows that the DGR is overlain by multiple low permeability formations, including 280 m of low permeability limestone, shale and dolostone before the first higher permeability formation (Guelph Formation- Figure 3.2).

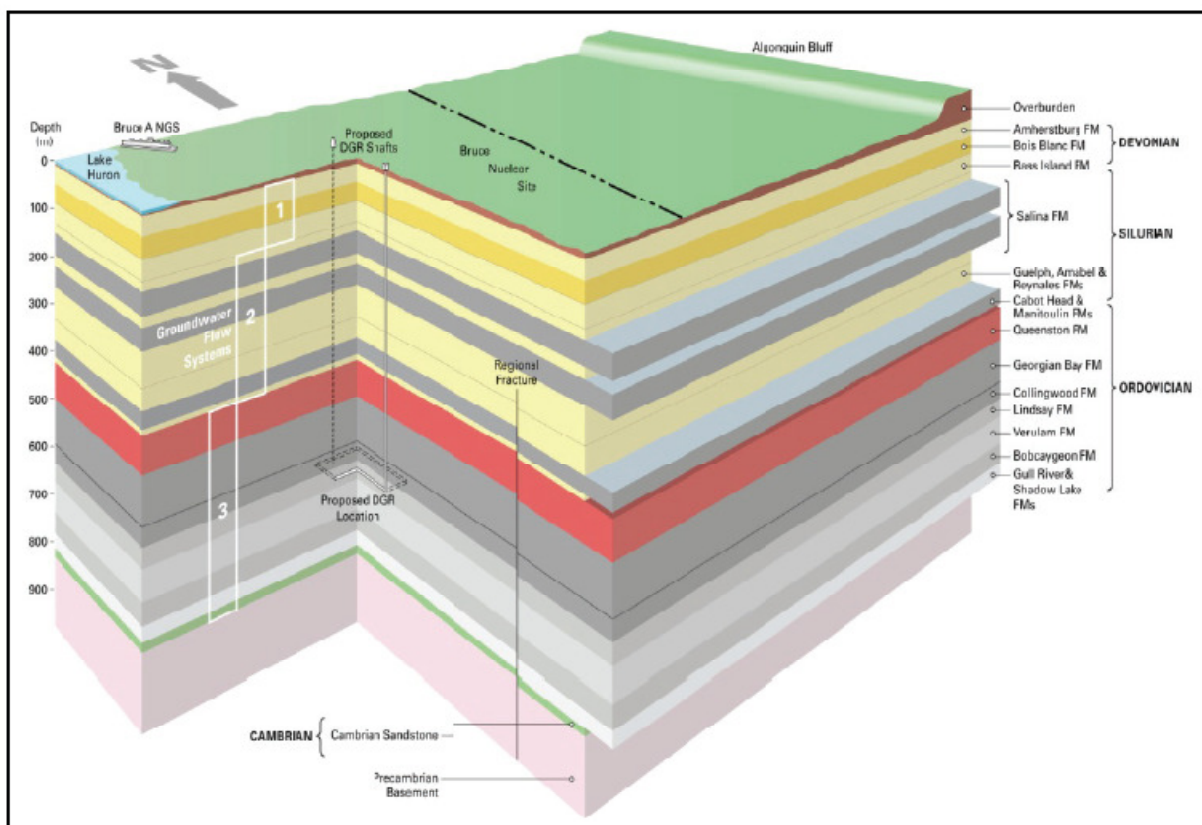
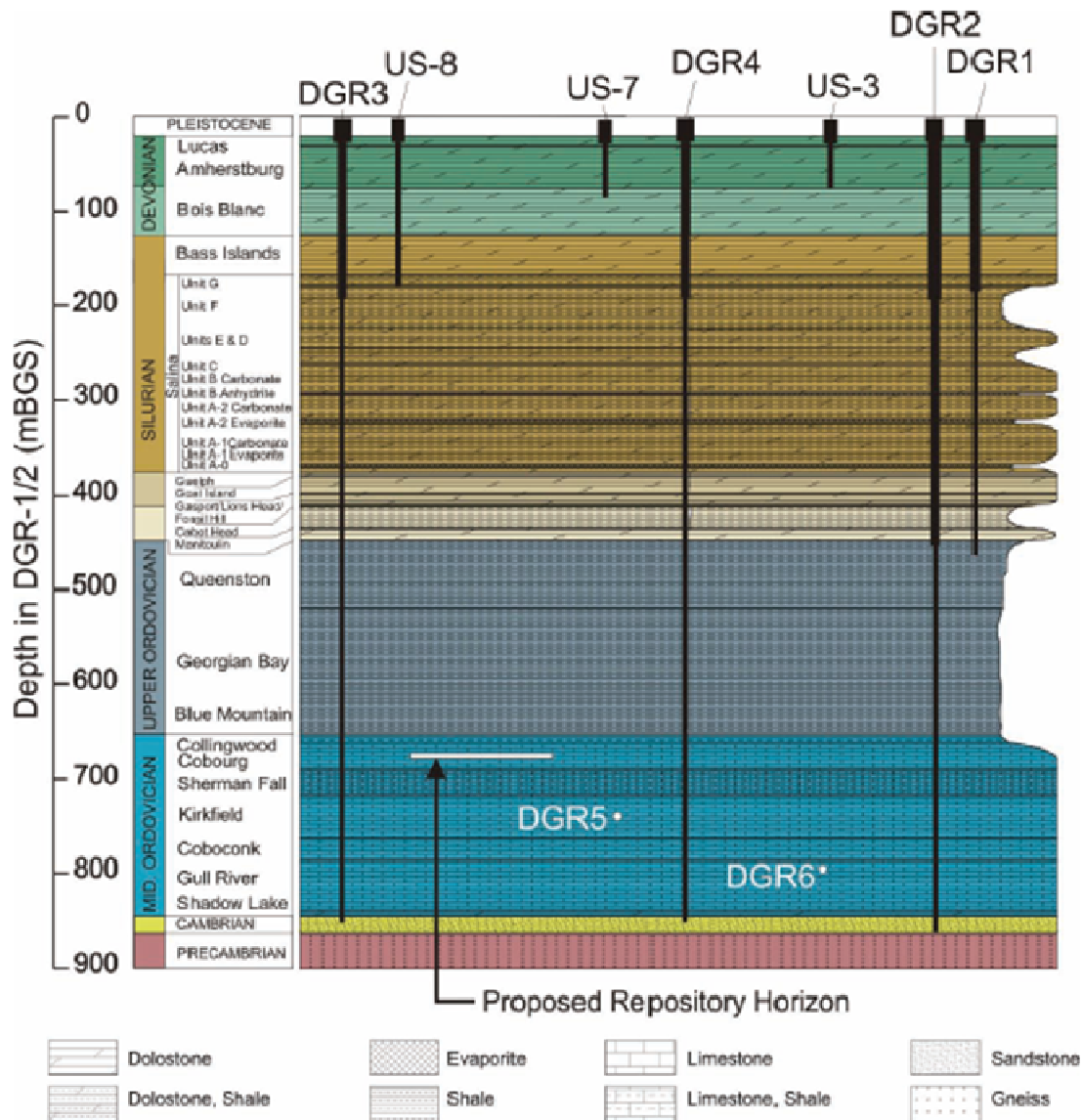


Figure 3.2. Conceptual geosphere model of the proposed DGR (Gartner Lee Limited, 2008)

The shale and anhydrite units with lower permeability are above the Guelph Formation within the Silurian deposits. The DGR would be located in the Cobourg limestone and under the Queenston Shale. The deep groundwater system that exists in these Ordovician formations is very old and highly saline (approximately 300 g/L). The intermediate system covers all of the Silurian formations. This zone has mixed permeability formations (e.g., high permeability Guelph

Formation and low permeability shale/anhydrite beds in the Salina Formation) with groundwater salinity ranging from saline to slightly salty. The Devonian and Quaternary formations represent the shallow groundwater system (see Figure 3.2) for the successive formations and layers over the proposed DGR (Hobbs et al. 2008).



Notes: Vertical borehole penetration depths are indicated by vertical black lines. White dots indicate approximate depth of penetration for angled boreholes DGR-5 and DGR-6. Figure was developed based on information from INTERA (2011).

Figure 3.3. Subsurface stratigraphy in the study area (Gartner Lee Limited, 2008)

Transport of non-wetting fluids in a low-permeability formation, such as the Cobourg limestone and Queenston shale, is largely controlled by the microstructure of the rock. Hence, an assessment of gas transport processes in those formations requires careful consideration of both structure and texture. Figure 3.3a shows the samples of the upper Ordovician Queenston Shale and Upper Ordovician Cobourg (Lindsay) Limestone which were drilled during February 2005 in Niagara Falls, Ontario and in 1978, as part of geotechnical investigations and stored in an unheated core shed (Vilks and Miller, 2007).

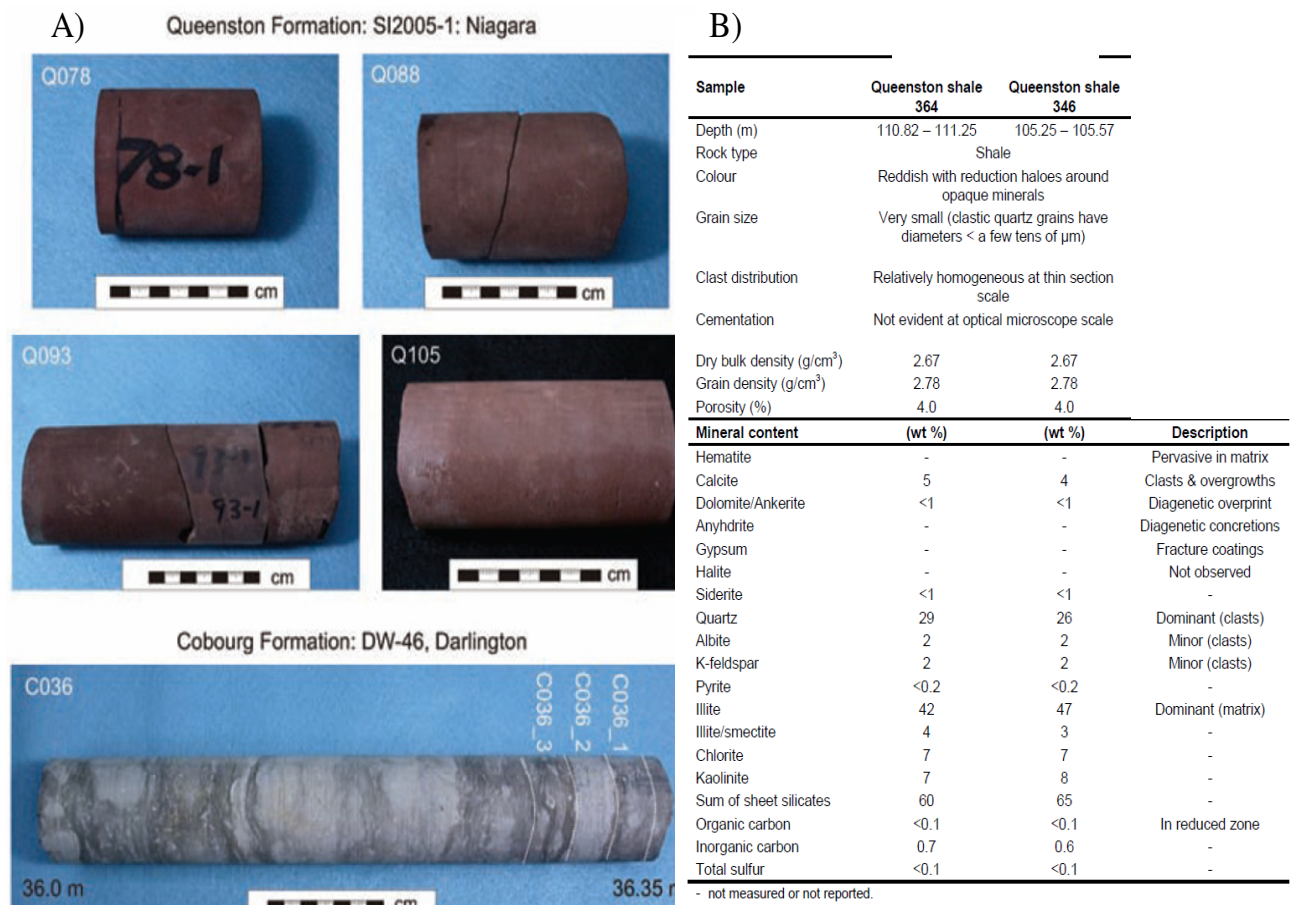


Figure 3.4. a) The drilled core samples from Queenstone Shale and Cobourg Formations, and b) mineralogical contents of Queenstone Shale and Cobourg Formations (Vilks and Miller, 2007)

The overall patterns of joints from all sources in southern Ontario, Michigan, Ohio and New York are compiled in Gartner **Lee Limited** (2008). The latter compiled the data from surficial joint sets; this does not necessarily imply that these joint sets will be consistent with depth at any one location. The collected data indicates a consistent joint set ranging from ENE to ESE in the upper 300 m. At

a greater depth, the NE-ENE trend becomes more consistent. A SSE set is found at below 760 m. In general, the NE-ENE is present across all depths, but other minor joint directions show no discernable pattern (Hill et al., 2002). In a recently released document (Itasca, 2008) on the evaluation of long-term stability of a possible cavern, instead of joint structures, the formation (especially in shale and Cobourg limestone) is modeled with separated horizontal layers.

Information is assembled with regards to the in-situ and regional geomechanical properties of sedimentary formations, as part of the site characterization work (Intera, 2006). The regional data comprise of over 700 test results from 29 sites as described in the public domain literature and laboratory reports (e.g., Gartner Lee Limited, 2008; Gorski et al. 2009, 2010). The database contains a wide range of information on bedrock formations that are of interest to the DGR project, ranging in age from Devonian to Ordovician. Table 3.1 summarizes the general geomechanical properties of the main formations in the study region.

Table 3.1. Laboratory geomechanical properties of rock units (NWMO, 2011)

Rock Formation/Unit		UCS (MPa)	Brazilian Tensile Strength (MPa)	Elastic Modulus (GPa)	Poisson's Ratio
Amherstburg (3)	Mean	98		43	0.21
	Range	71 - 126		28 - 51	0.12 - 0.29
Bois Blanc (3)	Mean	94		37	0.18
	Range	65 - 127		28 - 46	0.14 - 0.21
Bass Islands (3)	Mean	43		19	0.23(1)
	Range	34 - 58		11 - 29	-
Salina F Unit (3)	Mean	31		12	0.21 (2)
	Range	15 - 43		8 - 18	0.18 - 0.24
Salina C (3)	Mean	20		9	0.17
	Range	9.6 - 26		9 - 10	0.06 - 0.28
Salina B Unit (4)	Mean	8		3	0.40
	Range	3 - 11		0.5 - 6	0.11 - 0.67
Salina A2 Unit (2)	Mean	48		19	0.11
	Range	35 - 60		15 - 23	0.10 - 0.12
Salina A1 Carbonate (3)	Mean	143.1		41	0.23
	Range	115 - 196		33 - 47	0.14 - 0.36
Salina A0 (3)	Mean	197.6		63	.43
	Range	166 - 250		60 - 65	0.40 - 0.44
Guelph (3)	Mean	60		28	0.32
	Range	38 - 98		19 - 43	0.25 - 0.40
Goat Island (3)	Mean	148		37	0.37
	Range	101 - 185		31 - 41	0.31 - 0.40
Cabot Head (1)	Mean	13		4	0.38
	Range	-		-	-
Manitoulin (3)	Mean	66		23	0.24(2)
	Range	52 - 80		16 - 30	0.22 - 0.26
Queenston (14)	Mean	48	40 (6)	15	0.31
	Std. Deviation	14.6	-	8	0.09
	Range	19 - 70	2.2 - 8.3	5 - 25	0.09 - 0.44
Georgian Bay (11)	Mean	32	5.6 (8)	12	0.23

Table 3.1 (continued)

Rock Formation/Unit		UCS (MPa)	Brazilian Tensile Strength (MPa)	Elastic Modulus (GPa)	Poisson's Ratio
	Std. Deviation	17.4	-	8.1	0.18
	Range	15 - 63	1.4 - 9.1	3 - 18	.02 - 0.5
Blue Mountain (3)	Mean	21	1.5 (3)	5	0.10
	Range	21 - 24	0.9 - 2.6	5 - 6	0.09 - 0.11
Collingwood (5)	Mean	107	6.2 (5)	30	0.27(4)
	Range	58 - 145	4.8 - 7.8	22 - 40	0.15 - 0.37
Cobourg (67)	Mean	113	6.5 (8)	39	0.3
	Std. Deviation	25.6	-	6.8 (8)	.07
	Range	58 - 175	3.7 - 8.9	19 - 56	0.1 - 0.45
Sherman Fall (8)	Mean	49	4.9 (7)	23(7)	0.22
	Range	32 - 75	3.2	9 - 27	0.08 - 0.47
Kirkfield (5)	Mean	64		26	0.2
	Range	44 - 113		14 - 46	0.11 - 0.44
Coboconk (2)	Mean	188		68	0.33
	Range	186 - 189		67 - 68	0.32 - 0.33
Gull River (2)	Mean	132		56	0.27
	Range	109 - 156		54 - 58	0.24 - 0.29
Cambrian (2)	Mean	72		23	0.33
	Range	60 - 85		21 - 24	0.29 - 0.36

Notes: (x) = number of measurements. Data are from Gorski et al. (2009a, 2009b, 2010a, 2010b and 2010c) and Murphy and Heagle (2010).

For the upper Ordovician shale layers, both the Queenston and Georgian Bay Shales show moderate strength with estimated mean values of 44 MPa and 35 MPa, respectively. Figure 3.4 shows histograms of the UCS data for both the Queenston and Georgian Bay Shales from the regional data.

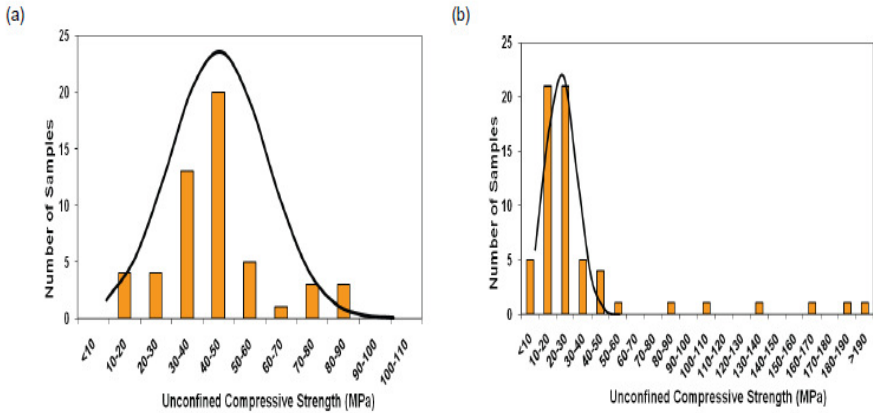


Figure 3.5. Unconfined compressive strength of: (a) Queenston, and (b) Georgian Bay Shales from regional data (Gartner Lee Limited, 2008).

Uniaxial compressive strength of the Cobourg Formation (as an argillaceous limestone), have been obtained by using the results of the 94 samples. These specimens were retrieved from sites at Mississauga, Pickering, Bowmanville, Wesleyville and Port Hope, Ontario. Despite a large data range from 22 to 140 MPa, a well-defined distribution of strength measurements is shown on Figure 3.5. The arithmetic mean of the uniaxial compressive strengths is 72 MPa. Figure 3.5 also illustrates a histogram of the corresponding elastic modulus of the limestone. It has a mean elastic modulus of 31.5 GPa. Table 3.2 shows mechanical properties obtained from one deep borehole at the site of the proposed DGR. The average value for uniaxial compressive strength obtained from that borehole is higher for the COBL compared to the regional data (109.7 MPa vs. 70-80 MPa), and lower for the QES (31.1 MPa vs 40-50 MPa).

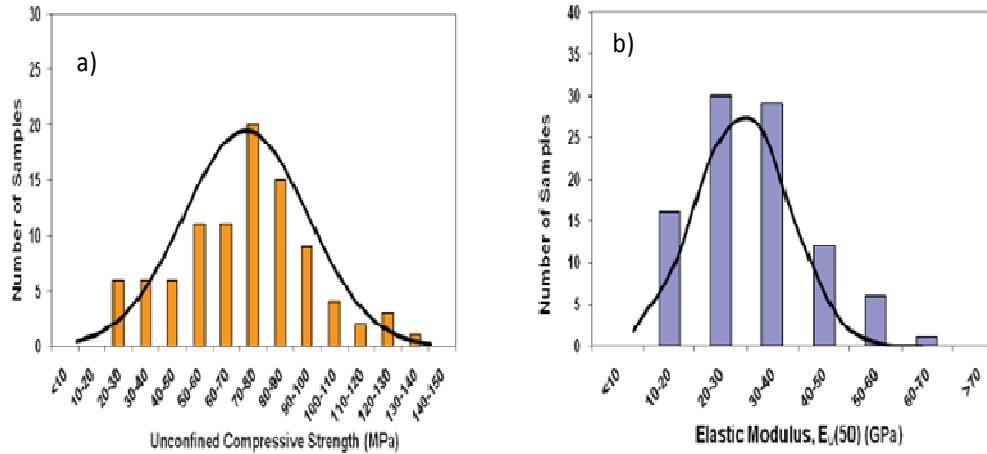


Figure 3.6. a) Unconfined compressive strength and b) elastic modulus of the Cobourg Formation from regional data (Gartner Lee Limited, 2008b)

Most of the available in-situ stress data in Paleozoic rock (Gartner Lee Limited, 2008) were collected from over 20 sites in the Great Lake region. Figure 3.6 shows a plot of the maximum and minimum horizontal stresses (σ_H and σ_h) as a function of depth. There are only a few deep boreholes with in-situ stress measurements drilled within a few hundred kilometers of the selected repository site. A part of these boreholes were completed in Ordovician limestone between 45 and 208 m in depth. Based on these measurements, the σ_h varies between 8.3 and 9.5 MPa within the Ordovician Formations (75 – 208 m). The σ_H for the two rock types was determined to vary between 10.6 MPa and 15.4 MPa in the Ordovician rock and between 17.2 MPa and 19.6 MPa in shield rock.

A recent study at the Norton Mine, which is slightly west of Akron in Ohio, was accomplished by the overcoring method at a depth of about 700 m, yielding an average σ_H and σ_h of 36.7 MPa and 28 MPa, respectively. A higher σ_H was measured by using the same method ($\sigma_H = 44.7$ MPa and $\sigma_h = 23.4$ MPa). The stress value is consistent with earlier hydraulic fracturing measurements (Bauer et al., 2005), where an average σ_H of 44.6 MPa and σ_h of 23.2 MPa were reported for the southern portion of the mine. Also, at the repository horizon, σ_H / σ_v will likely vary from 1.7 to 2.5; σ_h / σ_v from 1.0 to 1.2; and σ_H / σ_h from 1.5 to 2.1 (Gartner Lee Limited, 2008). The scatter in data with depth can be followed in Figure 3.6.

Table 3.2. Average test results for samples from borehole DGR-2 at the site (Damjanac, 2008)

	Elevation (m)	UCS (MPa)	E (GPa)	ν	σ_{cd} (MPa)	σ_{ci} (MPa)	σ_{cd}/UCS	σ_{ci}/UCS
shale	580.99	18.73	3.63	0.02				
		53.31	13.44	0.10	45.82	20.34	0.86	0.38
		41.31	9.57	0.17	39.08	16.56	0.95	0.40
		21.73	4.09	0.09	17.30	9.06	0.80	0.42
		20.78	5.76	0.09	15.81	6.79	0.76	0.33
	average	31.17	7.30	0.09	29.50	13.19	0.84	0.38
Cobourg	652	144.83	36.18	0.21	109.60	45.09	0.76	0.31
		58.32	22.64	0.05	48.60	27.37	0.83	0.47
		128.99	47.46	0.20	125.26	75.00	0.97	0.58
		165.59	42.47	0.24	161.78	74.44	0.98	0.45
		110.60	39.99	0.20		53.08		0.48
		84.23	34.22	0.26	44.88	34.99	0.53	0.42
		78.40	27.79	0.12	55.63	28.23	0.71	0.36
		111.86	38.49	0.13		46.18		0.41
		121.06	43.34	0.15	116.51	49.53	0.96	0.41
		108.74	33.45	0.25	105.02	55.95	0.97	0.51
		94.49	30.37	0.24	84.63	43.49	0.90	0.46
	average	109.74	36.04	0.19	94.66	48.49	0.84	0.44
weak Sherman Fall	685.6	31.98	4.79	0.03	30.63	13.80	0.96	0.43
		39.54	16.70	0.13	13.79	2.25	0.35	0.06
	average	35.76	10.75	0.08	22.21	8.03	0.65	0.24
Sherman Fall	695	67.32	36.76	0.47	49.04	16.92	0.73	0.25
		58.21	20.63					
		50.19	15.53	0.38	34.02	24.20	0.68	0.48
		38.86	30.55	0.11				
		31.66	9.43	0.08	21.45	10.74	0.68	0.34
	737.16	113.04	45.82	0.13	113.04	41.59	1.00	0.37
	average	59.88	26.45	0.23	54.39	23.36	0.77	0.36

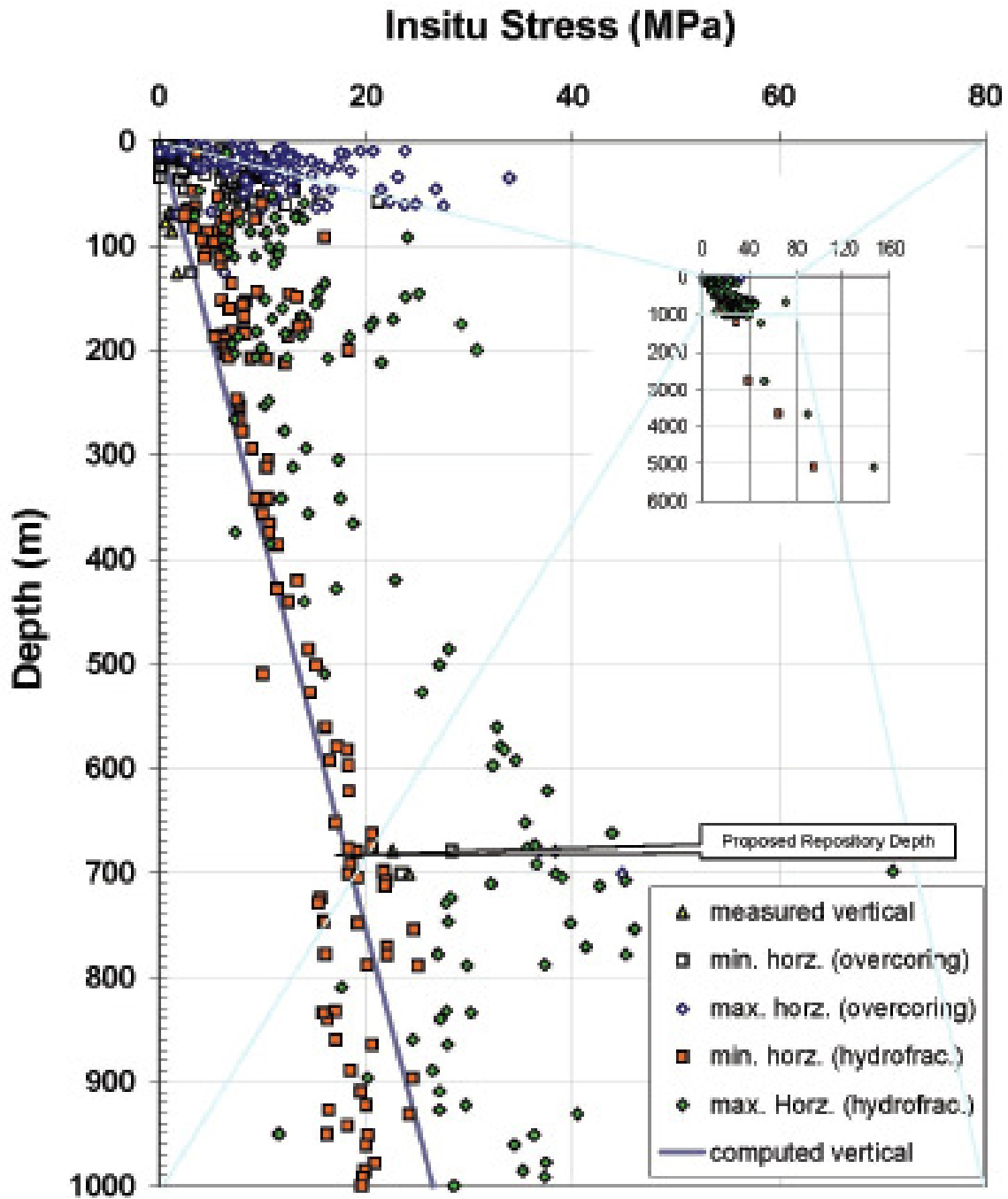
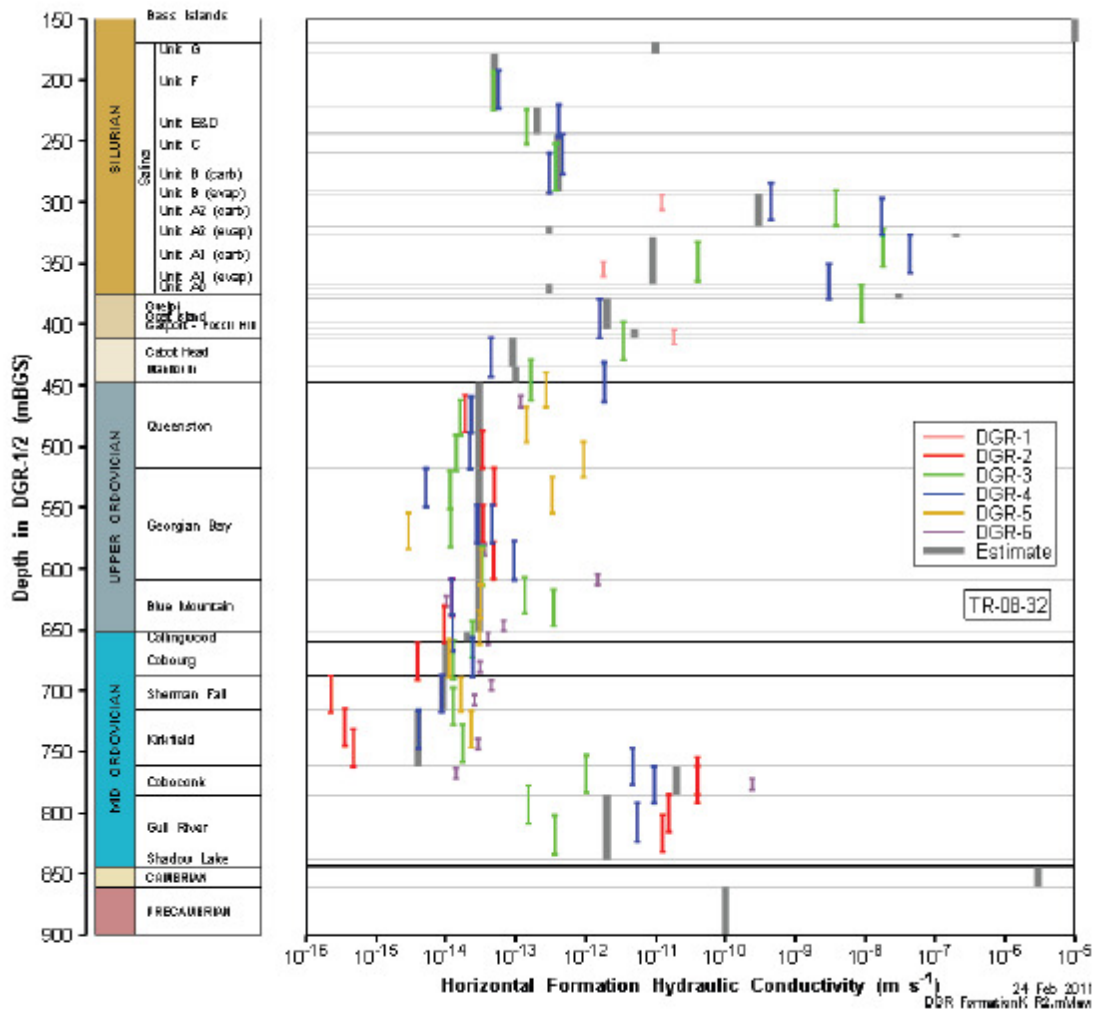


Figure 3.7. Distribution of principal stress with depth in the Appalachian and Michigan Basins. Included are both hydro-fracturing and over-coring results (Gartner Lee Limited, 2008).

The measurements of in-situ stress orientations show an ENE (N70°-75E) direction and are similar to that in the North American continent as defined in the World Stress Map. There is a lack of site specific information on in situ stresses.

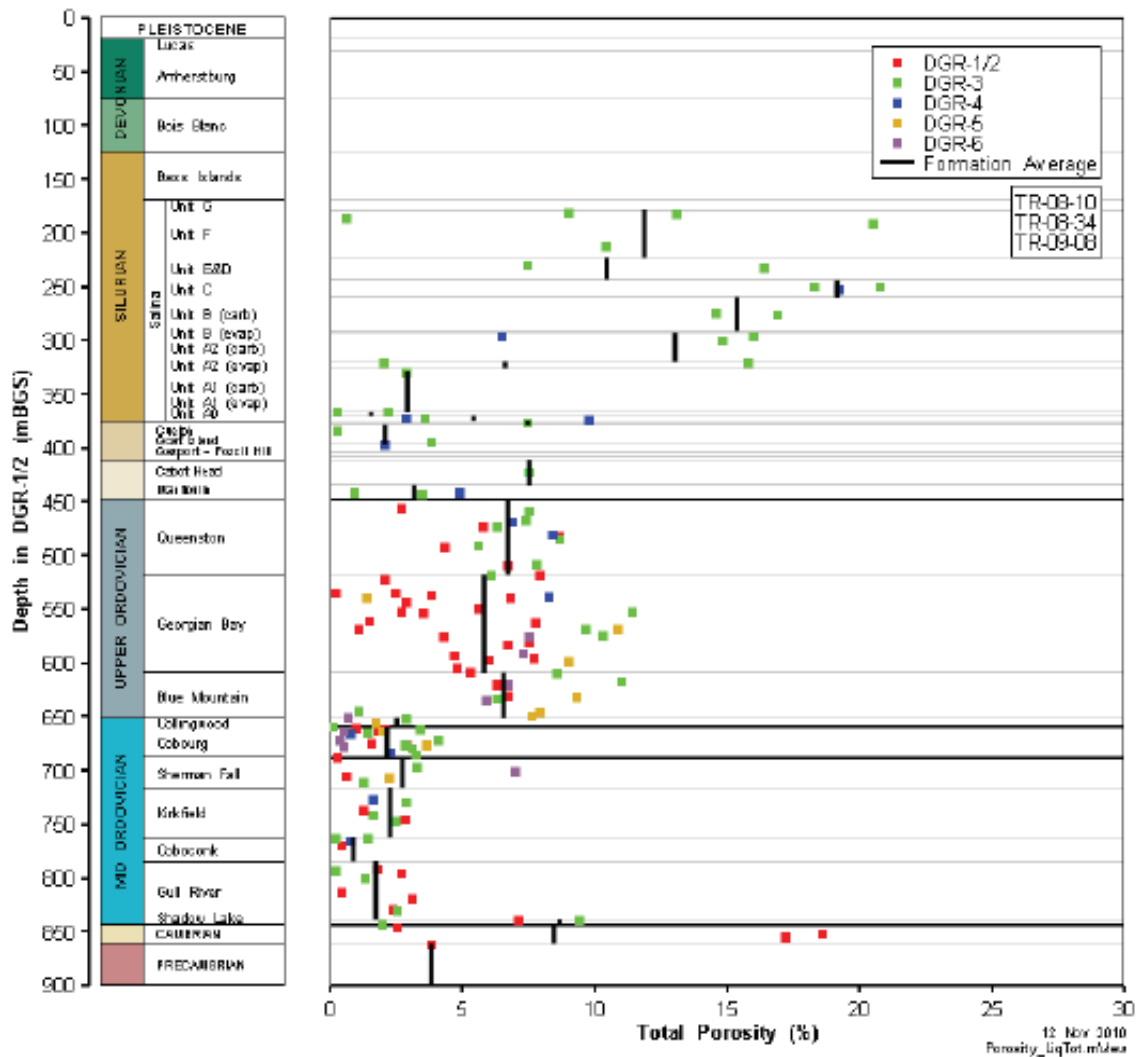
3.2.2 Hydraulic and hydrochemical properties

Hydraulic conductivity and porosity values for each formation are shown in Figure 3.6 and 3.7, respectively. Anisotropy at intra- and inter-formation scales within the nearly horizontally layered bedrock formations is expected to be an important factor that influences fluid and solute migration. Gartner Lee Limited (2008) indicated that there is a vertical anisotropy of 10:1.



Notes: Formation estimates determined from all tests are shown by the thick grey bars. From Walsh (2011; their Figure 1).

Figure 3.6. Horizontal formation hydraulic conductivity and estimate average values (NWMO 2011)



Notes: From INTERA (2011; their Figure 4.3).

Figure 3.7. Total Porosity vs depth in the study area (NWMO, 2011)

Salinity plays an important role in groundwater movement. Salinity significantly increases with depth in the Michigan Basin, from fresh shallow groundwater to deep saline brines. The increase in salinity (density) with depth influences vertical hydraulic gradients and water viscosity for the Na-Ca-Cl fluids. Groundwater total dissolved solid (TDS) values for the study area are shown in Figure 3.8.

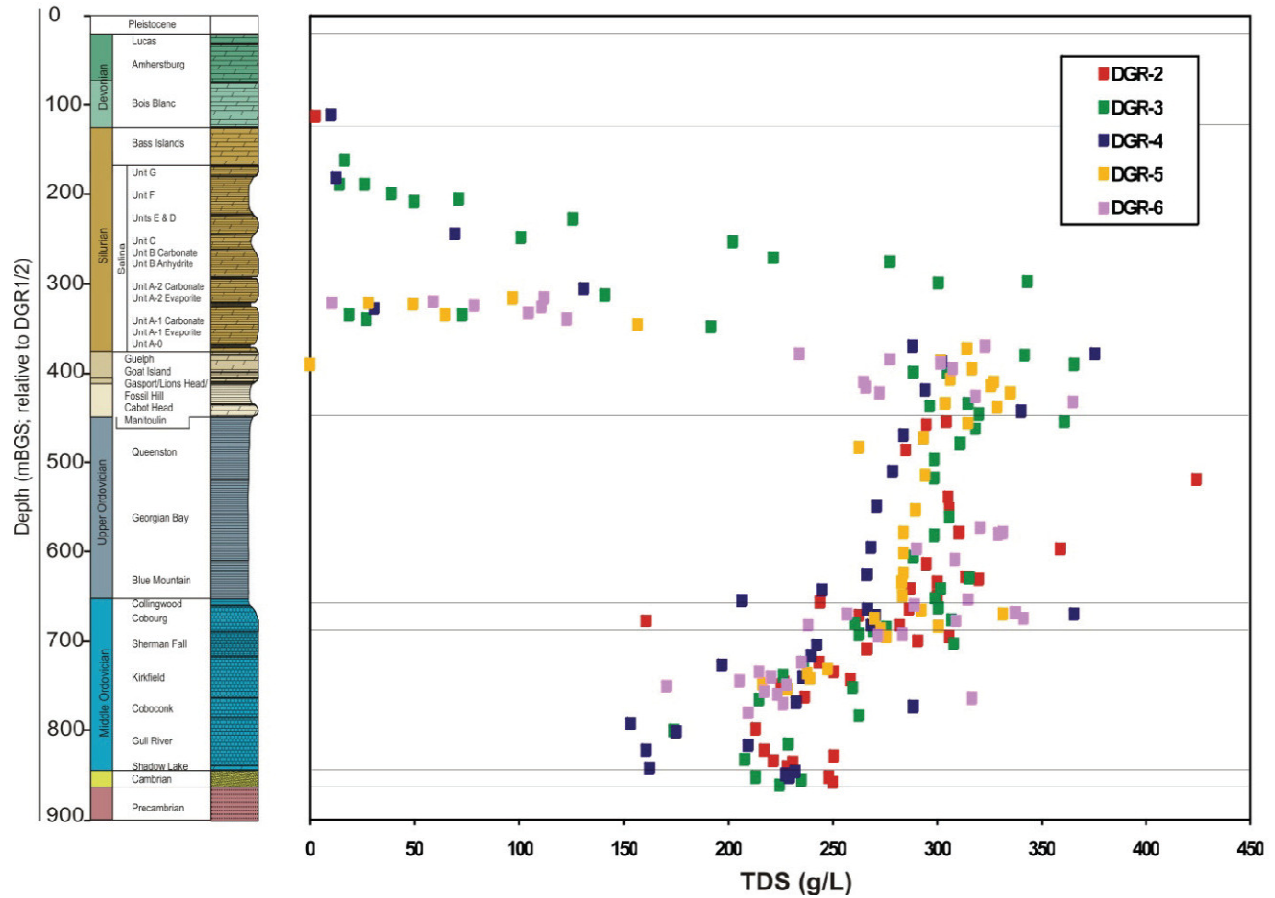
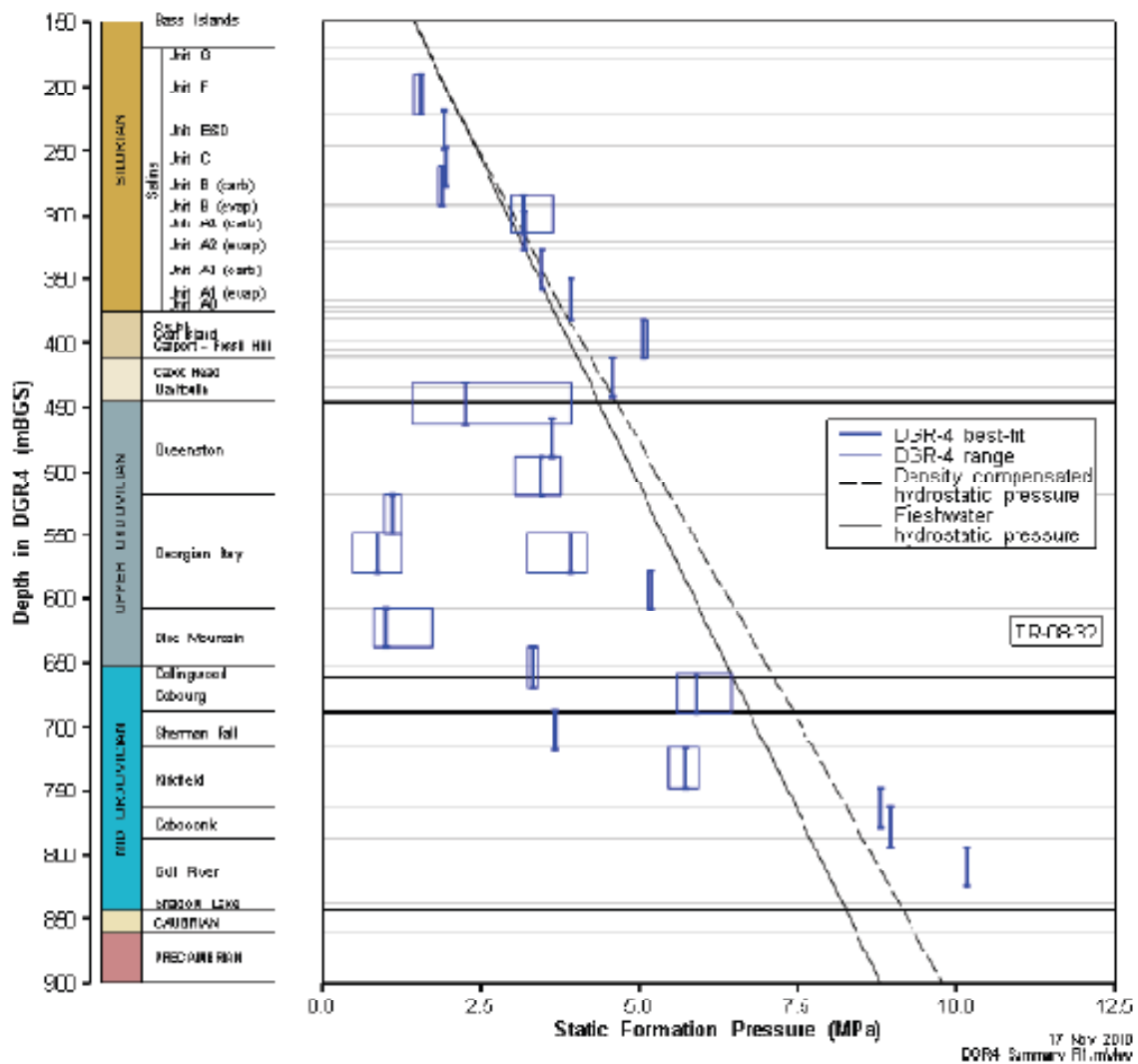


Figure 3.8. TDS vs depth in the study area (NWMO, 2011)

Figure 3.9 shows the measured formation pressures from DGR-4. The pressure profile shows an upward gradient from the permeable Cambrian to the under pressured Ordovician Georgian Bay Formation and downward gradients from the Silurian Niagaran Group to the Georgian Bay Formation (Sykes et al. 2008).



Notes: From Roberts et al. (2011; their Figure 4-77).

Figure 3.9. Formation pressures vs. depth in the study area (Straddle-packer tests in DRG-4)

Figure 3.10 illustrates the variation of the laboratory effective diffusion coefficients (D_e) for NaI with depth. From this figure, it can be observed that the majority of the effective diffusion coefficients (D_e) values are in the range $10^{-13} < D_e < 10^{-11}$ m²/s. These values are low. The lower porosity of the Middle Ordovician limestones (< 2%) leads to low D_e values (in the range $10^{-13} < D_e < 10^{-12}$ m²/s) (NWMO, 2011).

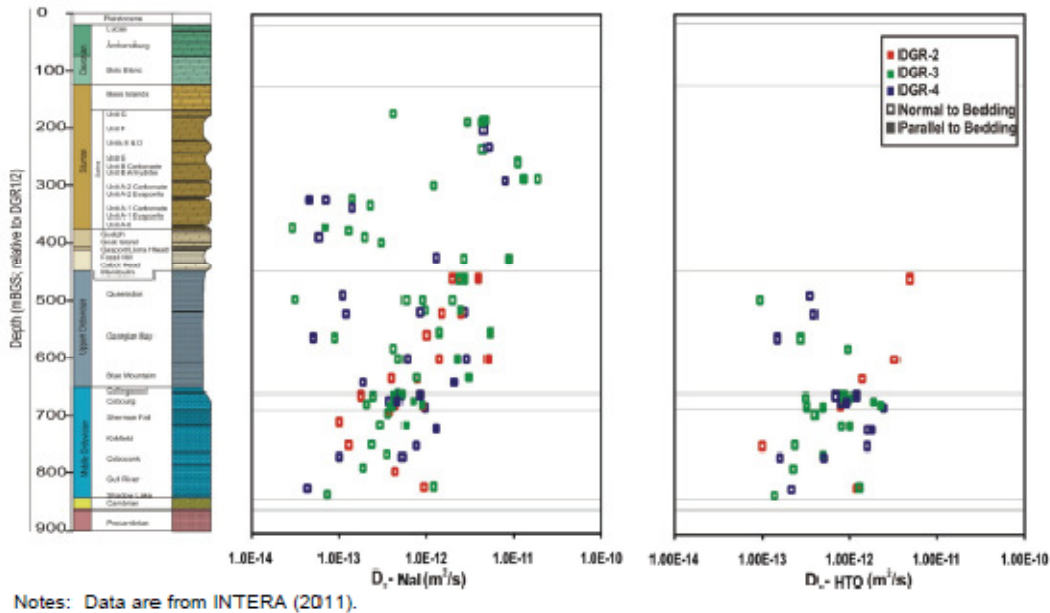


Figure 3.10. Effective diffusion coefficient for NaI vs depth in the study area

3.2.3 Thermal properties

Using the linear regression of records from deep borehole temperature measurements versus depths in the Lower Peninsula of Michigan (Vugrinovich 1989) as shown in Figure 3.11, the following equation is proposed for the geothermal gradient in the Michigan Basin: $(T(^{\circ}\text{C}) = 14.5 + 0.0192 \times \text{depth(m)})$. Thermal properties of the formations are listed in Table 3.4. The experimental results show that thermal properties of rocks are temperature dependent so that there is a decrease of thermal conductivity and diffusivity and an increase of specific heat with increasing temperature as shown in Figure 3.12 for various kinds of rocks (Mongelli et al. 1982).

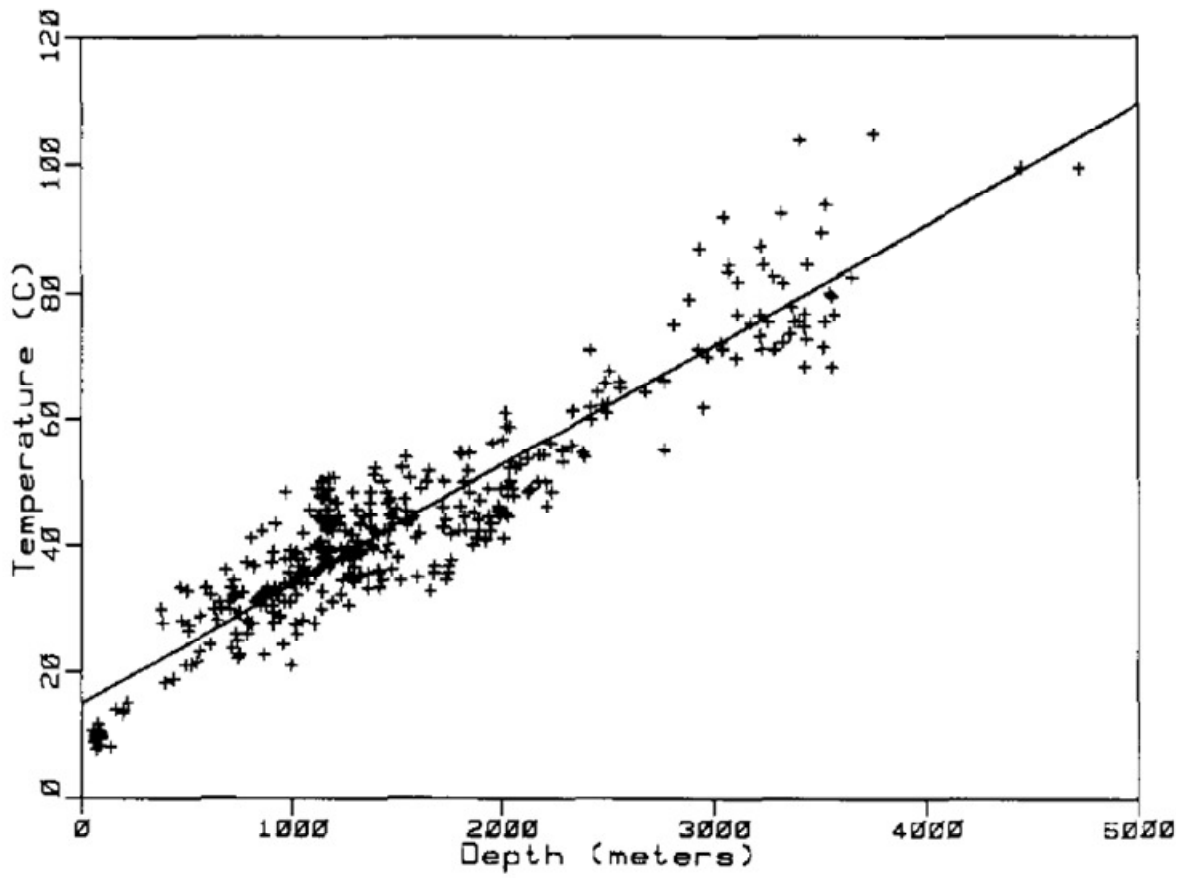


Figure 3.11. Subsurface temperatures vs. depth. Straight line is the least-squares 'best-fit' (Vugrinovich 1989).

Table 3.4. Thermal properties of sedimentary rocks in the study area (source of data: Everham 2004, Clauser and Huenger 1985, Cemak and Rybach 1982).

Geological period	Rock formation	Rock type	Thermal conductivity W/mK	Heat capacity J/kg.K
Quaternary		Drift	2.0	
Devonian	Amherstburg	Limestone / Dolostone	1.63, 2.29, 2.28, 3.63	0.67, 0.75
	Bois Blanc	Limestone / Dolostone	1.63, 2.29, 2.28, 3.63	0.67, 0.75
Silurian	Bass Islands	Limestone / Dolostone	1.63, 2.29, 2.28, 3.63	0.67, 0.75
	Salina	See details A		
	Guelph/Amabel/Fossil Hill	Limestone / Dolostone	1.63, 2.29, 2.28, 3.63	0.67, 0.75
	Gabot head	Shale	2.07	
	Manitoulin	Limestone / Dolostone	1.63, 2.29 2.28, 3.63	0.67, 0.75
Upper Ordovician	Queenston	Shale	2.07	
	Georgian Bay	Shale	2.07	
	Blue Mountain	Shale	2.07	
Mid Ordovician	Collingwood Cobourg	Limestone / Dolostone	1.63, 2.29, 2.28, 3.63	0.67, 0.75
	Sherman Fall	Limestone / Dolostone	1.63, 2.29, 2.28, 3.63	0.67, 0.75
	Kirkfield	Limestone / Dolostone	1.63, 2.29, 2.28, 3.63	0.67, 0.75
	Coboconk	Limestone / Dolostone	1.63, 2.29, 2.28, 3.63	0.67, 0.75
	Gull River	Limestone / Dolostone	1.63, 2.29, 2.28, 3.63	0.67, 0.75
	Shadow Lake	Sandstone	2.4	
	Cambrian	Cambrian	Sandstone	2.4
Vendian (Precambrian)	Precambrian	Granitic Gneiss	1.37,	0.67

*Heat capacity in kJ/kg.K

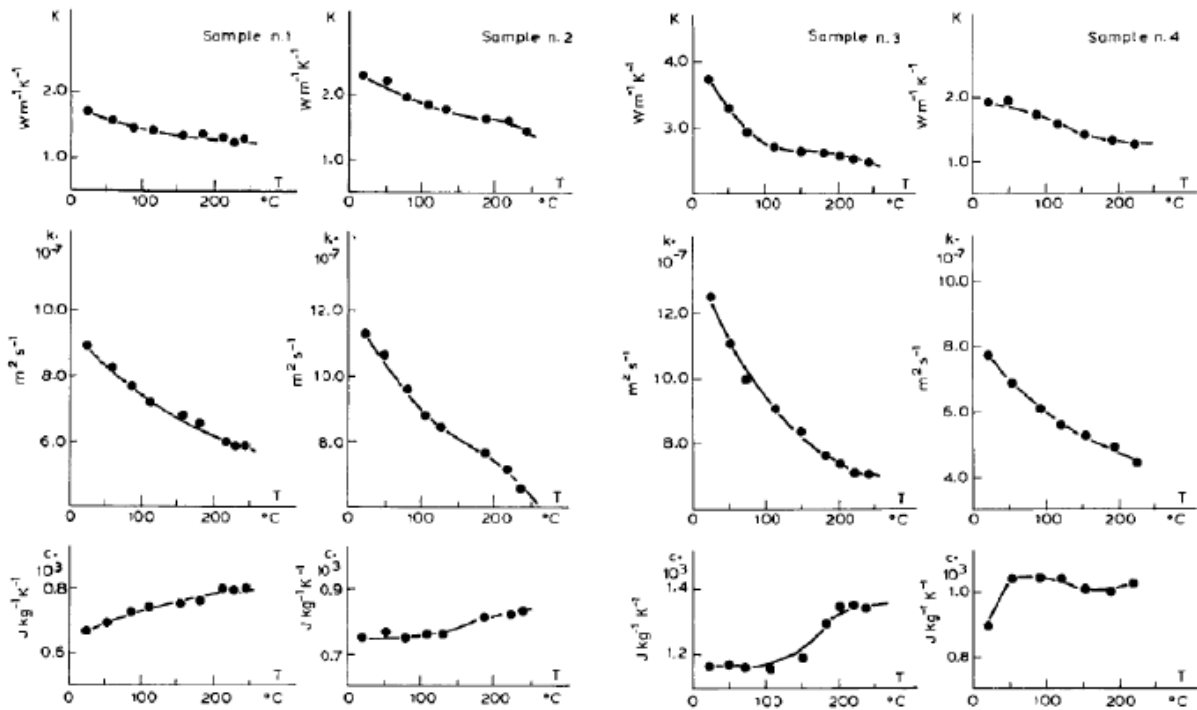


Figure 3.12. Effect of temperature on the thermal properties of rocks

3.3 Review of experimental data related to gas migration in European low permeable formations

3.3.1 Introduction

In this section, we will summarize and discuss relevant results from several large scale, small scale and laboratory tests (gas injection and permeability in samples, boreholes and chambers) that were performed in Europe during the past decades to investigate and characterize the behaviour of natural (host rock) and engineered barriers with respect to gas migration. The collected information would be examined for transferability, and usefulness for the development of a THM model of gas generation and migration from a hypothetical repository in Ontario.

In the following sections, we will summarize the information that is related to the gas transport phenomena in three main large scale tests located at Mont Terri (gas transport properties

of the OPA), in the MEGAS and PROGRESS projects (Boom Clay), at Meuse/Haute-Marne URL (COX argillite) and the Grimsel GTS (gas migration test (GMT)). Furthermore, relevant results of small scale (laboratory) tests on gas behaviour and migration in bentonite, clay and limestone will be reviewed. The information and data presented in this section are important for the development, calibration and validation of the aforementioned THMC model as well as the understanding of gas migration in the study area.

3.3.2 Gas transport properties of Opalinus clay

As part of the Swiss waste disposal program, gas transport processes were studied in a potential host rock called the OPA (Nagra 2004; Nagra 2006). The field investigations included hydraulic packer tests and gas injection tests in boreholes. These field tests were complemented by studies of an unsaturated zone around the ventilated tunnels at Mont Terri. The laboratory investigations on OPA drill cores from Benken and Mont Terri consisted of micro structural analyses, determination of the capillary pressure relationship and gas permeability measurements.

The OPA was deposited 180 Ma ago in a shallow marine environment (Marschall et al. 2005). The OPA formation is a moderately overconsolidated clay stone. On a regional scale, the mineralogical composition of the OPA exhibits moderate lateral variability and a slight increase in clay content with depth. Quantitative laboratory analyses of core samples from Benken and Mont Terri provided a total mass fraction of 54.66% clay minerals, 14.20% quartz and 13.16% calcite.

The fraction of swelling clay minerals, with 11.14% illite/smectite mixed layers, is of particular interest for gas-related studies. Other minerals are siderite, pyrite and feldspar. The mass fraction of organic carbon is < 1%. Figure 3.13 illustrates the mineralogical and structural features of the OPA. The pore space of the rock is formed by a network of micro/meso- and macropores. This network of pores actually dominates the flow and transport properties of the rock. Table 3.5 presents the main physical properties of OPA.

In low permeability media, the understanding of the pore network as a prevalent structure for gas (generally fluid) flow is necessary. Therefore, deduction of the pore size distribution and the water retention function (capillary pressure-saturation relationship) is necessary. Figure 3.14 shows the results of mercury intrusion porosimetry (MIP) data (only pores with a radius larger than 3.7 nm). Assuming that the OPA samples have a physical porosity of 0.12, the volume fraction of pores with radii larger than 25 nm is estimated to be about 10%, the fraction with radii between 3.7 and 25 nm

about 51%, and the fraction with radii below 3.7 nm about 39% from the MIP data. Figure 3.15 shows the water adsorption and desorption data and the mercury injection data interpreted as water retention functions (capillary pressure-saturation relationship).

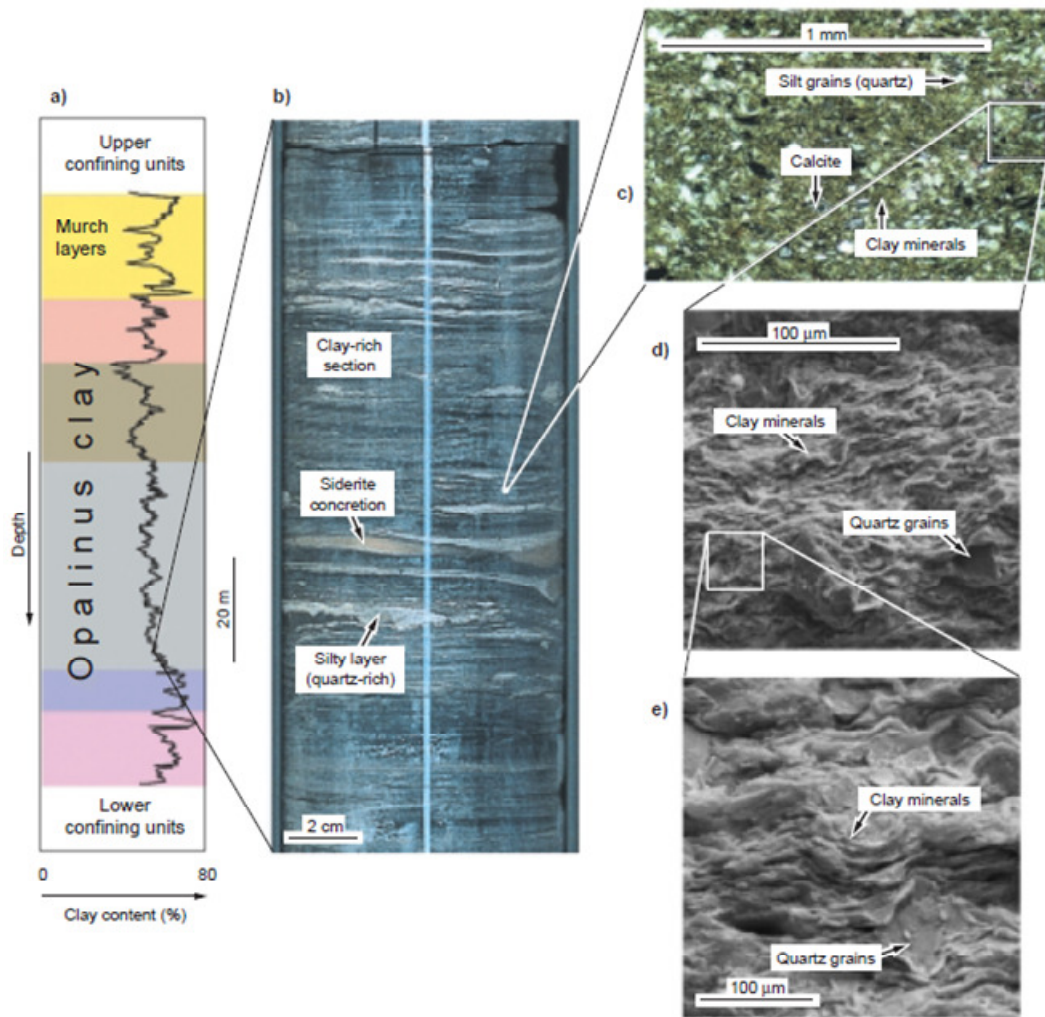


Figure 3.13. Mineralogy and structure of the OPA at different scales, based on data from the Benken borehole: a) vertical profile of clay content determined by petrophysical logging, b) core sample, (c) thin sections, and (d+e) SEM images (Nagra, 2002).

Table 3.5. Physical properties of OPA from Benken and the Mont Terri rock laboratory (Marschal et al. 2005)

	Benken		Mont Terri		Remarks
	Mean	Range	Mean	Range	
Bulk dry density (Mg m^{-3})	2.43	2.37-2.53	2.31	2.28-2.32	
Grain density (Mg m^{-3})	2.72	2.69-2.74	2.74	2.70-2.77	
Water loss porosity (-)	0.11 ^(a)		0.16 ^(a)		Drying at 105°C
Specific surface area ^(b) BET N_2 ($\text{m}^2 \text{g}^{-1}$)		19-49		24-37	External surfaces
Specific surface area ^(c) EGME or H_2O ($\text{m}^2 \text{g}^{-1}$)		56-129		112-147	Total surfaces, various methods

a: not all water will be driven off at 105°C; for Benken, the physical porosity is estimated to be about 1.1-1.2 times the water loss porosity, or somewhere in the range 0.12-0.13.

b: nitrogen cannot penetrate into the interlayer space, *i.e.* the pores between basic clay layers of expandable clays (smectites). Thus, only external surfaces are reached by nitrogen.

c: EGME (ethylene glycol monoethyl ether) is a polar liquid, which can, like water, also penetrate the interlayer space of expandable clays. Thus, EGME and H_2O are considered to reach all surface areas.

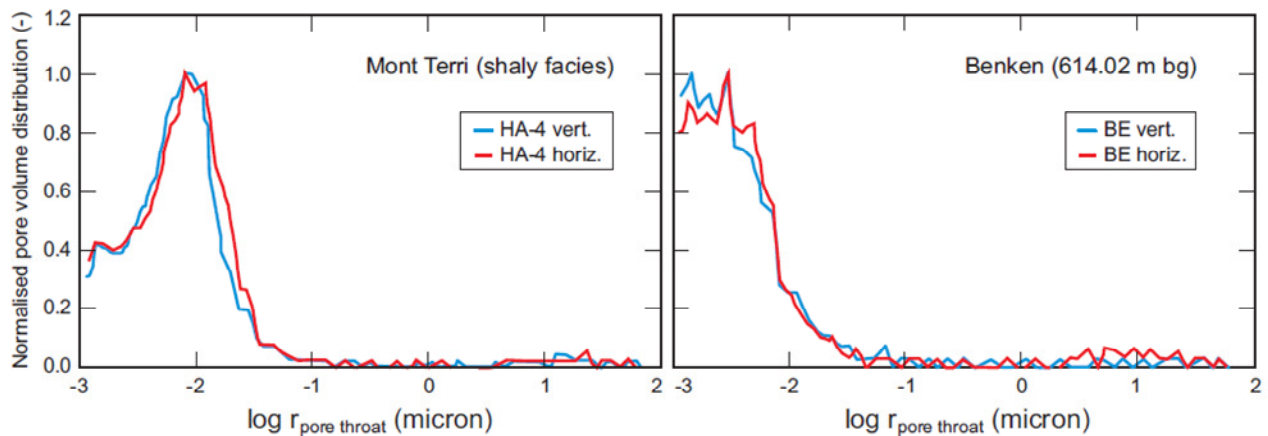


Figure 3.14. Equivalent pore size distributions in the mesopore range (Nagra, 2004)

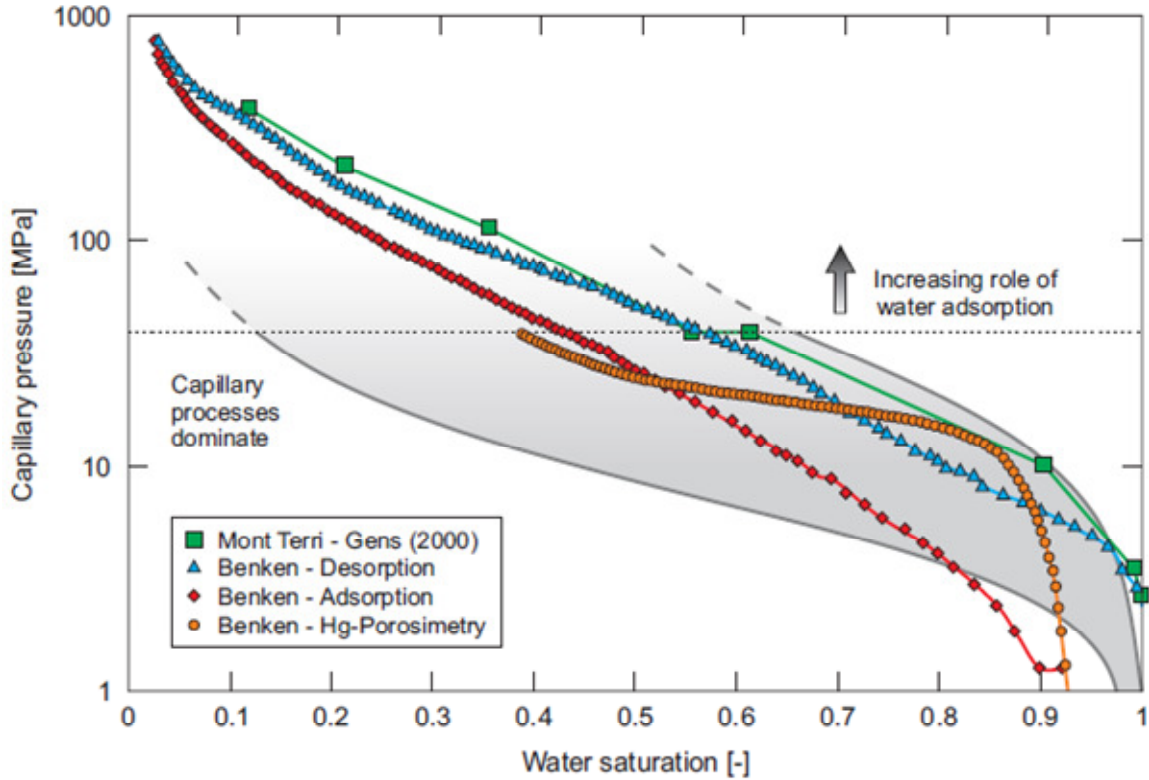


Figure 3.15. Capillary pressure - water saturation curves for OPA samples from Mont Terri and Benken (Nagra, 2004).

According to van Genuchten (1980), the functional relationship between water saturation and capillary pressure is given as:

$$p_c = \frac{1}{\alpha} \cdot (S_{ec}^{\frac{n}{1-n}} - 1)^{\frac{1}{n}} \quad (1)$$

$$S_{ec} = \frac{S_w - S_{wr}}{1 - S_{wr}}, \quad (2)$$

where p_c represents the capillary pressure, $1/\alpha$; the inverse of van Genuchten's α parameter, is known as the apparent gas entry pressure and n is the shape factor (pore size distribution index). The effective saturation (S_{ec}) can be determined when the actual pore water saturation (S_w) (volume of pore water per volume of pores) and the residual pore water saturation (S_{wr}) are given. The parameters of the van Genuchten function, such that it fits the measured adsorption and desorption data approximately, are: $n = 1.6$, $\alpha = 0.065 \text{ MPa}^{-1}$ for desorption, $n = 1.5$, $\alpha = 0.14 \text{ MPa}^{-1}$, and a maximum saturation of 0.95 for adsorption. The corresponding apparent gas entry values; $1/\alpha$, are about 7 MPa and 15 MPa, respectively (Marschall et al. 2005).

Six long-term gas permeability tests were conducted on OPA core samples from Mont Terri and Benken. Figure 3.16 shows a schematic sketch of the British Geological Survey (BGS) isostatic cell with the main components and the changes of the flow rate/pressure (upstream; downstream). The cylindrical rock specimen (diameter: 54 mm, thickness: 34 mm) is sandwiched between the end-caps and can be subjected to an isotropic confining stress up to 40 MPa. Testing has been performed in an air-conditioned laboratory at a temperature of $20 \pm 0.3^\circ\text{C}$. The test procedure is a sequence of the stages; namely, saturation and equilibration, constant rate water flow, pressure recovery, and sequence of constant gas pressure (CP) test stages. A numerical analysis of the entire hydraulic test sequence (water injection and pressure recovery) provided estimates of intrinsic permeability parallel and normal, respectively of, $3.8 \times 10^{-21} \text{ m}^2$ and $5\text{-}7 \times 10^{-22} \text{ m}^2$, suggesting an anisotropy ratio of approximately 10. Specific storage estimates ranged between 1×10^{-5} and $2 \times 10^{-5} \text{ m}^{-1}$. The gas pressure phase is a sequence of 6 pressure stages; CP1 to CP6, as shown in Figure 3.15b. Table 3.6 shows the results obtained from the laboratory tests.

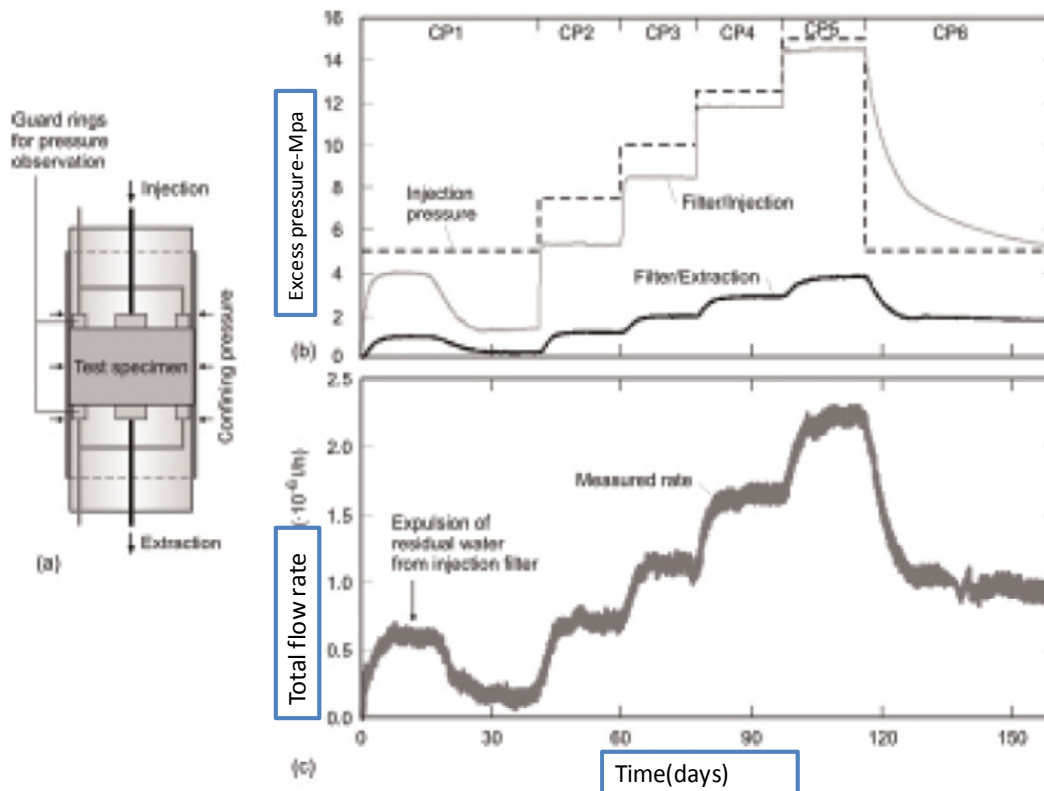


Figure 3.16. Gas permeability measurements on an OPA core sample from the Benken borehole (Marschall et al. 2005).

Table 3.6. Gas permeameter tests with core specimens from Benken and Mont Terri (Marschall et al. 2005)

Core sample	Injection period (d)	Direction of flow relative to bedding	Intrinsic permeability ^(a) k (m ²)	Gas entry pressure p_{ge} (MPa)
OPA-1	140	90°	$k_p = 3-6 \times 10^{-21}$ $k_n = 5-7 \times 10^{-2}$	~ 4
OPA-2	120	0°	3×10^{-21}	7.5-10
BED-B3 06 ^(b)	60	0°	2×10^{-18}	<0.03
BFP 16	110	50°	1.5×10^{-20}	0.5
BWS-E4 06	180	90°	2×10^{-20}	0.2
BED-C5/7	174	35°	2×10^{-20}	0.2

a: intrinsic permeability: k_p parallel to bedding, k_n normal to bedding.
 b: core sample is not representative of undisturbed Opalinus Clay (visible fracture in flow direction).

Also, Packer tests in boreholes were implemented in the OPA for the characterisation of gas transport properties. The general test procedure consists of a combination of hydrotests, gas injection and pressure recovery sequences (Figure 3.17). At the end of the hydraulic test sequence, the fluid in the test interval is replaced by gas (Figure 3.18) when the interval pressure has recovered (close to the static formation pressure). Usually, in situ gas tests are conducted with nitrogen (Senger et al. 2006). Gas threshold pressure is typically identified from the pressure build-up curve, indicating a deviation from linear increase when gas starts to migrate into the formation (Finsterle et al. 1999).

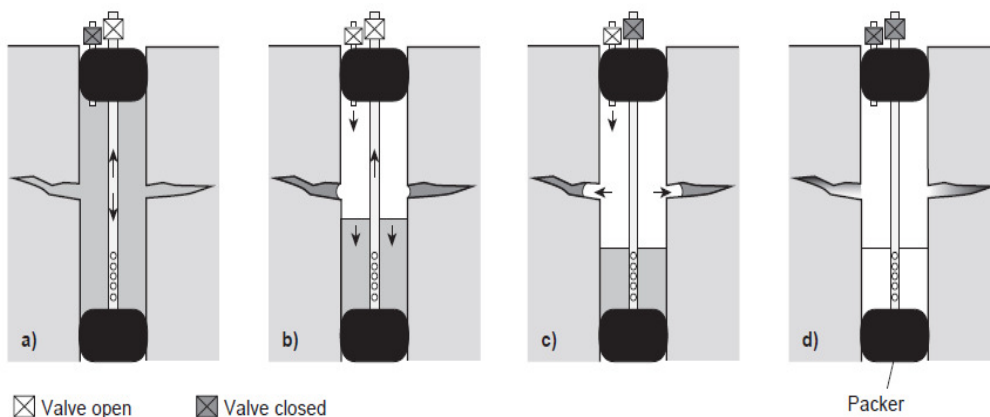


Figure 3.17. Gas threshold pressure testing in boreholes - test configuration and procedure: a) hydrotest sequence, b) water/gas displacement (DISP), c) gas injection phase (GRI), and d) gas pressure recovery phase (GRIS) (Marschall et al. 2005).

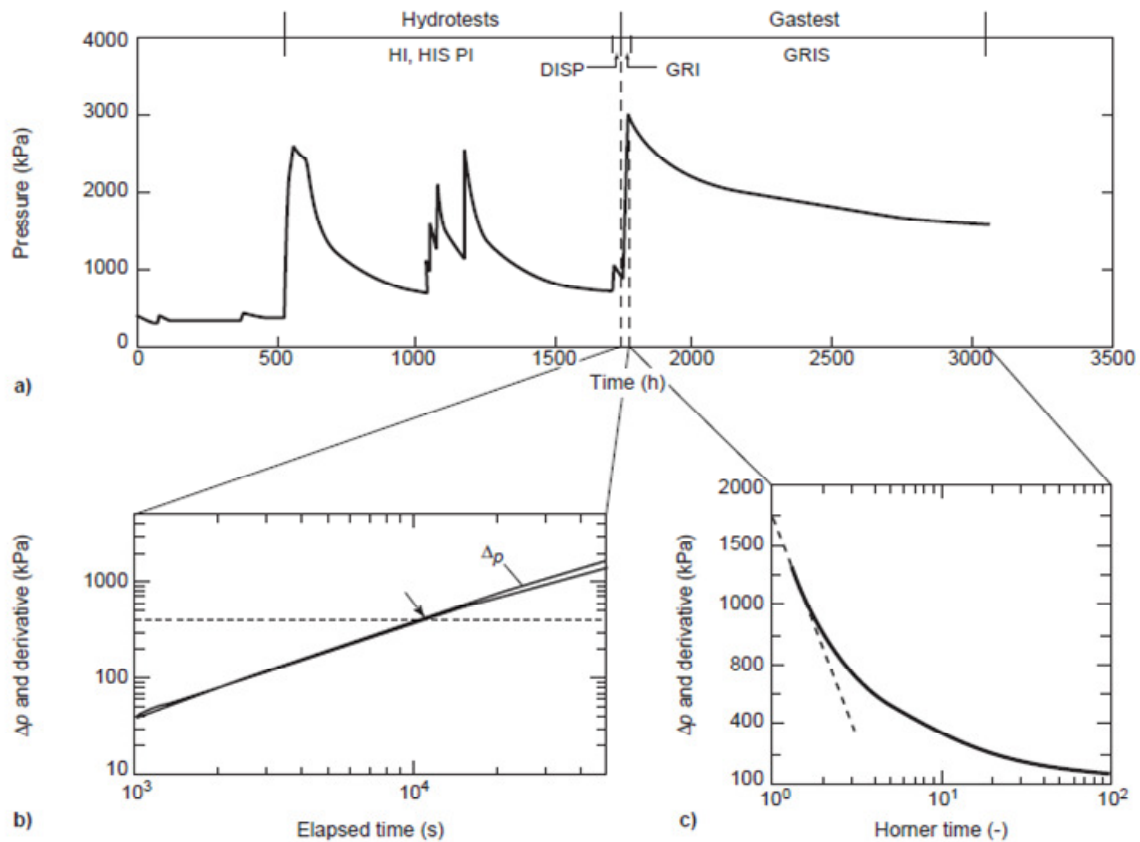


Figure 3.18. The results of gas threshold pressure test at Mont Terri: a) entire test phase comprising of a hydrotest and gas test sequence, b) log-log derivative plot, and c) Horner plot of the GRIS phase (Marschall et al. 2005)

Assuming an initial pressure (p_i), a linear increase of interval pressure (p) is seen during the wellbore storage. When the gas entry pressure is reached, p begins to deviate from the linear trend, because gas is released into the rock formation. On the log-log derivative plot, the graphs of pressure change $\Delta p = (p - p_i)$ and pressure derivative $\partial (\Delta p) / \partial (\log t)$ begin to deviate at this point. The Horner plot for gas pressure recovery phase (Figure 3.18c) extrapolates the stabilized interval pressure (p_s) at later periods in the recovery phase.

Given the maximum gas pressure (p_{max}) at the end of the gas injection phase (3 MPa) and the Horner intercept pressure (p_{ic}) in accordance to Figure 3.18c (1.8 MPa), the stabilized interval pressure of the recovery phase is nearly 1.2 MPa. Assuming a static formation pressure of 0.35 MPa (determined with the hydrotest analysis), the inferred gas entry pressure is 0.85 MPa. The overall results of the gas injection experiments can be found in Table 3.7.

Table 3.7. Gas injection experiments in the Benken borehole and at the Mont Terri rock laboratory (Marschall 2005)

Test	Injection period (h)	Specific gas flow rate ($\text{m}^3 \text{m}^{-2} \text{s}^{-1}$ STP)	Intrinsic permeability k (m^2)	Gas entry pressure p_{ae} (MPa)
Benken O5 (GTP)	~ 38	1×10^{-5}	1×10^{-11}	> 5
Mont Terri GS-2 (MSI)	~ 700	variable	$2 - 5 \times 10^{-20}$	~ 0.5
Mont Terri GP-4 (GTP)	~ 18	7×10^{-9}	$2 - 6 \times 10^{-20}$	0.4-0.8
Mont Terri GP-6 (GTP/MSI)	~ 150	2×10^{-8}	2×10^{-20}	~ 1.0

3.3.3 Boom Clay

The Boom Clay layer (see Figure 3.19) has been investigated as a potential host formation for the disposal of high-level (HLW) and medium-level radioactive waste (MLW) in Belgium. Experimental work on gas generation/migration that is associated with a theoretical waste repository in the Boom Clay has been performed with an integrated approach in several Belgian and European projects, especially MEGAS (Volckaert et al. 1995; Ortiz et al. 1997) and PROGRESS (Rodwell, 2000). Table 3.8 illustrates the properties of Boom clay based on the different literatures.

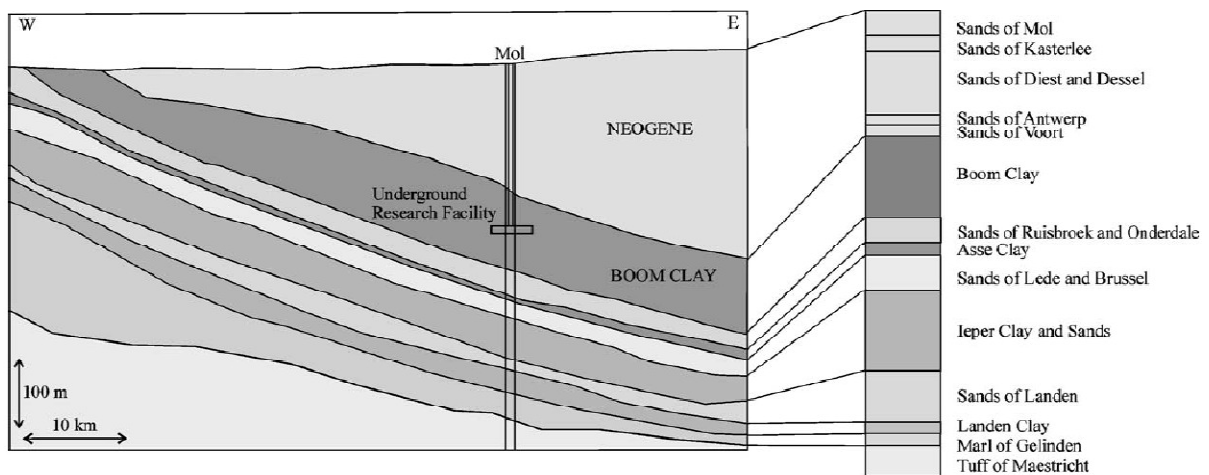


Figure 3.19. Boom Clay and the sequence of the formations (Ortiz et al. 1997)

Table 3.8. Boom Clay properties (Boom Clay properties, Su 2007, François et al. 2009)

Initial total stress	4.5 MPa
Initial pore pressure	2.25 MPa
Young's modulus E'	300 MPa
Poisson's coefficient ν'	0.125
Cohesion c'	300 kPa
Friction angle ϕ	18°
Dilatation angle ψ	0°-10°
Uniaxial Compression Strength	2 MPa
Porosity n	0.39
Water bulk modulus K_w	0.2 - 2 GPa
Hydraulic conductivity k	$2 \cdot 10^{-12}$ m/s – $4 \cdot 10^{-12}$ m/s
Plastic limit	23-29%
Liquid limit	55-80%
Plasticity index	32-51%
Water content (dry weight %)	22 to 27%

Different laboratory methods and tests that included the use of permeameters, oedometers, isostatics, and triaxial cells, were used to identify the basic control mechanisms of a two-phase flow through the Boom Clay (Horseman and Harrington, 1994; Volckaert et al., 1995; Ortiz et al., 1997). Some fundamental parameters were measured; namely, gas entry pressure, breakthrough pressure, gas and water flow-rates, and the saturation evolution.

The hydraulic conductivity of the Boom Clay around the gas injection source was first measured. Then, helium was injected between filters 13 and 14 (see Figure 3.20), and separated by 0.25 m on a multi-screen piezometer installed from the HADES underground laboratory in the clay formation. Also, three other piezometers were installed horizontally from the gallery and formed a three dimensional configuration network for pore pressure measurement.

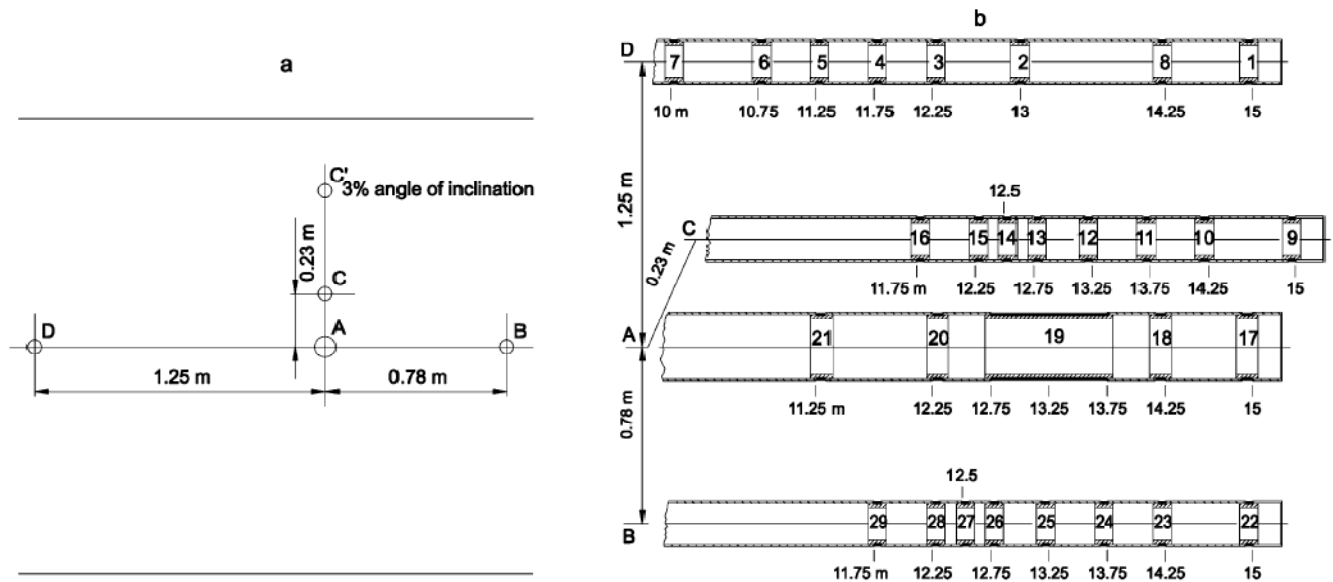


Figure 3.19. View of the three dimensional configuration of the multi-screen piezometers used for gas migration field experiments. (a) Position of the multi-screen piezometers in the plane of the main gallery axis. (b) Detailed view of the multi-screen piezometer layout with screen numbering and their respective distance indicated from the outer diameter of the main gallery (Ortiz et al. 2002).

An artificial gas pathway was opened between these two screens by maintaining a steady-state gas flow-rate of $2.1 \times 10^{-2} \text{ mls}^{-1}$, and standard temperature and pressure (STP) for 1 year by imposing a constant pressure gradient. Forty days after the end of the gas injection, a tritiated water (HTO) loop was connected to filter 13. By monitoring the HTO migration, it was possible to detect possible closings of the gas pathway. Figure 3.9 shows the experimental data during the first 350 days.

A comparison with a conventional transport model which was performed by using typical transport parameters showed that in less than 10 weeks after the end of the gas injection experiment, the former gas channel between filters 13 and 14 no longer constitutes a preferential pathway for the radionuclide transport (Ortiz et al. 2002). The results indicated that the preferential pathway phenomena, which are especially the case for relatively soft geo-materials, have a significant function in gas transport.

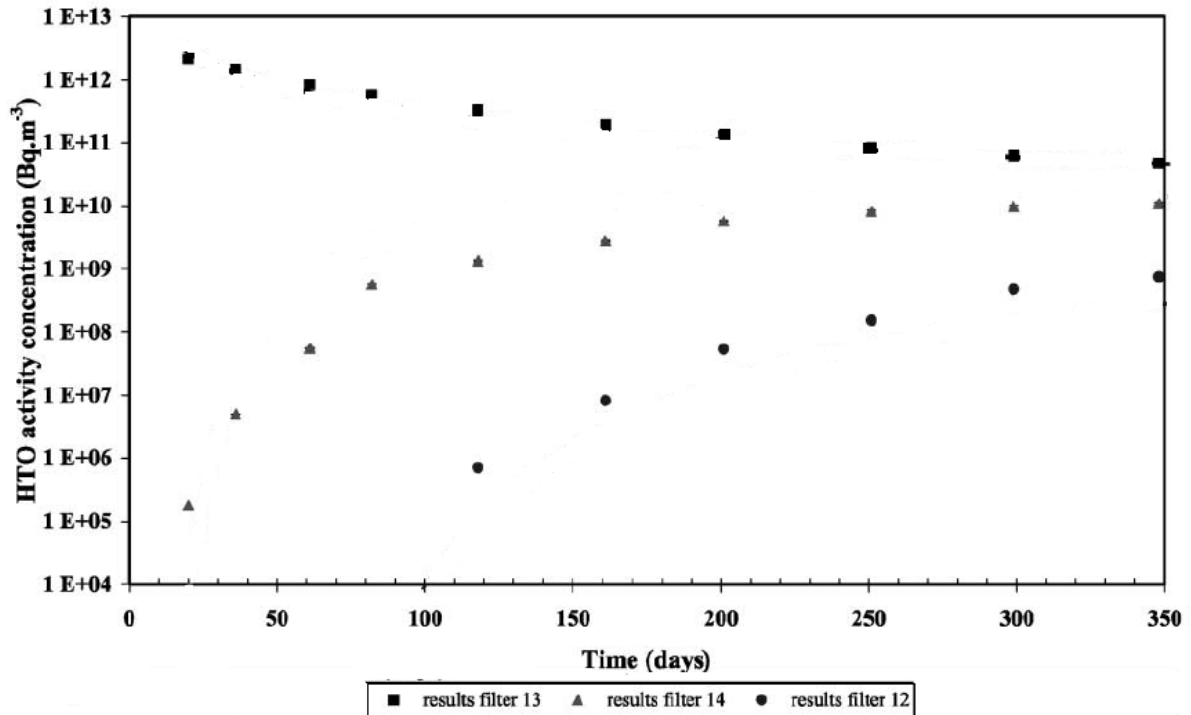


Figure 3.20. Experimentally measured HTO activities in pore- water (Ortiz et al. 2002).

3.3.4 Gas migration test (GMT) at the Grimsel Test Site (Switzerland)

GMTs at the GTS in central Switzerland were designed to investigate gas migration through an engineered barrier system (EBS). The EBS consisted of a concrete silo embedded in a sand/bentonite buffer that was emplaced in a cavern which intersected a shear zone in the surrounding granite host rock. The experiment was performed in a series of stages, which included: (1) excavation of the access drift and silo cavern; (2) construction and instrumentation; (3) saturation of the EBS; (4) water tests; (5) long-term gas injection at different rates; (6) post-gas water testing; (7) gas injection with a “cocktail” of gas tracers; and (8) depressurization and dismantling (Senger et al. 2006(b)). The detailed geometry of the EBS, which consists of the concrete silo, gas vent, sand/bentonite layers, and surrounding host rock, is shown in Figure 3.21.

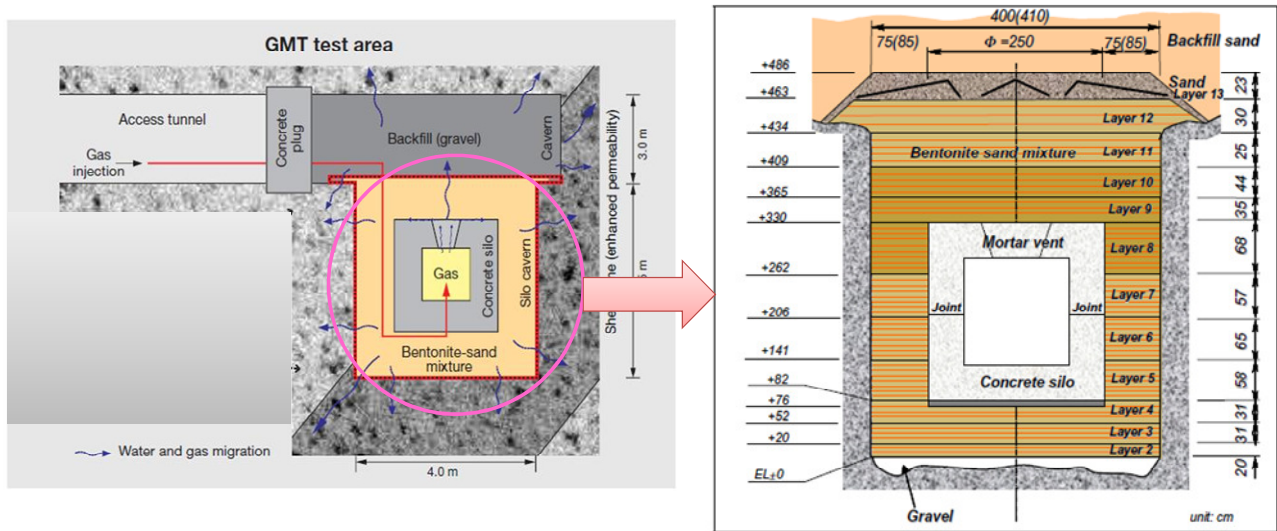


Figure 3.21. Detailed geometry of the EBS, showing layering of the sand/bentonite at GMT (Senger et al. 2006(b)).

The sand/bentonite buffer material which consisted of 20% bentonite and 80% sand (by weight) was emplaced as a series of lifts, typically 6-9 cm thick after compaction at an in-situ density of about 1.8 g/cm^2 and a water content of 11% (water saturation of about 70%). Instrumentation was arranged by layers (made up of between 3 and 9 lifts). The sand/bentonite in layers 8 to 10 was mixed with a lead-nitrate solution to visualize the gas flow-path. Initial estimates of hydraulic and two-phase properties were obtained from laboratory studies of sand/bentonite material; see Table 3.9 (Romero et al., 2003; Romero and Castellanos, 2006).

Table 3.9. Summary of initial hydraulic properties from laboratory studies of sand/bentonite material (Senger et al. 2006a)

Unit	Hydraulic Properties		
	Permeability k (m^2)	Porosity ϕ	Pore Compressibility C_p (Pa^{-1})
Granite (fracture)	5.E-17	0.01	3.4E-8
Granite (DRZ)	1.65E-16	0.01	3.4E-8
Granite (interface)	2.5E-14	0.01	0.
Gravel (bot. Drain)	1.E-12	0.3	3.3E-8
Concrete	1.E-18	0.2	1.35E-10
Tunnel fill/sand	1.E-12	0.32	7.71E-9
Silo backfill	1.E-12	0.32	7.5E-10
Gas vent	1.E-13	0.3	3.3.E-10
Tunnel seal	2.32E-15	0.1	2.7E-10
Shear zone path	7.5E-14	0.01	0.
SAND/BENTONITE			
Layers 2 – 6, 11-1	2.22E-19	0.3	3.3.E-8
Layer 7	$K_x=5.E-18$ $K_z=1.E-18$	0.3	3.3.E-8
Sand/Bent. Interface	$K_x=1.E-18$ $K_z=5.E-18$	0.3	3.3E-8
Layers 8 – 10	$K_x=2.46E-16$ $K_z=2.46E-17$	0.3	2.5E-8
Top Layer 8	$K=5.0E-16$	0.3	2.5E-8

The entire GMT test involved a series of experimental stages over a six year period which started in 1998, including: (1) excavation of the access drift and silo cavern; (2) construction and instrumentation; (3) saturation of the EBS by natural water inflow and water injection (ca. 12 months); (4) water testing (WT1) that included constant-rate injection (RI) and withdrawal (RW) and sinusoidal withdrawal (RWSin) from the silo, sinusoidal injection tests (CVRISin) in the upper cavern, and a withdrawal test (WL1) from layer 1 (4 months); (5) gas injection at different rates (RGI1.3b) into the concrete silo (8 months); (6) post-gas water testing (WT2, 3 months); (7) second gas injection phase (RGI4a-b) (3 months); (8) depressurization and dewatering, and (9) EBS excavation and characterization (Senger et al. 2006b). The pressure responses in selected sensors and the injection rates during the GMT that started with the saturation in stage 3 are shown in Figure 3.22.

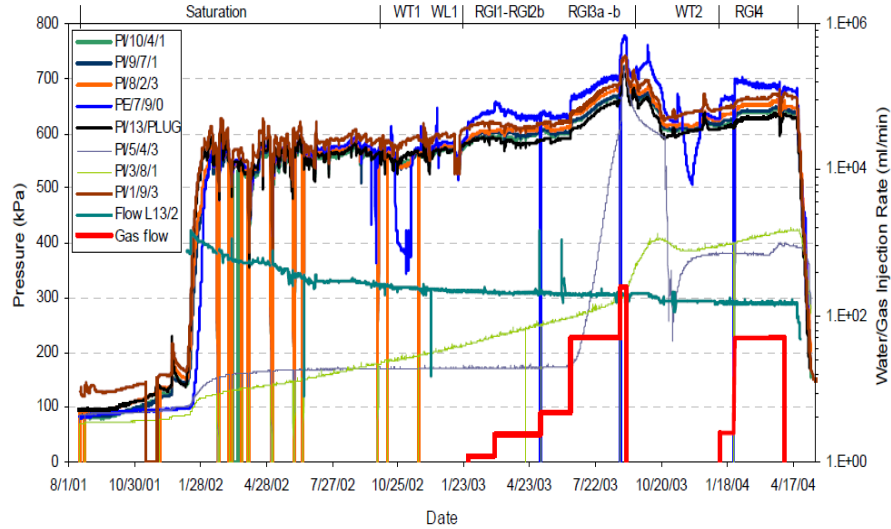


Figure 3.22. Measured pressures and injection rates during the GMT (PI/z/x/y indicates the transducer location in layer 'z' and 'y' corresponds to the max. radial distances: '0'=0.m, '1' <0.75m, '2' <1.25m, '3' <1.5m).

The saturation stage started with water injection in layer 1 at a relatively low rate, followed by water injection into the upper cavern (layer 13) in mid 2001. Fluctuations in the cavern injection rate (FlowL13/2) caused significant pressure responses in the upper cavern (PI/13/Plug) and S/B/Pb layers 8-10, whereas the lower permeability S/B layers 3-5 indicated only a gradual and significantly delayed response to the pressurization of the upper cavern (Senger et al. 2006b). The overall trend of the water injection indicated a decreasing rate whereas the cavern pressure increased prior to the gas injection phase (RGI1.RGI3; see Figure 3.22).

Following this first gas injection phase, the water injection rate was reduced to lower the upper cavern pressure to the level prior to gas injection. The first gas injection phase (RGI1 – RGI3b) was followed by increases in N₂-gas injection from 1.2 ml(STP)/min to 248 ml(STP)/min. The individual gas injections produced distinct increases in the silo pressure (PI/7/9/0) and lesser, but noticeable responses in S/B/Pb layers 8- 10. At the start of RGI3b, the pressure in the lower permeability S/B layer (PI/5/4/3) showed a steep increase, whereas the pressures in layer 3 indicated a more delayed response (PI/3/8/1) (Senger et al. 2006a).

The first gas injection phase was followed by a recovery period that included a constant-rate water injection at the top of the upper cavern (UCV-RI1), a reduction in water injection into the upper cavern, and removal of gas from the silo, vent (Figure 3.22). For the second gas injection phase (Stage 7) following WT2, gas was injected at two different rates: (a) 2.5ml(STP)/min (RGI4a), and (b) 50 ml(STP)/min (RGI4b-c). During the analysis of the large GMT performed in Grimsel, it was

proven that there are no reliable procedures to track the path of gas through a saturated buffer (Arnedo et al. 2008).

3.3.5 Gas threshold pressure test at Andra underground research laboratory, Bure (France)

A gas threshold pressure test (GTPT) in a deep borehole at Andra (Agence nationale pour la gestion des déchets radioactifs) near Bure, France, was conducted to better understand gas transport processes in low permeability clay formation under conditions of constant rate gas injection. In 2004, Andra conducted a GTPT in the borehole EST363. The primary objective of the GTPT was to gain an understanding of gas transport processes taking place in the undisturbed COX formation, under conditions of constant rate gas injection. The procedure of the overall testing is similar to the gas injection testing at the OPA. Table 3.10 provides data of the sample characteristics.

Table 3.10. Characteristics of the COX samples (Zhang and Rothfuchs 2008).

Characteristic	Rheological zone			Overall
	A' - upper	B' - median	C' - lower	
Depth (m)	420-455	455-515	515-550	420-550
Density (g/cm ³)	2.42 +/- 0.05	2.42 +/- 0.05	2.46 +/- 0.05	2.40 – 2.45
Water content (% mass)	6.1 +/- 1.5	7.1 +/- 1.	5.9 +/- 0.7	5.3 – 8.0
Porosity (%)				11.5 – 17.0
Young's Modulus (GPa)	7.0 +/- 2.9	5.4 +/- 1.4	5.8 +/- 1.5	6.0+/-1.9
Uniaxial Compressive Strength (MPa)	30 +/- 10.5	21 +/- 4.8	20 +/- 3.4	24+/-6.3
Uniaxial Tensile Strength (MPa)				2.6 +/- 1.2
Hydraulic conductivity (m/s)				<10 ⁻¹² (10 ⁻¹⁵ -10 ⁻¹⁴)

The EST363 packer-isolated wellbore interval was at a depth of 490.00 to 495.15 m with a wellbore radius of 0.76 m. The initial design of the GTPT consisted of a constant-rate gas injection phase (GRI1) followed by a recovery phase (GRIS1). Due to the apparent fracture or flow-path dilation event during GRI1, a second gas injection phase (GRI2) was followed by a second recovery phase (GRIS2) (Senger et al. 2006a). The entire gas injection sequence was followed by pulse withdrawal tests (PW1 and PW2), which is shown in Figure 3.23.

Induced fracturing and borehole closure appear to influence the injection phase data. GRI1 indicates a near linear pressure increase to a maximum pressure of 11.9 MPa, followed by a sudden pressure decline (Figure 3.23). For the GTPT, a relatively slow pressure build-up is required to better identify the onset of gas migration into the formation, based on a deviation from linear pressure increase, representing wellbore storage of gas filled test interval (Senger et al. 2006a).

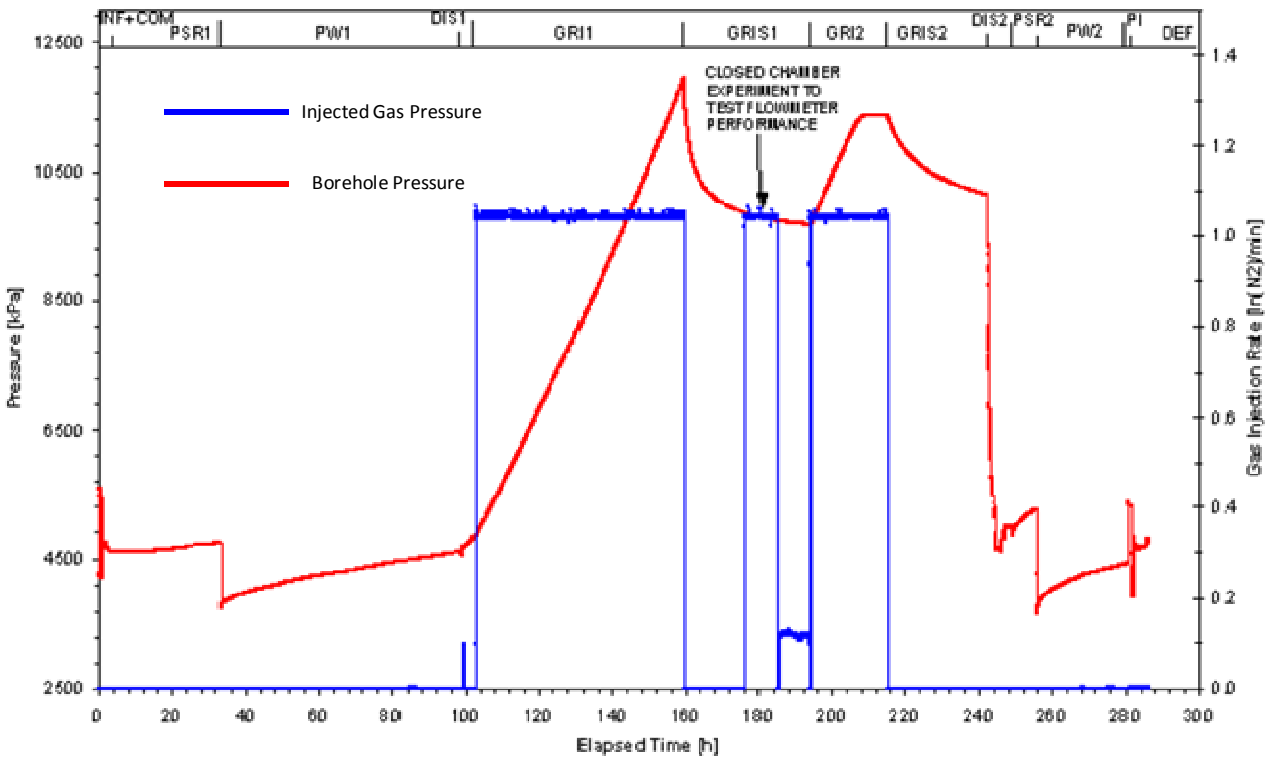


Figure 3.23. Pressure responses of the entire test sequence in the test zone-COX- and associated gas injection rates (Senger et al. 2006 b).

The diagnostic plot of the GRI1 sequence (Figure 3.24) in terms of the derivative of the pressure build-up (dP') indicates a noticeable deflection after about 23 hours at a dP of about 2.6 MPa. This pressure corresponds approximately to the air-entry pressure of the inner zone (disturbed). Gas threshold pressure of the outer zone can be obtained from the recovery periods following the GRI1 and GRI2 injection sequences (Figure 3.23). The Horner extrapolation of the recovery phases indicates a P_{gt} (gas threshold pressure = air entry pressure formation pressure) of about 9.5 MPa (Figure 3.14), which corresponds to a P_{e2} (air entry pressure) of 4.5 MPa for the outer zone, based on a static formation pressure of about 5.0 MPa. The estimated P_{e2} of 4.5 MPa is representative of the undisturbed formation, despite the fracture event that occurred at the end of GRI1 and fracture reopening during GRI2 (Senger et al. 2006a).

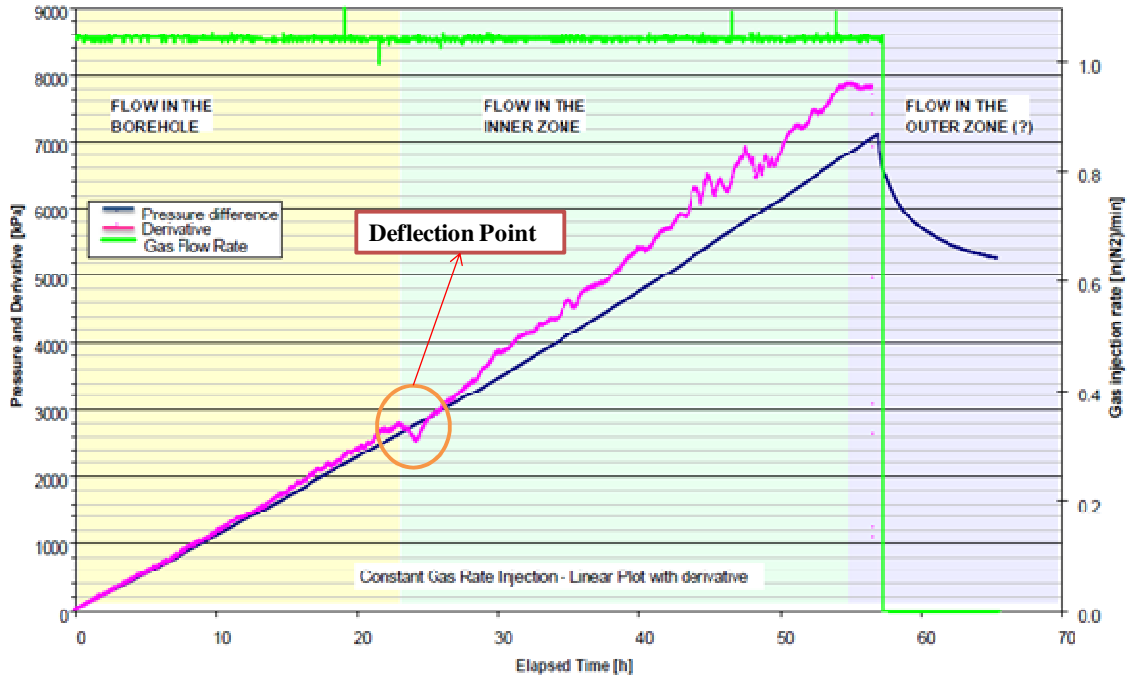


Figure 3.24. Diagnostic plot of GRI1 pressure response (Senger et al. 2006a).

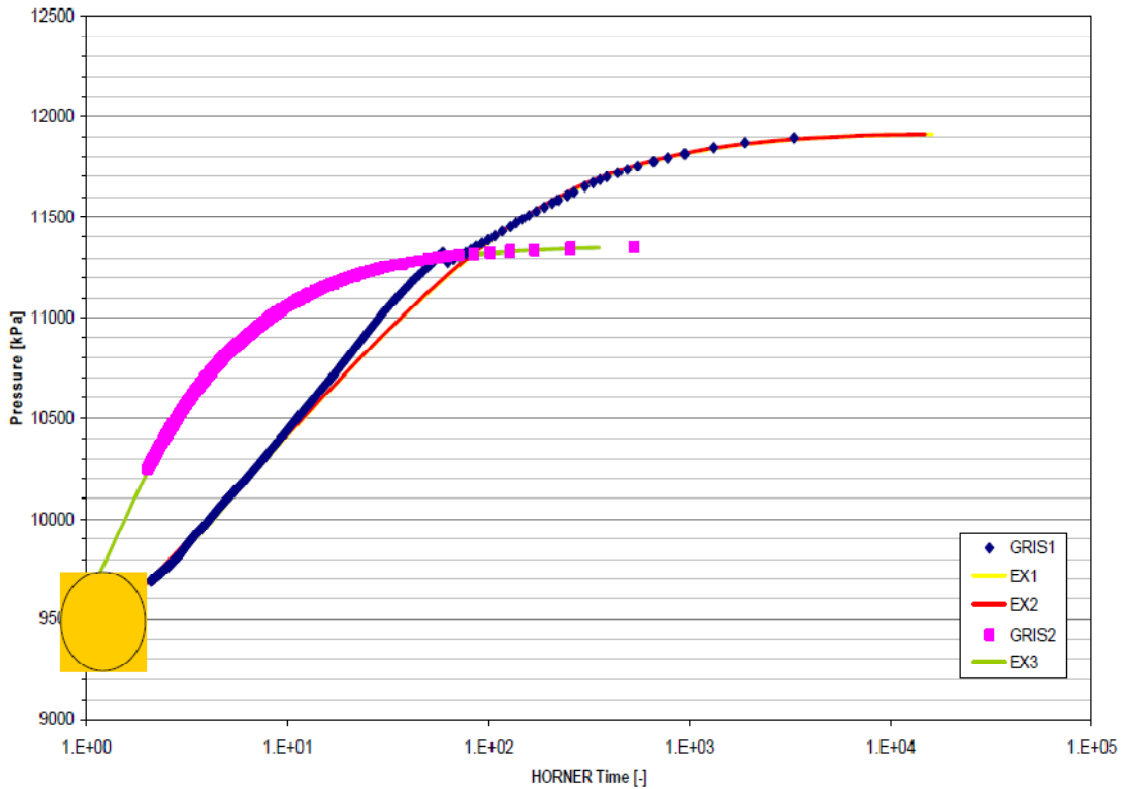


Figure 3.25. Horner extrapolation of GRIS1 and GRIS2 pressure recoveries (Senger et al. 2006 b).

3.3.6 Relevant gas migration behaviour in low permeability samples (small-scale tests)

In this section, some relevant laboratory tests on gas migration that were performed on bentonite, clay and limestone will be reviewed and discussed.

First, the Klinkenberg effect and its relevance on gas transport in low permeable porous media will be addressed. The Klinkenberg's effect can have a significant impact on gas flow behaviour, especially in low permeable media (Chastanet et al., 2004). Klinkenberg (1941) discovered that the permeability of a medium to gas is higher than that to water, and he attributed this phenomenon to a ‘‘slip flow’’ between gas molecules and solid walls.

In Darcy flow, molecular collisions dominate, and collisions between gas molecules and the pore wall, which are described as adherence at the fluid–solid boundary, are neglected. As the pore radius approaches the size of the mean free path of the gas molecules, the frequency of collisions between gas molecules and the solid walls increases. Therefore, this additional flux due to the gas flow at the wall surface, which is called the ‘‘slip flow’’, begins to effectively enhance the flow rate. This phenomenon is called the Klinkenberg effect and could be mathematically represented by the following equations (Tanikawa and Shimamoto 2009):

$$k_g = k_l \left(1 + \frac{4cl}{r}\right) = k_l \left(1 + \frac{c\kappa}{\pi\sqrt{2}r^3} \frac{T}{P}\right) = k_l \left(1 + \frac{b}{P}\right)$$

$$b = \frac{c\kappa T}{\pi\sqrt{2}r^3}; l = \frac{\kappa}{4\pi\sqrt{2}r^3} \frac{T}{P} \quad (3)$$

where k_g is the permeability of a medium to gas (m^2), k_l is the permeability of the medium to liquid (m^2), l is the mean free path of gas molecules (m), r is the pore radius (m), κ is Boltzmann's constant (J/K), T is the temperature (K), c is a dimensionless constant, P is the pore pressure (Pa), and b is the Klinkenberg slip factor (Pa).

The Klinkenberg factor b depends on the rock properties and the physical properties of gas to a lower degree. Some investigations showed that the relationship between Klinkenberg slip factor b and water permeability (k_l) (in about 100 core samples) follows a linear increase upon the scale of $\log b - \log k_l$ where the permeability range is between 10^{-12} to 10^{-17}m^2 ($b \propto k_l^{-0.36}$, Jones and Owens 1980, Tanikawa and Shimamoto 2009). A recent study on limestone showed that gas permeability is larger than water permeability by several times to one order of magnitude and increases with increasing pore pressure (Tanikawa and Shimamoto 2009). The relationship between the parameter b and water permeability for 30 sedimentary rocks from the western foothills of Taiwan (Pleistocene to Miocene rocks-330 points), is described by the formula (see Figure 3.26):

$$b = 0.15 \times k_f^{-0.37}$$

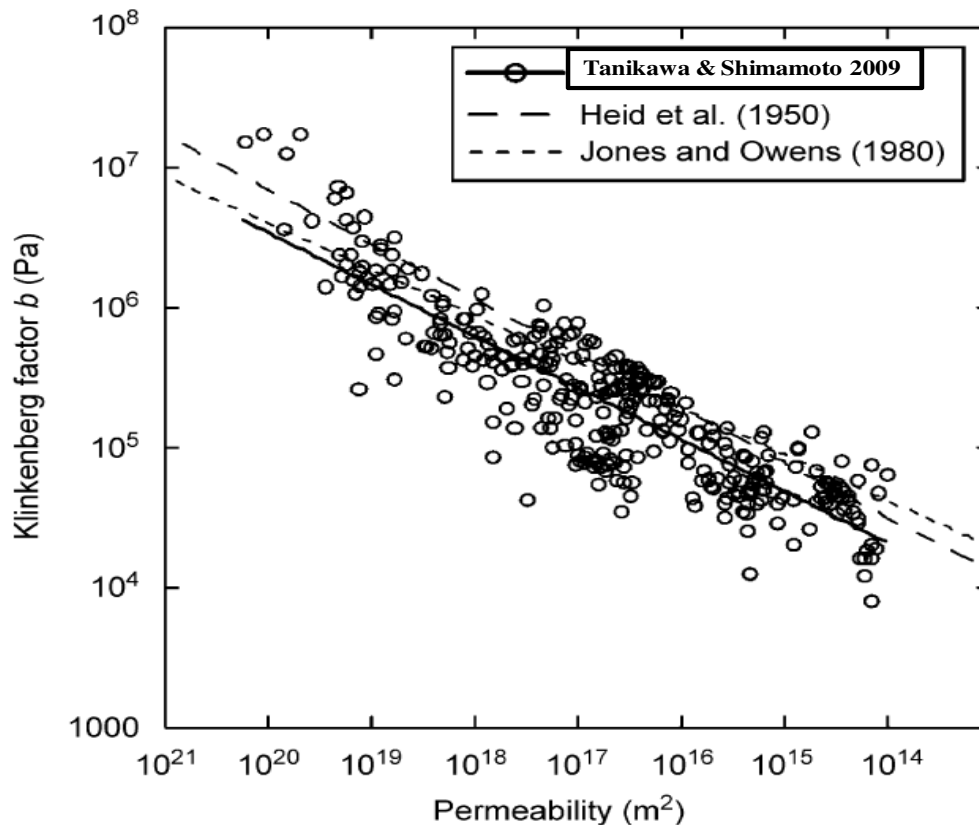


Figure 3.26. The Klinkenberg factor b and estimated water permeability power law relationship, obtained from the results of gas permeability tests of 30 sedimentary rocks from the western foothills in Taiwan (Tanikawa and Shimamoto 2009).

Aside from the GMT as a large scale test for analyzing gas migration in bentonite (+sand), some other laboratory tests have also been conducted. Related to the latter case, a comprehensive review on the most recent investigations for soft geomaterials was given in GAMBIT (CLAY Club Workshop on Gas Migration in Bentonite, Rodwell and Assurance 2005). The main features observed in the experiments on gas migration in bentonite can be summarized as follows (Rodwell and Assurance 2005):

- A threshold pressure for gas entry into the bentonite is observed in many experiments.
 - It appears that there is a displacement of only small volumes of water from saturated bentonite by migrating gas, although the amount of water displaced has often not been determined.
 - Changes in pore-water pressure and external stresses are observed in response to the applied gas pressure and the creation of gas pathways.

The aforementioned prevalent mechanisms are described in more details in the following references: Fall 2009, Horseman et al. 1999, Alonso 2006, Delahaye and Alonso 2002, Rodwell and Assurance 2005. The results of the experimental tests that were carried out by Horseman et al. (1999) are presented below as an illustration of gas migration mechanism in bentonite.

Horseman et al. (1999) performed two experiments in a constant volume and radial flow (CVRF) apparatus (see Figure 3.27). The bentonite sample had a diameter of 60 mm and length of 120 mm. The values quoted for the sample properties were in the following ranges: water mass fraction; 26.7–27.1, dry density; 1.568–1.582 Mg m⁻², and water saturation; 97.6–98.6%. The permeability and specific storage were determined from hydraulic tests for samples MX80-8 and MX80-9. The results showed that the average permeability from the CVRF test is 1.4×10^{-21} – 1.7×10^{-21} m², with a specific storage in the range 1 – 9×10^{-6} m⁻¹. This small value of specific storage is indicative of a fully-saturated constant volume system.

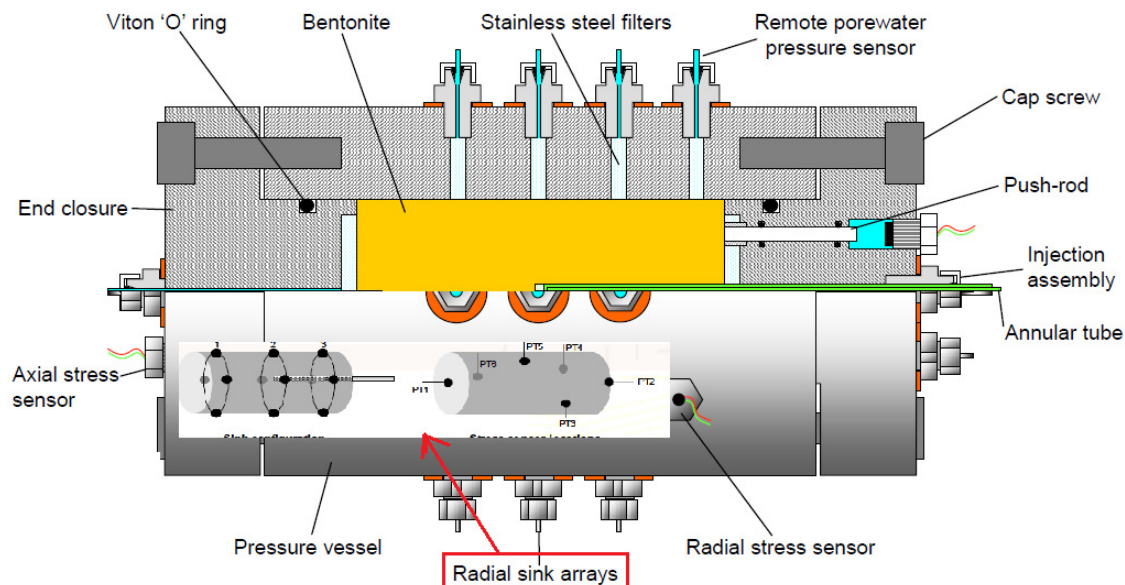


Figure 3.27. Cut-away diagram of CVRF apparatus (Rodwell and Assurance 2005)

The main features found in gas injection tests with the CVRF geometry and sample MX80-8 include the following (see Figure 3.28):

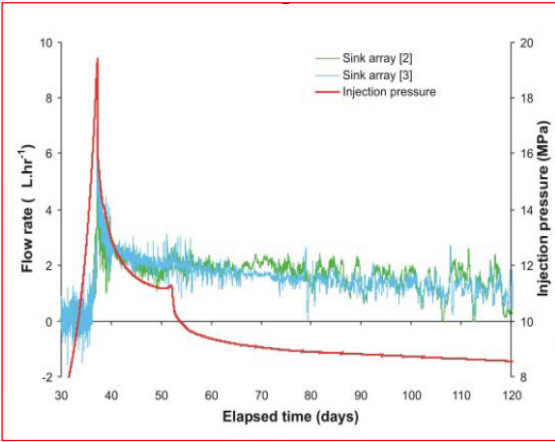
- As the upstream gas pressure rises, a very small amount of fluid is produced from the sinks at a gas pressure of 13.8 MPa (accompanied by a rise in axial and radial stress). At 18.7 MPa, gas pressure drops slightly (axial stress increases), but then increases again. This is

interpreted as the opening of a gas pathway that failed to intersect any of the 12 sinks around the circumference of the sample.

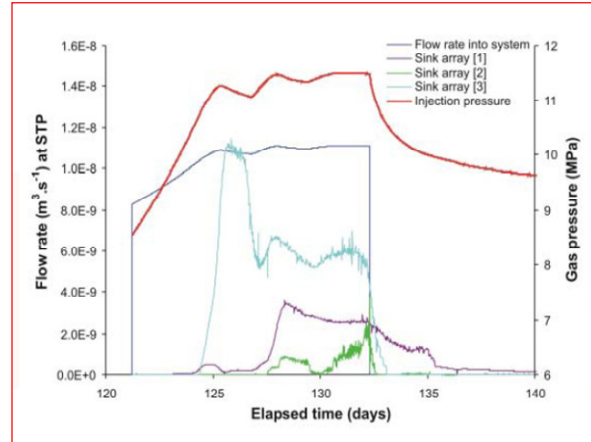
- The peak gas pressure reaches 19.4 MPa . At this point, there is a flow of large quantities of gas to one set of sink arrays (99.9%), indicating channelled gas flow. After breakthrough, the upstream gas pressure falls to a steady-state value of 11.2 MPa. When the injection pump is turned off, the upstream value falls towards a “shut-in pressure” of around 8 MPa at which flow from the sample ceases.

The tests with sample MX80-9 were carried out with a stress of 10 MPa that was applied to the floating end caps, and a water backpressure of 1 MPa was applied to the sinks on the circumference of the sample. In this test, the water injection pump is turned off when the pressure reaches 8.8 MPa (before gas breakthrough) and the upstream pressure is kept at this value for ~ 80 days. When gas injection resumed, the following features were observed (Rodwell and Assurance 2005):

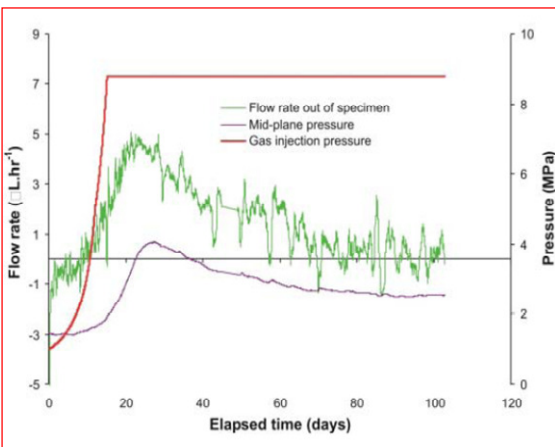
- There is a major gas breakthrough at a peak pressure below 10 MPa, followed by a rapid decline in pressure. This is consistent with the presence of unstable gas pathways. The shut-in pressure is around 8.2 MPa (Figure 3.28).
- When pumping is restarted after the shut-in, the flow rate out of the specimen begins at around 8.5 MPa. The gas pressure increases to a peak value of 9.3 MPa before decaying slightly to a steady state pressure of 9.2 MPa. A break seen in the slope of the pressure decline curve after termination of pumping is considered indicative of pathway closure.



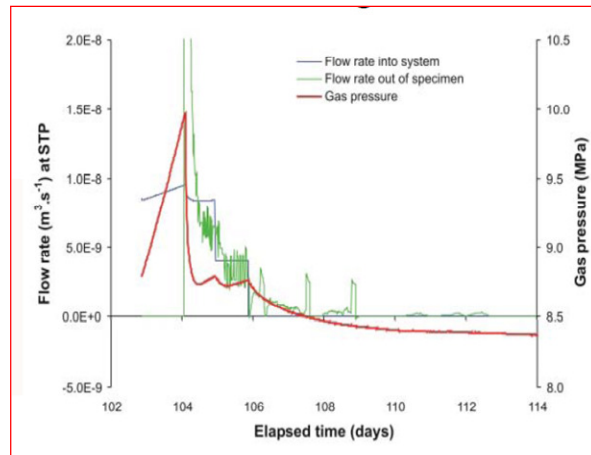
Mx80-8 background flow from sink arrays



Mx80-8 second gas injection history



Mx80-9 first 100 days of gas test



Mx80-9 main gas breakthrough event

Figure 3.28. The results of CVRF tests on two compacted bentonite samples (Rodwell and Assurance 2005)

3.4 Comparison, Discussion and Analysis of the Collected Data and Results

3.4.1 Introduction

A significant amount of data on the properties of sedimentary rock formations (which are potential host rocks for nuclear waste disposal repositories) in Ontario and Europe were presented in the previous sections. These data are valuable for the development of a mathematical and numerical model to predict the response of a hypothetical underground repository in Ontario to the migration of gases generated as well as analyze the safety of the repository with respect to gas transport. The comparison of data from Ontario (Cobourg limestone/Queenstone shale) and Europe will be a good

source for identifying their similarities and differences, i.e. to determine the suitability of the data obtained from Europe for studying gas transport issues in Ontario repositories.

Furthermore, previous chapters mentioned field and laboratory gas migration tests that were conducted on European sedimentary host rocks. These tests provided relevant information and parameters (e.g., gas entry pressure, intrinsic permeability, relative permeability, and water retention curve) for the development, calibration and validation of a mathematical model to study gas migration in European underground repositories.

In consideration of the facts that are mentioned above, the objectives of this section are:

- To compare the geochemical, geomechanical, hydraulic and thermal data on sedimentary rock formations in Ontario and Europe, and discuss their suitability for addressing gas transport issues in Ontario.
- To analyze the collected results of GMTs and develop relationships that will determine the relevant parameters that are necessary to model and analyze gas transport in sedimentary formations of Ontario.

3.4.1 Comparison and discussion of geomechanical, geochemical, hydraulic and thermal data on sedimentary host rock formations from Ontario and Europe

In this section, geomechanical, geochemical, hydraulic and thermal data, which are relevant for the study of gas generation and migration, and its effects on host rock formations in Ontario, will be compared with those of three well characterized European sedimentary host rock formations; namely, the COX in Bure, OPA in Benken (Zürcher Weinland) and Mont Terri in Switzerland. Furthermore, data, properties and processes that may (or may not) be transferable from European formations or locations to Ontario will be identified and discussed.

In Table 3.11, compiled information from the five aforementioned sedimentary rock formations (three from Europe and two from southern Ontario) are listed. The source of these data sets and their detailed descriptions can be found in Sections 2 and 3 as well as various references (e.g. Mazurek et al. 2008, Damjanac 2008, Gartner 2008, Gruescu et al. 2007, Mugler et al. 2006). From Table 3.11, the similarities and differences between the European and Ontario formations can be observed. The main similarities and differences as well as the transferability of the features and parameters will be discussed below.

Table 3.11. Basic characteristics of the considered formations

Property/Parameter	Callovo–Oxfordian at Bure	Opalinus Clay in the Zürcher	Opalinus Clay at Mont Terri	Cobourg Formation (COBL)	Queenston Formation (QUESS)
Depositional environment	Shallow marine	Shallow marine	Shallow marine	Marine	deltaic, marine to non-marine flood plains
Age	163– 158 Ma	ca. 174 Ma	ca. 174 Ma	Mid-Ordovician (488.3±1.7 to 443.7±1.5 Ma)	Upper-Ordovician
Maximum temperature reached during diagenesis (°C)	33-38	85	85	>90	>90
Present burial depth (centre (m))	488	596	275	685	550
Thickness (m)	138	113	160	50	200
Mineralogy & Porosity					
Clay–minerals (weight-%)	25–55	54	66	{ limestone shows distinct lithological variations }	65
Physical porosity (%)	11–17	12	16	0.4-3.6	4.0 - 5.3
Clay–mineral species (in the order of decreasing abundance)	Illite/smectite mixed-layers, illite, (chlorite, kaolinite)	Illite, kaolinite, ill/smec mixedlayers, chlorite	Illite, kaolinite, ill/smec mixedlayers, chlorite	Illite/ Quartz/ Chlorite –Kaolinite/ Calcite/ Illite/smectite	Illite/ Quartz/ Chlorite – Kaolinite/ Calcite/ Illite/smectite
Quartz (wt.%)	20-30	20	14	-	21-28
Feldspars (wt.%)	1	3	2	-	0-9
Calcite (wt.%)	20-38	16	13	-	5
Dolomite/ankerite (wt.%)	4	1	-	trace	<1
Clay mineral (%)	-	55	55	-	60
Swelling clay mineral	-	-	11.4	-	4
Hydrochemistry					
Pore-water type	Na–Cl–SO ₄	Na–Cl–SO ₄	Na–Cl–SO ₄	NaCl CaCl ₂ MgCl ₂ -KCl	NaCl+ CaSO ₄
Mineralization (mg/L)	<30(TDS(g/L))	<30(TDS(g/L))	<30(TDS(g/L))	300(TDS (g/L))1	300(TDS (g/L))
Hydraulic properties					
Hydraulic conductivity K _x (m/s), anisotropy factor ²	5E-14;5E-13; 2–10	2.4E-14, 1–10	4.0E-14, ca. 5	2.4E-14, 1–10	2.4E-14, 1–10
Effective diffusion coeff. (De) (m ² /s)	1.5 10 ⁻¹¹ (for HTO)	4.5 10 ⁻¹³ (for HTO)	4.5 10 ⁻¹² (for HTO)	10 ⁻¹² -10 ⁻¹³ (HTO)	10 ⁻¹² -10 ⁻¹³ (HTO)
Geomechanical properties					
Overconsolidation ratio	1.5-2.0	1.5-2.5	2.5-3.5	overconsolidated	overconsolidated
Uniaxial compressive strength normal to bedding (MPa)	21	30	16	113	48
Undrained E (tangent) modulus normal to bedding (MPa)	4000	5500	3600	36400	17650
Cohesion normal to bedding at low confining pressure (MPa)	6.4	8.6	5	19.09	2.05
Friction angle normal to bedding at low confining pressure	29	25	25	45	31
Thermal properties					

1 Total Dissolved Solids (often abbreviated as TDS) is an expression for the combined content of all inorganic and organic substances contained in a liquid which are present in a molecular, ionized or micro-granular (colloidal sol) suspended form

2. Anisotropy factor = value parallel/value normal to bedding

Thermal Conductivity(W/mk)	1.04-2.92	1.2-1.4	1.2-1.4	1.63-3.63	2.07
Specific heat C_p(J kg⁻¹ K⁻¹)	UD	800	800	670-750	670-750
Gas transport					
Gas entry Pressure (KPa)³	5000-9000	>5000	400-1000	2100-5100 ¹	<5100 ¹

(1) Estimated by using indirect modelling technique (see Chapter 4.4)

3.4.1.1 Geomechanical properties

In Table 3.11, some basic geomechanical parameters of rock formations in Ontario are compared with those of European formations. It can be observed that the geomechanical parameters for the formations in Ontario generally show higher values in strength, cohesion, Young's modulus and friction angle than those in Europe. However, the observed differences are relatively low for some parameters, such as uniaxial compressive strength, and friction angle. Moreover, there is a relative analogy with regards to overconsolidation and the maximum stress anisotropy. The European and Ontario formations are all overconsolidated (overconsolidation ratio data for Ontario formations are not available). The regional stress field in southern Ontario formation is characterised by high horizontal excess stresses, and the maximum principal stress is horizontal. This feature is beneficial from the viewpoint of fault sealing. The principal stress direction in Europe is however sub-vertical. The maximum stress anisotropy is only slightly higher in southern Ontario (1.9) when compared to OPA (1.4) (Mazurek, 2004). Given this relative analogy of geomechanical parameters and in situ stress, it can be assumed that some of the experience and conclusions about the mechanical behavior of the host rock in the OPA could be approximately extrapolated to the situation in southern Ontario.

3.4.1.2 Mineralogy and porosity

Mineralogy and porosity (or pore structure) are among the most important macroscopic parameters of argillaceous systems (argillaceous limestone, clay, and shale). Several processes and parameters are functions of mineralogy and porosity, and the understanding of this dependency is a key prerequisite for transferability and adaptation of information from one site to another site (Mazurek et

3 .The values of gas entry pressures for Cobourg (COBL) and Queenstone (QUESS) formations were predicted by using soft-computing modeling techniques (see chapter 4.3)

al. 2008). Table 3.12 shows how the transferability of features and parameters among different argillaceous formations is dependent on the mineralogy and porosity and/or on the state of the system (in situ stress, hydraulic head, temperature, pore-water salinity).

Table 3.12 Transferability of features and parameters among different shale formations (Mazurek et al. 2008)

Dependence on mineralogy and porosity	Dependence on the state of the system	Transferability	Example
None to weak	None to weak	Directly transferable	Thermodynamic and kinetic data
Strong	None to weak	Transferable using empirical relationships	Hydraulic conductivity, strengths
Strong	Moderate	Transfer is more complex (requires underlying conceptual models and model calculations)	Geometry of the excavation-damaged zone (EDZ), sorption characteristics
	Strong	Not transferable	Hydraulic head, pore-water composition

From a mineralogical point of view, a key factor that controls a number of relevant features and processes of argillaceous rocks is the presence of clay mineral, the type and amount of clay minerals that are present in the rocks. Indeed, the following processes and features are significantly dependent on the clay mineral (Mazurek et al. 2008):

- Advection and diffusion of water and gas depend on the structure of the pore space (interconnected network on a nanometric scale), which in turn, is determined by the spatial arrangement of clay platelets.
- Sorption is mainly determined by the high specific surfaces and reactivity of clay minerals (e.g., kaolinite, illite, and montmorillonite).
- Self sealing of fractures depends on the swelling properties of clay minerals and rheology of the rocks.
- Geomechanical properties, such as strengths and moduli, depend on the nature of the minerals as well as the microstructure of the pore space and its water content.
- The degree of anisotropy of transport and geomechanical properties is linked to the bedding; the parallel alignment of clay platelets.

In consideration of the facts mentioned above, the mineralogical compositions of the argillaceous rocks in Europe and Ontario in the framework of radioactive waste disposal are qualitatively and quantitatively compared. The comparisons are shown in Table 3.11 and Figure 3.29 (quantitative mineralogical composition of Cobourg limestone is not available). From the table and figure, it can be noticed that there is a high degree of overlap in the mineralogical composition (especially clay minerals); namely, Queenston shale and Cobourg limestone (only qualitative comparisons) formations with OPA. However, the proportion of swelling clay minerals present in the OPA at

Mont Terri (11.4% of illite/smectite mixed layers) is higher than that of Queenston Shale (4% of illite/smectite mixed layers). This may have a significant impact on swelling potential, fluid flow transport and sorption properties of the aforementioned formations and thereby limit the transferability of such properties.

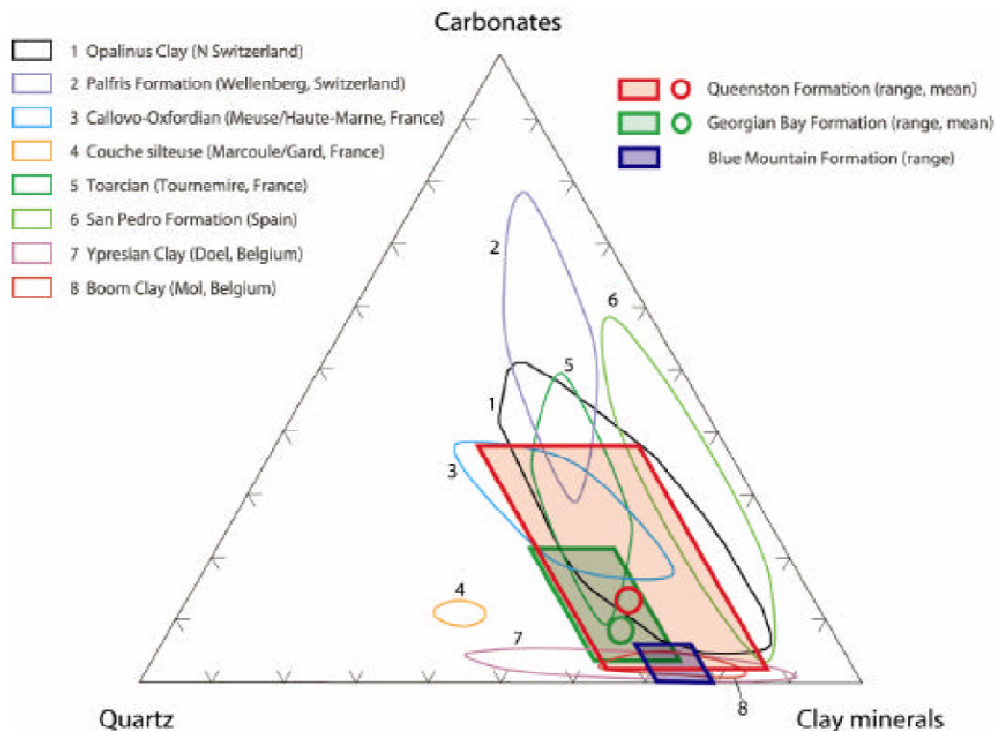


Figure 3-29: Mineralogical composition of various argillaceous formations compared with that of Upper Ordovician shales in southern Ontario (Mazurek et al. 2008). Adapted from Nagra (2000a), Ontario data from Russell & Gale (1982). Data represent weight proportions.

Aside from the mineralogy, the porosity or pore structure has significant impact on some properties (e.g. hydraulic conductivity, strength) of argillaceous rocks, and thus on the transferability of the features and parameters. The data presented in Table 3.11 highlight that the studied formations in Europe and Ontario all present low physical porosities ($\leq 16\%$). However, the Cobourg and Queenston Formations have lower porosities; 1.5 to 2.0% and 4.0 to 5.3%, respectively. These lower values could be explained by the higher degree of compaction and diagenetic (calcic) cementation in the Ontario formations.

3.4.1.3 Hydraulic properties

The European and Ontario formations show some common hydraulic properties. The hydraulic conductivity in both formations is anisotropic. The anisotropic factor is relatively similar (except for OPA at Mont Terri) as shown in Table 3.11. The vertical conductivity is approximately 10 times smaller than the horizontal conductivity. The hydraulic conductivities of both formations are low ($\leq 10^{-13}$ m/s) and comparable; i.e. advective transport is expected to be insignificant or low. The hydraulic conductivity values obtained in the European formations and the relatively similar anisotropy factor could be useful for the development of relationships to predict the hydraulic conductivities of Ontario formations and the transferability of features related to hydraulic conductivity. However, for hydraulic data such as the hydraulic head, which depends substantially on the state of the repository system, site-specific information is essential and transferring features from Europe to Ontario will be generally not possible. Furthermore, in contrast to several European disposal projects in sedimentary rocks, the host formations (whether Ordovician shales or limestones) are not directly bounded by aquifers that contain young, fresh waters. This could mean a lower risk of groundwater contamination and different boundary conditions for model development with regards to the Ontario situation.

3.4.1.4 Thermal properties

Thermal conductivity and heat capacity of the studied Ontario and European rock formations follow approximately a similar range.

3.4.1.5 Geochemical and hydrochemical properties

Significant differences in the hydrochemical properties of ground and pore waters between the European and Ontario sedimentary argillaceous rocks are noted. The ground and pore waters in the Cobourg Limestone and Queenston Shale formations are brines. TDS values of around 300 g/l have been determined in these formations (Table 3.11). Salinity increases significantly with depth in the Michigan Basin from fresh shallow ground waters to deep saline brines. The salinities of most European argillaceous formations are 1 - 2 orders of magnitude lower than those of shale and limestone in southern Ontario. Potential reason for this high salinity in Ontario is: episodes of sea water evaporation, particularly during the Silurian and Devonian periods, would have created an unstable high salinity brine layer in the upper stratigraphic levels of the basin (NWMO, 2011). This

important difference in water salinity will limit the transferability of some experience and conclusions with regards to gas generation and transport from European formations to the situation in Ontario as explained below.

- A higher corrosion rate of Ontario repository materials (e.g. waste canisters) than in European DRGs should be expected due to this higher salinity. In the Swedish safety case, a maximum salinity of 100 g/L is a design criterion for siting a repository (Mazurek et al., 2008). Thus, special attention is required in the estimation of the gas generation rate in Ontario. Values obtained in the European situation could underestimate the rate, which could result in safety issues.
- The capability of clay minerals (present in the host rock or bentonite backfill) to swell and self seal (in bentonite backfill, EDZ and natural faults of the host rock) will be probably affected by the high salinity in Ontario formations. Extrapolations from European sites may not be valid due to the different hydrochemical environments.
- Geochemical modeling (e.g. speciation, dissolution/precipitation and sorption equilibria) of the Ontario formations with respect to gas migration may be more complex than the European formations, which are dilute systems, due to substantial deviations of activity coefficients from ideal behaviour.
- The increase in salinity with depth influences vertical hydraulic gradients and water viscosity for the Na-Ca-Cl fluids when it increases gas entry pressure.

3.4.1.6 EDZ permeability and evolution

In contrast to European formations where several measurements of the hydraulic properties of the EDZ were performed, no permeability measurements of EDZ in the Ontario argillaceous host rocks are available. However, given the relatively similar geomechanical properties (e.g. in situ stress state, uniaxial compressive strength, and degree of compaction) between the Cobourg limestone and the OPA, it can be expected that the initial permeability of the formations will be relatively similar. Therefore, a transfer of observations and measurements pertinent to the initial permeability of the EDZ may be feasible. However, a transfer of the observations and measurements pertinent to the evolution (with time) of the permeability of the EDZ in OPA to Cobourg formations will be not appropriate, because the high salinity of the ground and pore waters in the Cobourg Formations will

certainly inhibit the swelling potential of the clay minerals, and thereby reduce the self sealing potential of the EDZ.

3.5 Gas migration

In the previous section, information was provided on the conduction of several gas migration tests in the European argillaceous rocks. These tests provided relevant information on the gas transport mechanisms and gas transport parameters (e.g. gas entry pressure, relative permeability). However, no testing has been performed in Ontario host rocks yet. Despite this, it can be assumed that the transport mechanisms of gas in Ontario formations, if chemical effects are assumed to be negligible, will be similar to that in European argillaceous rock (see Figure 3.30, and Fall 2009) because both formations and the argillaceous rocks present relatively similar geomechanical properties.

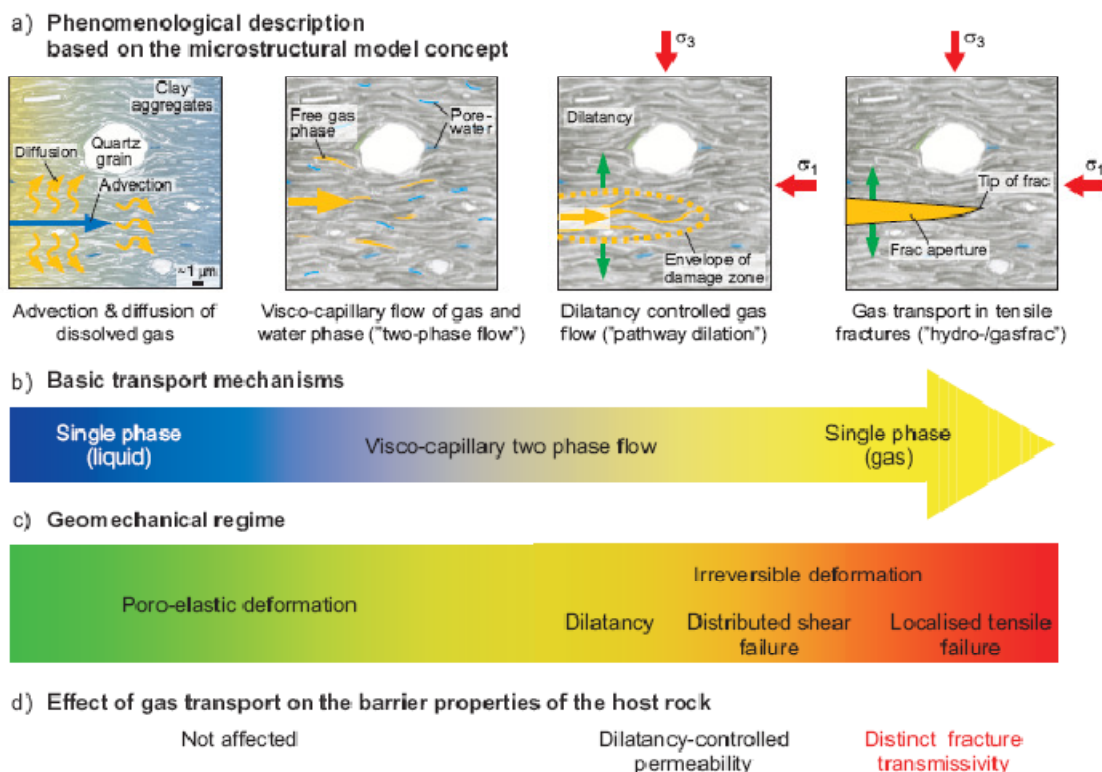


Figure 3.30. Classification and analysis of gas transport processes in Opalinus clay (Nagra 2008)

However, due to the differences in porosity or pore structure, the gas transport parameters, such as gas entry pressure and relative permeability as well as the Klinkenberg factor should not be transferred from the European to the Ontario situation.

3.6 Conclusion

The following objectives are achieved in the present work:

- (i) Compilation of published geochemical, mechanical, hydraulic and thermal data on sedimentary rock formations in Ontario, which are relevant to the study of gas generation and transport.
- (ii) Review and analysis of the results of gas transport tests performed in European URLs
- (iii) Comparison of the Ontario data to those from European sedimentary rocks.
- (iv) Discussion and analysis of the usefulness and transferability of the research results in Europe to the Ontario situation.

The European and Ontario potential host rock formations present some similarities and differences. However, no gas transport test has been performed in Ontario. Hence, there is a need to predict the relevant gas transport parameters for Ontario based on the European data.

The main common property of the above formations is the low/very low permeability media of fine grained rock (sedimentary rocks). This attribute, which is one of the main characteristics of gas migration behaviour in association with gas permeability and water retention related parameters, has been used to recognize possible successive changes of gas behaviour regimes (along with time).

The results show that despite some differences between the geomechanical properties of Cobourg limestone and OPA, the gas procedure evolves in the same way. Furthermore, some additional comments which must be taken into account within the analysis are as follows:

1. The geochemical property of the Cobourg limestone /Queenston shale includes a relatively high value of brine. Salinity plays an important role in groundwater movement. Salinity increases significantly with depth in the Michigan Basin from fresh shallow ground waters to deep saline brines. The increase in salinity with depth influences vertical hydraulic gradients and water viscosity for Na-Ca-Cl fluids. This salinity will certainly have an impact on the self sealing ability of the EDZ. This is a major difference with the European host rocks.
2. A higher corrosion rate of Ontario repository materials (e.g. waste canisters) than in European DRGs should be expected due to this higher salinity. In the Swedish safety case, a maximum salinity of 100 g/L is a design criterion for siting a repository (Mazurek et al., 2008). Thus, special attention is required in the estimation of the gas

generation rate in Ontario. Values obtained in the European situation could underestimate the rate, which could result in safety issues.

4 Development and validation of a mathematical model to predict gas migration from in DGR in sedimentary rocks

4.1 Introduction

The following tasks will be performed in the present chapter:

- Task # 1: Develop constitutive relationships and mathematical models to determine the disturbances of sedimentary rock due to gas generation from a repository. The development of the models should be calibrated with results from tests performed on materials from European underground research laboratories, such as the Tournemire in France and Mont-Terri in Switzerland.
- Task # 2: Validate and calibrate the developed models with results from laboratory tests performed on materials from European underground research laboratories, such as the Tournemire in France and Mont-Terri in Switzerland.
- Task # 3: Validate and calibrate the developed models with results from field tests performed in European underground research laboratories, such as the Tournemire in France and Mont-Terri in Switzerland.

To achieve the objectives of the aforementioned tasks, two main stages are carried out:

- the first stage includes the development of mathematical models to predict and analyze gas migration in sedimentary host rocks; and
- the validation and calibration of the developed model against gas migration experimental tests and numerical simulations will be carried out on European sedimentary rocks.

4.2 Development of the THM model

4.2.1 Basis of the mathematical formulations and general assumptions

For modelling purposes of the porous medium (host sedimentary rock), we will adopt a continuum approach, in which a representative elementary volume (REV) around any mathematical point considered in the domain always contains both solid and fluid phases, and classical mass balance laws of continuum mechanics hold for each phase. The total volume of the medium is given by:

$$V = V_s + V_v \quad (1)$$

where V represents the total volume; V_s refers to the solid volume; and V_v refers to the void spaces occupied by the fluids (gas, liquid).

Since the porous medium is made of three phases (solid, s ; liquid, l ; and gas, g), it can be written that

$$V = V_s + V_l + V_g \quad (2)$$

$$M = M_s + M_l + M_g \quad (3)$$

where V_l and V_g refer to the volumes of the liquid (water) and gas; and M , M_s , M_l , M_g are the total mass of the medium, the mass of the solid, liquid and gas, respectively.

The governing equations of the model result from a combination of a set of balance and constitutive equations. The balance equations include: (i) momentum; (ii) mass; and (iii) energy conservation equations. The fundamental macroscopic balance of an extensive thermodynamic property (e.g., mass, momentum, energy density) is applied here to derive the aforementioned balance equations as described below. The macroscopic balance equation of any thermodynamic property in a continuum can be expressed in the following general form (Bear 1991).

$$\frac{\partial}{\partial t} M_\pi^\kappa + \nabla \cdot (\mathbf{j}_\pi^\kappa) - f_\pi^\kappa = 0 \quad (4)$$

where the quantity M_π^κ can refer to the mass or energy per unit volume of the porous medium, with κ the mass components (air, water or solid) or “heat component”, and π

the phases (gas, liquid or solid). \mathbf{j}_π^κ is the total flux (vector) with respect to a fixed reference system, and f_π^κ is the rate of the production/removal of component κ per unit volume.

To develop the aforementioned governing equations, the following main assumptions are made:

- (i) the porous medium includes three constituents: a solid and two fluids (water, gas). These constituents are considered as three independent overlapping continua in the context of the theory of mixtures. Water is wetting, whereas gas is not. The voids of the solid skeleton are partially filled with liquid water, and partially with gas;
- (ii) the three constituents are distributed in the three phases as mentioned above. The gas phase is considered as an ideal gas mixture composed of dry air (gas generated by the repository; air is considered in this study; *ga* index) and water vapour (*gw* index). The solid matrix is chemically inert with regard to the fluid contained in its pores. The only reaction that can occur in the porous medium is a change of phase from liquid to vapour. The liquid phase consists of water and dissolved gas (air);
- (iii) local thermal equilibrium is assumed for the three-phase system, i.e. locally, the phases are at the same temperature and heat transfer between phases can only occur during phase transition; and
- (iv) deformations are small and strains are infinitesimal with regards to the mechanical response.

4.2.2 Mechanical response

Based on a poroelasticity framework, a non-isothermal poroelastic model is developed to describe the mechanical behavior of the sedimentary rock in the DGR. To describe the solid deformation in unsaturated porous mediums, consider a representative elementary volume of an unsaturated bulk porous medium subjected to external stress, σ_{ij} . The linear momentum balance equation for the whole mixture, neglecting inertial effects and in case the body loads come solely from gravity, can be written as:

$$\nabla \cdot \boldsymbol{\sigma} + \rho \mathbf{g} = 0 \quad (5)$$

where $\boldsymbol{\sigma}$ is the stress tensor (positive for tension), \mathbf{g} is a vector for the acceleration that results from the gravity, and ρ is the average density of the mixture.

$$\rho = (1 - \phi)\rho_s + \phi S_l \rho_l + \phi S_g \rho_g \quad (6)$$

where ϕ is the porosity, ρ_s the density of the solid, ρ_l the density of the liquid (water), and ρ_g the density of the gas. S_l and S_g are the degrees of saturation for water and gas. The respective degrees of saturation, S_l and S_g , sum to one.

$$S_l + S_g = 1 \quad (7)$$

Neglecting the inertial terms, the momentum equation can be also written as:

$$\frac{\partial \sigma_{ij}}{\partial x_j} + F_i = 0 \quad (8)$$

where F_i represents the supply of momentum by the body forces, and σ_{ij} refers to the external (total) stresses.

Assuming that tensile stresses and pore fluid pressures are positive in the following and considering the Bishop's principle for effective stress, the total stress in an incremental form can be given by:

$$d\sigma_{ij} = d\sigma'_{ij} - \alpha \bar{p} \delta_{ij} \quad (9)$$

where σ'_{ij} is the effective stress, $\alpha (\leq 1)$ is the Biot's coefficient ($\alpha = 1 - \frac{K_D}{K_s} \leq 1$, where

K_D and K_s are the bulk modulus of the porous medium and solid phase, respectively) which allows accounting for the volumetric deformability of the particles, δ_{ij} is the Kronecker's delta, and \bar{p} is an average pore pressure, which depends on gas and liquid pressures. This average pressure can be evaluated by using the following equation (Bear and Bachmat 1991, Zienkiewicz et al. 1977).

$$\bar{P} = S_l P_l + S_g P_g = S_l P_l + (1 - S_l) P_g \quad (10)$$

For an isotropic and thermo-elastic porous medium, the stress-strain relationship can be written based on Lamé constants, G and λ , as follows:

$$\sigma'_{ij} = 2G\varepsilon_{ij} + \lambda\varepsilon_{kk}\delta_{ij} - \delta_{ij}K_D\beta_T dT \quad (11)$$

where ε_{ij} is the skeleton strain, K_D ($K_D = \frac{E}{3(1-2\nu)} = \lambda + \frac{2G}{3}$) is the bulk modulus of the porous medium, T is the temperature, β_T is the coefficient of the volumetric thermal expansion ($^{\circ}\text{C}^{-1}$), and G is the shear modulus (Pa) expressed as:

$$G = \frac{E}{2(1+\nu)},$$

$$\text{and } \lambda = \frac{E\nu}{(1+\nu)(1-2\nu)}$$

where E is the elastic modulus and ν is Poisson's ratio. δ_{ij} is the Kronecker delta tensor defined as 1 for $i = j$ and 0 for $i \neq j$.

Equations 9 and 11 result in

$$d\sigma_{ij} = 2G\varepsilon_{ij} + \lambda\varepsilon_{kk}\delta_{ij} - \alpha\bar{p}\delta_{ij} - \delta_{ij}K_D\beta_T dT \quad (12)$$

Under the basic assumption of small strain, the relation between the strain and displacement in continuum mechanics is usually defined as:

$$d\varepsilon_{ij} = \frac{1}{2} \left(\frac{\partial u_i}{\partial x_j} + \frac{\partial u_j}{\partial x_i} \right) \quad (13)$$

where u_i denotes the displacements of the solid skeleton.

Combining Equations 8, 11 and 12 yields

$$G \frac{\partial^2 u_i}{\partial x_j \partial x_j} + (\lambda + G) \frac{\partial^2 u_j}{\partial x_i \partial x_j} - \alpha \frac{\partial \bar{p}}{\partial x_i} + -K_D \beta_T \frac{\partial dT}{\partial x_i} + dF_i = 0 \quad (14)$$

Equation 14 is the differential equation that governs the deformation phenomenon in unsaturated sedimentary rock under a combination of changes in applied stresses, fluid pressures, and temperature.

- **Effect of damage**

From a certain level of mechanical load or pressure of the gas generated within the DGR, repository microcracks can be generated within the sedimentary host rock. The generation of microcracks, and their growth and coalescence into macroscopic cracks, generally result in the deterioration of the sedimentary rock (rock mechanical damage) such as the decrease of strength, rigidity, toughness, stability and residual life. To account for these deterioration processes, it is necessary to introduce a mechanical damage variable, D ($0 \leq D \leq 1$), to the mechanical constitutive model of the host rock. The concept of a damage variable was first proposed by Kachanov (1958) and then further developed by several authors such as Lemaitre (1971); Lemaitre and Chaboche (1990); Voyiadjis and Venson (1995); and Krajcinovic (1996). The damage variable is a macroscopic measurement of the microscopic degradation of a representative volume element (RVE). Kachanov considered the damage in a cross section to be measured by a relative area of voids. Thus, his theory defines a ‘modified effective stress’ $\tilde{\sigma}$ and takes into account the damage D as a parameter, measuring the reduction of resistant area due to crack beginning and spreading (Mazars 1984 and 1986, Mazars and Pijaudier-Cabot 1989).

$$\tilde{\sigma} = \sigma \frac{A}{\tilde{A}} = \frac{\sigma}{1-D} \quad (15)$$

where A is the resistant area of the uncracked rock, whereas \tilde{A} is the resistant area of the damaged rock. It should be emphasized that the meaning of modified effective stress is

different from that of Equation 9. The effective stress in Equation 15 has to be introduced into Equation 9 ($\tilde{\sigma}_{ij} = \frac{\sigma_{ij}}{1-D}$) and the subsequent equations.

The damage parameter, D , is determined according to the approach proposed by Tang et al. (2002). According to this model, the strain-stress behaviour can be divided into an elastic phase and a damage phase. In the elastic linear phase, there is no damage in the rock or irreversible damages will not occur under loading or unloading conditions, whereas the rock starts to fail by crack generation and void-growth when the stress conditions attain a failure level, i.e. they satisfy the failure criterion. According to continuum elastic-damage mechanics, the elastic modulus of the rock may progressively degrade as damage grows or rock degradation progress, and the elastic modulus of the damaged element is defined as follows:

$$\mathbf{E} = (1-D)\mathbf{E}_0 \quad (16)$$

where E and E_0 are the elastic modulus of the damaged and undamaged elements, respectively. It should be emphasized that since the element and its damage are assumed to be isotropic and elastic, E , E_0 , and D are all scalar.

The rock around a repository is predominantly subjected to compressive loads, but they can also be subjected to tensile loads. Rock behaves differently in tension and compression loadings. The damaging mechanisms are different in compression and traction. To account for such a difference, two damage parameters, D_t and D_c , are introduced which correspond to the cases of tension and compression (Tang 2002) as explained below.

According to Tang (2002), when the tensile stress in an element attains its tensile strength f_t , that is:

$\sigma_{3\leq} f_t$ (17) (i.e. the minimum principal stress exceeds or is equal to the tensile strength of the element)

the damage variable can be defined as:

$$D = \begin{cases} 0 & \epsilon_{to} \leq \epsilon \\ 1 - \frac{f_{tr}}{E_o \epsilon} & \epsilon_{tu} \leq \epsilon \leq \epsilon_{to} \\ 1 & \epsilon \leq \epsilon_{tu} \end{cases} \quad (18)$$

where f_{tr} represents the residual tensile strength (Tang 2002). The definition of the other parameters given in Equation 18 is described in Figure 4.1 (Tang 2002).

To describe the parameter damage under a compressive or shear stress condition, Tang (2002) selected the Mohr–Coulomb criterion as the second damage criterion, that is:

$$F = \sigma_1 - \sigma_3 \frac{1 + \sin\phi}{1 - \sin\phi} \geq f_c \quad (19)$$

where ϕ is the friction angle and f_c is the uniaxial compressive strength. The damage variable under uniaxial compression is described as:

$$D = \begin{cases} 0 & \epsilon \leq \epsilon_{co} \\ 1 - \frac{f_{cr}}{E_o \epsilon} & \epsilon_{co} \leq \epsilon \end{cases} \quad (20)$$

where f_{cr} is the residual compressive strength.

Tang (2002) stated: “when 18, 19 and 20 are extended to three dimensional cases, we can use principal strain ϵ_3 to replace the tensile strain ϵ in Eq. 18; ϵ_1 to replace the tensile strain ϵ in Eq.20.

In multiaxial stress cases, the damage variable is defined as a combination of D_t and D_c as:

$$D = \xi_c D_c + \xi_t D_t \quad (21)$$

in which ξ_c and ξ_t are parameters determined from the state of stress. The parameters are given in the original work of Mazars (1984, 1986).

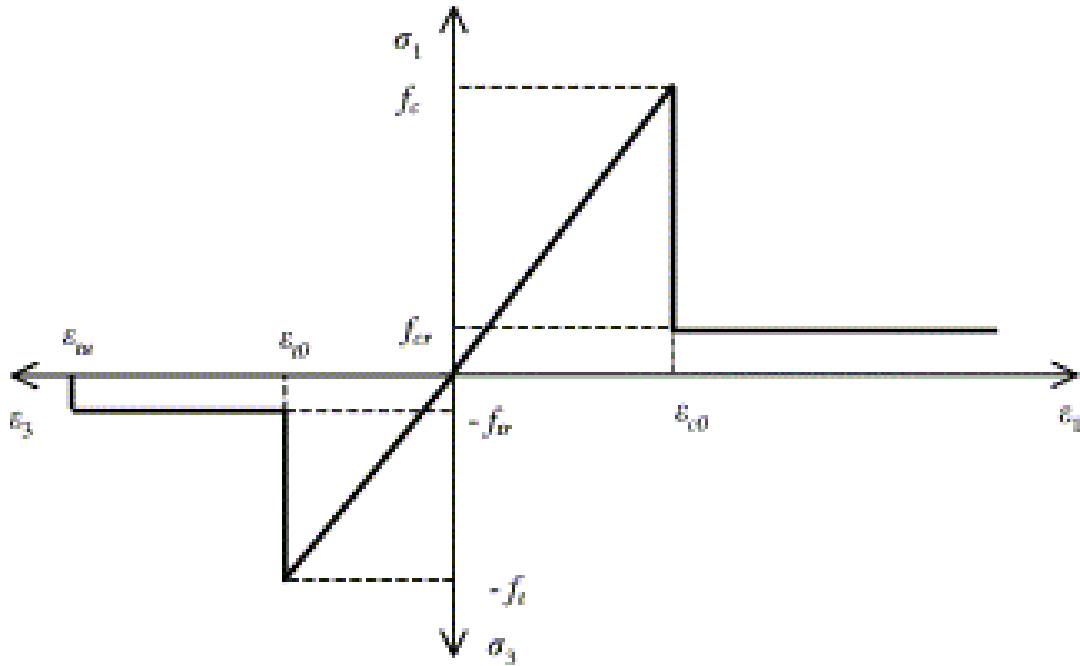


Figure 4.1. Elastic damage constitutive law for elements under uniaxial compressive stress and tensile stress (Tang 2002).

4.2.3 Solid mass conservation equations

By applying the co-moving time derivative to track the motion of a solid particle along its trajectory, expressed as:

$$\frac{D}{Dt}(\cdot) = \frac{\partial}{\partial t}(\cdot) + v_s \cdot \nabla(\cdot) \quad (22)$$

and defining the volume fraction of phase π as:

$$\phi^\pi = \frac{V_\pi}{V}, \quad (23)$$

the partial or apparent mass density as:

$$\rho^\pi = \frac{M_\pi}{V} \quad (24)$$

with the following constraints:

$$\phi^s + \phi^l + \phi^g = 1; \rho^s + \rho^l + \rho^g = \rho = \frac{M}{V}, \quad (25)$$

the general mass balance equation of each phase (Equation 4) can be written in the following general form:

$$-\nabla \cdot (\rho_\pi \mathbf{v}^\pi) = \rho_\pi \frac{D\phi^\pi}{Dt} + \phi^\pi \frac{D\rho_\pi}{Dt} + \rho_\pi \phi^\pi \nabla \cdot \mathbf{v}_s - f_\pi^k \quad (26)$$

where $\mathbf{v}^\pi \equiv \phi^\pi \mathbf{v}_\pi^r$ the apparent velocity vector of phase π , with $\mathbf{v}_\pi^r = \mathbf{v}_\pi - \mathbf{v}_s$ the intrinsic velocity vector of phase π relative to the solid skeleton, and \mathbf{v}_s is the velocity vector of the solid phase.

The mass balance equation of the solid phase is expressed as:

$$\frac{\partial M_s}{\partial t} + \nabla \cdot (M_s \mathbf{v}_s) = 0 \quad (27)$$

by introducing the following definition of solid mass M_s (per unit volume of porous medium),

$$M_s = (1 - \phi) \rho_s \quad (28)$$

where ϕ is the porosity of the sedimentary rock, ρ_s the density of the solid, the Eulerian form of the mass balance equation of the solid phase can be written as:

$$\frac{\partial((1 - \phi) \rho_s)}{\partial t} + \nabla \cdot ((1 - \phi) \rho_s \mathbf{v}_s) = 0 \quad (29)$$

Considering that $\phi^s = 1 - \phi$ according to Equation 26, the mass balance equation of the solid can be expressed as follows:

$$\frac{D(1 - \phi)}{Dt} + \frac{(1 - \phi)}{\rho_s} \frac{D\rho_s}{Dt} + (1 - \phi) \nabla \cdot \mathbf{v}_s = 0 \quad (30)$$

According to Rutqvist et al. (2001), intrinsic density ρ_s can be expressed in terms of fluid pressure, temperature and volumetric strain by using the following equation:

$$\frac{(1 - \phi)}{\rho_s} \frac{D\rho_s}{Dt} = -(1 - \alpha) \frac{D\varepsilon_v}{Dt} + \frac{(\alpha - \phi)}{K_s} \frac{D\bar{P}}{Dt} - (\alpha - \phi) \beta_T \frac{DT}{Dt} \quad (31)$$

ε_v is the volumetric strain, α the Biot's coefficient, and K_s the bulk modulus of the solid grains.

$\nabla \cdot \mathbf{v}_s$ can be written in terms of skeleton volume strain ε_v (Bear and Bachmat 1991):

$$\nabla \cdot \mathbf{v}_s = \frac{D\epsilon_v}{Dt} \cong \frac{\partial \epsilon_v}{\partial t} ; \nabla \cdot \epsilon_v \ll \frac{\partial \epsilon_v}{\partial t} \quad (32)$$

Thus, considering the above assumptions and combining Equations 30 and 31, we can write

$$\frac{\partial \phi}{\partial t} - (\alpha - \phi) \left(\frac{\partial \epsilon_v}{\partial t} + \frac{1}{K_s} \frac{\partial \bar{P}}{\partial t} - \beta_T \frac{\partial T}{\partial t} \right) = 0 \quad (33)$$

4.2.4 Liquid flow model

4.2.4.1 Liquid flow equations

The most common method to model liquid flow in an unsaturated porous medium is to combine a linear momentum balance equation for the liquid phase with the mass balance equation of the fluid (Khalili and Loret 2001). Neglecting the inertial and viscous effects, the relative apparent velocity of the liquid phase (water), which includes a pressure driving and a thermo-osmosis component, can be written as:

$$\begin{aligned} \mathbf{v}^{lr} &= \phi S_1 \mathbf{v}_1^r = \phi S_1 (\mathbf{v}_1 - \mathbf{v}_s) \\ \mathbf{v}^{lr} &= -\frac{\mathbf{k}_r \mathbf{k}}{\mu_1} (\nabla p_1 + \rho_1 \mathbf{g}) - k_T^l \nabla T \quad (34) \end{aligned}$$

where ϕ is the porosity, S_1 refers to the liquid saturation degree, the first term of Equation 34 represents the contribution of advection through consideration of the multiphase extension of Darcy's law for relative permeability, \mathbf{k}_r is the intrinsic permeability vector, \mathbf{k} is the dynamic viscosity of the liquid, \mathbf{u}_1 , and ρ_1 is the density of the liquid and \mathbf{g} the gravitational acceleration vector. The second term in Equation 34 represents the liquid flow due to thermal gradients; k_T^l ((m²/(s°C))) is the coefficient of thermal coupling for the liquid flux, i.e. it is a phenomenological coefficient associated with the influence of the thermal gradient on liquid (water) flux (thermo-osmosis). Thermo-osmosis can significantly contribute to liquid transfer in a low-permeable porous media. In some cases, its contribution in a low-porous medium can exceed that of advection due to the conventional Darcy flux (e.g., Chen et al. 2009).

The thermal coupling coefficient k_T^1 ($(m^2/(s^\circ C))$) can be expressed as (Chen et al. 2010):

$$k_T^1 = k_{T0}^1 S_1 \quad (35)$$

where k_{T0}^1 in m^2/sK is the thermal coupling coefficient for liquid water in saturated conditions.

The dynamic viscosity of the liquid water μ_1 [Pa s] strongly depends on the temperature and can be evaluated, with sufficient accuracy in a wide temperature range, by using the following relation (Thomas and Sansom, 1995).

$$\mu_1 = 0.6612(T-229)^{-1.562} \quad (36)$$

where the unit of μ_1 is Pa s, and T the absolute temperature.

Neglecting the influence of osmotic suction and adsorbed liquid water, the degree of liquid saturation S_l is assumed to depend on capillary pressure P_c and temperature, and the following relations apply:

$$S_l = S_l(P_c, T) \quad (37)$$

$$P_c = P_g - P_l \quad (38)$$

$$S_g = 1 - S_l \quad (39)$$

We can write

$$dS_l = C_{Sp}d(p_g - p_l) + C_{ST}dT \quad (40)$$

where P_l , P_g , S_g are the liquid water pressure, total gas pressure and gas saturation degree, respectively.

$$C_{Sp} = \frac{\partial S_l}{\partial s} \text{ and } C_{ST} = \frac{\partial S_l}{\partial T} \quad (41)$$

From Equation 41, it is shown that the water degree of saturation S_l is affected by suction (s) and temperature (T). C_{sp} and C_{ST} are isothermal and thermal liquid water capacities obtained from the water retention curve ($s = p_g - p_l$).

Considering that the volume fractions of the different phases of the porous medium are linked through the following relations:

$$\phi^s = 1 - \phi; \quad \phi^l = \phi S_l; \quad \phi^g = \phi(1 - S_l); \quad (42)$$

and introducing Equation 42 into Equation 26, the liquid mass conservation equation can be expressed as follows:

$$-\nabla \cdot (\rho_l v^{lr}) = \rho_l \frac{D(\phi S_l)}{Dt} + \phi S_l \frac{D\rho_l}{Dt} + \rho_l \phi S_l \nabla \cdot v_s + Q_\pi^{lg} \quad (43)$$

In Equation 43, Q_π^{lg} represents an evaporation-condensation term for water mass exchange between the gas and the liquid phase (negative for condensation and positive for vapourization). Mechanisms of interphase mass transfer for the water component include evaporation into the gas phase and corresponding condensation of the water vapour from the gas phase. The evaporation-condensation term can be computed by using Dalton's law (Marshall and Holmes 1988) as follows:

$$Q_\pi^{lg} = \omega(p_{sgw} - p_{gw}) \quad (44)$$

where ω ($\omega > 0$) is the liquid transfer coefficient, p_{gw} is the vapour pressure, and p_{sgw} is the saturated vapour pressure. The liquid phase transfer coefficient in a porous media can be determined from the following relation (Chen et al. 2009):

$$\omega = \frac{C}{\rho_l} \sqrt{\frac{1}{2\pi R_{gw} T}} = 0.01856 \frac{C}{\rho_l \sqrt{T}} \quad (45)$$

where the unit of ω is m s/kg, R_{gw} is the specific constant of vapour and T the absolute temperature. Symbol C refers to the accommodation coefficient, by which Equation 45 is used to express the intensity of phase transfer over a unit volume.

In Equation 44, p_{sgw} can be calculated by using Kelvin's law (Stallman 1964):

$$p_{sgw} = p_{svo} \exp\left(\frac{-p_c M_l}{\rho_l R T}\right) \quad (46)$$

where M_l refers to the molecular mass of liquid (=18 g/mol for water), R (=8.134 J/mol/K) represents the universal gas constant, p_c is the capillary pressure, and p_{svo} which depends on temperature only, is the saturated vapour pressure in contact with the liquid over a planar surface. This saturated vapour pressure can be obtained by using the empirical vapour pressure data available in the literature (e.g. Maidment 1992) or computed based on the Clausius-Clayperon equation (e.g. Tong et al. 2010) as:

$$p_{svo} = 101325 \cdot \exp\left\{-4895.36 \left[\left(\frac{1}{T}\right) - \left(\frac{1}{373}\right) \right]\right\} \quad (31a) \quad (47)$$

Substituting Equation 47 into 46 yields

$$p_{sgw} = 101325 \cdot \exp\left[-4895.36 \left(\frac{1}{T} - \frac{1}{373} \right) - 0.002165 \frac{p_c}{\rho_l T} \right] \quad (48)$$

As small deformations are assumed, to further simplify the formulation of the mass balance equation of the liquid water (Equation 43), the following small strain approximations can be made:

$$\nabla \cdot \mathbf{v}_s = \frac{D\varepsilon_v}{Dt} \quad (49)$$

$$\frac{D(\cdot)}{Dt} = \frac{\partial(\cdot)}{\partial t} \quad (50)$$

In Equation 49, we introduced the volume strain $\varepsilon_v = \nabla \cdot \mathbf{u}$ in terms of the divergence of the displacement vector, (\mathbf{u}).

Assuming that the liquid water is a barotropic fluid, the following relationships thus apply:

$$\rho_l = \rho_l(P_l, T) \quad (51)$$

$$\frac{1}{\rho_1} d\rho_1 = C_{ip} dp_1 - C_{iT} dT \quad (52)$$

in which $C_{ip} = \frac{1}{\rho_1} \frac{\partial \rho_1}{\partial p_1}$ and $C_{iT} = -\frac{1}{\rho_1} \frac{\partial \rho_1}{\partial T}$ are the coefficients of compression and thermal expansion for the liquid water, respectively. The following formula will be used here to compute the dependence of the liquid water density upon its temperature and pressure (Chen 2010):

$$\rho_1 = \frac{\rho_{iT}}{1 - C_{ip}(p_1 - p_{10})} \quad (53)$$

where the compressibility of the water C_{ip} is assumed to be constant and equal to 0.465 GPa^{-1} , and p_{10} represents a reference water pressure, which can take 0 or one atmosphere pressure (Chen 2010). ρ_{iT} is the density of water changes in a non-linear manner with temperature under a constant pressure, thus the following relation (Tong et al. 2010) will be used to calculate the density of water as a function of the temperature for the following temperature range (0.01 – 350°C).

$$\rho_{iT} = 1000.066219 + 0.020229T - 0.00602137T^2 + 0.0000163T^3, \quad (54)$$

where ρ_{iT} is the density at atmospheric pressure in units of kg/m^3 , and T is the temperature in °C.

The formula given by Chen (2010) is used here to compute the thermal expansion coefficient of the water, in a temperature range between 0.01 and 260°C:

$$C_{iT} = 3.0240 \times 10^{-6} + 1.1383 \times 10^{-5} T - 5.7556 \times 10^{-8} T^2 + 1.7769 \times 10^{-8} T^3 \quad (55)$$

where C_{iT} is in $^{\circ}\text{C}^{-1}$ and T in °C.

Considering Equations 49 to 50, and substituting Equation 34, 40 and 52 into 43, the differential equation that governs non-isothermal liquid flow through the unsaturated porous medium becomes:

$$\begin{aligned} \nabla \cdot \left[\rho_l \frac{k_{rl} \mathbf{k}}{\mu_l} (\nabla p_l + \rho_l \mathbf{g}) \right] &= \rho_l \phi S_l \frac{\partial \epsilon_v}{\partial t} + \phi \rho_l (S_l c_{lp} - c_{sp}) \frac{\partial p_l}{\partial t} + \rho_l \phi c_{sp} \frac{\partial p_g}{\partial t} + \phi \rho_l (-S_l c_{IT} + c_{ST}) \frac{\partial T}{\partial t} + \rho_l S_l \frac{\partial \phi}{\partial t} \\ &+ Q_{\pi}^{lg} + \nabla \cdot [\rho_l k_T^l \nabla T] \end{aligned} \quad (56)$$

4.2.4.2 Intrinsic permeability and relative permeability, capillary pressure

i) Intrinsic permeability

Intrinsic permeability (tensor \mathbf{k}) depends on the pore structure (volume of pores, distribution of pores, cracks) of the porous medium. Since, a sedimentary rock deforms due to stress around a DGR, the pore structure of the rock can change. Thus, intrinsic permeability is a function of deformation, i.e., in terms of the independent variables, a function of displacements. In this paper, to take into account the effect of deformation on permeability, intrinsic permeability is approximated as a function of the total porosity of the rock (ϕ) by using the following relationships (modified from Davis and Davis 1999, Rutqvist and Tsang 2002).

$$\mathbf{k} = k_0 \exp \left[A \left(\frac{\phi}{\phi_0} - 1 \right) \right] \quad (57)$$

where k_0 is the initial (zero stress) intrinsic permeability, and ϕ_0 the initial porosity, A is an empirical (calibration) factor that has to be determined from laboratory tests.

Besides the aforementioned deformation, mechanical damage can result in the generation and propagation of cracks within sedimentary rocks; in other words, change in their pore structure. This damage effect on intrinsic permeability should also be considered. Thus, an additional constitutive relationship will be needed to capture the damage induced evolution of rock permeability. There are some well-known models that describe the relationships between damage and permeability changes (e.g., Souley et al. 2001, Gawin et al. 2001, Tang et al. 2002). In this study, based on the approach proposed by Meschke

and Grasberger (2003), the following relation is used to estimate the permeability of the damaged sedimentary rock:

$$k = k_{UD} + k_D \quad (58)$$

where k_{UD} is the permeability of the undamaged rock, where k_D (isotropic damage permeability) is the damage enhanced permeability, which reflects the increase in permeability that is induced by damage. Thus, the permeability of the damaged medium is based on the additive decomposition of the permeability into two parts, k_{UD} and k_D .

where

$$k_{UD} = k_0 \exp \left[A \left(\frac{\phi}{\phi_0} - 1 \right) \right]$$

Using available experimental data in the literature with regards to the permeability vs mechanical damage and a phase transition approach (Kadanoff, 1966), Eq. (59) was formulated to capture the damage induced increase in permeability:

$$k_D = \frac{D}{D_{k_{\max}}} (k_{\max} - k_{UD}) \quad (59)$$

where k_{\max} is the maximum permeability of the damaged sedimentary rock, $D_{k_{\max}}$ is the rock damage value that corresponds to k_{\max} ; $D_{k_{\max}}$ and k_{\max} should be determined experimentally for the rock studied.

Combining Equations 58-59, the following relation is suggested to describe the effect of deformation and damage on intrinsic permeability:

$$k = k_0 \exp \left[A \left(\frac{\phi}{\phi_0} - 1 \right) \right] + \frac{D}{D_{k_{\max}}} \left(k_{\max} - k_0 \exp \left[A \left(\frac{\phi}{\phi_0} - 1 \right) \right] \right) \quad (60)$$

ii) Water retention curve and relative permeability

In this study, the relation between liquid saturation degree S_l and capillary pressure ($P_c = p_g - p_l$) is expressed by (Gerard et al. 2008, van Genuchten 1984):

$$S_l = S_{res} + \frac{S_{max} - S_{res}}{\left[1 + \left(\frac{P_c}{P_r}\right)^n\right]^m} \quad (60)$$

S_l is the liquid saturation, S_{max} the maximal saturation, S_{res} is the residual saturation, n and m are the coefficients of van Genuchten's law with $m = 1 - \frac{1}{n}$ and P_c / p_r is quantitatively equivalent to αh_c originally proposed by van Genuchten (1980), where h_c is the capillary pressure head defined as P_c / γ_w . The capillary pressure head function is given by $h_c = \frac{1}{\alpha} (1 - S_e^{-1/n})^{(1-n)}$. The relation 60 is a function of the pore structure of the porous medium as well as the temperature. This means rock deformation and temperature will have an effect on the water retention curve. The Leverett function (*Leverett J function*) is used in this study to take into account the variations of the porosity (induced by stress) in the water retention curve.

$$p_c = p_{c0}(S_l) \left(\frac{\sqrt[3]{k/\phi}}{\sqrt[3]{k_0/\phi_0}} \right) \quad (61)$$

The relative permeability of the liquid phase was assumed to be given as such by Nuth and Lalaoui (2008):

$$k_{rl} = (S_l)^{1/2} \left[1 - (1 - S_l^{1/m})^m \right]^2 \quad (62)$$

where k_{rl} is the relative permeability of the liquid phase (water), S_l is the liquid saturation degree

4.2.5 Gas flow model

4.2.5.1 Gas flow equations

The gas phase within the pores of the sedimentary host rock is considered to be a binary mixture of two ideal gases, dry air and water vapour. Dry air may dissolve into liquid water. It is assumed that the mixture of gases obeys the ideal gas law and Dalton's law. Thus, for all the gaseous constituents, i.e. dry air (ga), water vapour (gw) and gas (moist air, g), the Clapeyron equation of the state of perfect gases is:

$$p_{ga} = \frac{\rho_{ga} TR}{M_a} = \rho_{ga} R_{ga} T \quad (63)$$

$$p_{gw} = \frac{\rho_{gw} TR}{M_w} = \rho_{gw} R_{gw} T \quad (64)$$

$$P_g = \frac{\rho_g TR}{M_g} = \rho_g R_g T \quad (65)$$

and Dalton's law is

$$p_g = p_{ga} + p_{gw} \quad (66)$$

where R is the universal gas constant; M_g the molecular mass of the gas mixture, T is the absolute temperature, p_{ga} is the partial dry air pressure, R_{ga} is the specific gas constant for dry air, and P_g is the absolute gas pressure.

The molecular mass of the gas mixtures M_g satisfies, $\frac{\rho_g}{M_g} = \frac{\rho_{ga}}{M_{ga}} + \frac{\rho_{gw}}{M_{gw}}$ (67)

ρ_g , ρ_{gw} , ρ_{ga} are the densities of the gas, water vapour and dry air, respectively.

To satisfy the conservation of mass for the gas phase, the gas mass conservation equation is written according to Equations 26 and 42 as follows.

$$-\nabla \cdot (\rho_g \mathbf{v}^{gr}) = \rho_g \frac{D[\phi(1-S_l)]}{Dt} + \phi(1-S_l) \frac{D\rho_g}{Dt} + \rho_g \phi(1-S_l) \nabla \cdot \mathbf{v}_s + Q_\pi^{lg} \quad (68)$$

where \mathbf{v}^{gr} is the relative apparent velocity vector of the mixture of dry air and water vapour with respect to the deforming solid, Q_π^{lg} represents an evaporation-condensation term for water mass exchange between the gas and liquid phase (negative for condensation and positive for vapourization), and ρ_g is the gas density, which satisfies

$$\rho_g = \rho_{ga} + \rho_{gw}.$$

The mass averaged advective velocity of the air-vapour mixture (gas) with respect to the moving solid is due to both pressure and temperature gradients. Thus, the relative apparent velocity of the gas can be expressed as:

$$\mathbf{v}^{gr} = \phi(1-S_l) \mathbf{v}_g^r = -\frac{k_{rg} \mathbf{k}}{\mu_g} (\nabla p_g + \rho_g \mathbf{g}) - \mathbf{k}_T^g \nabla T \quad (69)$$

where \mathbf{k} is the intrinsic permeability, μ_g is the viscosity of gas, k_{rg} is the gas relative permeability, ρ_g is the density of gas, \mathbf{g} is the gravitational acceleration vector, and \mathbf{k}_T^g is the coefficient of thermal coupling for gas fluxes.

Since the air-vapour mixture is considered as an ideal gas, its density can be expressed as follows.

$$\rho_g = \frac{P_g M_g}{TR} = \frac{P_g}{R_g T} \quad (70)$$

The derivative of equation 70 allows us to write

$$\frac{1}{\rho_g} d\rho_g = \frac{1}{P_g} dP_g + \frac{1}{T} dT = C_{gp} dP_g + C_{gT} dT \quad (71)$$

in which C_{gp} and C_{gT} represent the coefficients of compressibility and thermal expansion of the gas mixture, respectively.

Neglecting the effect of pressure changes on dynamic viscosity, the dynamic viscosity (μ_g) of the gas mixture is computed by using Sutherland's formula (Crane, 1988):

$$\mu_g = \mu_0 \frac{0.999T_0 + c}{0.999T + c} \left(\frac{T}{T_0} \right)^{1.5} \quad (72)$$

For standard air, $c = 120$ K; $T_0 = 291.15$ K; $\mu_0 = 1.827 \times 10^{-5}$ Pa s, and μ_g is in Pa s.

The thermal coupling coefficient for the gas flux is considered as a linear function of the degree of saturation (Chen et al. 2010)

$$k_T^s = k_{T_0}^s (1 - S_l) \quad (73)$$

where $k_{T_0}^s$ in m^2/sK is the thermal coupling coefficient for gas fluxes in a completely dry state, respectively.

Since dry air is a component of the gas phase, the dissolved air in the water should be taken into account in the gas flow model. Henry's law allows us to determine the volume of air present in the liquid water. Thus, by using Henry's law to take into account the dissolved air in the pore water, according to Equations 26 and 42, the conservation of dry air flow dictates that

$$-\nabla \cdot (\rho_a H \mathbf{v}^r) = \rho_a \frac{D(H\phi S_l)}{Dt} + H\phi S_l \frac{D\rho_a}{Dt} + \rho_a H\phi S_l \nabla \cdot \mathbf{v}_s \quad (74)$$

where H is Henry's coefficient of solubility of gas in liquid defined by Henry's law.

Henry's law determines air concentration as (Sander 2010):

$$M^a H(t) p_n^a = p_i^a \quad (75)$$

where M^a is molar air and H is the solubility of the air (gas) in water and p_n^a is the partial pressure of air in the non-wetting phase. Concentration (C^a) will be defined (mol/m^3) by:

$$C_i^a = H(t) P_g^a = \frac{P_i^a}{M^a} \quad (76)$$

For air, we have $M^a = 2 \text{ g/mol}$ and $H(t) = 20.65 \times 10^{-6} \text{ mol.pa}^{-1} \cdot \text{m}^{-3}$. Taking into account the fact the dry air is mainly made of oxygen and nitrogen, Henry's coefficient of solubility of gas in liquid water can be given by the superposition of solubility of nitrogen and oxygen (Chen et al. 2010):

$$H = \left\{ 8.2115 \times 10^{-5} \exp \left[1700 \left(\frac{1}{T} - \frac{1}{298} \right) \right] + 1.34857 \times 10^{-4} \exp \left[1700 \left(\frac{1}{T} - \frac{1}{298} \right) \right] \right\} (p_g - p_{gw}) \quad (77)$$

where the units of gas pressure p_g and vapour pressure p_{gw} are in MPa, and T is the absolute temperature.

Dry air is considered as an ideal gas ($\rho_{ga} = \frac{P_{ga} M_{ga}}{TR} = \frac{P_{ga}}{R_{ga} T}$) and Dalton's law applies.

Noticing Equation 66 and following the same procedure in Equation 71, we can write:

$$\frac{1}{\rho_{ga}} d\rho_{ga} = \frac{1}{P_{ga}} dP_{ga} + \frac{1}{T} dT = C_{gap} dP_{ga} + C_{gaT} dT \quad (78)$$

in which C_{gap} and C_{gaT} represent the coefficients of compressibility and thermal expansion of the dry gas mixture, respectively.

Thus, the mass conservation equation of the gas is given by the following equation.

$$\begin{aligned}
& \nabla \cdot \left[\rho_g \frac{\mathbf{k}_{rg} \mathbf{k}}{\mu_g} \nabla p_g + \rho_{ga} H \frac{\mathbf{k}_r \mathbf{k}}{\mu_1} (\nabla p_1 + \rho_l \mathbf{g}) + (\rho_g k_T^g + \rho_{ga} H k_T^l) \nabla T \right] = \\
& \phi [\rho_g (1 - S_1) + \rho_{ga} H S_1] \frac{\partial \varepsilon_v}{\partial t} + \phi (\rho_g - \rho_{ga} H) c_{Sp} \frac{\partial p_1}{\partial t} - \rho_{ga} H \phi S_1 c_{gap} \frac{\partial p_{gw}}{\partial t} \\
& + \phi [\rho_g (1 - S_1) c_{gp} + \rho_{ga} H S_1 c_{gap} - (\rho_g - \rho_{ga} H) c_{Sp}] \frac{\partial P_g}{\partial t} \quad (79) \\
& - \phi [\rho_g (1 - S_1) c_{gT} + \rho_{ga} H S_1 c_{gaT} + (\rho_g - \rho_{ga} H) c_{ST}] \frac{\partial T}{\partial t} \\
& + [\rho_g (1 - S_1) + \rho_{ga} H S_1] \frac{\partial \phi}{\partial t} + Q_\pi^lg
\end{aligned}$$

Equation 79 can be rearranged as follows:

$$\begin{aligned}
& \nabla \cdot \left[\rho_g \frac{\mathbf{k}_{rg} \mathbf{k}}{\mu_g} \nabla p_g \right] = \\
& \phi [\rho_g (1 - S_1) + \rho_{ga} H S_1] \frac{\partial \varepsilon_v}{\partial t} + \phi (\rho_g - \rho_{ga} H) c_{Sp} \frac{\partial p_1}{\partial t} - \rho_{ga} H \phi S_1 c_{gap} \frac{\partial p_{gw}}{\partial t} \\
& + \phi [\rho_g (1 - S_1) c_{gp} + \rho_{ga} H S_1 c_{gap} - (\rho_g - \rho_{ga} H) c_{Sp}] \frac{\partial P_g}{\partial t} \\
& - \phi [\rho_g (1 - S_1) c_{gT} + \rho_{ga} H S_1 c_{gaT} + (\rho_g - \rho_{ga} H) c_{ST}] \frac{\partial T}{\partial t} \quad (80) \\
& + [\rho_g (1 - S_1) + \rho_{ga} H S_1] \frac{\partial \phi}{\partial t} + Q_\pi^lg \\
& - \nabla \cdot \left[\rho_{ga} H \frac{\mathbf{k}_r \mathbf{k}}{\mu_1} (\nabla p_1 + \rho_l \mathbf{g}) \right] \\
& - \nabla \cdot [(\rho_g k_T^g + \rho_{ga} H k_T^l) \nabla T]
\end{aligned}$$

4.2.5.2 Additional constitutive relationships and parameters

- Water retention and relative permeability

The gas relative permeability of sedimentary rock (k_{rg}), similarly as for most porous materials, could be described based on the van Genuchten Mualem model as:

$$k_{rg} = (1 - S_1)^{1/2} [1 - S_1^{1/m}]^{2m} \quad (81)$$

Variations in the pore structure could be also caused by damage of the rock. Hence, the effects of damage should be inserted into a Leverett function. This is done in this study by using the Leverett function. The following function is used.

$$p_c = p_{c0}(S_1) \left(\frac{\sqrt[3]{k/\phi^*}}{\sqrt[3]{k_0/\phi_0}} \right) \quad (82)$$

where ϕ^* is the porosity of the damaged rock. This porosity ϕ^* is defined as the sum of the total porosity of the undamaged material ϕ , and damage-induced mechanical porosity ϕ_D due to the opening of micro-cracks.

$$\phi^* = \phi + \phi_D \quad (83)$$

Damage-induced mechanical porosity ϕ_D is obtained by multiplying the scalar damage parameter D by the volume fraction of the skeleton $1 - \phi_0$ (Kuhl et al. 2004). This definition of ϕ_D considers that micro-cracking only occurs within the skeleton material. The micro-cracks located in the rock skeleton can be interpreted according to Kachanov (1958) as micro-pores:

$$\phi_D = (1 - \phi).D \quad (84)$$

Including Equation 84 into Equation 83 yields

$$\phi^* = \phi + (1 - \phi).D \quad (85)$$

where D is the damage scalar, $0 < D \leq 1$.

4.2.5.3 Vapour flow equations

The vapour is transported within the gas phase by non-advective (diffusion due to vapour gradient) and advective fluxes (advection due to the movement of gas). This means that the relative apparent velocity of vapour with respect to the deforming solid \mathbf{v}^{gwr} includes both diffusive velocity of the vapour \mathbf{v}_d^{gw} and the advective velocity \mathbf{v}_a^{gw} of the vapour.

Considering that the diffusive mass flux is governed by Fick's law, the diffusive relative velocity of the vapour can be expressed as:

$$\mathbf{v}_d^{gw} = -\phi S_g \mathbf{D}_{gw} \frac{1}{\rho_{gw}} \nabla \rho_{gw} = -\phi(1 - S_l) \mathbf{D}_{gw} \frac{1}{\rho_{gw}} \nabla \rho_{gw} \quad (86)$$

where \mathbf{D}_{gw} is the tensor of molecular diffusivity of vapour, with units of $\text{m}^2/\text{s Pa}$. \mathbf{D}_{gw} is a function of the tortuosity factor (τ), temperature and pressure. The tortuosity accounts for the tortuous nature of the pathway in sedimentary rock. Indeed, the porous space of a sedimentary rock can have a very complex inner structure, which influences the vapour diffusion process. Therefore, tortuosity should be taken into account in the diffusion process. The tortuosity factor of the porous medium can be approximated by using the formula proposed by Millington and Quirk (1961), i.e.

$$\tau = \phi^{1/3} S_g^{7/3} = \phi^{1/3} (1 - S_l)^{7/3} \quad (87)$$

Furthermore, Daian (1989) proposed the following relationships to express the coupled effects of temperature (T) and gas pressure (P_g) on the diffusivity of vapour in the air.

$$\mathbf{D}_{gw}(T, P_g) = \mathbf{D}_{gw,0} \left(\frac{T}{T_0} \right)^B \frac{P_{g,0}}{P_g} \quad (88)$$

where $\mathbf{D}_{gw,0} = 2.58 \times 10^{-5} [\text{m}^2 \text{s}^{-1}]$ is the diffusion coefficient of vapour species in the air at the reference temperature $T_0 = 273.15 [\text{k}]$ and pressure $P_{g,0} = 101325 [\text{Pa}]$ (Forsyth and Simpson, 1991), and B is a constant that has to be experimentally determined. In this study, a value of $B = 1.667$ (Dain, 1989) is used.

Since the vapour is considered as an ideal gas, thus, similar to Equation 63, we can write that:

$$\frac{1}{\rho_{gw}} d\rho_{gw} = \frac{1}{P_{gw}} dP_{gw} + \frac{1}{T} dT = C_{gwp} dP_{ga} + C_{gwT} dT \quad (89)$$

in which C_{gwp} and C_{gwT} represent the coefficients of compressibility and thermal expansion of the vapour, respectively.

Substituting Equations 34, 51, 52, 65 and 70 into an equation of the conservation of water vapour mass (Equation 90), the vapour flow in the sedimentary rock of the DGR is given by Equation 91.

The equation of the conservation of water vapour mass

$$-\nabla \cdot (\rho_g v^{gwr}) = \rho_{gw} \frac{D[\phi(1-S_l)]}{Dt} + \phi(1-S_l) \frac{D\rho_{gw}}{Dt} + \rho_g \phi(1-S_l) \nabla \cdot v_s + Q_\pi^{lg} \quad (90)$$

the vapour flow in the sedimentary rock of the DGR

$$\begin{aligned} & \nabla \cdot \left[\rho_g \frac{\mathbf{k}_{rg} \mathbf{k}}{\mu_g} \nabla p_g \right] = \\ & \phi \rho_{gw} (1-S_l) \frac{\partial \varepsilon_v}{\partial t} + \phi \rho_{gw} c_{Sp} \frac{\partial p_l}{\partial t} - \phi \rho_{gw} c_{Sp} \frac{\partial P_g}{\partial t} + \phi \rho_{gw} (1-S_l) c_{gwp} \frac{\partial P_{gw}}{\partial t} \\ & - \phi \rho_{gw} [(1-S_l) c_{gwT} + c_{ST}] \frac{\partial T}{\partial t} \\ & + \rho_{gw} (1-S_l) \frac{\partial \phi}{\partial t} + Q_\pi^{lg} \\ & - \nabla \cdot [\rho_{gw} \phi (1-S_l) C_{gwp} \mathbf{D}_{gw} \nabla p_{gw}] \\ & - \nabla \cdot [\rho_{gw} (\mathbf{k}_T^g - \phi(1-S_l) C_{gwT} \mathbf{D}_{gw}) \nabla T] \end{aligned} \quad (91)$$

4.2.6 Heat transport

The approach proposed by Tong et al. (2010) is adopted in this section. Given any spatial volume V , the time rate of change of the total internal energy of phase π in volume V must be equal to the heat flux of that phase across the boundary Γ_v of volume V , plus the heat source Q_T^π and the energy supply $\hat{\epsilon}^\pi$ to the π phase due to the interactions with the other phases (Tong et al. 2010).

The energy conservation can then be expressed as (Tong et al. 2010)

$$\frac{d}{dt} \int (\rho^\pi c_\pi T_\pi) dV = - \int_{\Gamma_v} \mathbf{q}^\pi \cdot \mathbf{n} dS + \int_v Q_T^\pi dV + \int_v \hat{\epsilon}^\pi dV \quad (92)$$

In a differential form, this relation can be written as

$$D_t \cdot (\rho^\pi c_\pi T_\pi) = -\nabla \cdot \mathbf{q}^\pi + Q_T^\pi + \hat{\epsilon}^\pi \quad (93)$$

Assuming that the solid, liquid and gas phase temperatures are in local thermal equilibrium, the combination of the energy balance and constitutive equations results in the following final heat transport equation (the details of the steps of the development are given in Tang (2010)):

$$\begin{aligned} & \nabla \cdot \left[\boldsymbol{\sigma} \frac{\partial \mathbf{u}}{\partial t} + \rho_g \frac{\mathbf{k}_{rg} \mathbf{k}}{\mu_g} \nabla P_g + \rho_l \frac{\mathbf{k}_{rl} \mathbf{k}}{\mu_l} (\nabla p_l + \rho_l \mathbf{g}) + (\lambda + \rho_g \mathbf{k}_T^g + \rho_l \mathbf{k}_T^l) \nabla T \right] = \\ & - \rho_g \frac{\partial \mathbf{u}}{\partial t} + \left[(1-\phi) \rho_s C_s + \phi S_l \rho_l C_l + \rho_g \phi (1-S_l) C_g \right] \frac{\partial T}{\partial t} \\ & - \left[\mathbf{v}^{lr} - c_{sp} \left(\frac{1}{S_l} P_l \mathbf{v}^{lr} - \frac{1}{1-S_l} P_g \mathbf{v}^{gr} \right) \right] \cdot \nabla P_l \\ & - \left[\mathbf{v}^{gr} - c_{sp} \left(\frac{1}{S_l} P_l \mathbf{v}^{lr} - \frac{1}{1-S_l} P_g \mathbf{v}^{gr} \right) \right] \cdot \nabla P_g - \frac{1}{\phi} (P_l \mathbf{v}^{lr} - P_g \mathbf{v}^{gr}) \cdot \nabla \phi + L Q_\pi^{lg} \\ & + \left[\rho_l C_l \mathbf{v}^{lr} + \rho_g C_g \mathbf{v}^{gr} - c_{ST} \left(\frac{1}{S_l} P_l \mathbf{v}^{lr} - \frac{1}{1-S_l} P_g \mathbf{v}^{gr} \right) \right] \cdot \nabla T \end{aligned} \quad (94)$$

where λ is the thermal conductivity of the sedimentary rock, C_π is the specific heat capacity of the phase (solid, liquid, gas), and L is the latent heat of vapourization.

The following relationship is used to describe the variation of the thermal conductivity with water saturation degree and porosity (Tong 2009).

$$\lambda = \lambda_{dry} \left[1 + 4 \frac{\phi S_l \rho_l}{(1-\phi)\rho_s} \right] \quad (95)$$

The equation 95 can be rearranged as follows:

$$\begin{aligned} & \nabla \cdot \left[\boldsymbol{\sigma} \frac{\partial \mathbf{u}}{\partial t} \right] = \\ & - \rho \mathbf{g} \frac{\partial \mathbf{u}}{\partial t} + \left[(1-\phi)\rho_s C_s + \phi S_l \rho_l C_l + \rho_g \phi (1-S_l) C_g \right] \frac{\partial T}{\partial t} \\ & - \left[\mathbf{v}^{lr} - c_{Sp} \left(\frac{1}{S_l} P_l \mathbf{v}^{lr} - \frac{1}{1-S_l} P_g \mathbf{v}^{gr} \right) \right] \bullet \\ & \nabla P_l - \left[\mathbf{v}^{gr} - c_{Sp} \left(\frac{1}{S_l} P_l \mathbf{v}^{lr} - \frac{1}{1-S_l} P_g \mathbf{v}^{gr} \right) \right] \bullet \\ & \nabla P_g - \frac{1}{\phi} (P_l \mathbf{v}^{lr} - P_g \mathbf{v}^{gr}) \bullet \nabla \phi + LQ_{\pi}^{lg} \\ & + \left[\rho_l C_l \mathbf{v}^{lr} + \rho_g C_g \mathbf{v}^{gr} - c_{ST} \left(\frac{1}{S_l} P_l \mathbf{v}^{lr} - \frac{1}{1-S_l} P_g \mathbf{v}^{gr} \right) \right] \bullet \nabla T \\ & - \nabla \cdot \left[\rho_g \frac{\mathbf{k}_{rg} \mathbf{k}}{\mu_g} \nabla p_g \right] \\ & - \nabla \cdot \left[\rho_l \frac{\mathbf{k}_{rl} \mathbf{k}}{\mu_l} (\nabla p_l + \rho_l \mathbf{g}) \right] \\ & - \nabla \cdot \left[(\lambda + \rho_g \mathbf{k}_T^g + \rho_l \mathbf{k}_T^l) \nabla T \right] \end{aligned}$$

4.3 Simulation of laboratory and field experiments

4.3.1 Introduction

The objective of the present section is to verify the capability of the developed mathematical model to predict and analyze gas migration in sedimentary host rocks of a DGR.

To achieve the aforementioned objective, two main stages are carried out:

- the first stage is the simulation of laboratory gas injection tests
- the second stage is the simulation of the field tests.

The main results of the simulations are presented below. It should be emphasized that all laboratory and field tests were performed at isothermal and constant temperature conditions. Thus, the non-isothermal thermal effect is not considered in the validation.

4.3.2 Simulation of laboratory tests

4.3.2.1 Comparison of numerical and experimental results

To provide confidence in the developed model for gas migration in DGR two sets of experimental results from laboratory scale gas injection tests on Opalinus clay were used. Triaxial loading and strength tests were performed in a standard Kármán-cell in a servo-hydraulic testing machine (RBA2500, Schenk/Trebel Germany – using MTS-TestStar software) which allowed for independent control of the radial ($\sigma_2 = \sigma_3$) and axial stresses (σ_{Ax}) (Figure 4.2). In addition, by using special developed piston sets, acoustic velocities (V_p and V_s) and gas-permeability were measured parallel to the sample cylinder axis (dimensions: 80 mm in diameter and 160 mm in length). As a standard procedure, the sample volume changes ΔV were determined by a volume balance of the mantle oil volume changes as measured via a pressure intensifier and the axial piston displacement in the cell. The details of the experimental set up and program are available in elsewhere (e.g., Popp and Salzer 2007).

- The first set of results (Set # 1) used come from the gas injection tests on Opalinus clay with constant confinement pressure (Figure 4.3).

- The second set results (Set # 2) used come from the gas injection tests on Opalinus clay with increased confinement pressure (Figure 4.4).

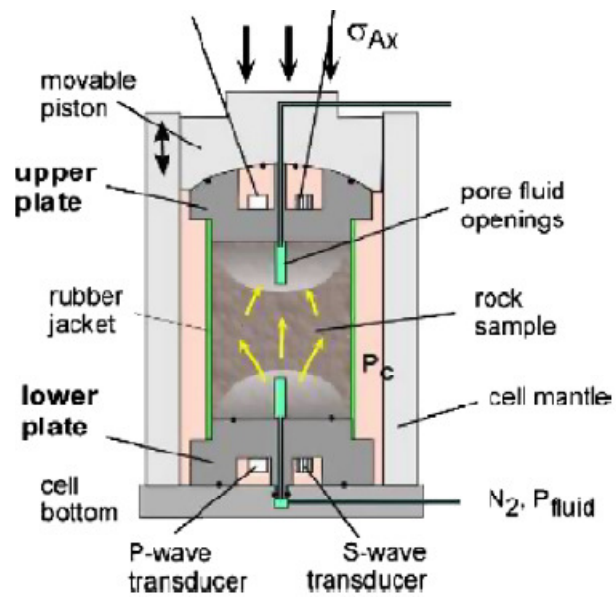


Figure 4.2. High-pressure triaxial cell used for the gas injection tests (Popp and Salzer 2007).

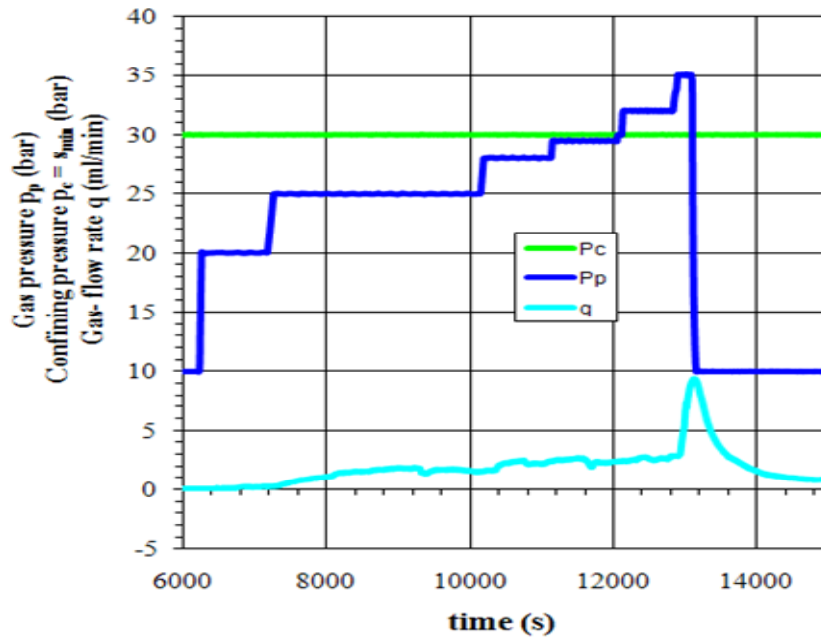


Figure 4.3. Gas injection pressure versus Time (p_p) and constant confinement pressure (p_c) vs out-flow rate variation (q)

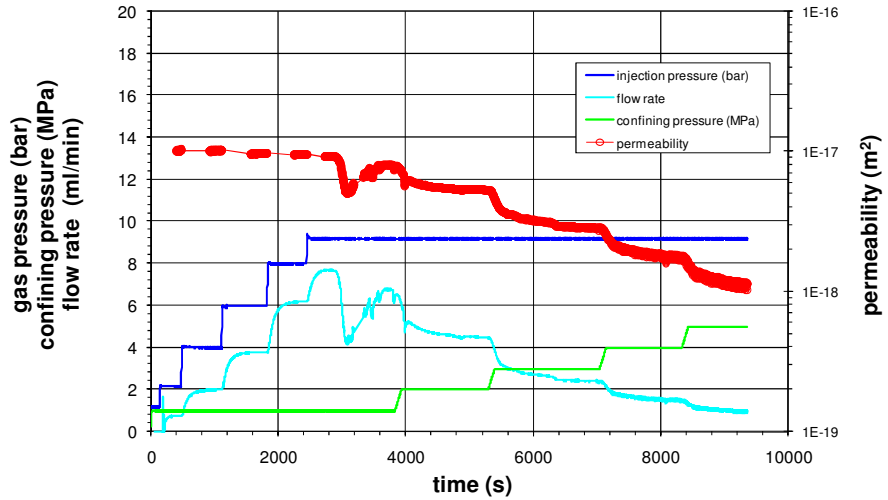


Figure 4.4. Gas injection Pressure Versus Time (p_p) and evolutive confinement pressure (p_c) vs out-flow rate (q)

4.3.2.1 Gas injection tests with constant confinement pressure

Hydrostatic loading was performed with constant confinement pressure $p_c = 3$ MPa and gas pressure was increased as a step-wise function (Figure 3.34). The values of the main parameters used for modeling the gas injection with constant confinement pressure (Set # 1) are given in Table 4.1 and Topp and Salzer (2007). It should be emphasized that several values of α (1 - 0.0016), were considered in the modeling to study the sensitivity of the model response to the value of α . It was found that the value of α (between 1 and 0.0016) doesn't have a significant effect on the model response. Thus, $\alpha = 0.1$ was selected for the numerical simulation in order to achieve a better numerical stability. The boundaries conditions used are described in Figures 4.5 and 4.7. The comparison between simulated and experimental results is presented in Figure 4.8. From this Figure 4.8, it can be seen that there is a good agreement between the predicted and experimental results providing confidence in the ability of the developed model to predict the gas migration.

Table 4.1. Material properties for the validation model (constant confinement pressure)

Parameters	Value
Initial permeability (m^2)	9.5×10^{-19}
k_{max} Permeability (at damage max. $D_{kmax}=0.3$) (m^2)	2.75×10^{-18}
Initial porosity	0.16
Initial saturation (%)	90
Residual saturation (%)	0
Modulus of elasticity (GPa)	10
Poisson ratio	0.27
van Genuchten's parameters	
L	1
M	0.5
α (1/m)	0.1
Damage equation parameters	
Strain ϵ_t	0.9×10^{-4}
Residual tensile strength (MPa)	0.8
Strain ϵ_{co}	7.2×10^{-4}
Friction angle ($^\circ$)	24
Cohesion (MPa)	7

f_c is the uniaxial compressive strength	12
f_{cr} is the residual compressive strength.	3.0
f_t represents the tensile strength	2.5
Permeability vs Porosity fitting constant (A)	200

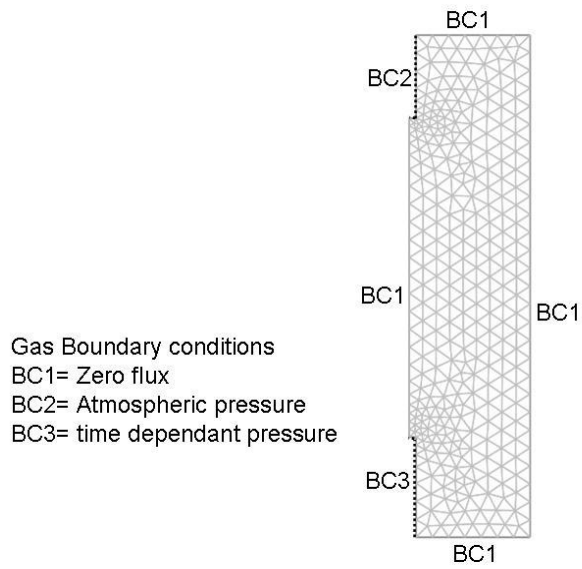


Figure 4.6. Gas boundary conditions

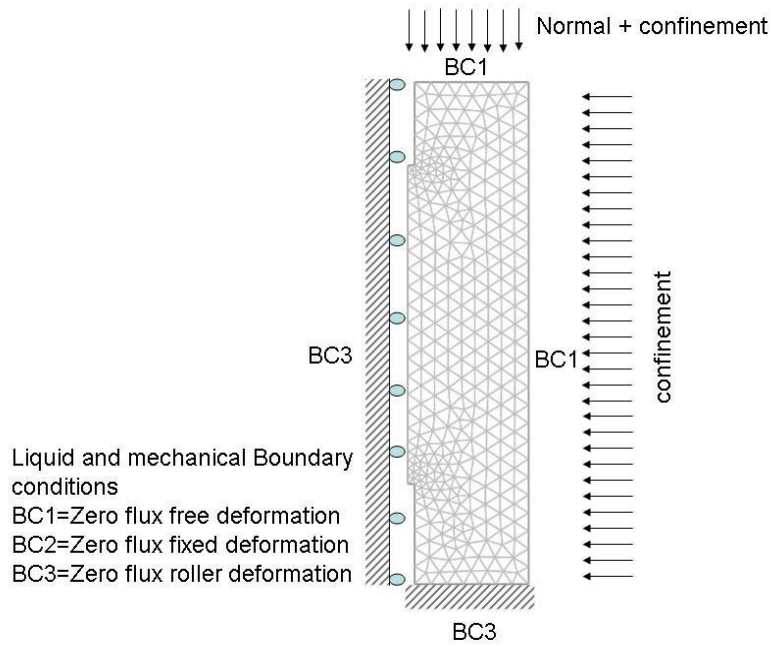


Figure 4.7. Liquid and gas boundary conditions

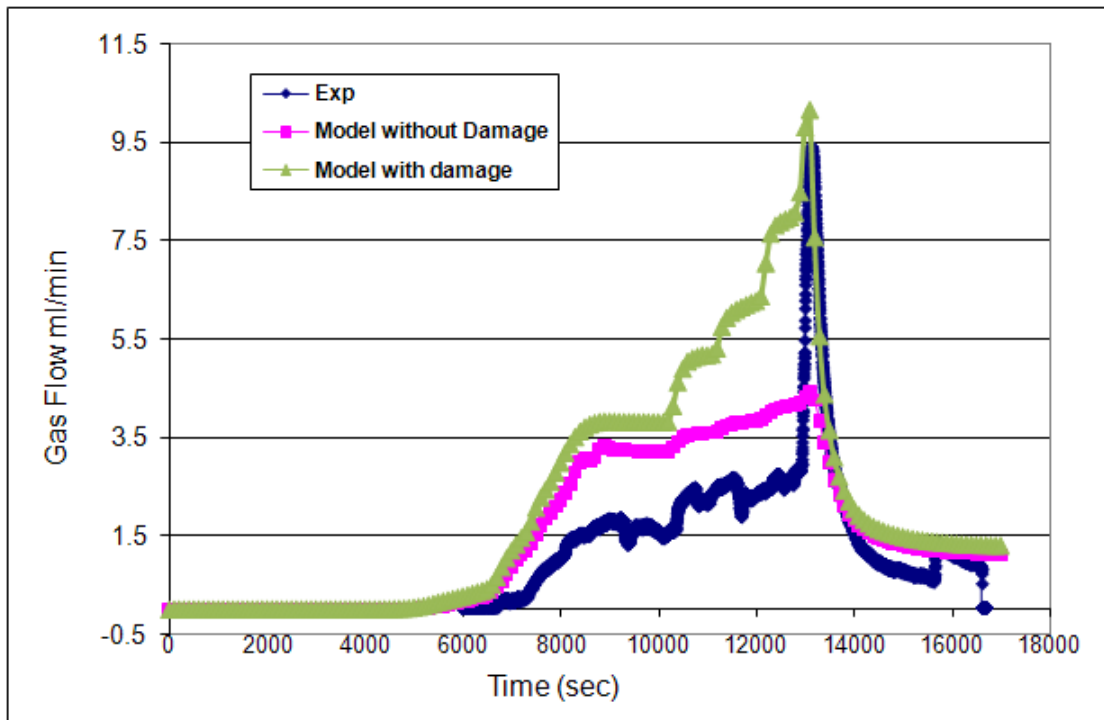


Figure 4.8. Comparison between the predicted and experimental gas flow rate (constant confinement pressure)

4.3.2.2 Gas injection tests with increased confinement pressure

The validation results are presented in Figure 4.9. From this figure, again, it can be observed that the developed model can accurately predict the gas migration under increased confinement pressure.

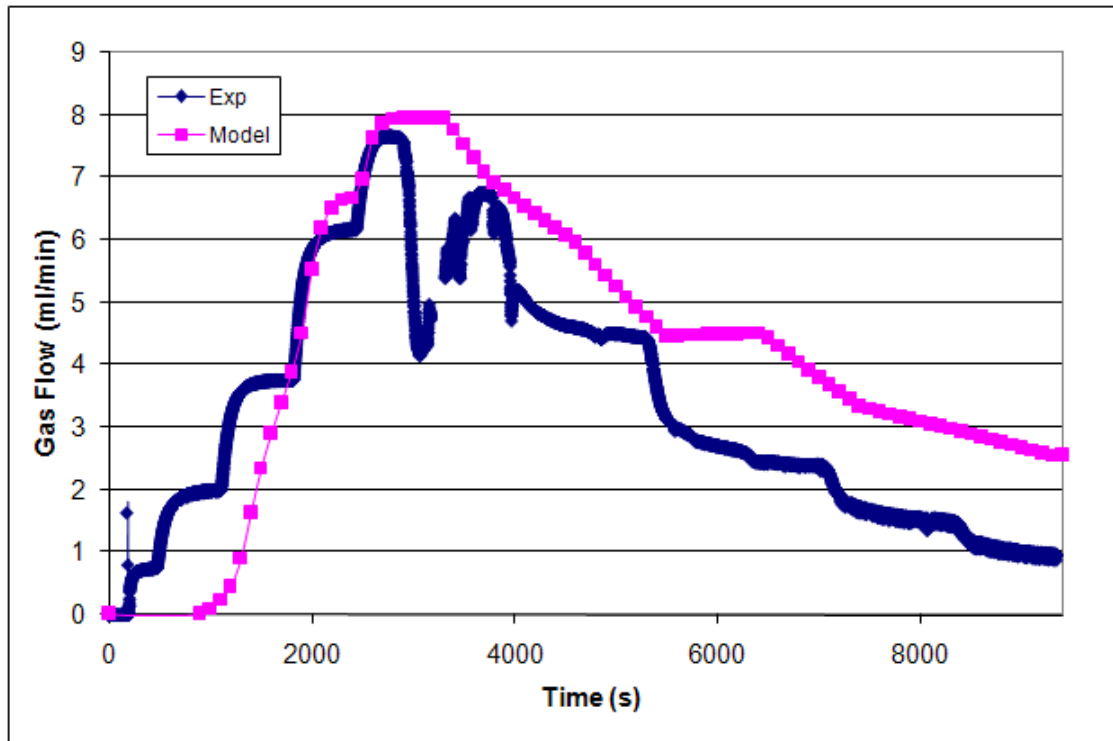


Figure 4.9. Comparison between the predicted and experimental gas flow rate (increased confinement pressure)

4.3.2.2 Other results from the simulation of laboratory gas injection tests

In this section other results from the numerical simulation of the laboratory gas injection tests (presented in the section 4.3.2.1) are presented in order to illustrate the key physical processes that would help understand the nature of the gas flow through Opalinus Clay. The physical conditions to which the sample is subjected (pressures applied by the injection and recovery systems, confinement pressure) have been reproduced in the model. The conceptual model, boundary and initial conditions adopted are already explained in the previous sections. The main results of the simulations are presented in

Figures 4.10, 4.11 and 4.12. Figure 4.10 shows the computed evolution of the spatial distribution of the gas pressure within the Opalinus clay sample. It can be seen from this figure that a maximum gas pressure of around 3.5 MPa is reached at the injection point, when the maximum gas flow rate is achieved; furthermore, over 60% of the sample shows a gas pressure higher than 2.5 MPa. Figure 4.11 and 4.12 illustrate the simulated evolution of the spatial distribution of the rock damage and permeability, respectively. Figure 4.11 graphically demonstrates that high gas pressures can result in the damage of the sedimentary rock. This damage changes the rock permeability (Figure 4.10). However, from Figure 4.12 (2) it can be noticed that the volumetric deformation can also affect the rock permeability.

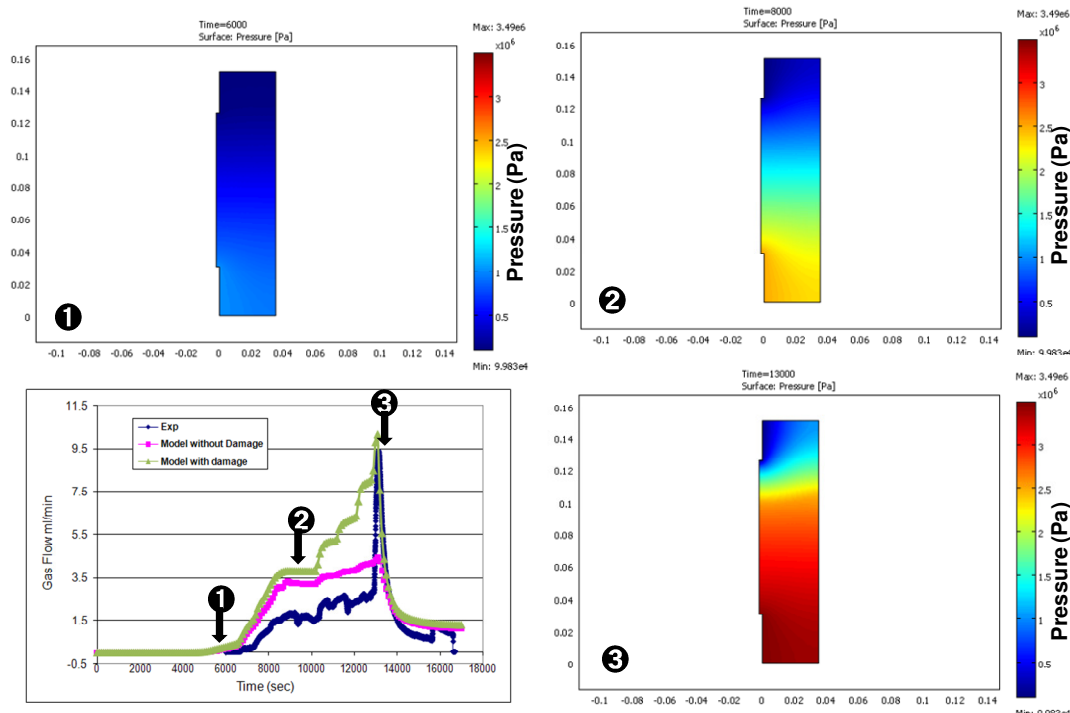


Figure 4.10. Simulated evolution of the spatial distribution of the gas pressure

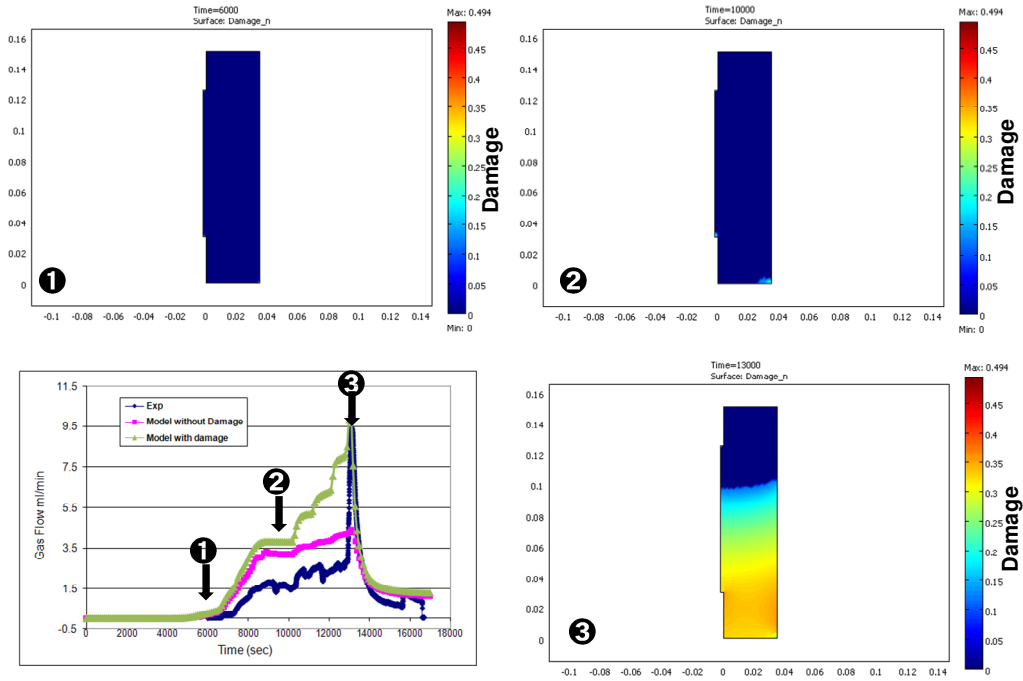


Figure 4.11. Computed evolution of the spatial distribution of the rock damage induced by gas pressure

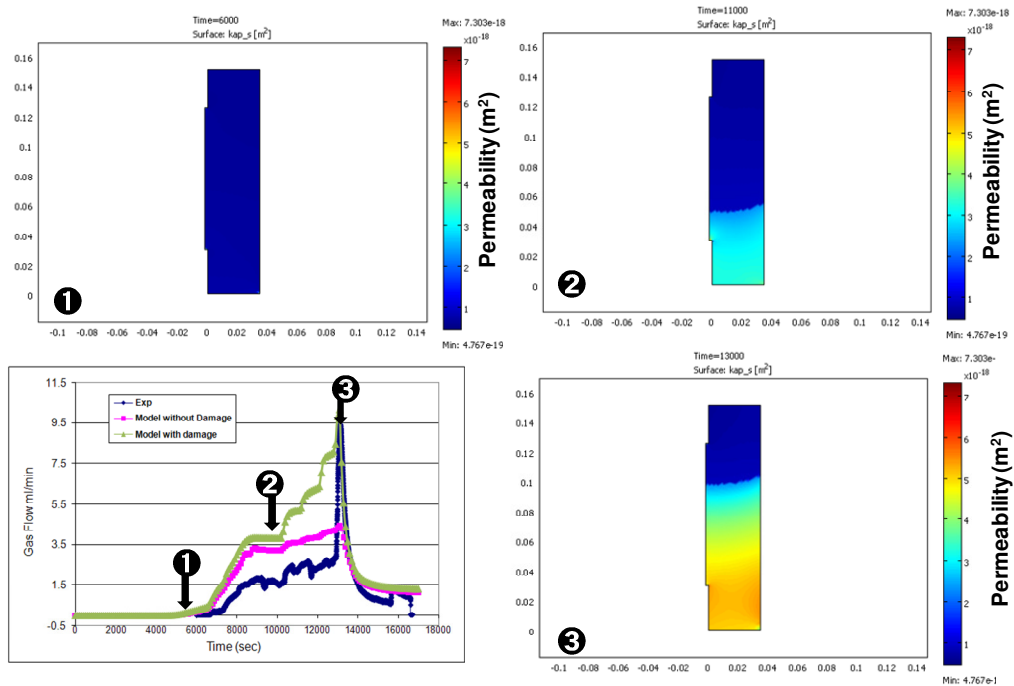


Figure 4.12. Computed evolution of the spatial distribution of the rock permeability

4.3.3 Simulation of field tests

4.3.3.1 Comparison of numerical and simulated results

The model was used to simulate field gas injection tests on Opalinus clay performed at the Mont Terri Underground laboratory in Switzerland. Figure 4.13 shows a schematic presentation of those field tests. Four boreholes were used for hydraulic testing and seismic monitoring. The boreholes were perpendicular to the bedding plane. The fluid would therefore preferentially flow in a direction parallel to the bedding with relative high permeability (Figure 4.13). The length of the boreholes was about 10m. The gas was injected in a 1-m isolated section at the end of the central borehole BHG-B9 (9 - 10m). Three series of gas injection tests were carried out in the test interval. Each series consisted of a couple of tests with stepwise increasing of gas injection pressure. The gas used was nitrogen. The details about the gas injection tests and the in-situ geomechanical conditions are given in Hua and Kristof (2009).

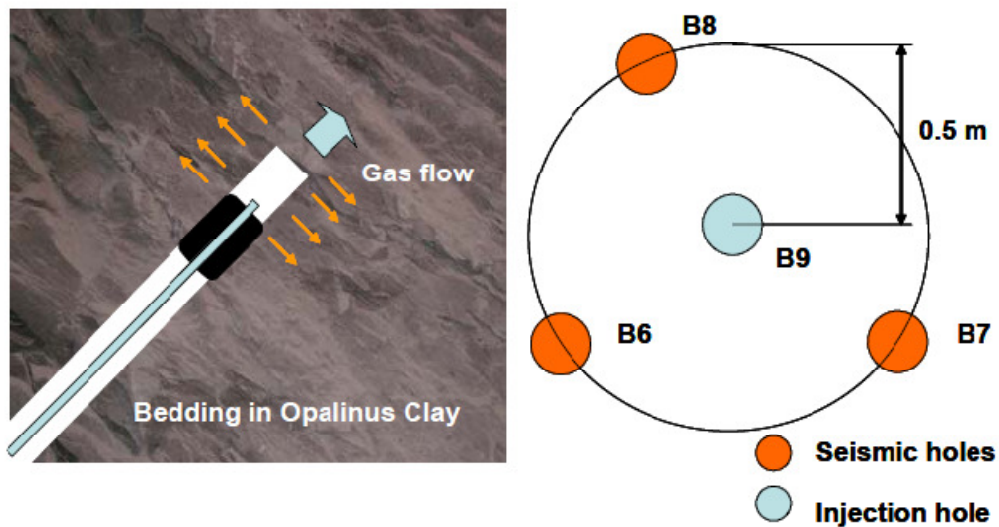


Figure 4.13 Schematic presentation of field gas injection test carried out in the Underground laboratory Mont Terri (Source: Hua and Kristof, 2009)

In order to simulate the in-situ test, a rectangle with 5 m edge length is defined. The borehole has a diameter of 86 mm. Figure 4.14 shows the graphical description of the conceptual model with the defined boundary conditions. A special code was developed to

apply the gas boundary conditions. The gas test was carried out in the last meter section of the borehole. The initial saturation degree of the rock is 100%. The material properties used are shown in Table 4.2. It should be emphasized that several values of α (1 - 0.0016), were considered to study the sensitivity of the model response to the value of α . It was found that the value of α (between 1 and 0.0016) doesn't have a significant effect on the model response.

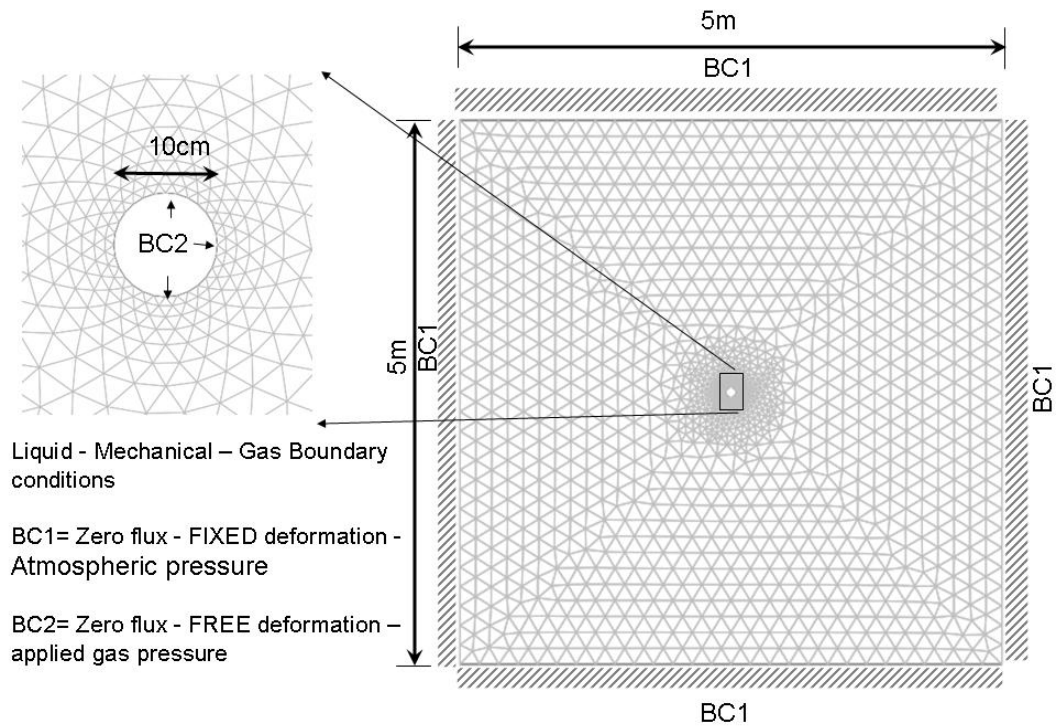


Figure 4.14: Two dimensional model mesh

Table 4.2. Material properties used

Parameter	unit	value
porosity	[-]	0.12
permeability	[m ²]	1e-20
k _{max} Permeability (at damage max. D _{kmax} =0.3) (m ²)	[m ²]	2xe-18
Initial saturation	%	100
residual water saturation	[-]	0
residual gas saturation	[-]	0
Young's modulus	[GPa]	11.4
Poisson ratio	[-]	0.27
friction	[°]	24.5
cohesion	[MPa]	8.6
tensile strength	[MPa]	2.5
Residual tensile strength	[MPa]	0.8
Strain ϵ_{t0}	-	0.9x10 ⁻⁴
Van Genuchten's parameters; L = 1; M = 0.5; α : 0.1		
f_c is the uniaxial compressive strength	[MPa]	12
f_{cr} is the residual compressive strength	[MPa]	3.0
Strain ϵ_{co}		7.2 x10 ⁻⁴
Permeability vs Porosity fitting constant (A)		200

Figure 4.15 shows that there is good agreement between the results from the HM-model (with damage) and the experimental gas pressure values. Figure 4.15 shows that the mechanical component of the gas transport model cannot be neglected. Indeed, it can be noticed that, at high gas pressure there is a discrepancy between the predicted (by considering only the flow of gas) and the experimental results. This would imply the prediction of gas migration from a DGR in sedimentary rock should not be based on two-phase flow modelling approach when the gas pressure is high. In such a case, the mechanical response of the rocks has significant impact on the gas transport.

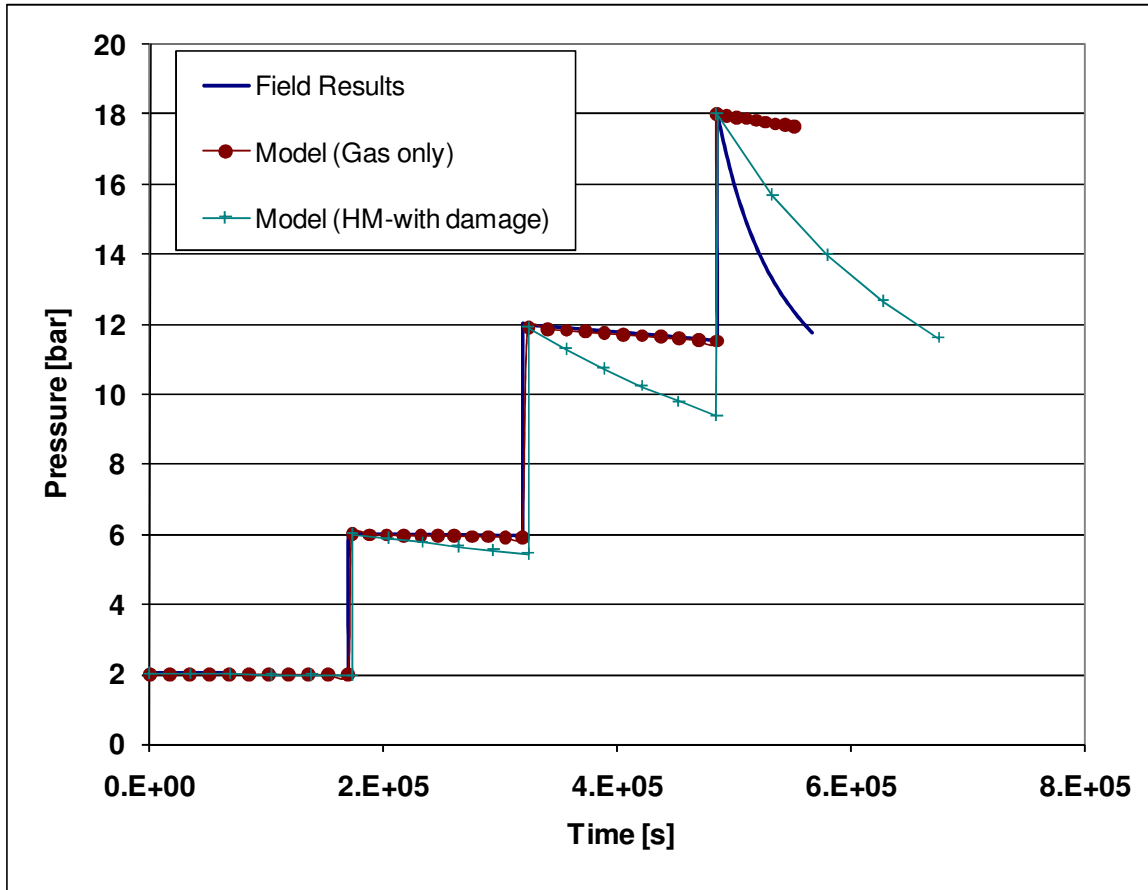


Figure 4.15. Comparison between the predicted and measure gas pressure

4.3.3.2 Other simulated results of the field gas injection tests

Figure 4.16 presents the evolution of the spatial distribution of the gas pressure within the rockmass, whereas Figure 4.17 illustrates the computed evolution of the water flow velocity (arrow) and water pressure within the rockmass. These figures show that with increased gas pressure the gas front migrates into the rockmass. However, the maximum gas pressure remained concentrated on the injection point. From Figure 4.16, it can be seen that a maximal gas pressure is reached at the injection zone and just before the gas breakthrough (point ③, Figure 4.18). It can be also noted that after the gas breakthrough, the gas pressure (Figure 4.16) and flow velocity (Figure 4.17) decrease. This can be attributed to the openings and propagation of cracks within the rock (mechanical damage). This explanation is in agreement with the simulation results presented in Figure

4.18. This figure illustrates the spatial and temporal evolution of the mechanical damage of the rockmass. It can be observed that a significant mechanical damage of the rock occurs just before the gas breakthrough (point ③) and the maximum damage is concentrated on the areas surrounding the gas injection point.

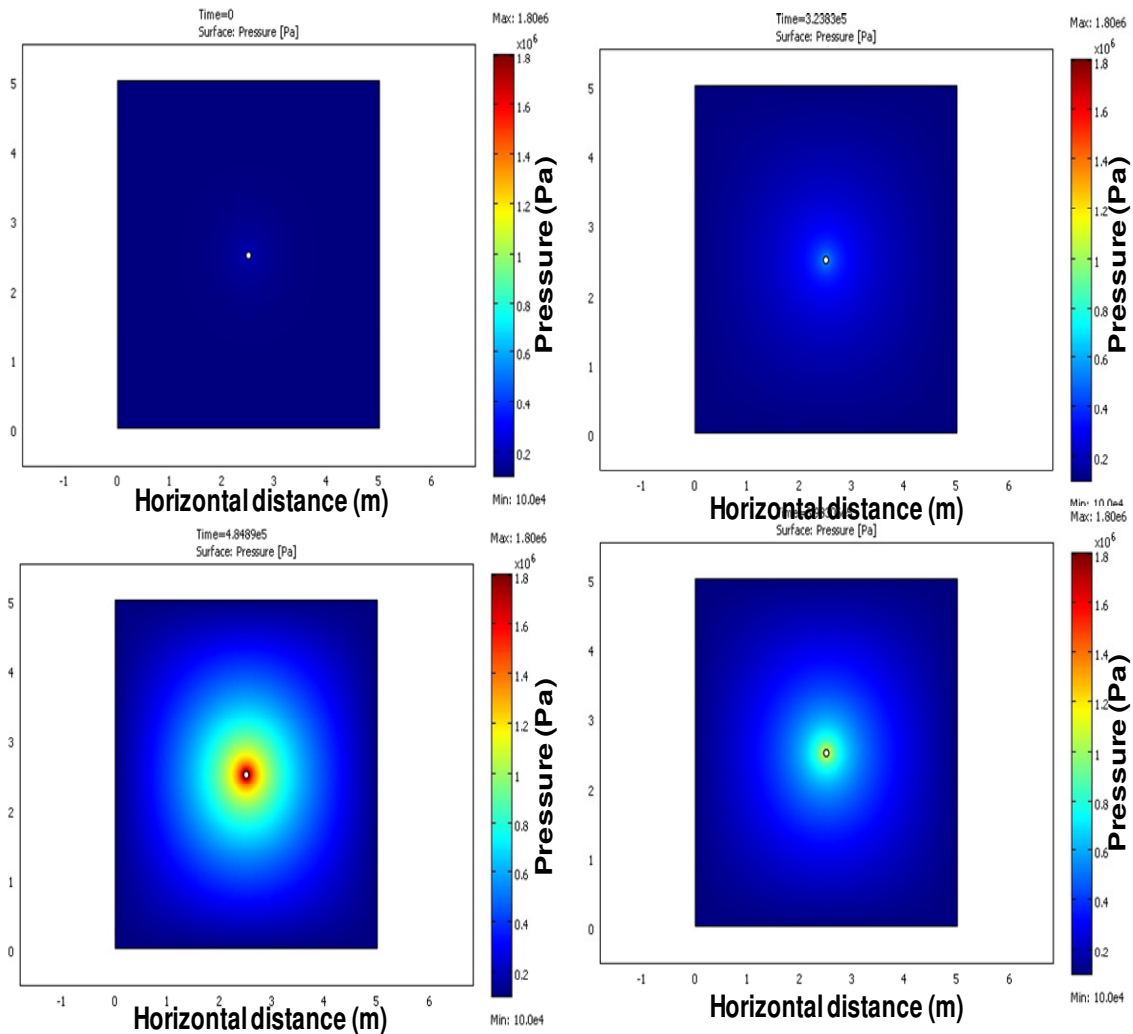


Figure 4.16. Simulated evolution of the spatial distribution of the gas pressure within the rockmass

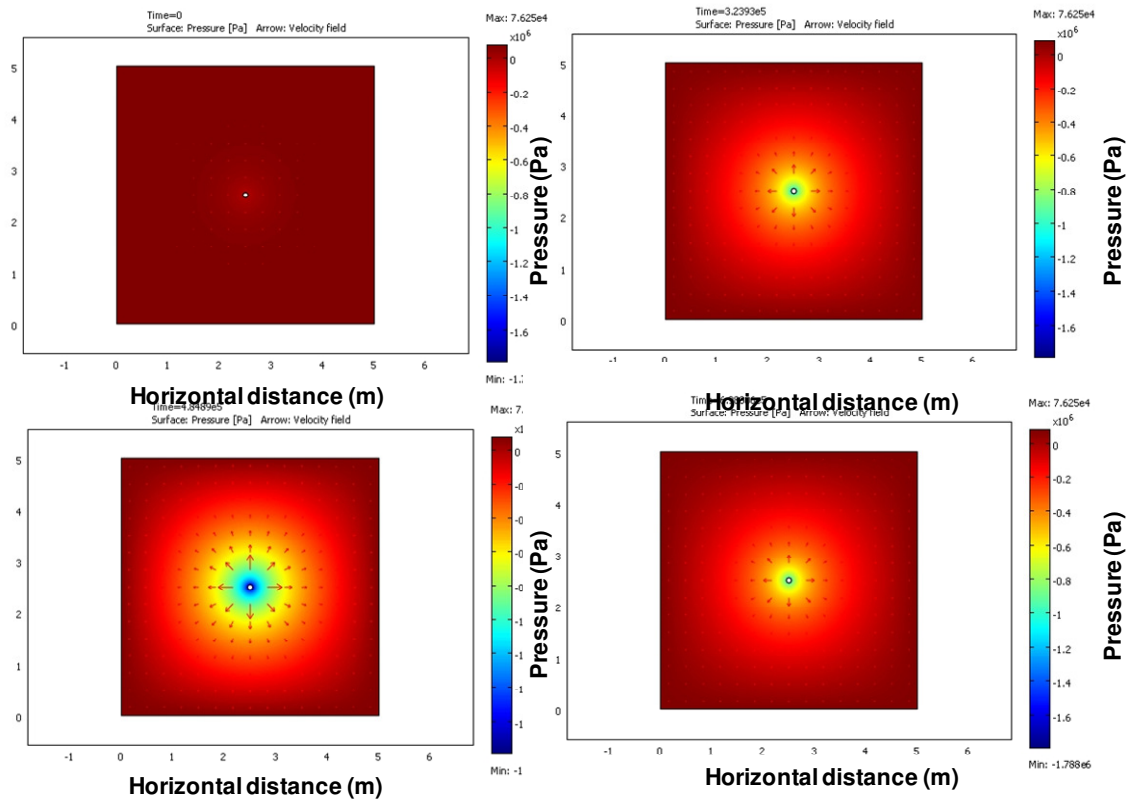


Figure 4.17. Computed evolution of water flow velocity (arrow) and water pressure within the rockmass

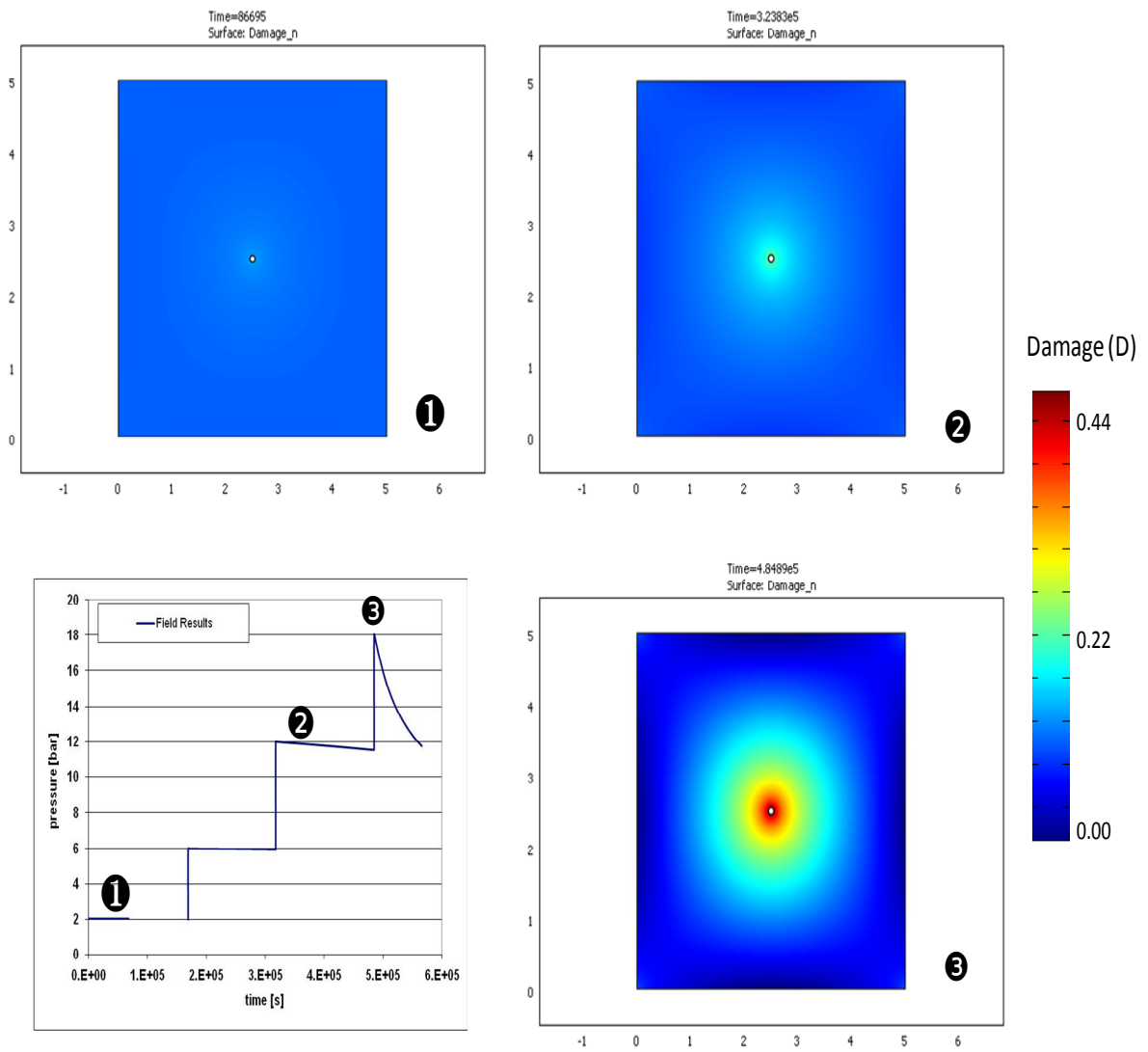


Figure 4.18. Evolution of the spatial distribution of the rock damage induced by gas pressure

4.4 Conclusion

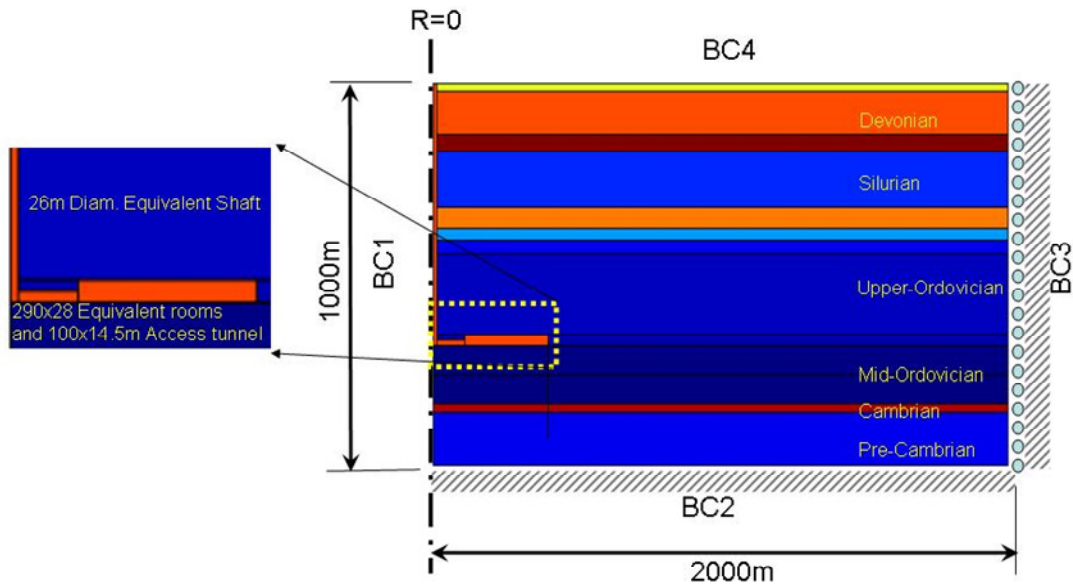
The objective of the present chapter is to develop and validate constitutive and mathematical models to predict and analyze gas migration from the repository and determine the disturbances of sedimentary rocks induced by gas migration. Based on the results obtained in this report, the following conclusions can be drawn:

- A coupled THM model for predicting and analysing gas migration in sedimentary rock is developed;
- A detailed formulation coupling heat, moisture (liquid water and water vapour) and gas transfer in a deformable porous medium is given;
- The mechanical response of the rock is described by non-isothermal poro-elastic-damage model;
- The model takes into account mechanical damage-controlled gas flow as well as coupling of two-phase flow and mechanical stresses;
- The presented model also considers the modification of capillary pressure due to the variation of the pore structure of the sedimentary rock. This variation can result from rock deformation and/or mechanical damage;
- The prediction ability of the developed model is tested against results from laboratory and field scale experiments performed on sedimentary rocks (Opalinus Clay) from European underground research laboratory (Switzerland). Good agreement between model predictions and laboratory experimental results was obtained. This provides confidence in the use of the developed model for scoping analyses of gas migration for the proposed DGR for LILW in Ontario in sedimentary formations of the Michigan Basin .
- The results of the numerical simulation on laboratory and field gas injection tests performed on Opalinus Clay provide valuable information for a better understanding of the main physical processes governing gas migration in a sedimentary rock and its effect on the integrity of the rock.

5 Numerical simulations of gas injection tests and gas migration from in DGR in Ontario's sedimentary rocks

5.1 Model conceptualization, initial and boundary conditions

The numerical model is shown in Figure 5.1. An equivalent shaft area with a radius of 13m including the EDZ effects is used to model the two shafts proposed in the OPG's design. Axi-symmetric conditions are assumed with the axis of symmetry centred along the equivalent shaft. Furthermore, it is assumed that the gas generated will also accumulate in the access tunnel and will reach its maximum pressure in the tunnel. From the perspective of gas modelling, this is conservative as the large space or void of the tunnel would reduce the gas pressure originated from the chambers. Thus, the obtained results will be on the safe side from an engineering point of view. The selected initial and boundary conditions are shown in Figure 5.1. The initial hydraulic (water) conditions are set as linear hydrostatic, and at the same time, the self-weight of the rock formations is assumed to be based on a rock density of 2500 kg/m^3 for the initial mechanical stresses. The initial horizontal stresses are estimated to be equal to the elastic horizontal stresses. Two cases are considered with regards to the gas pressure applied in the tunnel, as shown in Figure 5.2. In the first case, the peak repository gas pressure is in the range of 7 to 8 MPa. In the second case, a peak repository gas pressure of 15 MPa is considered. The geotechnical and hydrogeological rock material properties used as input data are obtained from NMWO (2011). Table 5.1 to 5.3 show some typical examples of rock material properties used for the numerical simulation. It should be stressed that various values of α (0.1 to 0.0015) were considered in the modeling study. The selected value of α did not have significant effect on the model response. The initial hydraulic and mechanical properties of the shafts and their associated EDZ are also obtained from NWMO (2011e); and assumed to be equivalent to one material for the sake of simplicity. Two cases are considered with regards to the properties of the shaft: (i) a normal case and (ii) a failed shaft case where the material properties (e.g., permeability, porosity) are deteriorated. The main properties of the shaft for the failed shaft case are summarized in Table 5.3.



Fluid – Mechanical Boundary conditions

BC1 = Axi-symmetric axis

BC2 = Zero flux –fixed deformation

BC3 = Zero flux – Roller

BC4 = Zero pressure – free deformation – atmospheric pressure

BC 4 for liquid is zero, for gas is zero; BC1 for liquid is axi-symmetric, for gas is axi-symmetric; BC 2 and 3 for liquid is zero flux, for gas is zero flux

Figure 5.1. Conceptual numerical model and boundary conditions (the gas initial pressure is zero; the water initial pressure is hydrostatic pressure)

Peak Pressure
Value 8.2×10^6 Pa
Time 1.0×10^6 a

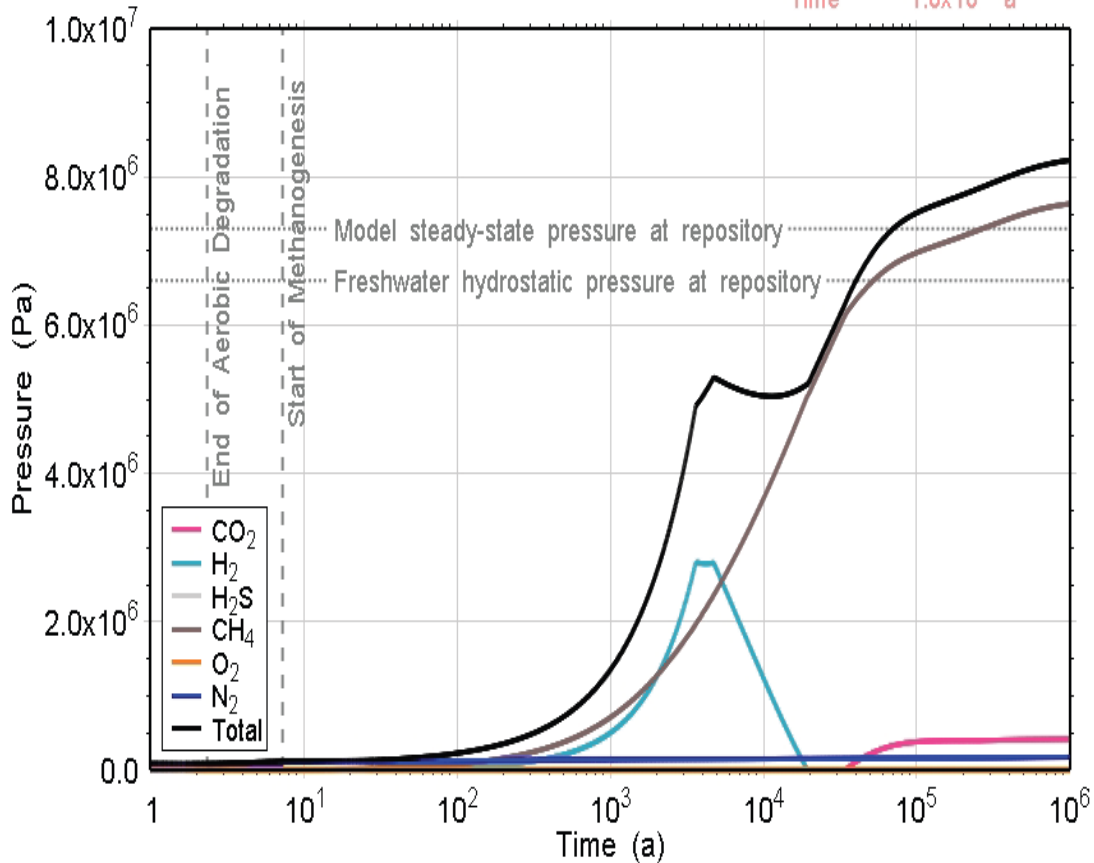


Figure 5.2. Total gas pressure in the repository (Source NWMO 2011)

5.2 Simulation results

Several numerical simulation results have been obtained. Key samples of results are presented in the present report. The main simulation results with regards to the normal case (Peak gas pressure = 8 MPa, shaft not failed) are presented in Figures 5.3-5.4. Figure 5.3 illustrates the spatial distribution and temporal evolution of the gas pressure in the DGR repository and host rock. Figure 5.4 shows the spatial distribution of the gas pressure and gas flow velocity in the study area after 0 year, 400,000, 600,000 and 1,000,000 years, respectively. It should be recalled that over the 1 Ma period, the peak repository gas pressure is approximately 8 MPa, converging towards or somewhat higher than the steady-state hydrostatic water pressure at the repository horizon of around 7 MPa, and much less than the lithostatic pressure of 17 MPa (NWMO, 2011). According

to Figure 5.3 the gas pressure increases with time to reach approximately a maximum value of 8 MPa in the tunnel and 5-6 MPa in the surrounding near-field after 1,000,000 years. Gas pressure in the tunnels exceeds the hydrostatic formation pressure. The high gas pressure is contained in the natural shale barrier layer. Furthermore, for all of the cases the maximum gas pressure in the surrounding near-field is below the lithostatic pressure, suggesting that no tensile fractures would develop in the host rock. This is positive with regards to the safety of the DGR. Figure 5.4 shows two patterns of gas flow in the host rock: (i) one vertical pattern (upward or downward) in the rock formations with lower permeability; (ii) another horizontal pattern in the rock formations with higher permeability (e.g., Salina formation). In the shaft, the gas flow is vertical. From Figure 5.4, it can be seen that, up to 600,000 years after the closure of the repository, the high gas pressure and gas migration is still contained in the natural shale barrier layer. This suggests that the limestone and shale formations act as a very effective barrier with regards to gas migration up to 600,000 years after the closure of the repository. At 1,000,000 years, the simulation results show that some gas can reach the shallow bedrock (e.g., Salina formation) groundwater zone.

Table 5.1. Material properties for Sherman Fall

Parameters	Value
k_{max} Permeability (at damage max. $D_{kmax}=0.3$) (m^2)	4.75×10^{-18}
Initial porosity	0.01
Initial saturation (%)	100
Residual saturation (%)	0
Modulus of elasticity (GPa)	26.45
Poisson ratio	0.23
van Genuchten's parameters	
L	1
M	0.5
α (1/m)	0.003
Damage equation parameters	
Strain ε^o	0.9×10^{-4}
Residual strength (MPa)	0.8
Permeability vs Porosity fitting constant (A)	200

Table 5.2. Material properties for Cobourg Limestone

Parameters	Value
k_{max} Permeability (at damage max. $D_{kmax}=0.3$) (m^2)	8.75×10^{-18}
Initial porosity	0.02
Initial saturation (%)	100
Residual saturation (%)	0
Modulus of elasticity (GPa)	36.04
Poisson ratio	0.19
van Genuchten's parameters	
L	1
M	0.5
α (1/m)	0.003
Damage equation parameters	
Strain ε^o	0.9×10^{-4}
Residual strength (MPa)	1.0
Permeability vs Porosity fitting constant (A)	200

Table 5.3. Material properties for Shale

Parameters	Value
k_{max} Permeability (at damage max. $D_{kmax}=0.3$) (m^2)	7.75×10^{-18}
Initial porosity	0.09
Initial saturation (%)	100
Residual saturation (%)	0
Modulus of elasticity (GPa)	7.3
Poisson ratio	0.09
van Genuchten's parameters	
L	1
M	0.5
α (1/m)	0.003
Damage equation parameters	
Strain ε^o	0.9×10^{-4}
Residual strength (MPa)	0.8
Permeability vs Porosity fitting constant (A)	200

Table 5.4. Main properties of the shaft adopted (worst case scenario for a failed shaft; data from NWMO2011e)

Property	Value
Hydraulic conductivity (m/s)	10^{-7}
Permeability (m ²)	10^{-14}
Density (kg/m ³)	2500
Poisson ratio (-)	0.2
Modulus of elasticity (GPa)	20
Porosity	0.5
Biot coefficient	0.9

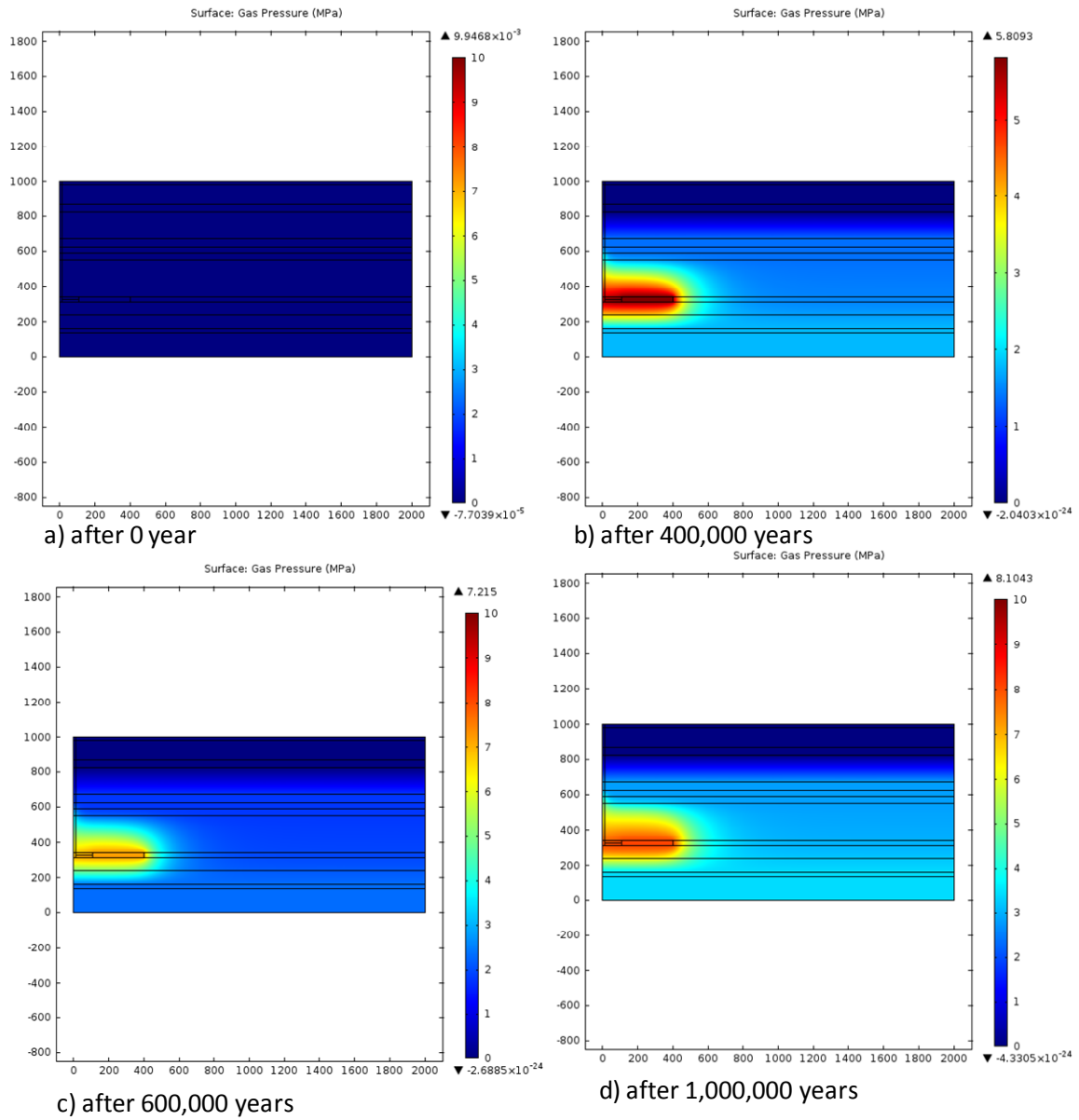


Figure 5.3. Spatial distribution of the gas pressure (MPa) vs time (normal scenario)

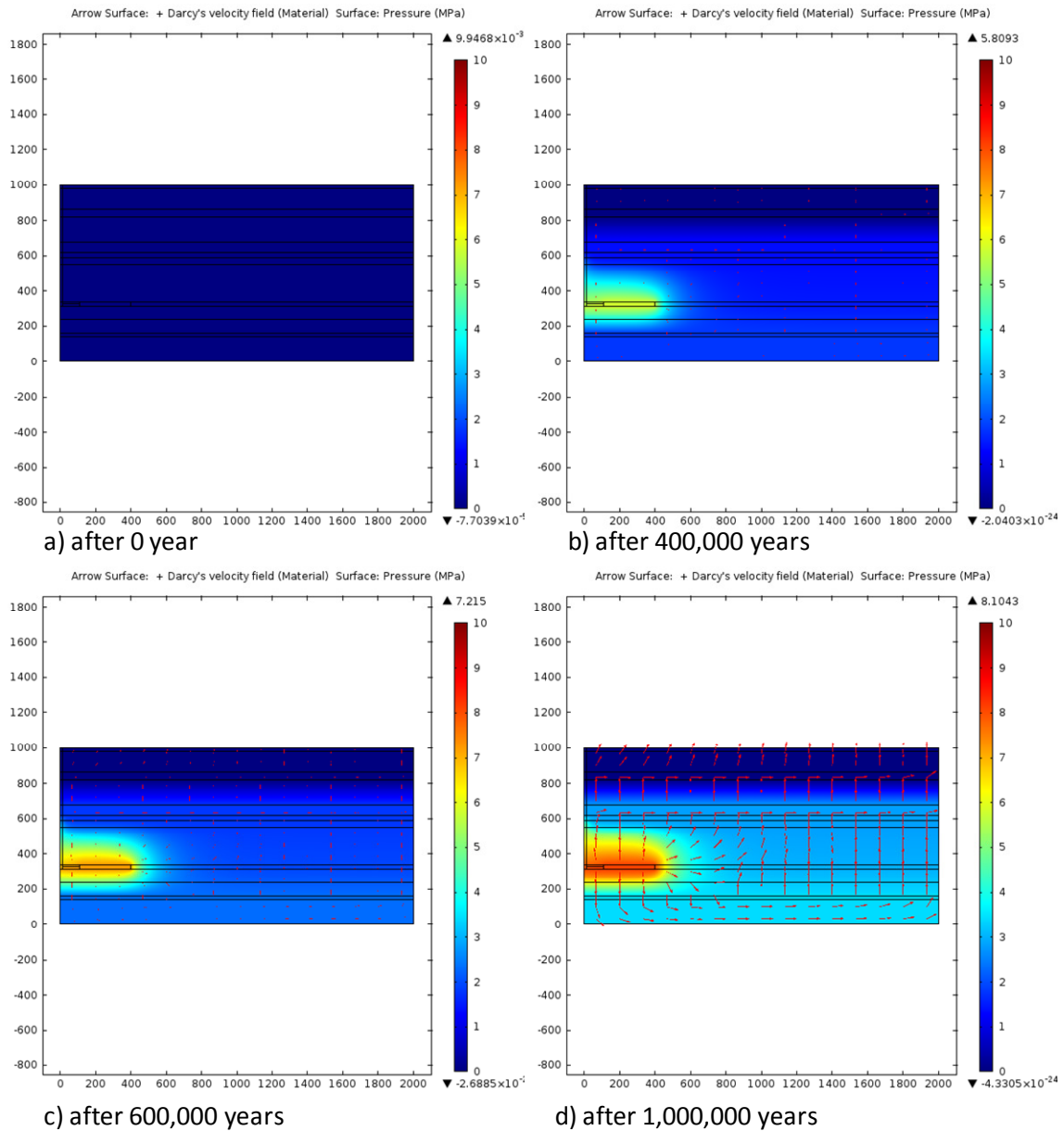


Figure 5.4. Evolution of the gas flow velocity and gas pressure (normal scenario)

The main simulation results with regards to the worst case scenario (Peak gas pressure = 15 MPa, shaft failed) are presented in Figures 5.5-5.7. Figure 5.5 shows the spatial distribution and temporal evolution of the gas pressure in the DGR repository and host rock. The 3D representation of the gas saturation distribution after 1,000,000 years is given in Figure 5.6. Figure 5.6 presents the spatial distribution of the gas pressure and gas flow velocity in the study area after 0 year, 400,000, 600,000 and 1,000,000 years, respectively. Again, the analysis of the Figures 5.5, 5.6 and 5.7 shows that, at 1,000,000

years, the gas flowing upward through the host rock and failed shaft can reach the shallow bedrock (e.g., Salina formation) groundwater zone. Consequently, the effects of gas reaching the shallow rock formations, particularly when the shaft fails, should be considered in the safety assessment.

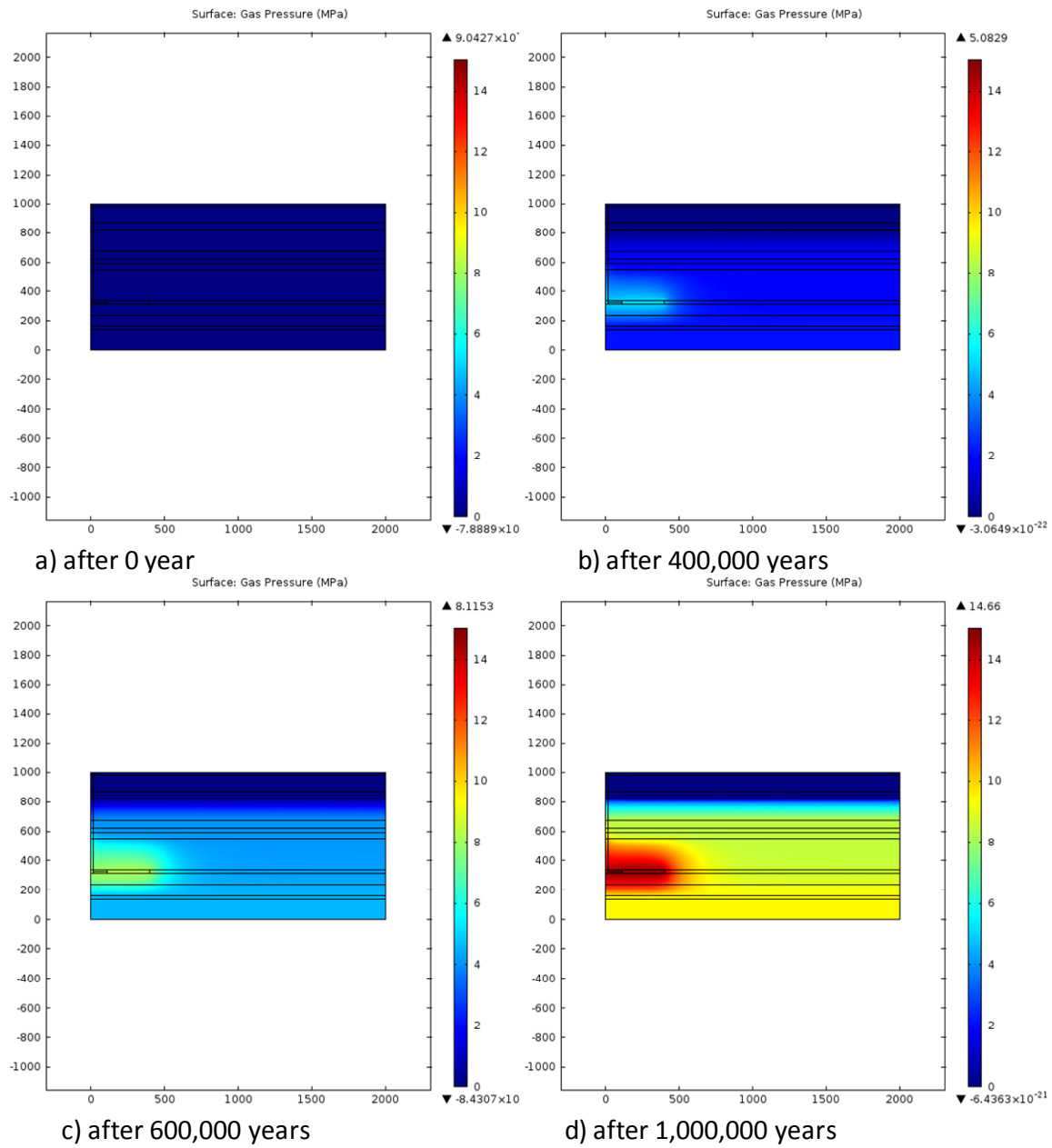


Figure 5.5. Spatial distribution of the gas pressure (MPa) vs time (worst case scenario)

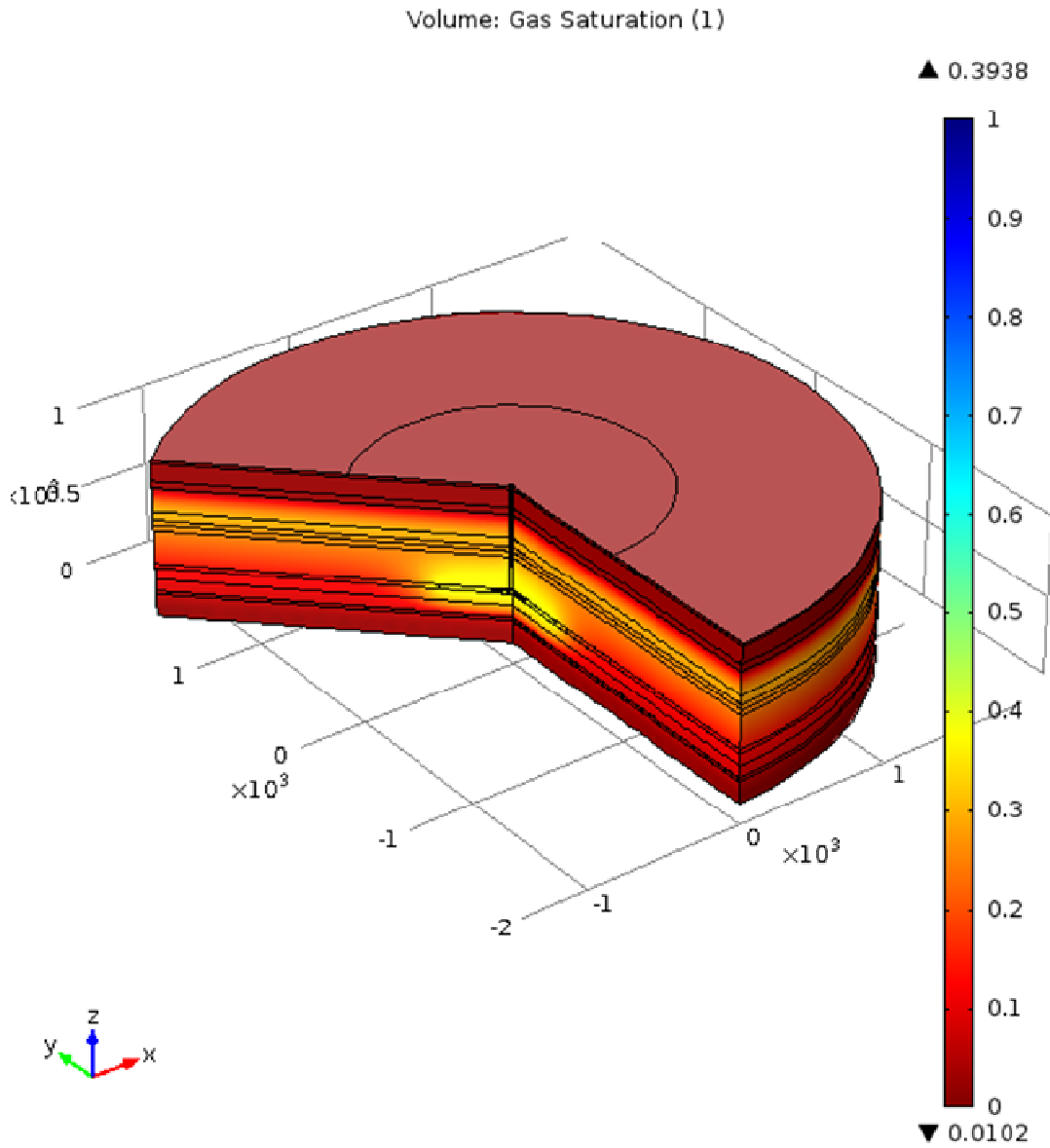


Figure 5.6. Spatial distribution of the gas saturation after 1,000,0000 years (worst case scenario)

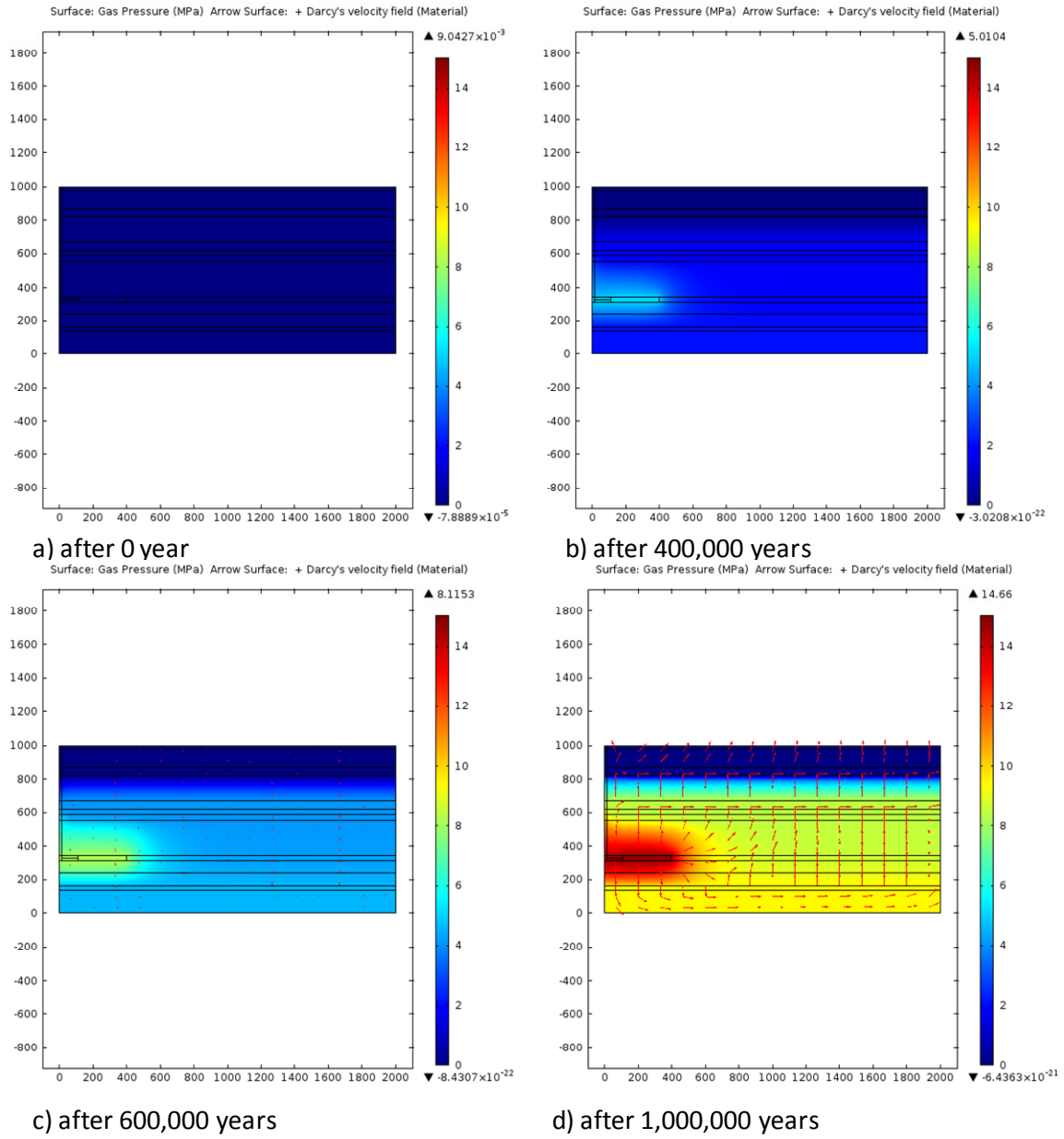


Figure 5.7. Evolution of the gas flow velocity and gas pressure (worst case scenario)

6 Conclusion

The following objectives are achieved in the present work:

- Review of the current experimental and theoretical research on gas generation and migration from a repository in sedimentary rock formations. Comprehensive review of the state-of-art conceptual and mathematical models for the simulation of gas generation and transport. Based on the extensive literature review, valuable information on gas generation and transport mechanisms, conceptual and modelling approaches as well as experimental studies on gas generation and transport are obtained.
- Compilation of published geochemical, mechanical, hydraulic and thermal data on sedimentary rock formations in Ontario, which are relevant to the study of gas generation and transport. Review and analysis of the results of gas transport tests performed in European URLs. Comparison of the Ontario data to those from European sedimentary rocks. Discussion and analysis of the usefulness and transferability of the research results in Europe to the Ontario situation.
- Development of a THM model to predict and analyze gas migration from a DGR in sedimentary rocks induced by gas migration. The developed THM model is successfully validated against laboratory and field gas injection tests performed on European host sedimentary rocks (Opalinus Clay).
- Application of the developed model to simulate laboratory and field gas injection tests on Opalinus Clay as well as predict the gas migration in Ontario's host sedimentary rocks. Relevant results are obtained. It is found that, up to 600,000 years after the closure of the proposed DGR in Ontario and regardless of the scenario considered (normal, worst case), the high gas pressure and gas migration will still remain in the natural shale barrier layer. This is positive with regards to the safety of the DGR and may suggest that the limestone and shale formations act as a very effective barrier with regards to gas migration up to 600,000 years after the closure of the repository. In contrast, at 1,000,000 years and independently of the scenario selected, the simulation results show that the gas flowing (upward) through both the DGR and the shaft can reach the shallow bedrock (e.g., Salina formation) groundwater zone. The quantity of gas reaching

- the shallow bedrock should be estimated for use in long term safety assessments. The estimate of that quantity should be performed using mathematical models developed based on sound physical principles derived from available experimental data. Such an example of model development is shown in this study.
- Furthermore, the gas migrating through the host rock could induce a complex interplay of multiphase flow, dissolution/precipitation, and geochemical reactions that may have significant impacts on the long-term performance of the host rock. Thus, the effects of gas-fluid-rock interactions on the performance of the host rock should be investigated in the future studies.
 - The commercial finite element (FE) software (COMSOL Multiphysics) used in this study (as recommended by CNSC) is a very userfriendly FE software which is capable of handling multiphysic problems. However, it has shown several and serious numerical stability problems in the modeling of gas migration (particularly in the Ontario's sedimentary rocks) due to the complexity of the coupled processes, and boundary and intitial conditions considered as well as the strong non-linearity of the equations (especially the capillary pressure). Signicant amount of time was spent to solve the stability problems mentioned above. These stability issues should be addressed by COMSOL Multiphysics to improve the performance of the software with regards to numerical stability.

7 References

- Ahrenholz B., Tölke J., Lehmann P., Peters A., Kaestner A., Krafczyk M., Durner W. (2008). Prediction of Capillary Hysteresis in a Porous Material Using Lattice-Boltzmann Methods and Comparison to Experimental Data and a Morphological Pore Network Model. *Advances in Water Resources*, Volume 31, Issue 9. Pages 1151-1173.
- Alkan H., Cinar Y., Pusch G. (2007). Rock salt dilatancy boundary from combined acoustic emission and triaxial compression tests, *International Journal of Rock Mechanics and Mining Sciences* 44 (1) (2007), pp. 108–120.
- Alkan H., Müller, W. (2008). Approaches for modelling gas flow in clay formations as repository systems. In: *J. Phys. Chem. Earth*. 33, 2008, p. 5260 - 5268.
- Alonso E.E., Olivella S., Arnedo D. (2006). Mechanisms of gas transport in clay barriers, *Journal of Iberian Geology* 32 (2) (2006), pp. 175–196.
- ANDRA (2005). Dossier 2005 Argile. Les recherches de l'Andra sur le stockage géologique des déchets radioactifs à haute activité et à vie longue. Collection les rapports.
- Arnedo D., Alonso E.E., Olivella, Romero E. (2008). Gas injection tests on sand/bentonite mixtures in the laboratory. Experimental results and numerical modelling. *Physics and Chemistry of the Earth, Parts A/B/C*. Volume 33, Supplement 1, 2008, Pages S237-S247.
- ASM. (1987). Corrosion of Carbon Steels. In *Metals Handbook*, Ninth edition, Volume 13, Corrosion. American Society for Metals International, Metals Park, OH, pp. 509-530.
- Bai M., Elsworth D. (2000). Coupled processes in subsurface deformation, flow, and transport – Mathematics - 334 p.
- Bear J, Bachmat Y. (1991). Introduction to modeling of transport phenomena in porous media. Netherlands: Kluwer Academic, Publisher, 1991. 553 p.
- Biot M.A. (1941). General theory of three-dimensional consolidation - *Journal of applied physics* 12: 155-164.
- Blümling P., Bernier F., Lebon P., Martin C.D. (2007). The Excavation Damaged Zone in Clay Formations Time-Dependent Behaviour and Influence on Performance

- Assessment. *Physics and Chemistry of the Earth, Parts A/B/C*, Volume 32, Issues 8-14, Pages 588-599.
- Chen W., Tan X., Yu H. Wu G., Jia S. (2009). A fully coupled thermo-hydro-mechanical model for unsaturated porous media. *Journal of Rock Mechanics and Geotechnical Engineering* 1(1):31-40.
- Collin F., Li X. L., Radu J. P., Charlier R. (2002). Thermo-Hydro-Mechanical Coupling in Clay Barriers. *Engineering Geology* 64: 179-193.
- Crane Co. (1988). Flow of fluids through Valves, fittings and Pipe. Technical paper No. 410, 1988. Crane Company, Joliet, Illinois.
- Dain J. F. (1989). Condensation and isothermal water transfer in cement mortar, Part II- transient condensation of water vapour. *Transport in Porous media* 44: 1-16.
- Damjanac B. (2008). Phase I Long-Term Cavern Stability, OPG 00216-REP-01300-00005-R00.
- Autio J., Gribi P., Johnson L., Marschall P. (2006). Effect of excavation damaged zone on gas migration in a KBS-3H type repository at Olkiluoto. *Physics and Chemistry of the Earth, Parts A/B/C* Volume 31, Issues 10-14, 2006, Pages 649-653.
- Barrenblatt G.I., Zheltov I.P., Kochina I.N. (1960). Basic concepts in the theory of seepage on homogeneous liquids in fissured rocks, *Journal of Applied Mathematics* **24** (1960), pp. 1286–1303.
- Bear, J. (1972): *Dynamics of fluids in porous media*. American Elsevier Pub., New York.
- Bennethum L.S., Murad M.A., Cushman J.H. (1997). Modified Darcy's law, Terzaghi's effective stress principle and Fick's law for swelling clay soils, *Computers and Geotechnics* 20 (¾), pp. 245–266.
- Blumling P., Bernier F., Lebon B., Martin D. (2007). The excavation damaged zone in clay formations time-dependent behaviour and influence on performance assessment, *Physics and Chemistry of the Earth* 32, 588–599.
- BNFL, 2002a. Drigg Post-Closure Safety Case: Near-Field Biogeochemistry. BNFL Report.
- Brown R.C. (1999). A multiple front propagation model for gas migration through clay, *Engineering Geology* 54 (1999), pp. 151–158

- Brush LH, Garner JW, Storz LJ (1994). Development of a gas generation model for the waste Isolation Pilot Plant. Scientific basis for nuclear waste management XVII. In Barkatt A., Van Konynenburg RA (eds); Proceedings of Materials Research Society Symposium, vol. 333: 241-246.
- Dagan G. (1989). Flow and transport in porous formations. Springer Press, New York.
- Damjanac B. (2008). Phase I Long-Term Cavern Stability, OPG 00216-REP-01300-00005-R00.
- Davies P. B. (1991). Evaluation of the Role of Threshold Pressure in Controlling Flow of Waste-Generated Gas Into Bedded Salt at the Waste Isolation Pilot Plant (WIPP). Sandia Rep. SAND 90-3246, Sandia National Laboratories, Albuquerque, New Mexico.
- Davis J.P., Davis D.K. (1999). Stress-dependent permeability: characterization and modeling. Society of Petroleum Engineers 6 (2): SPE Paper no 56813:224-235.
- Davy C.A., Skoczylas F., Barnichon J.-D., Lebon P. (2007). Permeability of macro-cracked argillite under confinement: Gas and water testing Physics and Chemistry of the Earth, Parts A/B/C, Volume 32, Issues 8-14, 2007, Pages 667-680.
- DECHEMA. (1990). Corrosion Handbook: Corrosive Agents and their Interaction with Materials, Volume 7, and Atmosphere.
- Delahaye C. H., Alonso E. E. (2002). Soil Heterogeneity And Preferential Paths For Gas Migration; Engineering Geology, Volume 64, Issues 2.3, May 2002, Pages 251-271.
- Dixon D.A. (2000). Pore-Water Salinity and the Development of Swelling Pressure in Bentonite Based Buffer and Backfill Materials. Nagra Technical Report 00-04.
- Du Y., Wang W., Kolditz O. (2006). Dual-Continua Model for Unsaturated Flow and Application to Decovalex Task D, Geosys Preprint-10. Tübingen, March 2006.
- Duppender S.J., Dohmen L., Welte D.H. (1997). Numerical modelling of petroleum expulsion in two areas of the lower saxony basin, northern Germany. In: Petroleum Migration, Geol. Soc. of London, Special Publication 59, pp. 47-64.
- Fall M. (2009). Review of Research on Gas Generation and Transport; A report submitted to the CNSC; Ottawa, Canada.
- Fenchel T., King G.M., Blackburn T.H. (2000). Bacterial Biogeochemistry: The ecophysiology of Mineral Cycling, Academic Press, San Diego, USA (2000).

- Feng XT., Hudson JA.(2004). The Ways Ahead For Rock Engineering Design Methodologies. *Int J Rock Mech Min Sci*; 41:255–73.
- Finsterle S. (1999). ITOUGH2 User's Guide. Report LBNL-40040 Lawrence Berkeley National Laboratory, Berkeley, Calif.
- François B., Laloui L., Laurent C. (2009). Thermo-Hydro-Mechanical Simulation of ATLAS in Situ Large Scale Test in Boom Clay. *Computers and Geotechnics*, Volume 36, Issue 4, May 2009, Pages 626-640.
- Gelhar L.W. (1993): Stochastic subsurface hydrology. Prentice Hall, 390pp.
- Galle C., 2000. Gas breakthrough pressure in compacted Fo–Ca clay and interfacial gas overpressure in waste disposal context. *Appl. Clay Sci.* 17, 85–97.
- Gartner Lee Limited. (2008). Phase I Regional Geology, Southern Ontario. Supporting Technical Report for OPG's Deep Geological Repository for Low and Intermediate Level Wastes. Prepared for Ontario Power Generation. OPG 00216-REP-01300-00007-R00.
- Gawin D., Majorana C.E., Schrefler B.A. (2001). Modelling thermo-mechanical behaviour of high performance concrete in high temperature environment, *Fracture mechanics of concrete structure*, de Borst et al. (eds).
- Gerard P., Charlier R., Barnichon J.D, Su K. (2008). Numerical Modelling of Coupled Mechanics and Gas Transfer around Radioactive Waste in Long- *Journal of Theoretical and Applied Applied Mechanics* 38(1-2): 25-44.
- Gerke H.H., van Genuchten M.T. (1993). A dual-porosity model for simulating the preferential movement of water and solutes in structured porous media, *Water Resources Research* 29 (2) (1993), pp. 305–320.
- Gorski, B., T. Anderson and B. Conlon. 2009a. Laboratory Geomechanical Strength Testing of DGR-1 & DGR-2 Core. Intra Engineering Ltd. Document TM-07-03 Rev.1. CANMET Mining and Mineral Sciences Laboratories, Natural Resources Canada. Ottawa, Canada.
- Gorski, B., T. Anderson and B. Conlon. 2009b. DGR-2 Long-Term Strength Degradation

- Tests, Bruce DGR Project - Task GM5. Intera Engineering Ltd. Document TM-08-11R01. CANMET Mining and Mineral Sciences Laboratories, Natural Resources Canada. Ottawa, Canada.
- Gorski, B., T. Anderson and B. Conlon. 2010a. Long-Term Strength Degredation Testing of DGR-3 & DGR-4 Core. Intera Engineering Ltd. Report TR-08-36 Rev.1. CANMET Mining and Mineral Sciences Laboratories, Ottawa, Canada.
- Gorski, B., T. Anderson and B. Conlon. 2010b. Laboratory Geomechanical Strength Testing of DGR-2 to DGR-6 Core. Intera Engineering Ltd. Report TR-09-07 Rev.0. CANMET Mining and Mineral Sciences Laboratories, Ottawa, Canada.
- Gorski, B., T. Anderson and B. Conlon. 2010c. Supplementary Uniaxial Compressive Strength Testing of DGR-3 and DGR-4 Core. Intera Engineering Ltd. Report TR-08-39 Rev.1. Ottawa, Canada.
- Graham J., Plant R., Small J., Smalley D. (2003). Program User's Guide for the code GRM, Version 4.1. BNFL Report 00/EN0127/7/1. 2002 Post Closure Safety Case Report DTP/150.
- Green J.R., Hillesland V.E., Roetman J.G. 1998. Radcalc for Windows Version 2.01. Volume I: User's Manual and Radcalc for Windows Version 2.01 Volume II: Technical Manual, HNF-2549, Rev. 0, Westinghouse Hanford Company, Richland Washington.
- Harrington J.F., Horseman S.T., and Noy, D.J. (2001). Swelling and Osmotic Flow in a Potential Host Rock. In: Delage, P. (ed.): Proc. of the 6th International Workshop on Key Issues in Waste Isolation Research (KIWIR-2001), Ecole Nationale des Ponts et Chaussées, Paris, France, 28-30 November.
- Honda A., Teshima T., Tsurudome K., Ishikawa H., Yusa Y. and Sasaki N. (1991). Effect of Compacted Bentonite on the Corrosion Behaviour of Carbon Steel as Geological Isolation over Pack Material. Materials Research Society Symposium Proceedings 212 (Materials Research Society, Pittsburgh, PA), pp. 287-294.
- Hohenemser H., Prager W. (1932). Ueber die Ansaetze der Mechanik der isotorper Kontinua. Journal of Angewandte Mathematik und Mechanik 12:216-226.
- Horne R.N. (1995). Modern Well Test Analysis. Petroway Inc., Palo Alto, California.

- Horseman S., Harrington J.F. and Sellin P. (1999). Gas Migration in Clay Barriers. *Eng. Geol.* 54, 139 – 149.
- Horseman and Harrington, 1994. Horseman, S.T., Harrington, J.F., 1994. Migration of repository gases in an overconsolidated clay. British Geological Survey Technical Report WE/94/7.
- Horseman S.T. Harrington J.F., (1996). Evidence for Thresholds, Pathways and Intermittent Flow in Argillaceous Rocks, Nuclear Energy Agency Workshop, Fluid Flow Through Faults and Fractures in Argillaceous Media, Berne, June 10–12.
- Horseman S.T., Harrington, J.F. (1997). Study of gas migration in Mx80 buffer bentonite. BGS internal report WE/97/7 to SKB.
- Horseman S.T., Harrington J.F., Sellin P. (1999). Gas migration in clay barriers. *Engineering Geology*, 54: 139-149.
- Horseman S. (2000). Gas migration through indurated clays (mudrocks). In *Proceedings of the Workshop: Gas Generation and Migration in Radioactive Waste Disposal Safety-relevant Issues*, pp-81-85.
- Horseman S.T. (2001). Gas Migration through Indurated Clays (Mudrocks). In: *Gas Generation and Migration in Radioactive Waste Disposal. Proc. of the NEA Workshop in Reims 2000, France.*
- Hua S., Kristof S. (2009). Permeability Measurements of Opalinus Clay (Mont Terri) HG-B: Combined Permeability Tests and Borehole Seismic Measurements. Technical report, 9Y3211030000
- Humphreys P.N., Johnstone T., Trivedi D., Hoffmann A., (1995). The biogeochemical transport code DRINK: a mechanistic description. In: *Materials Research Society. Symp. Proc.*, vol. 353, pp. 211–218.
- Humphreys P., McGarry R., Hoffmann A., Binks P., (1997). DRINK: a biogeochemical source term model for low level radioactive waste disposal sites, *FEMS Microbiol. Rev* 20 (1997), pp. 557–571.
- Intera Engineering Ltd.(2008a). OPG’s Deep Geologic Repository for L and IL Waste, Phase 2 Geoscientific Site Characterization Plan. OPG 00216-REP-03902.00006-R00.
- Jang JSR. Sun CT., Mizutani E. (1997). *Neuro-Fuzzy and Soft Computing* .Englewood Cliffs, NJ: Prentice-Hall; 1997.

- Jennings, J. E. B., Burland, J. B. (1962). Limitations to the use of effective stresses in unsaturated soils. *Geotechnique* 12: 125–144.
- Johnson L., Marschall P., Wersin P., Gribi P. (2005). HMCBG Processes Related to the Steel Components in the KBS-3H Disposal Concept. Posiva Working Report 2005–09. Posiva Oy, Eurajoki, Finland.
- Jones FO, Owens WW. (1980). A Laboratory Study of Low-Permeability Gas Sands. *J Pet Technology*: 1631–40.
- Joshi P.S., Venkateswaran G., Venkateswarlu K.S., Anaji Rao K. (1993). Simulated decomposition of $\text{Fe}(\text{OH})_2$ in the presence of AVT chemicals and metallic surfaces—relevance to low-temperature feedwater line corrosion. *Corros. Sci.* 49 (4), pp. 300–309.
- Kachanov L. M. (1958). Time of the rupture process under creep conditions. *IZV. AN SSSR, OTD. TEHN. NAUK* (1958) (NO 8): 26-31 (In Russian).
- Kadanoff L. P. (1966). Scaling laws for Ising models near T_c . *Physics* 2: 263–272.
- Khalili N. Loret B. (2001). An elasto-plastic model for non-isothermal analysis of flow and deformation in unsaturated porous media: formulation. *International Journal of solids and structures* 38 (46-47):8305-8330.
- Klinkenberg L. J. (1941). *The Permeability of Porous Media to Liquids and Gases*. American Petroleum Institute, *Drilling and Productions Practices*, 200–213.
- Kohonen T. (1987). *Self-Organization and Associate Memory*. 2nd ed. Berlin: Springer.
- Krajcinovic D. (1996). *Damage Mechanics*. Elsevier, Amsterdam.
- Kuhl D., Bangert F., Meschke G. (2004). Coupled Chemo-Mechanical Deterioration of Cementitious Materials. Part I: Modeling. *International Journal of Solids and Structures* 41:15–40
- Lege T., Shao H., (1996). The Brush Model—a New Approach to Numerical Modelling of Matrix Diffusion in Fractured Claystone, Fluid Flow Through Faults and Fractures in Argillaceous Formations, NEA/EC Workshop, Berne, June.
- Lemaitre J. (1971). Evaluation of dissipation and damage in metals submitted to dynamic loading. *Proc. I.C.M.* 1, Kyoto, Japan.
- Lemaitre J., Chaboche J.-L. (1990). *Mechanics of Solid Materials*. Cambridge University Press, London.

- Leverett M.C. (1941). Capillary behaviour in porous solids. Transactions of the AIME (142): 159–172.
- Li S., Wu XY., Ma FS. (1998). Application of Precedent Type Analysis (PTA) In the Construction of the Ertan Hydro-Electric Station China. Int J Rock Mech Min Sci 1998; 35(6):787–95.
- Lide, D. (ed.) (2000): Handbook of chemistry and physics, CRC Press. Boca Raton, Florida.
- Marshall T.J., Holmes J.W. (1988). Soil Physics. Cambridge University Press, Bristol, England, 317 p.
- Marschall P., Horseman S., Gimmi T. (2005). Characterisation of Gas Transport Properties of the Opalinus Clay, a Potential Host Rock Formation for Radioactive Waste Disposal. Oil & Gas Science and Technology – Rev. IFP, Vol. 60 (2005), No. 1, pp. 121-139.
- Maßmann J., Ziefle G., Kohlmeier M., Zielke W., Shao H. (2006). Coupled hydro-mechanical modeling of seasonally affected unsaturated claystone. In: GeoProc 2006 – Second International Conference on Coupled T-H-M-C Processes in Geo-systems: Fundamentals, Modeling, Experiments and Applications, Nanjing, China 05/2006.
- Mazars J. (1984). Application de la mecanique de l'endommagement au comportement non lineaire et la rupture du beton de structure. Thesis of Doctorat d'Etat, L. M. T., Universite de Paris, France.
- Mazars J. (1986). A description of micro and macroscale damage of concrete structures. Journal Engineering Fracture Mechanics, 25:729–737.
- Mazars J. (1986). Description of the behaviour of composite concretes under complex loadings through continuum damage mechanics. reprinted from Proc. 60th °.S. National Congress of Applied Mechanics, J. P. Lamb ed., published by The American Society of Mechanical Engineering.
- Mazars J., Pijaudier-Cabot J. (1989). Continuum damage theory-application to concrete. Journal of Engineering Mechanics ASCE, 115(2): 345-365.
- Mazurek, M. (2004). Long-term used nuclear fuel waste management – Geoscientific-review of the sedimentary sequence in southern Ontario- Report NWMO. 116 p.

- Mazurek M., Gautschi A., Marschall P., Vigneron G., Lebon P., Delay J.(2008). Transferability of Geoscientific Information from Various Sources (Study Sites, Underground Rock Laboratories, Natural Analogues) to Support Safety Cases for Radioactive Waste Repositories in Argillaceous Formations; Physics and Chemistry of the Earth 33 ; S95–S105.
- McFadden J.G. (1999). Radcalc for Windows Benchmark Study: A comparison of Software Results with Rocks Flats Hydrogen Gas Generation Data. Safety Analysis 99’.
- McFadden J.G., Hillesland K.E., Field J.G. (1998). Radcalc for Windows Version 2.01. Volume I: User’s Manual and Radcalc for Windows Version 2.01 Volume II: Technical Manual, HNF-2549, Rev. 0, Westinghouse Hanford Company, Richland Washington.
- McGinnes D.F. (2002). Model Radioactive Waste Inventory for Reprocessing Waste And Spent Fuel. Nagra Technical Report NTB 01.01. Nagra, Wettingen, Switzerland.
- Metcalf R, Watson SP, Rees, P (2008). Gas generation and migration from a deep geological repository for radioactive waste - A review of Nirex/NDA’s work. NWAT Report: NWAT/NDA/RWMD/2008/002.
- Meschke G., Grasberger S. (2003). Numerical modeling of coupled hydromechanical degradation of cementitious materials. Journal of Engineering Mechanics 129(4): 383-392.
- Millington R.J., Quirk J.P. (1961). Permeability of porous solids. Trans. Faraday Soc. 57: 1200-1207.
- Mongelli, L., Loddo, m., and Tramacere, A. (1982), Thermal Conductivity, Diffusivity and Specific Heat Variation of Some Travale (Tuscany) Rocks versus Temperature, Tectonophysics 83, 33-43.
- Mueller (1992). Produktion und Verbleib von Gasen im Grubengebäude eines salinaren Endlagers. GSF-Bericht 3/92, Braunschweig.
- Mueller W. (2000). Gas generation. In Proceedings of the Workshop: GGM in RWD, pp-67-72
- Nagra (2002a). Projekt Opalinuston – Synthese der geowissenschaftlichen Untersuchungsergebnisse. Entsorgungsnachweis für abgebrannte Brenn-elemente,

- verglaste hochaktive sowie langlebige mittelaktive Abfälle. Nagra Tech. Rep. NTB 02-03. Nagra, Wettingen, Switzerland.
- Nagra (2002b). Projekt Opalinuston – Konzept für die Anlage und den Betrieb eines geologischen Tiefenlagers. Entsorgungsnachweis für abgebrannte Brennelemente, verglaste hochaktive sowie langlebige mittelaktive Abfälle. Nagra Tech. Rep. NTB 02-02. Nagra, Wettingen, Switzerland
- Nagra (2004). Effects of post-disposal gas generation in a repository for spent fuel, high-level waste and long-lived intermediate level waste sited in Opalinus Clay. Nagra Technical Report NTB 04-06, Nagra, Wettingen, Switzerland.
- Nagra (2008). Konzept für die Anlage und den Betrieb eines geologischen Tiefenlagers. Entsorgungsnachweis für abgebrannte Brennelemente, verglaste hochaktive sowie langlebige mittelaktive Abfälle. Technical Report, 175 p.
- Nauk D., Klawoon F., Kruse R. (1997). Foundations of Neuro-Fuzzy Systems. New York: Wiley; 1997.
- Nuclear Waste Management Organization (2011). Geosynthesis. NWMO DGR-TR-2011-11
- Nuth M., Laloui L. (2007). Effective Stress Concept in Unsaturated Soils: Clarification and Validation of a Unified Framework. International Journal for Numerical Analytical Methods In Geomechanics 32: 771-801.
- Olivella S., Gens A., Carrera J., Alonso E.E. (1995). Numerical formulation for a simulator (CODE_BRIGTH) for the coupled analysis of saline media. Engineering Computations, 13: 87-112.
- Ortiz L., Impey M., Einchomb S. (1996). Characterization of Gas Flow in Boom Clay, a Low Permeability Plastic Rock, Fluid Flow through Fractures in Argillaceous Formations, NEA /EC Workshop June 1996.
- Ortiz L., Volckaert G., de Cannière P., Put M., Sen A., Horseman S., Harrington J., Impey M. and Einchcomb S. (1997). MEGAS – Modeling and Experiments on Gas Migration in Repository Host Rocks. Final report: Phase2. EUR 17453 EN. European Commission, Brussels, Belgium.

- Ortiz L., Volckaert G., Mallants D. (2001). Gas generation and migration in Boom Clay, a potential host rock formation for nuclear waste storage. *Engineering Geology* 64: 287-296.
- Ortiz L., Volckaert G., Mallants D. 2002. Gas generation and migration in Boom Clay, a potential host rock formation for nuclear waste storage. *Engineering Geology*, Volume 64, Issues 2.3, Pages 287-296.
- Pal S.K. and Mitra P. (2004), *Pattern recognition algorithms for data mining*, CRC Press, Boca Raton, Florida.
- Pawlak Z. (1982). Rough Sets. *Int J Comput Inform Sci* 11, pp. 341–356.
- Pawlak Z. (1991). *Rough Sets: Theoretical Aspects Reasoning About Data*. Kluwer, Boston .
- Parkhurst D.L., Thorteston D.C., Plummer L.N. (1980). PHREEQE-A computer program for geochemical calculations. *US Geol. Surv., Water Resour. Invest. Rep.* 80-96. Available from: <<http://water.usgs.gov/software/phreeqe.html>>.
- Popp T., Salzer K. (2007). Anisotropy of seismic and mechanical properties of Opalinus clay during triaxial deformation in a multi-anvil apparatus. *Physics and Chemistry of the Earth Parts A/B/C* 32 (8–14): 879–888.
- Pusch R., Ranhagen L., Nilsson K. (1985). *Gas Migration through MX-80 Bentonite*, Nagra Technical Report, NTB-85-36, Wettingen, Switzerland.
- Reardon E.J. (1995). Anaerobic corrosion of granular iron: measurement and interpretation of hydrogen evolution rates. *Environ. Sci. Technol.* 29, pp. 2936–2945.
- Rodwell (1999). Gas migration and two-phase flow through engineered and geological barriers for a deep repository for radioactive waste. *A Joint EC/NEA Status Report*, EUR 19112 EN, Brussels.
- Rodwell, 2000. W. Rodwell, Editor, *Research into previous term Gasnext term Generation and Migration in Radioactive Waste Repository Systems (PROGRESS Project)*. Final Report European Commission, [Report] EUR 19133 EN (2000).
- Rodwell W., Norris S., Cool W., Cunado M., Johnson L., Maentynen M., Sellin P., Snellman M., Talandier J., Vieno T., Vines S. (2003). *A Thematic Network on gas issues in safety assessment of deep repositories for radioactive waste (GASNET)*. Final report, EURATOM, 45 p.

- Romero, E., Garcia, I., Alonso, E., GMT/IR 02-02: Laboratory tests on compacted sand/bentonite buffer material used in the GMT in-situ emplacement, Nagra Project Report 03-03, Wettingen, CH, 2003.
- Romero E. and Castellanos E. (2006). Tests On In Situ Sand/Bentonite Buffer Material. UPC report.
- Russell S.B. and Simmons G.R. (2003). Engineered Barrier System for A Deep Geological Repository in Canada. In Proc. 10th Int. High-Level Radioactive Waste Management Conf., Las Vegas, NV, March 30-April 2, 2003 (American Nuclear Society, La Grange Park, IL), pp. 563.570.
- Rutqvist J., Boergesson L., Chijimatsu M., Kobayashi L., Jing L., Nguyen T.S., Noorishad, Tsang C.F.. (2001). Thermohydromechanics of partially saturated geological media: governing equations and formulation of four finite element models. International Journal of Rock Mechanics and Mining Sciences 38:105–127.
- Sander, R. 2010. Henry's constant solubilities. www.henrys-law.org.
- Schikorr G.Z. (1929). The iron–water system. Elektrochimica **35**, pp. 62–65.
- Senger R., Marschall P. and Lavanchy J.-M. (1998). Gas Threshold Pressure Tests in Deep Boreholes for Determining Two-Phase Flow Properties of the Host Rock at the Proposed L/ILW Repository, Switzerland, Mat. Res. Soc., Symp. Proc. Vol. 506, 829-838.
- Senger R., Lanyon B., Marschall P., Vomvoris S., Fujiwara A.(2006a) .Tough2/iTough2 Analysis Of Gas Migration Test (GMT) At The Grimsel Test Site (Switzerland) .PROCEEDINGS, TOUGH Symposium 2006 Lawrence Berkeley National Laboratory, Berkeley, California, May 15–17, 2006.
- Senger R., Enachescu C., Doe T., Distinguin M., Delay J. (2006b). Design and Analysis of a Gas Threshold Pressure Test in Low-Permeability Clay at ANDRA's Underground Research Laboratory, Bure (France). PROCEEDINGS, TOUGH Symposium 2006 Lawrence Berkeley National Laboratory, Berkeley, California, May 15–17, 2006.
- Senger R., Marschall P., Finsterle S. (2008). Investigation Of Two-Phase Flow Phenomena Associated With Corrosion In An SF/HLW Repository In Opalinus Clay, Switzerland. Physics and Chemistry of the Earth, Parts A/B/C, Volume 33, Supplement 1, 2008, Pages S317-S326

- Small J.S., Humphreys P.N., Johnstone T.L., Plant R., Randall M.G., Trivedi D.P. (2000). Results of an aqueous source term model for a radiological risk assessment of the Drigg LLW site, UK. In: Smith R.W., Shoesmith D.W. (Eds.), *Scientific Basis for Nuclear Waste Management XXIII. Materials Research Society Symp. Proc.*, vol. 608, pp. 129–134.
- Small J., Nykyri M., Helin M., Sarlin T., Itäevaara M. (2008). Experimental and modelling investigations of the biogeochemistry of gas production from low and intermediate level radioactive waste. *Applied Geochemistry* 23(6):1383-1418.
- Souley, M. Homand F., Pepa S., Hoxha D. (2001). Damage-induced permeability changes in granite: a case example at the URL in Canada. *International Journal of Rock Mechanics and Mining Sciences* 38(2):297-310.
- Stallman R.W. (1964). Multiphase flow in porous media – A review of theories pertinent to hydrologic studies. US Geological survey, paper no. 411-E, 51 p.
- Su K. (2007). Development of hydro-mechanical models of the Callovo-Oxfordian Argilites for the geological disposal of radioactive waste. MODEX report. EUR 20844.
- Su K. (2007). Development of hydro-mechanical models of the Callovo-Oxfordian Argilites for the geological disposal of radioactive waste. MODEX report. EUR 20844.
- Sykes E.A., Sykes J.F., Normani S.D., Sudicky E.A. and Park Y.J.(2008). Phase I Hydrogeologic modelling. OPG's Deep Geologic Repository for Low and Intermediate Level Waste, Supporting Technical Report. GLL 61.123; OPG 00216-REP-01300-00009-R00.
- Tanai JNC, Gallé C. (1998). Migration des gaz et pression de rupture dans une argile destinée à la barrière ouvragée d'un stockage profond. *Bull. Soc. Geol. France* 169 5, pp. 675–680.
- Tang C. A., Tham L. G., Lee P. K. K., Yang T. H., Li L. C. (2002). Coupled analysis of flow, stress and damage (FSD) in rock failure. *International Journal of Rock Mechanics and Mining Sciences* 39 (4): 477-489.
- Tanikawa W., Shimamoto T. (2009). Comparison of Klinkenberg-Corrected Gas Permeability and Water Permeability in Sedimentary Rocks. *International Journal of Rock Mechanics and Mining Sciences* 46 229– 238.

- Therrien R., Sudicky E.A. and McLaren R.G. (2004). FRAC3DVS; an Efficient Simulator for Three-Dimensional, Saturated-Unsaturated Groundwater Flow and Density-Dependent, Chain-Decay Solute Transport I Porous, Discretely-Fractured Porous or Dual-Porosity Formations. User's Guide. Groundwater Simulations Group, University of Waterloo, Waterloo, Ontario, Canada.
- Thomas H.R., Sansom M.R. (1995). Fully coupled analysis of heat, moisture and air transfer in unsaturated soil. *Journal of Engineering Mechanics* 121(3): 392-405.
- Tong F., Zimmerman W. L. R. (2010). A fully coupled thermo-hydro-mechanical model for simulating multiphase flow, deformation and heat transfer in buffer material and rock masses. *International Journal of Rock Mechanics & Mining Sciences* 47: 205–217.
- Tsang F., Bernier, C. Davies (2005). Geohydromechanical processes in the excavation damaged zone in crystalline rock, rock salt, and indurated and plastic clays, *International Journal of Rock Mechanics and Mining Sciences* 42 (1) (2005), pp. 109–125.
- UKNL (2003). Generic Repository Studies: Generic post-closure Performance Assessment, United Kingdom Nirex Limited, Nirex Report no. N/080.
- Valko P., Economides M.J. (1997). Hydraulic fracture mechanics. John Wiley, New York.
- Van Genuchten M.Th. (1980). A Closed-Form Equation for Predicting the Hydraulic Conductivity of Unsaturated Soils. *Soil Sci. Soc. Am. J.*, Vol. 44.
- Vilks P. and Miller N.H. (2007). Evaluation of Experimental Protocols for Characterizing Diffusion in Sedimentary Rocks. NWMO TR-2007-11.
- Volckaert G., Ortiz L., De Cannière P., Put M., Horseman S.T., Harrington J.F., Fioravante V. and Impey M.D. (1995). MEGAS: Modeling and Experiments on GAS Migration in Repository Host Rocks. Final report phase 1. Eur. Comm., [Rep.] EUR 16235 EN (1995).
- Volckaert G., Bernier F., Sillen X., Van Geet M., Mayor J., Göbel I., Blümling P., Su K. (2004). Similarities and Differences in the Behaviour of Plastic and Indurated Clays. *Euradwaste 2004*.
- Voyiadjis G.Z., Venson A.R. (1995). Experimental damage investigation of a SiC–Ti aluminide metal matrix composite. *International Journal of Damage Mechanics* 4: 338–361.

- Vugrinovich R.(1988). Relationship between regional hydrogeology and hydrocarbon occurrences in Michigan Basin. *J. Pet. Geol.* 11 4 (1988), pp. 429–442.
- Vugrinovich R. (1989). Subsurface Temperatures and Surface Heat Flow In The Michigan Basin And Their Relationships To Regional Subsurface Fluid Movement. *Marine and Petroleum Geology*, Volume 6, Issue 1, February, Pages 60-70.
- Wai, R. S. C., and K. Y. Lo. 1982. Temperature effects on strength and deformation behaviour of rocks in southern ontario. *Canadian Geotechnical Journal* 19, (3): 307-319.
- Warren H., Root P.J. (1963). The behaviour of naturally fractured reservoirs, *Soc. Pet. Eng. J.* (1963).
- Wileveau Y and Bernier F. (2008). Similarities in the Hydromechanical Response of Callovo-Oxfordian Clay and Boom Clay during Gallery Excavation. *Physics and Chemistry of the Earth* 33 S343–S349.
- Xu T., Senger R., Finsterle S. (2008). Corrosion-Induced Gas Generation in a Nuclear Waste Repository: Reactive Geochemistry and Multiphase Flow Effects. *Applied Geochemistry*, Volume 23, Issue 12, December 2008, Pages 3423.3433.
- Yim M-S., Simonson S.A., Sullivant M. (1996). Investigation of ¹⁴C release in an engineered low-level waste disposal facility. *Nuclear*, 114 (2): 254-271.
- Zhang CL. and Rothfuchs T. (2008). Damage and sealing of clay rocks detected by measurements of gas permeability. *Physics and Chemistry of the Earth, Parts A/B/C*, Volume 33, Supplement 1, Pages S363.S373.
- Zienkiewicz O.C., Chan A.H.C., Pastor M., Paul D.K., Shiomi T. (1990). Static and dynamic behaviour of soils: a rational approach to quantitative solutions. I. Fully saturated problems. *Proceedings of the Royal Society of London 1990; Series A Mathematical and Physical Sciences* (429): 285-309.